Stable Heavy Hadrons in ATLAS

Thesis submitted for the degree of
philosophiæ doctor in physics

by

Rasmus Mackeprang

August 10, 2007

Experimental High Energy Physics Group
Niels Bohr Institute
University of Copenhagen

Contents

List of Figures

Everything starts somewhere, though many physicists disagree.

[Terry Pratchett, 1948 -]

Chapter 1

Introduction

The Standard Model (SM) of particle physics has withstood many experimental tests in the last decades. Observations made at high-energy physics experiments have been described in great detail and today we have a solid understanding of physics up to the scale of $\mathcal{O}(100$ GeV). There are, however, compelling arguments that the SM cannot be a fundamental theory of nature. In fact there is reason to expect to see new physics at the TeV scale. This energy scale is becoming accessible with the Large Hadron Collider (LHC) which is presently under construction at CERN outside Geneva, Switzerland. The LHC will be a proton-proton collider operating at a centre of mass energy of 14 TeV. The machine will operate at unprecedented luminosities of up to 10^{34} cm$^{-2}s^{-1}$ allowing for a physics reach solidly into the TeV region.

Several extensions to the SM feature heavy long-lived particles with masses of $\mathcal{O}(10^2 - 10^3$ GeV/c^2) and mean lifetimes fulfilling $c\tau \gtrsim 10$ m. Among such theories are supersymmetric scenarios as well as extra-dimensional models in which the heavy new particles are seen as Kaluza-Klein excitations of the well-known SM particles. Such particles will, from the point of view of a collider experiment be seen as stable. This thesis is concerned with the case where the exotic heavy particles *can* be considered stable while traversing the detector. Specifically the case is considered where the particles in question carry the charge of the strong nuclear force, commonly referred to as *colour charge*. A simulation kit has been developed using GEANT4. This framework is the current standard in experimental particle physics for the simulation of interactions of particles with matter, and it is used extensively for detector simulation. The simulation describes the interactions of these particles with matter which is crucial for the discovery and identification of stable massive particles and the understanding of the possible underlying theories predicting them. The simulation is presented and compared to earlier work. It has been incorporated into the simulation software of the ATLAS experiment allowing for the simulation of full events for the varying physics scenarios. An analysis is presented using the simulation software to evaluate the discovery potential for heavy gluon-like objects exemplified by a quasi-stable gluino as the next-lightest supersymmetric particle (NLSP) of split supersymmetry. This analysis is the first analysis for this type of phenomenology to use full simulation as well as trigger simulation. The detailed analysis is then used as a template to comment on the feasibility of observing stable massive particles as they appear in other models. One such model is here exemplified by an extra-dimensional scenario.

Part I
Theory

There is a theory which states that if ever anyone discovers exactly what the Universe is for and why it is here, it will instantly disappear and be replaced by something even more bizarrely inexplicable.
There is another theory which states that this has already happened.

[Douglas Adams, 1952 - 2001]

Chapter 2

The Standard Model

The theories that have established themselves as providing the best description of particles and phenomena at short distances and high energies are *quantum field theories* (QFTs). While even a cursory review of QFT is beyond the scope of this thesis this chapter will highlight some of the features of QFT and in doing so, the Standard Model (SM) of particle physics will be described up to and including experimental and theoretical motivations to search for extensions beyond the SM.

2.1 Fundamental Symmetries

The SM rests upon the concept of *gauge invariance*. Gauge invariance is the imposition of the requirement that the Lagrangian density of the theory be invariant under certain symmetry transformations. This can be put more plainly as a requirement that the parameters of nature as we measure them be unchanged by these symmetry transformations. As examples of *global* symmetries we have translational invariance:

$$q \to q + \Delta q. \tag{2.1}$$

Here q represents a set of (generalised) coordinates, and the statement that the laws of nature be invariant under translational invariance turns out to be equivalent to demanding conservation of momentum in quantum mechanical transition amplitudes [PS]. The terminology that the symmetry is global means that the transformation is applied to all points in space.

Other examples of global symmetries are Lorentz invariance and rotational invariance. Many models of physics *Beyond the Standard Model* (BSM) also infer or rely on additional global symmetries.

When specifying a complete model in QFT it entails a little more work than merely the imposition of global symmetries on a physical system. A *gauge* symmetry is the requirement that the Lagrangian density of a theory be invariant under *local* (i.e. position dependent) symmetry operations. Such operations may be for instance rotations in Minkowski space or complex mixings between the fermions of the theory. The set of obeyed symmetries are contained within a symmetry group and the structure of the group dictates *in a unique way* the possible interactions of the theory. Having formulated a theory of interacting fields it

then needs to be "anchored" in nature by the process of renormalisation and measurements of free parameters.

2.1.1 Quantum Electro-Dynamics as a Gauge Theory

The primordial example of a gauge theory in QFT is *Quantum Electro Dynamics* (QED). The ansatz of the formulation of QED is the Lagrangian density of a free fermion field[1]:

$$\mathcal{L}_0 = \overline{\psi}(x)(i\not{\partial} - m)\psi(x) \tag{2.2}$$

We note that $\mathcal{L}_0$ is indeed invariant under the global transformation

$$\psi \to e^{i\chi}\psi, \qquad \overline{\psi} \to \overline{\psi}e^{-i\chi} \tag{2.3}$$

as

$$\mathcal{L}_0 \to \overline{\psi}e^{-i\chi}(i\not{\partial} - m)e^{i\chi}\psi = \mathcal{L}_0. \tag{2.4}$$

The symmetry group in this case is $U(1) = (\{e^{i\chi}|\chi \in \mathbb{R}, \cdot\})$. If we expand the symmetry to be local the transformation (2.3) becomes

$$\psi(x) \to e^{i\chi(x)}\psi(x), \qquad \overline{\psi}(x) \to \overline{\psi}(x)e^{-i\chi}(x) \tag{2.5}$$

which leaves eq. (2.2) non-invariant due to the fact that the ∂ operator does not transform covariantly under gauge transformations. To remedy this situation the *covariant derivative* is defined as

$$D_\mu = \partial_\mu + \mathcal{A}_\mu(x) \tag{2.6}$$

which transforms as

$$D'_\mu = e^{i\chi(x)}D_\mu e^{-i\chi(x)} \tag{2.7}$$

given that

$$\mathcal{A}'_\mu(x) = \mathcal{A}_\mu(x) - i\partial_\mu\chi(x) \tag{2.8}$$

The dynamics of this field turns out to be exactly that of the photon field in QED. This can be realised by defining the tensor

$$\mathcal{F}_{\mu\nu} = [D_\mu, D_\nu]. \tag{2.9}$$

Substituting the definition of the covariant derivative it turns out that

$$\mathcal{F}_{\mu\nu}(x) = \partial_\mu\mathcal{A}_\nu(x) - \partial_\nu\mathcal{A}_\mu(x). \tag{2.10}$$

The definition of $\mathcal{F}$ is thus not only gauge covariant but also gauge invariant. We can now construct a Lorentz invariant gauge invariant contribution to the total Lagrangian as $\gamma\mathcal{F}_{\mu\nu}\mathcal{F}^{\mu\nu}$ where γ is a dimensionless constant.

For a suitable definition of $\gamma = \frac{\varepsilon_0}{4e^2Q^2}$ and the definition $ieQF_{\mu\nu} = \mathcal{F}_{\mu\nu}$ we may now write:

$$\begin{aligned}\mathcal{L} &= \overline{\psi}(x)(i\not{D} - m)\psi(x) - \frac{\varepsilon_0}{4}F_{\mu\nu}(x)F^{\mu\nu}(x) \\ &= \underbrace{\overline{\psi}(x)(i\not{\partial} - m)\psi(x)}_{\mathbf{I}} - \underbrace{\frac{\varepsilon_0}{4}F_{\mu\nu}(x)F^{\mu\nu}(x)}_{\mathbf{II}} - \underbrace{eQ\overline{\psi}(x)\not{A}\psi(x)}_{\mathbf{III}}.\end{aligned} \tag{2.11}$$

This is exactly the Lagrangian of QED separated into three terms defining the physics of QED:

[1] $\not{\partial} = \partial_\mu\gamma^\mu = \sum_{\mu=1}^{4}\partial_\mu\gamma^\mu$

I This term describes only the fermion field. It gives rise to the fermion propagator.

II In this term there are only terms of $F_{\mu\nu}$ giving rise to the photon propagator.

III This term is a product of two fermion fields and a photon field. It consequently describes the photon-fermion coupling.

2.1.2 Yang-Mills Theory

The treatment outlined in 2.1.1 can be generalised to any continuous symmetry group $\mathcal{G}$. Let us in particular consider the case where the symmetry transformations can be represented by $n \times n$ unitary matrices V. The fermion fields will form an n-plet (e.g. the quark field triplet of QCD as an $SU(3)$ theory). The gauge transformation of the field becomes

$$\psi(x) \to V(x)\psi(x) \tag{2.12}$$

We may now expand V in terms of generators $\mathbf{T}^a$ of the Lie algebra of $\mathcal{G}$ as

$$V(x) = \mathbf{1} + i\alpha^a(x)\mathbf{T}^a + \mathcal{O}(\alpha^2) + \ldots \tag{2.13}$$

where a is the index of the Dirac multiplet and α is any function of x. Summation is implied. To get a general expression for the field strength tensor $F_{\mu\nu}$ one begins by introducing a matrix representation of the Lie algebra

$$[\mathbf{T}^a, \mathbf{T}^b] = if^{abc}\mathbf{T}^c \tag{2.14}$$

where f is completely antisymmetric in a, b and c.

The covariant derivative associated with $\mathcal{G}$ becomes

$$D_\mu = \partial_\mu - igA^a_\mu \mathbf{T}^a. \tag{2.15}$$

Defining the field strength tensor in analogy with (2.9) one obtains

$$[D_\mu, D_\nu] = -igF^a_{\mu\nu}\mathbf{T}^a \tag{2.16}$$

leading to

$$F^a_{\mu\nu} = \partial_\mu A^a_\nu - \partial_\nu A^a_\mu + gf^{abc}A^b_\mu A^c_\nu. \tag{2.17}$$

The Yang-Mills Lagrangian in analogy with (2.11) becomes:

$$\mathcal{L} = \overline{\psi}(i\not{D} - m)\psi - \frac{1}{4}F^a_{\mu\nu}F^{\mu\nu a} \tag{2.18}$$

from which for example the QCD Lagrangian may be immediately derived by choosing $\mathcal{G} = SU(3)$ and summing over all flavours f:

$$\begin{aligned} \mathcal{L}_{QCD} &= \sum_f \left\{ \bar{q}^{(f)}(i\not{D} - m_f)q^{(f)} \right\} + \frac{1}{4}F^a_{\mu\nu}F^{\mu\nu a} \\ &= \sum_f \left\{ \bar{q}^{(f)}(i\not{\partial} - m_f)q^{(f)} \right\} + \sum_f \left\{ g\bar{q}^{(f)}\mathbf{T}^a \not{A}^a q^{(f)} \right\} - \frac{1}{4}F^a_{\mu\nu}F^{\mu\nu a} \end{aligned} \tag{2.19}$$

where

$$F^a_{\mu\nu}F^{\mu\nu a} = (\partial_\mu A^a_\nu - \partial_\nu A^a_\mu)(\partial^\mu A^{\nu a} - \partial^\nu A^{\mu a}) + 2g f_{abc} A^b_\mu A^c_\nu (\partial^\mu A^{\nu a} - \partial^\nu A^{\mu a}) + g^2 f_{abc} f_{ab'c'} A^b_\mu A^c_\nu A^{\mu b'} A^{\nu c'}. \quad (2.20)$$

Equations (2.19) and (2.20) immediately show the structure of QCD in as much as interactions of gluons with quarks fields are apparent from (2.19) and gluon-gluon cubic and quartic couplings can be seen in (2.20). In other words the complete structure of the strong interaction pops out of the theory by the simple assumptions of Lorentz invariance and $SU(3)$ gauge symmetry.

2.1.3 Contents of the Standard Model

To describe the various phenomena observed in particle physics in the 20th century the SM of particle physics is based on the gauge group $SU(3) \times SU(2) \times U(1)$. The $SU(3)$ part describes the strong nuclear force. The weak nuclear force and the electromagnetic force are in the SM described as manifestations of the same force embodied in the $SU(2) \times U(1)$ part of the SM gauge group. This approach to the unification of the two forces is known as the Glashow-Salam-Weinberg model (GSW).

Giving a meaningful review of the complete derivation of $\mathcal{L}_{SM}$ is a task that has been thoroughly covered in literature such as [PS] or [Pet94]. Furthermore it has little bearing on the specifics of the project described in this thesis. For this reason only a cursory review of the contents of the SM will be given.

Quarks			Charge
u	c	t	$2/3$
d	s	b	$-1/3$
Leptons			**Charge**
ν_e	ν_μ	ν_τ	0
e	μ	τ	-1

Table 2.1: *Matter particles of the SM. The three generations of matter each contain two leptons and two quarks.*

The complete fermionic content of the SM is listed in table 2.1. All fermions in the SM interact through the weak nuclear force while only the quarks feel the strong nuclear force and only particles with charge are susceptible to electromagnetic interactions. The forces of nature encompassed within the SM are carried by a variety of vector bosons also commonly referred to as *gauge bosons* as outlined in table 2.2.

Electromagnetism:	γ	$SU(2) \times U(1)$
Weak force:	$Z^0, W^\pm$	
Strong force:	g	$SU(3)$

Table 2.2: *The force carrying particles of the SM and the symmetry groups to which they are associated.*

These fermion and boson fields stem directly from the underlying gauge structure of the theory. The $U(1)$ symmetry of the SM is not identical to that of QED, though. It is a linear combination of electromagnetic and weak fields.

2.1.4 Electroweak Symmetry Breaking

Having written down a gauge invariant theory for a given symmetry group one has uniquely specified the structure of the theory in terms of matter content and force carriers. The method leaves, however, no room for mass terms in the Lagrangian. Such terms would be quadratic in the field in question, and indeed no $A_\mu A^\mu$ terms are found in (2.11). Furthermore adding them would break the gauge invariance of the Lagrangian. Several mechanisms to remedy this point have been proposed of which only the Higgs mechanism will be described here. For a review of other possibilities the reader is referred to [Pes97].

The Higgs mechanism was originally proposed by Peter Higgs [Hig64, Hig66]. The main point is that the masses of the gauge bosons arise dynamically from the interactions of the bosonic fields with the so-called *Higgs field*. To realise this we begin by considering the Lagrangian of a scalar (classical) field:

$$\mathcal{L} = \frac{1}{2}\partial_\mu\varphi\partial^\mu\varphi - V(\varphi) \tag{2.21}$$

For a free field the potential would take the form $V(\varphi) = \frac{1}{2}m^2\varphi^2$ with m being the mass of the particles of the quantized theory. Consider the slightly more complicated case of

$$V(\varphi) = \lambda(\varphi^2 - v^2)^2, \tag{2.22}$$

where λ and v are positive constants. The vacuum state of the theory is the state that minimises $V(\varphi)$. Note that this is *not* $\varphi = 0$. Instead the vacuum expectation value (VEV) of φ becomes v. If we now consider a field ψ which couples to φ as $g\overline{\psi}\psi\varphi$ one sees that the field φ, the *Higgs field*, induces a mass of ψ, such that

$$m\overline{\psi}\psi \sim g\overline{\psi}\psi v \tag{2.23}$$

meaning that $m \sim gv$.

Applying this way of thinking to the electroweak part of the SM one obtains an interaction of the Higgs field with the electroweak bosonic fields of the form

$$|D_\mu\varphi|^2 = v^2 \times \left[\frac{g^2}{2}W_\mu^- W^{+\mu} + \frac{1}{4}(g'B_\mu - gA_\mu^3)^2\right] \tag{2.24}$$

for a suitable choice of VEV for φ, showing that the W fields do indeed acquire a mass, $g\frac{v}{2}$. The Z^0 field

$$g'B_\mu - gA_\mu^3 = \sqrt{g^2+g'^2}(\sin\theta_W B_\mu - \cos\theta_W A_\mu^3) = \sqrt{g^2+g'^2}Z_\mu \tag{2.25}$$

acquires the mass $\sqrt{g^2+g'^2}\frac{v}{2}$. The θ_W parameter is called the *Weinberg angle*. It is defined by

$$\frac{M_Z}{M_W} = \frac{1}{\cos\theta_W}. \tag{2.26}$$

The photon on the other hand remains massless, as there is no quadratic term in $\gamma = g'B_\mu + gA^3_\mu$ in equation (2.25).

This leads to the famous relations between M_W and M_Z

$$M_Z^2 = \frac{v^2}{2}(g^2 + g'^2) \tag{2.27}$$

$$M_W^2 = \frac{v^2}{2}g^2 \tag{2.28}$$

that have served as rigorous tests of the SM in the 1990's.

It should be noted here, that the shape of the Higgs potential is unknown. We have no a priori reason to assume any particular functional form over another. The only thing that must be satisfied, is the possibility for electroweak symmetry breaking. A common ansatz to V is

$$V(\varphi) = -\mu^2\varphi^\dagger\varphi + \lambda(\varphi^\dagger\varphi)^2. \tag{2.29}$$

This potential is minimised for $\varphi^\dagger\varphi = \frac{\mu^2}{2\lambda}$ leading to a VEV of

$$v^2 = \frac{\mu^2}{\lambda}. \tag{2.30}$$

This potential thus fulfills our demand for EW symmetry breaking. The mass term of the Higgs field is

$$m_h^2 = 2\mu^2 \tag{2.31}$$

and the VEV is given by the measured EW couplings to be $v = 246$ GeV [Pes97].

2.1.5 $\mathcal{L}_{SM}$

Having introduced the Higgs field it is instructive at this point to consider the full Lagrangian of the SM as it is presented for instance in [Pes97]. Using a convenient short-hand notation and implied summation over flavours $\mathcal{L}_{SM}$ may be written

$$\begin{aligned}\mathcal{L} = {} & \overline{q} i \not{D} q + \overline{\ell} i \not{D} \ell - \frac{1}{4}(F^a_{\mu\nu})^2 \\ & + |D_\mu|^2 - V(\varphi) \\ & - (\lambda_u^{ij}\overline{u}^i_R \varphi Q^j_L + \lambda_d^{ij}\overline{d}^i_R \varphi^* Q^j_L + \lambda_\ell^{ij}\overline{e}^i_R \varphi^* L^j_L + h.c.).\end{aligned} \tag{2.32}$$

The two first lines of (2.32) have been explained in the preceding sections. The third line provides a way for the Higgs field to endow the fermion fields with masses in a generic way. Mass terms for fermions are not completely trivial to write into the Lagrangian. This is due to the fact that left-handed and right-handed fields transform differently under $SU(2)\times U(1)$. As they should have the same mass the naïve way of doing this would be to add terms to $\mathcal{L}$ coupling the right-handed with the left-handed fields. This construction, however, is *not* gauge invariant. A construction that *is* allowed is to add trilinear couplings linking left- and right-handed fields to the Higgs field. This is only rather loosely constrained by gauge symmetry. In fact three complex 3×3 matrices of couplings are allowed. These couplings will appear as mass terms in $\mathcal{L}$ for a Higgs field with a non-zero VEV opening up for the possibility of a (very) complicated hierarchy of fermion masses.

2.2 The Need for Physics Beyond the Standard Model

Successful as the SM has been in describing physics up to the energy scale of $\mathcal{O}(10^2$ GeV) compelling arguments exist that it must at the very least be expanded to accommodate physics at the TeV scale. The first fundamental observation that one can make to this effect is the observation that the SM cannot be universally valid simply due to the fact that it contains an ultraviolet divergency and hence a cut-off is always implied no matter which renormalisation scheme is used in calculations of the theory. Above the energy scale defined by this cut-off one or more couplings of the theory can be expected to diverge leading to a break-down of perturbation theory. It is also worth noting that the arbitrariness of the choice in cut-off scale induces a theoretic uncertainty on perturbative calculations (e.g. cross sections).

An other objection that is often raised against the SM is the sheer number of parameters contained within the model. We need look no further back than section 2.1.5 where we saw the Higgs trilinear couplings be contained within three complex 3×3 matrices. While this is not a strict argument against the SM as such, it does question to which degree it can be considered a possible *fundamental* theory of nature.

Other, more rigorous arguments, exist against the SM. Among these is the very fact that it is a QFT and that it as such cannot describe gravitation in a regular fashion. This is due to the fact that general relativity viewed as a field theory is inherently non-renormalisable [D$^+$74]. We are thus relegated to explore other paths such as string theory in order to get a unified description of *all* the forces of nature. Such a theory in general needs to be valid up to the so-called Planck scale Λ_p. This scale is defined as the scale where the gravitational energy of two masses Λ_p placed at a distance of one Compton wavelength from each other equals their rest energy:

$$G\frac{\Lambda_p\Lambda_p}{\Lambda_p^{-1}} = \Lambda_p \Leftrightarrow \Lambda_p = \frac{1}{\sqrt{G}} \approx 1.22 \times 10^{19} \text{ GeV} \tag{2.33}$$

Many other objections may be (and have been) raised against the SM for its failure to adequately explain a number of observations in nature. Among these objections are:

- Why are there three generations of matter? It seems that nature contains exactly three generations of fermions. At least measurements from LEP have limited the number of light neutrinos to three [ℵ90], so any new generations of matter would have to possess fundamentally different properties than the ones we know.

- Neutrinos are treated as massless in the SM. Many measurements in the later years seem to indicate that not only do neutrinos have mass. They also mix due to non-degenerate masses leading to differences between weak eigenstates and mass eigenstates [MSTV04]. This leads to the so-called neutrino oscillations which result from the time evolution of mixed states. Different models have of course been proposed to add neutrino masses to the SM but none have acquired a canonical status of inclusion into the SM.

Two observations are in particular often used as arguments against the SM. These will be treated in detail below.

2.2.1 The Hierarchy Problem

When choosing a cut-off scale for the SM one is faced with the problem of radiative corrections to the masses of the theory. This is in general not a problem. It just needs to be correctly addressed. One problem pops up, when considering the Higgs mass, though.

The bare mass term of φ in $\mathcal{L}$ is

$$\mathcal{L}_{m_h} = -\mu^2 \varphi^\dagger \varphi \tag{2.34}$$

We might conceivably set the μ term to zero. It would, however, in that case be generated dynamically by radiative corrections as illustrated in figure 2.1.

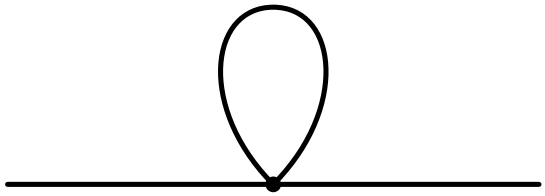

Figure 2.1: *First order contribution to the Higgs mass in the SM. This loop diagram describes the Higgs self-interaction and it is quadratically divergent in the cut-off chosen.*

The diagram shown in figure 2.1 is of course infinite, so as usual a cut-off scale Λ needs to be defined. Cutting off the loop integral at this scale gives a Higgs mass contribution of

$$\begin{aligned} -im^2 &= -i\lambda \int \frac{d^4k}{(2\pi)^4} \frac{1}{k^2} && (2.35) \\ &= -i\frac{\lambda}{16\pi^2}\Lambda^2. && (2.36) \end{aligned}$$

We see from this that the radiative corrections to the Higgs mass are non-zero. They diverge quadratically with the cut-off scale and they are positive. Calculating similar mass corrections

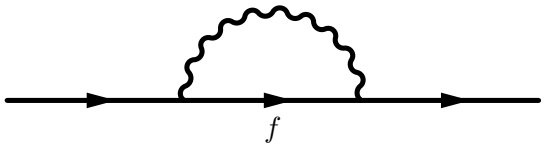

Figure 2.2: *Correction to a fermion mass m_f. The corrections needed to renormalise the mass are of $\mathcal{O}(m_f) \ll \Lambda_p$.*

for a fermion f through diagrams such as the one shown in figure 2.2, one finds that the corrections needed in the renormalization procedure are of $\mathcal{O}(m_f)$ while the corrections needed to keep a scalar mass m_h such as the Higgs on $\mathcal{O}(200\text{ GeV} - 1\text{ TeV})$ are of $\mathcal{O}(\Lambda)$. If the SM is valid to very high energies such as the Planck scale ($\Lambda = \Lambda_p$), the corrections needed to fine tune the Higgs mass are so many orders of magnitude larger than the Higgs mass itself that the EW scale is simply not a natural scale for the Higgs mass to be. In other words it is unnatural that $\Lambda_p \gg m_h$. This observation is known as the *hierarchy problem* and it is one of the central arguments for why the SM cannot be a fundamental theory of nature.

Whether the hierarchy problem is really a problem is open for debate. We do not know that nature writes down Lagrangian densities and consequently the hierarchy problem might really

be a problem with our formalism rather than physics problem inherent in nature. Several solutions have been proposed for the hierarchy problem, though, and some of these will be treated in the following chapter.

2.2.2 Unification of Gauge Couplings

For many years a central theme in fundamental physics has been the concept of *Grand Unification*. This concept is based in part on the observation that the coupling constants of the forces encompassed in the SM seem to converge at a high scale. This gives the hope that a scale exists at which the forces of nature may be described as one "Grand Unified" force and that the forces we observe are merely low-energy manifestations of this force.

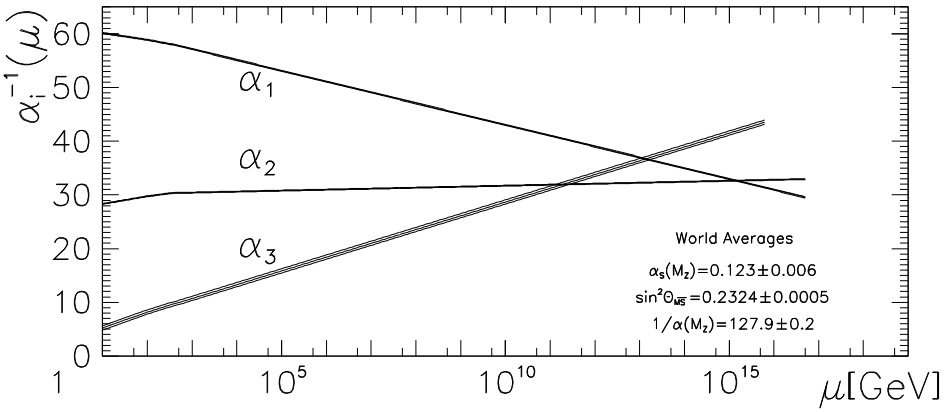

Figure 2.3: *The running of the coupling constants of the SM as shown in [dB94]. α_1, α_2 and α_3 are α_{EM}, α_{Weak} and α_{Strong} respectively. The couplings are seen to converge but not to unify within the errors.*

It turns out, however, that the SM does not inherently contain this feature. Figure 2.3 shows the evolution of the coupling constants using the SM alone. As can be seen from the figure the couplings do *not* converge within the errors and new physics is therefore needed if the combined theory is to possess grand unification. This is of course not a strong formal argument. It does, however, appear as an unfounded assumption that all physics defining the forces of nature should be found at the TeV scale or lower. We have no a priori reason to assume that no new physics should appear in the many orders of magnitude up the the Planck scale.

As was the case for the hierarchy problem one may pose the question if the lacking unification of the SM really poses a problem. We have nothing but aesthetic arguments that "this would be a nice feature" and some indications that it is indeed possible. Plenty of new (and conceivably experimentally inaccessible) physics in the intermediate orders of magnitude between the EW scale and the Planck scale could also provide for this unification. Some suggestions for models are treated in the next chapter.

Chapter 3

Physics Beyond the Standard Model

The preceding chapter illustrates the need for new physics. This need is addressed in myriads of theoretical constructs of which only a tiny fraction can be treated here. This chapter will motivate the search for heavy hadrons through supersymmetry and extra-dimensional scenarios. Also hidden valley models will be addressed at the end of the chapter.

3.1 Supersymmetry

As pointed out in chapter 2 coupling constant unification and a solution to the hierarchy problem are among the theoretical and aesthetical problems that are often mentioned in connection with the SM. These are addressed by the concept of *supersymmetry* (SUSY) in at least some incarnations of the theory.

SUSY addresses the point that Coleman and Mandula discovered in [CM67] which was that the amount of symmetries one can impose on a QFT is limited. Discerning between space-time symmetries and so-called *internal* symmetries (e.g. gauge symmetries) the largest allowed set of symmetries is a *direct product* of the internal symmetries with the so-called Poincaré group. The Poincaré group is the group of isometric (i.e. norm-conserving) operations on Minkowski space-time. It includes translations, boosts, rotations as well as the discrete symmetries of charge, parity and time reversals. Any attempt to impose on a theory a larger symmetry than this such as for instance a symmetry mixed between space-time and internal symmetries will render the theory non-interacting as the S-matrix will be reduced to unity. We do, however, retain one possibility to form new symmetries. We may introduce *supersymmetries* [HLS75], which are symmetries generated by spin 1/2 operators linking the fermionic and the bosonic field contents of a theory. There may be several operators $Q^i,\ i \in \{1, \ldots, N\}$ generating the transformations between fermions and bosons but the description here is limited to $N = 1$ supersymmetry where only one such transformation exists.

As the operator Q links fermions with bosons it must itself transform with half-integral spin. The SUSY algebra becomes [Pes97]:

$$\{Q_a^\dagger, Q_b\} = (\overline{\sigma}^\mu)_{ab} P_\mu \tag{3.1}$$

The curly brackets denote an anti-commutator and $\overline{\sigma}^{\mu} = (1, -\vec{\sigma})$ is defined from the Pauli sigma matrices. P_{μ} is the four-momentum. The immediate contents of this algebra is that the square of the SUSY charge Q is the energy-momentum and that the square of a SUSY transformation is a spatial translation. These observations imply in turn that SUSY must act on every particle and field in our theory (or in nature indeed). The Q and $Q^{\dagger}$ operators may be rewritten with suitable normalisations to operators obeying the algebra of fermion raising and lowering operators:

$$\{a^{\dagger}, a\} = 1 \tag{3.2}$$

It follows that in a SUSY theory every state of nonzero energy has a partner (commonly referred to as a *superpartner*) differing in angular momentum by $\Delta J^3 = \pm\frac{1}{2}$ thus obeying opposite statistics. This of course applies also specifically for single-particle states, and the particle contents of a SUSY theory falls into *supermultiplets* which are irreducible representations of the SUSY algebra being thus closed under the operations Q and $Q^{\dagger}$. A *chiral* supermultiplet consists of a left-handed fermion, its antiparticle a complex boson and its conjugate. A *vector* supermultiplet couples a massless vector field (two transversely polarized states) with a left-handed fermion and its antiparticle. The supermultiplets are thus defined in terms of the massless fields *before* EW symmetry breaking.

Deeper consequences extend from the SUSY transformations transcending the framework of renormalisable QFT. If one assumes gravity to be mediated by a spin-2 graviton field the graviton will obtain a superpartner, the gravitino. The gravitino field can be shown to be the *gauge field of local SUSY* [Pes97]. This implies deep connections between the concept of supersymmetry and the geometry of space-time.

One should note at this point that as Q and $Q^{\dagger}$ are neutral with respect to the gauge interactions and as they commute with the generators of the Poincaré group we may conclude that the members of a supermultiplet be identical in SM charges and in mass. This shows us that SUSY cannot be a conserved symmetry of nature as such partnerings simply do not exist in nature. If SUSY is inherent in nature it must be spontaneously broken to allow for superpartner masses high enough for us never to have observed any supersymmetric particles.

3.1.1 Supersymmetry and the Standard Model

When applying the concept of SUSY to the known "fauna" of SM particles we now have to introduce into our theory a lot of new fields corresponding to the superpartners of all the SM fields. Common notation is to add a "$\sim$" to the particle symbols and generating names for the SUSY scalars by prepending an "s" to the name. The new fermions are named by appending "ino" to the name of the corresponding SM bosons. Thus the particle contents in a supersymmetric version of the SM becomes what is shown in table 3.1. The fields and superpartners are listed before EW or SUSY breaking showing the pure gauge and SUSY structure of the theory. It is seen that the Higgs sector of the theory becomes somewhat more complicated as two Higgs doublets are needed to accommodate EW symmetry breaking. The SM with this minimal number of fields added is generally referred to as the *Minimal Supersymmetric Standard Model* (MSSM). Of course there is no a priori reason to assume that a supersymmetric extension to the SM be in any way minimal but most studies focus on such models to understand the phenomenology of SUSY in a well-described and relatively simple framework.

Supermultiplet	SM fields	Superpartners
	Gauge bosons:	Gauginos:
G	$g^a,\ a = 1, \ldots, 8$	$\tilde{g}^a$
W	$W^\alpha,\ \alpha = 1, 2, 3$	$\tilde{W}^\alpha$
B	B	$\tilde{B}$
	Quarks:	Squarks:
Q	(u_L, d_L)	$(\tilde{u}_L, \tilde{d}_L)$
U	$\overline{u}_R$	$\tilde{u}^*_R$
D	$\overline{d}_R$	$\tilde{d}^*_R$
	Leptons:	Sleptons:
L	(ν_L, l_L)	$(\tilde{\nu}_L, \tilde{l}_L)$
E	$\overline{l}_R$	$\tilde{l}^*_R$
	Higgs bosons:	Higgsinos:
H_1	(H^0_1, H^-_1)	$(\tilde{H}^0_1, \tilde{H}^-_1)$
H_2	(H^+_2, H^0_2)	$(\tilde{H}^+_2, \tilde{H}^0_2)$

Table 3.1: *The fields of the SM extended to SUSY. At this point the fields are listed before EW symmetry breaking and there is therefore no mixing.*

The new plethora of particles of opposite statistics bundled with the MSSM illustrate neatly how SUSY might solve the hierarchy problem. The main contribution to the Higgs mass is

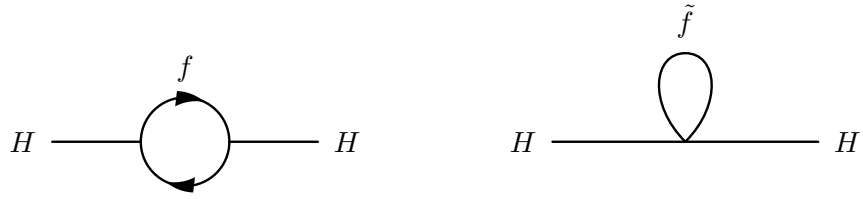

(a) A fermion mass contribution to the Higgs mass.

(b) A bosonic superpartner cancellation.

Figure 3.1: *An illustration of cancellating loops in the radiative corrections generating a Higgs mass. Supersymmetry provides term-wise cancellation between particles and their superpartner. This cancellation is only approximate for broken SUSY.*

the top loop as illustrated in figure 3.1(a). Loops like this give rise to quadratic divergencies as discussed previously in section 2.2.1. However, the introduction of new bosonic fields allow exactly for term-wise cancellation of these quadratic divergencies as shown in figure 3.1(b). This illustrates one of the central selling points for SUSY and motivates the common requirement that proposed mechanisms for SUSY breaking conserve the cancellation of the quadratic divergencies.

Addressing the matter of SUSY breaking is in general a rather complex task. The approach to the subject is to define *soft* SUSY breaking by adding to a supersymmetric Lagrangian of terms that are not invariant under SUSY transformations but which become unimportant at high energies. There is a finite set of such terms that can be added as was found in [GG82]. If SUSY is spontaneously broken then the superpartners to the SM fields are no

longer protected from acquiring mass and they may thus acquire masses from couplings to the SUSY breaking terms. The conventional way of viewing SUSY breaking in this context is to break it spontaneously in a new sector at high energy. The couplings of the particles in this new sector to the supermultiplets now generate the soft SUSY breaking terms at low energy. This is called the *mediation* of the SUSY breaking and it is done in different ways in different models.

The MSSM exists in many varieties depending on the SUSY breaking scheme. Two classes of schemes are prevalent. These are gravity mediated and gauge boson mediated schemes. The MSSM itself allows for this by having explicit mass terms for the sparticle contents of the theory. As is evident from table 3.1, however, many sparticles have similar quantum numbers allowing for mixing. It thus becomes necessary to introduce additional parameters for mixing matrices and CP-violating phases which lead to a lot of parameters. As a consequence of this most concrete incarnations of the MSSM try to constrain and relate the parameters to each other through the SUSY breaking and mediation scheme. In scenarios with mixing the gauginos will mix with the Higgsinos to form *neutralinos*, χ_n^0 and *charginos*, $\chi_n^\pm$. In the slepton sector the selectron and the smuon will not mix while the two stau states, $\tilde{\tau}_L$ and $\tilde{\tau}_R$ will mix to form the mass eigenstates $\tilde{\tau}_1$ and $\tilde{\tau}_2$ numbered by increasing mass. In the squark sector similar mixing will occur for stops and sbottom squarks.

The MSSM also allows for unification of couplings at higher energies. Just as masses are influenced by radiative corrections, so are of course couplings. Figure 3.2 illustrates how a

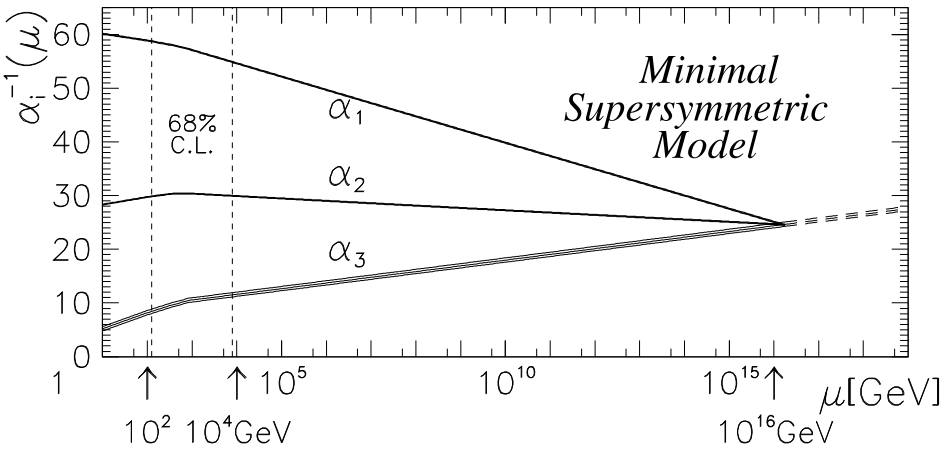

Figure 3.2: *Unification of gauge couplings in the MSSM [dB94]. The 68% confidence limit in the SUSY scale is shown as two dashed lines while the uncertainty of the coupling constants are indicated by the thickness of the lines. This is only one example of a SUSY model providing unification.*

suitable choice of parameters in the MSSM will indeed allow for unification of the forces of nature encompassed in the SM at some scale of $\mathcal{O}(10^{16}$ GeV), commonly referred to as the *GUT scale*.

3.1.2 A Note on R-parity

Supersymmetry allows not only for a large set of new particles. The interactions of the theory result in a variety of new vertices due to the simple fact that the sparticles have the same

SM charges as their SM counterparts. This seemingly harmless observation turns out to have disastrous consequences as it allows for vertices violating lepton number as well as baryon number. Put very simply this very often (i.e. in many models) results in rapid proton decays which is solidly at odds with observations putting the current lower limit of the life time of the proton at 6.7×10^{32} years at 90% confidence level [SuperK99]. To remedy this flaw the most common construction is to impose upon the theory a global symmetry defined by the conservation of the multiplicative quantum number *R-parity*. This is defined using baryon number B, lepton number L and spin s to form the quantity

$$R = (-1)^{3B+L+2s} \tag{3.3}$$

which will be equal to +1 for SM particles and -1 for sparticles. Introducing such a symmetry has the interesting consequence that the *Lightest Supersymmetric Particle* (LSP) becomes stable. It may thus account for the *Cold Dark Matter* (CDM) density of the Universe. To fit with observations the LSP in such a scenario should be neutral and weakly interacting and it is thus a common strategy of SUSY searches to look for missing transverse energy possibly stemming from such *Weakly Interacting Massive Particles* (WIMPs) escaping the detector without decaying.

3.1.3 Common SUSY Models

In this section a brief description of selected SUSY models will be given. As the primary focus of this thesis is not SUSY itself but rather the phenomenology associated with heavy parton-like long-lived particles, the description of the individual models will not be very detailed.

The framework known as *Minimal Supergravity* (mSUGRA) is based on the extension of the global supersymmetry to a local symmetry. The SUSY algebra implies that invariance under a local SUSY transformation implies invariance under local coordinate transformations. This is exactly the governing principle of the general theory of relativity [Ole07]. Local SUSY is thus linked with gravity although the name appears somewhat misleading due to the fact that it is *not* a theory of quantum gravity. The theory is defined in terms of five parameters at the Planck scale(!). These are the universal fermion mass $m_{1/2}$, the universal boson mass m_0, the ratio $\tan\beta$ between the VEVs of the Higgs doublets, the trilinear $\tilde{H}ff$ coupling A_0 and the sign of the μ-parameter of the Higgs potential.

Supersymmetry is broken in some hidden sector at high energies and the Lagrangian is then constructed in a way as to automatically transmit the SUSY breaking from the GUT scale to the EW scale using gravity as the mediating field [DP96]. In other words the theory is fixed at $\mathcal{O}(10^{16}$ GeV) and one then generates the masses and couplings of the SM by radiative corrections. Taking into account the fact that the LHC will be operating at 10^4 GeV it is indeed a bold assumption that this is allowed or even possible.

The theory of mSUGRA does, however, have its merits. Many of these are quite pragmatic. It is a well defined theory in which to define benchmark points. It also spans many different mass hierarchies of sparticles opening up for studies of widely different SUSY phenomenologies. It is described in detail in [B$^+$00, DM00].

In contrast to mSUGRA where the messenger fields from the hidden sector are gravitational fields, Gauge-Mediated Supersymmetry Breaking (GMSB) is a description used for theories

that use the interactions of the ordinary SM gauge interactions to communicate the high-energy SUSY breaking to the visible sector [GR99]. Theories are typically cast in terms of the parameters N, M, Λ, $\tan\beta$, c_{grav} and the sign of μ. The basic concept is to add N chiral $SU(5)$ supermultiplets at a mass scale M. These couple to the SM fields as well as to whichever SUSY breaking scheme is envisioned. The Λ parameter represents an effective SUSY breaking scale that is related to the fundamental SUSY breaking scale F through the relation $\Lambda = \frac{F}{M}$. The gravitino mass in this scheme is very small ($\mathcal{O}$(keV)) and the gravitino thus becomes the LSP. Its mass is related to F and c_{grav} as

$$m_{\tilde{G}} = 2.4 \text{ eV} \times c_{grav} \left(\frac{\sqrt{F}}{100 \text{ TeV}} \right)^2 . \tag{3.4}$$

A prime difference between the two approaches is the fact that gauge interactions do *not* distinguish between flavours or "families". The three generations of quarks couple with equal strength to the gluon while a gravity mediated SUSY breaking has no a priori reason to conserve flavour in the resulting low-energy vertices. This results in somewhat different phenomenologies between mSUGRA and GMSB.

The class of *Anomaly-Mediated Supersymmetry Breaking* consists of theories in which the SUSY breaking is mediated through so-called anomalous interactions [GH, RS99]. It is not uncommon for these theories to be inspired by string-theory and thus postulate effects from adding extra dimensions to our 3+1 dimensional space-time.

3.1.4 Heavy Stable Coloured Particles in SUSY

As indicated above, the parameter space for supersymmetry is vast and exclusion limits and constraints are often cast in terms of very specific minimal models. This section is devoted to motivating searches for hadrons containing heavy parton-like (s)particles in the context of SUSY.

The particles that are interesting in this context are naturally gluinos and squarks. Absolutely stable coloured sparticles are rare and heavily constrained (though not excluded [F$^+$07]) as they should result in the occurrence of the occasional super-heavy nucleus which has not been discovered. A scenario that has gained quite some following in recent years is *Split Supersymmetry* (SSUSY) [GR04, AHDGR05] in which the hierarchy problem is abandoned and left for either the anthropic principle or new physics to sort out while the theory attempts to fix the CDM density of the Universe and assure gauge coupling unification.

SSUSY in a snese has *two* SUSY scales. One scale is a low scale where the gauginos and the Higgsinos live while the other is an arbitrarily high scale at which the scalars are placed. The high mass scale of the scalars suppresses the corresponding loops in the Higgs mass (figure 3.1) and the hierarchy problem is thus not solved by SSUSY as mentioned above. It is argued in [GR04], though, that SSUSY is one of the few theories that emerge naturally if one imposes the requirement of a dark matter candidate and gauge coupling unification. Many SSUSY models feature a long-lived gluino due to the fact that it must decay to the LSP through a highly virtual squark as illustrated in figure 3.3.

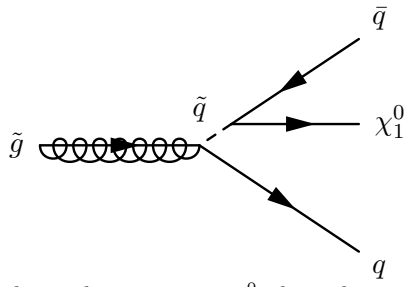

Figure 3.3: *An illustration of a gluino decaying to a χ_1^0 through a virtual squark. In a model where the squark is extremely heavy and this is the only decay channel open for the gluino this decay is suppressed to the point where the gluino may acquire even very long lifetimes.*

The lifetime of the gluino in this picture (expressed as $c\tau$) is approximately given by [HLMR04]

$$c\tau_{\tilde{g}} \approx 2.4 \times 10^9 \text{ m} \times \left(\frac{m_S}{10^9 \text{ GeV}}\right)^4 \times \left(\frac{1 \text{ TeV}}{m_{\tilde{g}}}\right)^5, \tag{3.5}$$

where $m_S \gg 1$ TeV is the SUSY breaking scale that may vary from 10^7 GeV up to the GUT scale with 10^{12-13} GeV favoured for cosmological reasons. It is seen that it is in the context of SSUSY by no means unreasonable to look for gluinos with lifetimes far in excess of $c\tau_{\tilde{g}} \sim 10$ m. Cosmological bounds on $\tau_{\tilde{g}}$ indicate that $\tau_{\tilde{g}} \lesssim 100$ s for $m_{\tilde{g}} \gtrsim 500$ GeV/c^2 and $\tau_{\tilde{g}} \lesssim 10^6$ years for $m_{\tilde{g}} \lesssim 500$ GeV/c^2 [ADG$^+$05]. Direct searches for long-lived gluinos performed with Tevatron data puts a limit of $m_{\tilde{g}} \gtrsim 170$ GeV/c^2 on the mass of a long-lived gluino for the case where only neutral hadrons are formed and where they remain neutral throughout the detector. This is a conservative estimate as hadronic interactions are probable to occur as will be described in parts II and IV. The limit is expected to be raised to $m_{\tilde{g}} \approx 430$ GeV/c^2 during the Tevatron Run II barring the occurrence of a signal [HLMR04].

Split supersymmetry does *not* allow for long lived squarks. In fact the high scale of m_S rules out the production of these particles at any collider. Other models do accommodate this phenomenology, though. GMSB scenarios exist in which the gravitino is the LSP and the $\tilde{t}$ is the NLSP. The lifetime of the $\tilde{t}$ becomes [GR99]

$$c\tau_{\tilde{t}} = 0.1 \text{ mm} \times \left(\frac{100 \text{ GeV}}{m_{\tilde{t}}}\right)^5 \times \left(\frac{m_{\tilde{G}}}{2.4 \text{ eV}}\right), \tag{3.6}$$

where $m_{\tilde{G}}$ is related to the SUSY breaking scale as shown in equation (3.4). Models have also been proposed where SUSY breaking is obtained using a compactified extra dimension. Extra-dimensional scenarios are treated in section 3.2 of this thesis. In the context of SUSY we just observe that the $\tilde{t}$ turns out to be the LSP in large parts of the possible parameter space.

From the above it is seen that supersymmetry in its various incarnations seem to supply the possibility for the existence of very heavy coloured particles with long lifetimes. These may be gluinos carrying colour octet charge or squarks carrying colour triplet charge as well as electromagnetic charge.

3.1.5 Heavy Hadrons in SUSY

Whether the model containing long-lived heavy (s)partons is GMSB or SSUSY the point remains that collider experiment events resulting in the creation of said partons will result in

the formation of heavy hadrons at the time of hadronisation. These hadrons are commonly referred to as R-hadrons due to the fact that they are kept (quasi-) stable by R-parity. The mass calculation of R-hadrons is treated in detail in [Kra04a] and it will thus not be presented here in its entirety. A brief outline will be given, though, to show the main line of arguments with the approximations used.

The mass of a hadron, heavy or not, may be approximated by [Clo, DRGG75]

$$m_h = \sum_i m_i - k \sum_{i \neq j} \frac{(\mathbf{F_i} \cdot \mathbf{F_j})(\mathbf{S_i} \cdot \mathbf{S_j})}{m_i m_j} \tag{3.7}$$

for the lowest lying state with no angular or radial excitation. The summation is over the constituent partons of the hadron. The masses m_i are the constituent masses of the partons, $\mathbf{F_i}$ represents the $SU(3)$ colour matrix for the i'th parton while $\mathbf{S_i}$ is the $SU(2)$ spin matrix. The constant k is an empirical constant. Choosing $k \approx 0.043$ GeV^3 reproduces the π/ρ, K/K^*, D/D^* and B/B^* masses and mass splittings reasonably well while the baryon sector is described using $k \approx 0.026$ GeV^3. For our purposes two observations are of key importance here:

- The mass splittings of the possible spin states are generated by the second term of equation (3.7).
- With constituent masses consistently of $\mathcal{O}(\mathrm{GeV/c^2})$ or lower and heavy parton masses orders of magnitude above, we may safely neglect the heavy parton in this term.

This simplifies the calculations immensely. Also the spin of the heavy parton disappears out of the direct mass calculation. The matrix elements are calculated in [Kra04a] where a thorough treatment is given for the complete mass calculation. In all cases the mass splittings are found never to exceed roughly 100 MeV/c^2 $< m_\pi$ why they are consequently neglected and the second term of equation (3.7) may be averaged and absorbed into an effective constituent mass.

In conclusion there are rich possibilities for the various models incorporating supersymmetry to encompass the existence of long-lived heavy coloured particles and thus of heavy hadrons. The search for such hadrons is consequently of great importance in the search for new physics at the LHC.

3.2 Extra Dimensions

Supersymmetry is not the only solution to the hierarchy problem. Other theoretical constructs exist that solve this problem. Among these are theories in which the flat 3+1 dimensional space-time is exchanged with a more complex structure of higher dimension. Such extra dimensions (ED) can be added to the SM in several ways. In general, of course, it has to be done in a manner not contradicting observations. The common feature of all extra-dimensional models is that the extra dimensions added are *compactified* i.e. curled up on a scale that is sufficiently small to allow for our known physics to be conserved on a large scale. The geometry of the compactification can be realised in many ways on sub-manifolds of varying complexity.

3.2.1 Why Extra Dimensions?

The motivation for proposing extra dimensions in the context of the hierarchy problem is the observation that the problem might simply be due to the fact that our simple calculation of the Planck scale in equation (2.33) is wrong [AHDD98]. We consider the case where instead of our $3+1$-dimensional space-time we substitute a $3+1+d$-dimensional space-time where the d extra dimensions are compactified at a scale R. For distances $r \ll R$ we may effectively consider the spatial dimensions to be $\mathbb{R}^{3+d}$. For two test masses m_1 and m_2 this leads to a gravitational potential of the form:

$$V(r) \approx -G_{N(4+d)} \frac{m_1 m_2}{r^{1+d}} \tag{3.8}$$

Moving out to distances $r \gg R$ the compactified dimensions factor out as the field lines in those dimensions will not extend out to r. We thus recover Newton's law of gravitation as

$$V(r) \approx -k \frac{G_{N(4+d)}}{R^d} \frac{m_1 m_2}{r}, \tag{3.9}$$

where k is a constant of $\mathcal{O}(1)$ related to the exact geometrical properties of the compactification of the extra dimensions. This is of course on the condition that the structure of the compactified dimensions does not depend on the position in $3+1$ dimensions. The Planck scale now enters by comparing these equations to equation (2.33). This yields a true Planck scale of

$$\Lambda_p^{true} \approx \Lambda_p^{(2/2+d)} R^{-d/(2+d)}. \tag{3.10}$$

This solves in a natural way the hierarchy problem of $\Lambda_p \gg m_h$. The introduction of extra dimensions at a scale $R \gg 1/m_h$ simply moves Λ_p down. There is of course another hierarchy problem between the spatial extents of the dimensions of space-time but the fine-tuning of the Higgs mass disappears.

The constraints on extra dimensions in terms of d and R originate among other things on tests of Newtons law of gravitation. This has been tested down to ~ 85 μm [K$^+$07]. Testing gravitation at small distances is difficult due to the small forces involved. The limits on R are different for *universal* and *non-universal* extra dimensions. Non-universal extra dimensions postulates a mechanism constraining the SM fields to the $3+1$ normal dimensions while leaving gravity to propagate in all $3+1+d$ dimensions. This provides a natural mechanism for explaining the relative weakness of gravity with respect to the SM forces. Such extra dimensions could have extents up to a scale of 10^{-4} m. Universal extra dimensions (UED) in contrast allow for all fields of he SM to propagate freely in the full set of dimensions. This requires, however, that the extra dimensions be a lot smaller with $R \sim \frac{1}{\Lambda_{EW}} \approx 10^{-18}$ m.

3.2.2 Phenomenology of Extra Dimensions

We begin by considering a particle propagating in all $3+1+d$ dimensions. The energy of the particle becomes

$$\begin{aligned} E^2 &= p^2 + m^2 \\ &= \sum_{i=1}^{3+d} p_i + m^2 \\ &= |\vec{p}|^2 + \sum_{i=4}^{3+d} p_i + m^2 \end{aligned} \tag{3.11}$$

As it turns out the momentum components along the compactified dimensions appear as a contribution to the effective mass M of the particle, $M = \sqrt{\sum_{i=4}^{3+d} p_i + m^2}$. The crucial point is now that as the extra dimensions are compact, the momentum components along these dimensions become discrete. A simple example is the so-called *toroidal compactification* where the extra dimensions are seen as a direct product of 1-spheres with the same radius, R. The allowed effective masses for a massless particle become

$$\frac{\sqrt{n_4^2 + n_5^2 + \ldots + n_{3+d}^2}}{R}, \qquad n_i \in \mathbb{N} \cup \{0\}, \tag{3.12}$$

resulting in a so-called *Kaluza-Klein (KK) tower* of possible states. Turning now to equation (3.10) and imposing that $\Lambda_p^{true} \approx 1$ TeV (up to which scale we assume the SM to be valid) one may draw conclusions on the relation between the allowed number and the size of the extra dimensions. Converting equation (3.10) to suitable SI units a rough relation between d and R is shown in table 3.2. The relation is $R \sim 10^{31/d-19}$. It is seen that the $d = 1$ case is excluded while already $d = 2$ is close to being possible. Higher dimensions are immediately seen to be within the limits of the experimental constraints.

d	R (m)
1	1×10^{13}
2	1×10^{-3}
3	5×10^{-9}
4	1×10^{-11}
5	3×10^{-13}

Table 3.2: *Allowed size R of the extra dimensions as a a function of d. Note how just one extra dimension is ruled out, while already two become a possibility with the present knowledge of gravity.*

Many different models exist with large variations in the phenomenology. In some models momentum conservation will appear violated at the TeV scale due to graviton production being enhanced at this scale. The gravitons are allowed to propagate away from the $3+1$-dimensional space-time resulting in an apparent violation of momentum conservation. In other models particles might propagate in all dimensions "intersecting" with normal space-time at a regular distance, R. This allows for reactions to occur implying that one might observe for instance a regular line of vertices spaced at a distance R in a high-energy physics experiment.

3.2.3 Heavy Stable Hadrons in UED

Several ED models predict potentially very long-lived KK-excitations of the gluon, g_{KK}. Some of these models are studied in [MMN02a] with a special focus on a model proposed in [ACD01]. In this model for simplicity (and due to looser experimental constraints at the time) d has been set to 1. Momentum conservation along the extra dimensions implies conservation of the KK-excitation number n at tree level dictating that the KK-states cannot be singly produced but will be pair-produced through reactions such as $gg \rightarrow g_{KK}g_{KK}$ or $q\overline{q} \rightarrow g_{KK}g_{KK}$. Even though the KK-number conservation is violated at the one-loop level the decay of the lowest lying KK-states into SM particles is forbidden to all orders if there is no mechanism in nature specifically allowing for this decay. Several mechanisms have been proposed for this but it does not from the context appear unreasonable to assume that the lowest lying states have lifetimes τ fulfilling the condition that $c\tau$ be large enough that we may from a collider physics point of view consider them stable.

As a consequence of this we might have gluon resonances being produced in pairs. This would at the LHC produce events containing two heavy, long-lived colour octets back to back traversing the detector. These states would then produce varying species of heavy hadrons, *KK-hadrons* in analogy with the gluino R-hadrons of SSUSY (section 3.1.4). The masses and possible mass splittings will in the approximations of section 3.1.5 be identical to those found in SSUSY as the spin of the heavy parton does not influence the mass calculation. We may thus expect a very similar phenomenology between KK-gluon hadrons and gluino R-hadrons.

3.3 Concluding Remarks

This part of the thesis has constituted a cursory overview of the most common theoretical contraptions yielding long-lived heavy parton-like particles. Supersymmetry and Extra Dimensions are vast fields that can generate many different phenomenologies. One should be careful, though, to proclaim such frameworks the only ones worth studying. Many other classes of models exist that reproduce SUSY- or ED-like phenomena while being conceptually different. Some of these address the problems of the SM while some do not.

For example it has been proposed that one might conceivably add an extra gauge group to the SM. A such gauge group would come complete with fermions and bosons. Adding an additional $U(1)$-group would result in the occurrence of a photon-like object commonly referred to as a *paraphoton*. More complicated non-Abelian groups would allow for QCD-like structure in the new sector.

As a little thought experiment we now consider the so-called *Hidden Valley* (HV) models [SZ00, Str00]. In these models we begin by adding an extra gauge group with a conserved charge X to the SM. This new charge is carried by the particles X_i, $i = 1, 2, \ldots, n$. It is immediately apparent that the production mechanism for the X_i can only be pair-production of these particles with ensuing cascade decays like for instance

$$X_9 \rightarrow H + X_8 \rightarrow b + \overline{b} + q + X_7 \rightarrow \ldots \rightarrow b + \overline{b} + q + \ldots + X_1. \tag{3.13}$$

As such particles have not been observed the X_1 must necessarily be electromagnetically and QCD neutral. This situation is extremely similar to the common SUSY scenarios in which

two heavy non-interacting objects leave the detector leaving behind a signature of missing transverse energy. We thus have a very SUSY-like scenario without making the wide-ranging assumption of supersymmetry.

The next step is to assume the existence of an ultra-weakly coupled sector coupling to the SM and the X-charge. We assume that this new sector contains at least one particle ξ carrying X-charge. If we furthermore assume that $m_\xi < m_{X_i}$ we have an interesting situation. In this picture the X_i will still be pair-produced but the decay to ξ will be suppressed by the low strength of the coupling. It will still decay but it might conceivably do so outside the detector like

$$X_1 \to b + W + \xi. \tag{3.14}$$

Note how X_i is now allowed to carry any combination of SM charges we might imagine. If we identify the X-charge with R-parity and the ξ particle with the gravitino we see the clear analogy to GMSB SUSY where the X_1 particle would then be the stop decaying to a t-quark and a gravitino.

In conclusion it is seen that heavy long-lived coloured particles appear in many extensions to the SM, and while it may not be a trivial task to discern between all the different models a model-independent approach to searching for such particles may prove of vital importance for the initial discoveries needed to point the direction for theoretical and experimental development in Particle Physics.

Part II
Simulation of Heavy Stable Hadrons in GEANT4

Right-ho, gents, it's another simulation gone mad, so murder and mayhem, standard procedure.

[Futurama, season 4, episode 1]

Chapter 4

Introduction to the Simulation Toolkit

In this part of the thesis a simulation toolkit will be presented that was developed by the author in collaboration with Andrea Rizzi from the CMS experiment. The toolkit is implemented in GEANT4 (G4)[G403] to facilitate the easy interfacing of the custom physics developed with the software systems of different high-energy physics experiments. At the time of the writing of this thesis it has been successfully interfaced to the software frameworks of the CMS experiment[Riz07] as well as the ATLAS experiment as will be demonstrated in part IV of this thesis.

This does not comprise usage documentation for the toolkit for which the reader is referred to [Usa].

4.1 About GEANT4

GEANT4 is an object-oriented physics simulation toolkit. The purpose of the toolkit is to describe the passage of particles through matter. This broadens the application of G4 to include such diverse fields as describing high-energy physics detectors, estimating radiation effects on satellite equipment and simulating medical imaging and cancer radiation treatments. In the context of high-energy physics G4 is most commonly used to understand and simulate the response of detectors to the decay products of hard processes resulting from particle collisions. Currently GEANT4 is the standard software package for detector simulation for HEP experiments. The previous version, GEANT3, was FORTRAN based and was extensively used by LEP experiments and in the preparation of the LHC experiments.

Due to GEANT4 being an object-oriented toolkit the interaction model presented here was implemented as a simple add-on. This meant that no modifications to the core of the toolkit were required. The implementation included a general mechanism for adding new particles (e.g. R-hadrons) and their corresponding interaction processes.

The basic structure of a GEANT4 job consists of three things:

- The geometry which is simulated. This geometry may be anything from simple geometric shapes composed of basic elements (e.g. a cubic piece of iron) to complex shapes consisting of various compounds in solid, liquid or gaseous states. The latter is the typical situation when simulating a particle physics experiment.
- The particles that are being simulated. The user may be interested in the behaviour of electrons while traversing a gaseous target or nuclear fragments in human tissue resulting from irradiation with anti-protons.
- The list of processes to be simulated (the so-called *physics list*). This list is basically an assignment of processes to the different particles in the job. Often GEANT4 simulation can be quite CPU intensive so much efficiency can be gained by tailoring the physics list to your needs. An example is that one might wish to not include low-energy nuclear processes for protons when the primary object of interest is photon conversions. Many standard physics list exist for different applications.

The toolkit presented here provides for general and easily configurable methods of introducing exotic heavy hadrons such as those exemplified in chapter 3 and assign to them nuclear interactions.

4.2 Particles in GEANT4

A particle in GEANT4 is represented by a pair of objects, a G4ParticleDefinition and a G4DynamicParticle. The G4ParticleDefinition contains the static information about the particle type such as name, mass, PDG code, spin etc. this means that the G4ParticleDefinition is a so-called *singleton*. Only one instance exists in memory no matter how many replicas of a given particle type is treated by G4. The dynamic properties of particles in contrast are contained in objects of the type G4DynamicParticle. These objects contain the four momenta of specific particles in an event.

The new package adds particle definitions for all particles in the relevant physics scenario. This is done by selectively breaking the singleton property of the G4ParticleDefinition to allow for instantiation of the needed number of new particles without recompiling. The particles are defined from a file that contains PDG-code of the particle, mass and name in a Susy Les Houches Accord (SLHA) like format [S^+04]. The particle definitions are all instances of a class called CustomParticle inheriting from G4ParticleDefinition that not only contains the normal static information but also allows the splitting of the particle into a heavy parton (HP, e.g. a gluino) and a light quark system (LQS). This is used to facilitate the treatment of interactions with matter in an easy and correct fashion.

4.3 Processes in GEANT4

The interactions with matter are described in a so called G4Process. In general a G4Process is the logic describing *when* something happens and exactly *what* happens. A common (simplified) structure is for the G4Process to calculate an interaction cross section with the material

that is traversed and use it to calculate a mean free path that is passed to G4. When a decision is reached by G4 that a specific process take place the G4Process has one or more methods (*Doit()*-methods) that transform the G4DynamicParticle representing the particle and introduce new particles as required. The simplest process imaginable in this context is transportation which takes care of actually moving a particle one step.

In relation to heavy coloured particles a dedicated G4Process has been implemented. This process provides a cross section calculation for nuclear processes of the exotic heavy hadrons configured as described in section 4.2. Following the cross section calculation the process needs to know the possible final states for the interactions of the individual hadronic state with the protons and neutrons of matter. This list of nuclear processes are defined from a file and it is read in at run-time.

In order to let GEANT4 know of this process it should be registered to the GEANT4 framework for each particle that undergoes the process. This is done in the physics list for the GEANT4 job. Such physics lists can be written, instantiated, merged and configured in many different ways with much configuration possible at run-time. In this context it is relevant to mention that the structure of GEANT4 and of the present toolkit makes it a simple task to add the new nuclear process to existing physics lists thus allowing the native GEANT4 processes to handle the normal reaction products of the nuclear interactions as well electromagnetic interactions of the heavy hadrons themselves.

Chapter 5

Modelling Interactions of Heavy Stable Hadrons

5.1 Interaction Cross Section

The cross section calculation follows closely that of [Kra04b]. The reader is therefore referred to that paper for a thorough review. One extension has been made, though, as the possibility to add a resonance to the cross section has been introduced.

The basic idea is to use a purely geometric cross section tuned to $\pi - p$ scattering. The heavy parton is neglected in this context. As the spatial extent of a wave function scales as $1/M^2$, the cross section contribution from the heavy parton becomes negligible. In this picture we are thus considering the heavy parton to be exclusively a reservoir of kinetic energy. Each light valence quark is assigned a total cross section of 12 mbarn per nucleon leading, for instance, to a value of 24 mbarn for a meson carrying a colour octet heavy parton (e.g. a gluino R-meson). This value stems from the fact that the size of the total cross section should be matched to the high energy limit of the total $\pi - p$ cross section. This cross section is shown in figure 5.1. It is characterised by a large resonance at low centre of mass energies and an asymptotic limit of $\frac{\sigma_{\text{elastic}}}{\sigma_{\text{total}}} \approx 15\%$ for high energies.

The cross section contribution for an s quark is set to 6 mbarn to conform with [Kra04b]. For the translation of a cross section per nucleon, $\sigma_{n/p}$, into a cross section per nucleus, σ_A, the same GHEISHA convention [Fes85] is used as in the GEANT3 work. The relation between the two cross sections is:

$$\sigma_A = 1.25 \times \sigma_{n/p} \times A^{0.7} \tag{5.1}$$

One additional feature that has been introduced is the ability to add to the flat cross section a non-relativistic Breit-Wiegner resonance. The user may at run-time specify resonance position, width and height as shown in figure 5.2. It should be emphasised here that no theoretical arguments exist for how such a resonance should look and what would be the physics reason for its existence. It has merely been included as an option for the sake of generality.

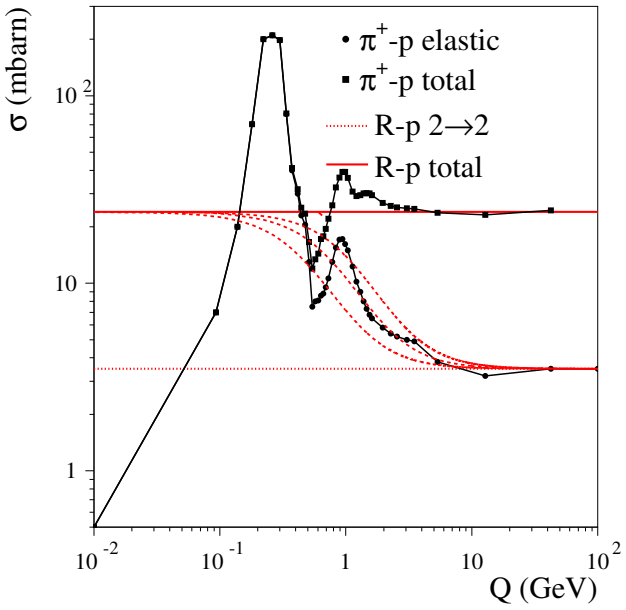

Figure 5.1: *The $\pi - p$ cross section as shown in [Kra04b]. Note the resonance at $Q \approx 2 - 300$ MeV as well as the asymptotic limit of the $2 \to 2$ cross section relative to the total cross section. The limit is approximately 15%.*

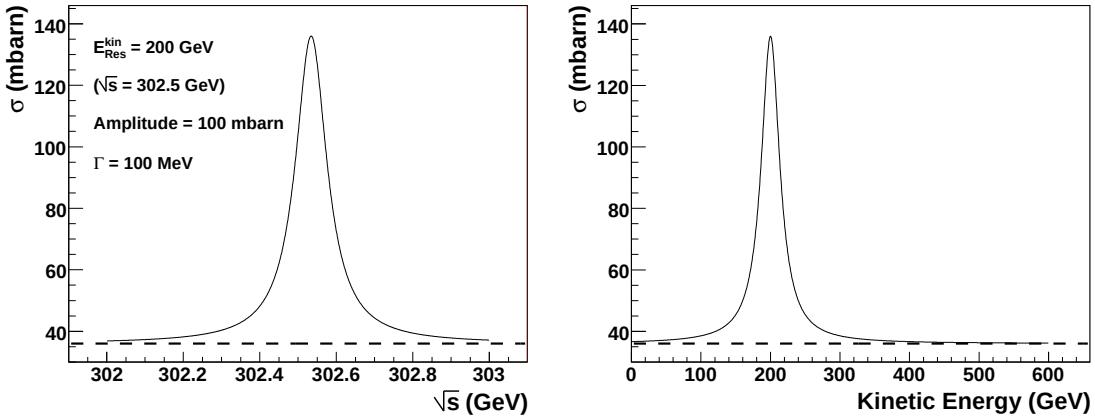

(a) In Centre of Mass System (CMS)

(b) In labframe (rest-frame of nucleus)

Figure 5.2: *An example showing how a resonance could be configured. This example is a gluino R-baryon ($\tilde{g}qqq$) with $m_{\tilde{g}} = 300\ GeV/c^2$. The base cross section is 36 mbarn and a 100 mbarn resonance is added. The E^{res}_{kin}-parameter denotes the kinetic energy of the R-baryon in the labframe at peak resonance.*

5.2 Choice of Final State

When a nuclear reaction occurs the choice of final state is made using a slightly modified decision tree with respect to the one used in the GEANT3 work, although the end result is the same. The ansatz of the selection is a list of possible final states given the incident particle (e.g. an R-hadron) and the target nucleon. This list of processes needs to be supplied by the user. It is modelled by reggeon and pomeron exchange as will be exemplified in sections 5.4.1 and 5.4.2 although this model is a purely phase space driven model. The decision tree is an iteration over the following steps until a process is selected.

- Populate a list of possible processes - i.e. processes with a positive Q-value, where $Q = \sqrt{s} - \sum_i m_i$, and the summation is over all final-state particles.
- Assign $2 \to 2$ and $2 \to 3$ processes a priori relative probabilities of 15% and 85% respectively, as elastic scattering amounts to approximately 15% of the total cross section for light hadrons at high momenta as mentioned in section 5.1.
- Choose a process at random, given the a priori probabilities.
- For $2 \to 3$ processes, a phase space function decides the probability of the process being accepted.

The phase space function describes the phase space fraction available for $2 \to 3$ scattering. It is defined using the same expression as in [Kra04b]:

$$F(Q) = \frac{\sqrt{1 + \frac{Q}{2m_\pi}} \left(\frac{Q}{Q_0}\right)^{3/2}}{1 + \sqrt{1 + \frac{Q}{2m_\pi}} \left(\frac{Q}{Q_0}\right)^{3/2}} \tag{5.2}$$

This choice of functional expression is motivated by the fact that the function is, by Lorentz invariance, expected to be a function of $Q = \sqrt{s} - \sum_i m_i$ where i enumerates the final state particles. As an ansatz one may use the expression

$$F(Q) = \frac{\frac{\mathrm{d}\phi_3(Q)}{\mathrm{d}\phi_3(Q_0)}}{\frac{\mathrm{d}\phi_2(Q)}{\mathrm{d}\phi_2(Q_0)} + \frac{\mathrm{d}\phi_3(Q)}{\mathrm{d}\phi_3(Q_0)}}, \tag{5.3}$$

where $\mathrm{d}\phi_N(Q)$ denotes the *absolute* phase space for N-body scattering at a scale Q. Note that the phase spaces are normalised to a scale Q_0 due to the fact that they have different dimension. The actual derivation of equation (5.2) is rather involved [Kra04a] and involves some approximations. The value of Q_0 is determined by imposing that $F(Q_0) = 0.5$ as required in equation (5.3). It turns out that the value becomes 1.1 GeV. F is shown as a function of some commonly used parameters in figure 5.3.

The relative frequencies with which $2 \to 2$ and $2 \to 3$ processes are chosen may be seen in figure 5.4.

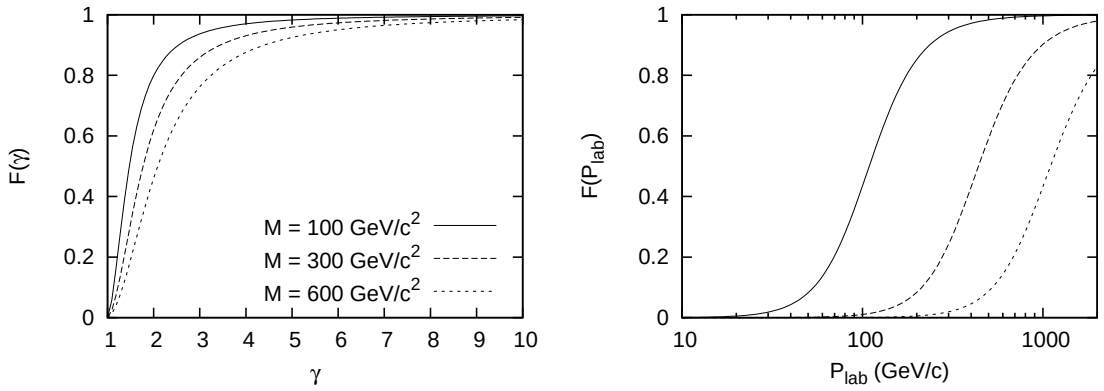

Figure 5.3: *Parametrisations of the phase space function $F(Q)$. M is here taken to be the mass of the heavy hadron. P_{lab} is the momentum in the labframe, and γ is the boost of the particle relative to the labframe.*

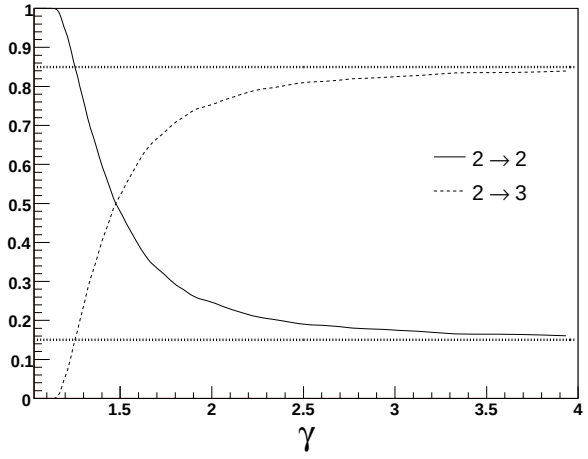

Figure 5.4: *Fraction of $2 \rightarrow 2$ and $2 \rightarrow 3$ processes selected as a function of γ of the incident particle. There is no discernible difference between different particle masses or types. Although this specific plot was made for 300 GeV/c^2 gluino baryons in iron, stop hadrons at other masses in other materials yield the same result.*

5.2.1 Charge Exchange Suppression

In a nuclear interaction a hadron containing a heavy parton may interact through pomeron exchange or reggeon exchange. Pomeron exchange will leave the charge unaltered whereas reggeon exchanges will allow charge to be transferred.

In the above discussion no preference has been selected between reggeon and pomeron exchange. This is due to the fact that we have no a priori reason to assume a difference in strength between the two mechanisms. Theoretical arguments might appear, however, as to why one exchange mechanism should dominate over the other and so an additional feature has been added to supply a charge exchange suppression mechanism. The mechanism is simply expressed as a probability of rejecting a process and rerun the final state selection if the selected final state changes the charge of the heavy hadron. Other ways to do this could be devised if theoretical basis could be found for a specific mechanism.

5.3 Kinematics of Reaction Products

Once the final state of an interaction is selected, several things may occur. Decisions need to be taken as to how momenta are assigned to the outgoing particles. Also the struck nucleus may undergo some changes. These decisions are highly model dependent and two models are presented here.

The basic tenet of both models is that the interaction between the heavy hadron and the nucleon takes place via the LQS alone. This is a logical extension of the geometric cross section calculation in section 5.1. As the heavy parton in this formulation is strictly a reservoir of kinetic energy, it has been assumed that it will not interact. Rather the LQS is assumed to interact exclusively. Imposing the requirement that the LQS and the heavy parton are co-moving leads to the condition that the LQS carries the kinetic energy $E_{kin,LQS} = \frac{M_{LQS}}{M_{tot}} E_{kin,tot}$, leading to the treatment as a low-energy collision in spite of the high energy carried by the hadron as a whole.

This treatment is naturally only valid as long as the condition $M_{LQS} \ll M_{Tot}$ is fulfilled.

5.3.1 Toy Model

This model embodied in the "ToyModelHadronicProcess" is included in the toolkit for scenarios where the user wishes to make initial conclusions while minimising the "black box" of the machinery and thus maintaining an overview. It is hardly valid for physics conclusions but it is a useful tool to test the process lists supplied as it is the simplest ansatz possible for a kinematics treatment.

The collision is treated as that between a free nucleon and the LQS of the heavy hadron. Quasi-elastic ($2 \rightarrow 2$) processes are handled by the boosting of the LQS and the target nucleon to the CMS and assigning the outgoing particles back to back momenta along a random axis. Momenta are then boosted back to the lab-frame. Upon creation of secondaries and assignment of momenta, the heavy parton (HP) and the LQS are re-coupled whilst imposing three momentum conservation and calculating the energy by keeping the heavy hadron on-shell. This re-coupling procedure results in an excess energy stemming from the

treatment of the recoupling as a completely inelastic collision between the HP and the LQS. The excess energy may be quantified by:

$$\Delta E = E_{LQS} + E_{HP} - \sqrt{(\vec{p}_{LQS} + \vec{p}_{HP})^2 + M_{Tot}^2} \tag{5.4}$$

where all quantities refer to the decoupled values for the HP and the LQS respectively. This energy is added as a local energy deposit in GEANT4. Inelastic ($2 \rightarrow 3$) processes are treated by generating the momenta as a flat distribution in a Dalitz plot. The same recombination procedure applies as for the $2 \rightarrow 2$ processes.

5.3.2 Parametrised Model

This model - implemented in the FullModelHadronicProcess - is based upon the parametrised model for light hadrons [G4] with revisions made to the G4ReactionDynamics class to eliminate flavour dependence. As in the toy model, the heavy parton and the LQS are decoupled from one another, sharing the available kinetic energy. The quark system is then passed on to the parametrised model to generate the secondaries as well as the "black track particles". These black track particles are nuclear fragments from a struck nucleus such as deuterons, tritons or α particles created with very low energies. The term derives from ages where photo-emulsion plates were used to detect energy depositions and where such particles would deposit a lot of energy very quickly leaving a "black track" in the emulsion.

As for the toy-model, the excess energy from the recombination is added as a local energy deposit by GEANT4. This local energy deposit is shown in figure 5.5 as mean value per interaction for gluino hadrons as well as stop hadrons in iron and carbon. The mass of the LQS in this case is taken from the constituent mass model used in PYTHIA. It is thus 950 MeV/c^2 for the gluino case and 650 MeV/c^2 for the stop case.

It should be stressed that this is the only point at which the physics content of the model deviates from GEANT3. In GEANT3 the heavy hadron was treated as one heavy object in the kinematics treatment, and the kinematic distributions were rescaled for nuclear evaporation to take into account that not all of the kinetic energy was available for production of secondaries. In the present work the reaction is viewed as being between a totally decoupled LQS and a nucleus with a subsequent re-coupling of the LQS with the heavy parton. All differences between GEANT3 and GEANT4 should thus be expected to have their origin in this difference of kinematical treatment.

5.4 Simulation Results

This section is devoted to the detailed study of the developed simulation for the physics cases of stop and gluino R-hadrons. Particle and process lists corresponding to the cases of stable gluino hadrons and stable stop hadrons were implemented. The terminology used is listed in table 5.1. The masses of the individual hadrons were chosen according to a simple constituent mass model as pointed out in section 5.3.2. This model is in accordance with the convention used in PYTHIA. This convention is in perfect agreement with section 3.1.4 with effective constituent masses as mentioned in section 5.3.2. The effective particle content of the model thus becomes the particles in table 5.2. A couple of remarks go with this table. First of all

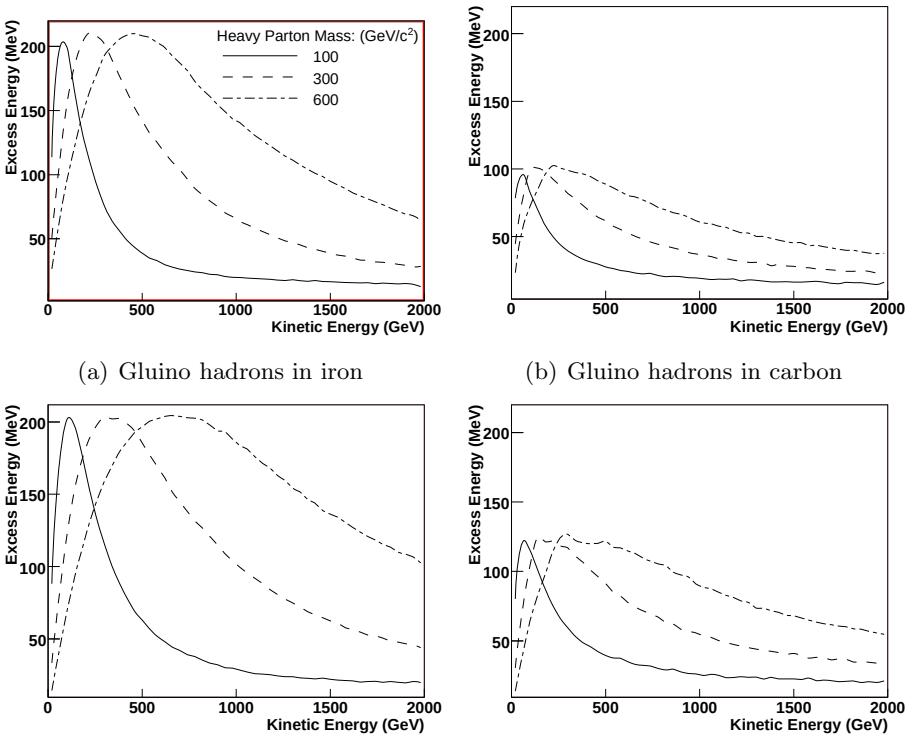

(a) Gluino hadrons in iron

(b) Gluino hadrons in carbon

(c) Stop hadrons in iron

(d) Stop hadrons in carbon

Figure 5.5: *Local energy deposit from momentum recombination. The kinetic energy is that of the heavy hadron as seen in the rest frame of the struck nucleus. The statistical error is consistently below 1 MeV.*

Flavour content:	Name:
$\tilde{g}q\bar{q}$	gluino meson
$\tilde{g}qqq$	gluino baryon
$\tilde{t}\bar{q}$	stop mesonino
$\bar{\tilde{t}}q$	anti-stop mesonino
$\tilde{t}qq$	stop sbaryon
$\bar{\tilde{t}}qq$	anti-stop sbaryon

Table 5.1: *R-hadron terminology summarised. The type-setting of the anti-stop sbaryon with one single line has been chosen for easier readability of the process lists of the corresponding process lists in section 5.4.2.*

(s)baryonic states containing heavier quarks than the s have been ignored as the production probability is vanishing due to the parton density functions relevant at the LHC. Also the PDG codes are non-standard, although adopted by the PDG [PDG06]. The spin-digit of the code does not - as is usual - denote $2s + 1$. Rather it denotes this value for the LQS alone. Putting in the $\tilde{t}$ and the $\tilde{g}$ explicitly using the 6 and 9 (which are really the t and g codes respectively) the SUSY nature of the particles is denoted by adding 1,000,000 to the individual code.

The masses of the R-hadrons in the table do not depend on the spin state of the LQS. This is in accordance with the arguments in [Kra04b] in which it is argued that the mass splittings are expected to be small enough to be safely neglected. The actual constituent masses used are simply the PYTHIA values for compatibility.

No mesonino-antimesonino oscillation have been assumed in the stop case. These oscillations are possible for neutral mesoninos through electroweak loops [ST00]. The amplitude is unknown, though, which is the reason it has here been ignored. No cross section resonance or charge exchange suppression was configured.

5.4.1 Process Lists for Gluino R-hadrons

When populating lists of processes for gluino R-hadrons we start by considering u and d quarks only for reasons of simplicity. As mentioned in section 5.2.1 the mechanism of the interaction is assumed to be reggeon / pomeron exchange as exemplified in figure 5.6. The figure shows an $R^{+}_{\tilde{g}u\bar{d}}$ hadron interacting with a neutron through pomeron exchange (figure 5.6(a)) and reggeon exchange (figures 5.6(b) and 5.6(c)). Using this picture (although the implemented model relies purely on phase space considerations) the writing down of processes now basically amounts to counting quarks in the reaction as shown in figure 5.7.

Performing all the permutations of u and d quarks for gluino R-mesons and R-baryons interacting with neutrons and protons one ends up with process lists identical to those used in [Kra04b]. These lists, however, do not consider heavier flavours than u and d quarks and anti-R-baryons are not treated.

Treating the inclusion of heavier quarks raises some problems. There is no simple way to calculate the life time of a strange R-hadron in flight. One might of course use the Kaon value for the life time but it has here been chosen to ignore this complication as the impact on the phenomenology is estimated to be absolutely minuscule. The decay of a quark cannot be

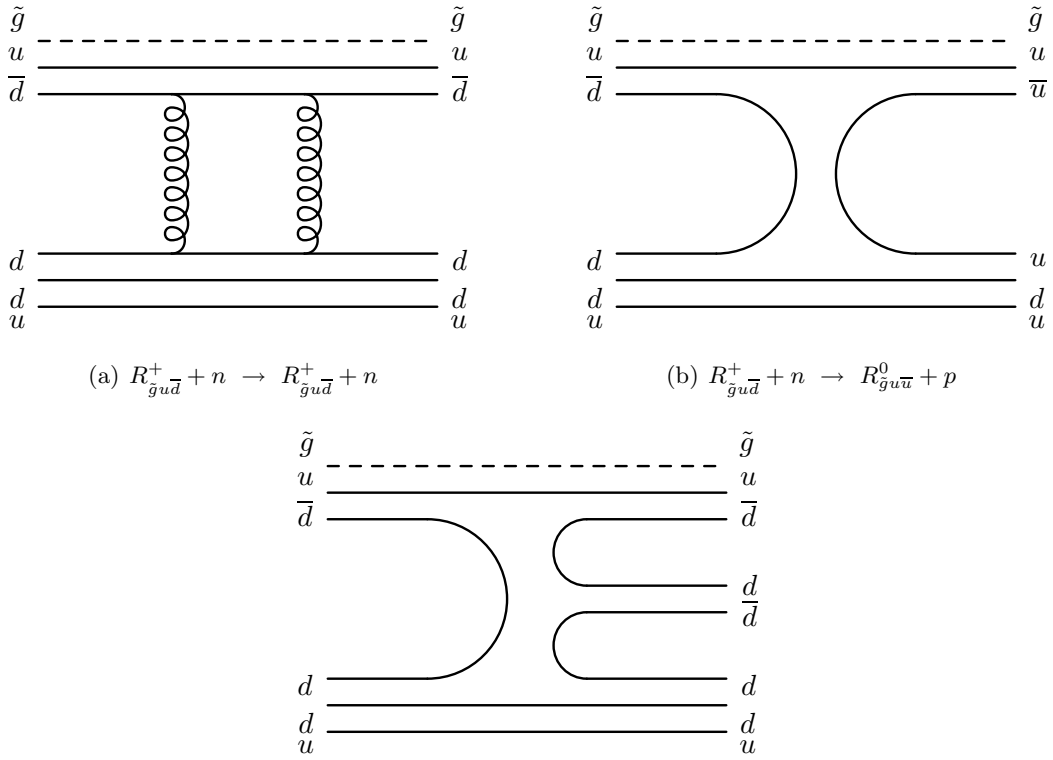

(a) $R^+_{\tilde{g}u\overline{d}} + n \;\rightarrow\; R^+_{\tilde{g}u\overline{d}} + n$

(b) $R^+_{\tilde{g}u\overline{d}} + n \;\rightarrow\; R^0_{\tilde{g}u\overline{u}} + p$

(c) $R^+_{\tilde{g}u\overline{d}} + n \;\rightarrow\; R^+_{\tilde{g}u\overline{d}} + n + \pi^0$

Figure 5.6: *Gluino R-mesons in* $2 \rightarrow 2$ *processes and* $2 \rightarrow 3$ *processes. Note how the gluino does not partake in the reaction at all while charge exchange and* $2 \rightarrow 3$ *processes arise naturally from the interactions of the light quarks accompanying the gluino.*

$$
\begin{array}{lrll}
R^+_{\tilde{g}u\overline{d}} + p = \tilde{g}u\overline{d} + uud & \rightarrow & \tilde{g}u\overline{d} + uud & = R^+_{\tilde{g}u\overline{d}} + p \\
& \rightarrow & \tilde{g}uuu + d\overline{d} & = R^{++}_{\tilde{g}uuu} + \pi^0 \\
& \rightarrow & \tilde{g}uud + u\overline{d} & = R^+_{\tilde{g}uud} + \pi^+ \\
& \rightarrow & \tilde{g}u\overline{d} + uud + d\overline{d} & = R^+_{\tilde{g}u\overline{d}} + p + \pi^0 \\
& \rightarrow & \tilde{g}u\overline{d} + udd + u\overline{d} & = R^+_{\tilde{g}u\overline{d}} + n + \pi^+ \\
& \rightarrow & \ldots &
\end{array}
$$

Figure 5.7: *Quark counting for gluino R-mesons interacting with protons. The summing up of all possibilities for final states of this reactions is achieved through the considerations illustrated in figure 5.6.*

Name	PDG code	M_{LQS} (MeV/c^2)
Gluino:		
$R^0_{\tilde{g}g}$	1000993	700
$R^0_{\tilde{g}d\overline{d}}$	1009113	650
$R^+_{\tilde{g}u\overline{d}}$	1009213	650
$R^0_{\tilde{g}u\overline{u}}$	1009223	650
$R^0_{\tilde{g}d\overline{s}}$	1009313	825
$R^+_{\tilde{g}u\overline{s}}$	1009323	825
$R^0_{\tilde{g}s\overline{s}}$	1009333	1800
$R^-_{\tilde{g}ddd}$	1091114	975
$R^0_{\tilde{g}udd}$	1092114	975
$R^+_{\tilde{g}uud}$	1092214	975
$R^{++}_{\tilde{g}uuu}$	1092224	975
$R^-_{\tilde{g}sdd}$	1093114	1150
$R^0_{\tilde{g}sud}$	1093214	1150
$R^+_{\tilde{g}suu}$	1093224	1150
$R^-_{\tilde{g}ssd}$	1093314	1300
$R^0_{\tilde{g}ssu}$	1093324	1300
$R^-_{\tilde{g}sss}$	1093334	1600

Name	PDG code	M_{LQS} (MeV/c^2)
Stop:		
$R^+_{\tilde{t}\overline{d}}$	1000612	325
$R^0_{\tilde{t}\overline{u}}$	1000622	325
$R^+_{\tilde{t}\overline{s}}$	1000632	500
$R^0_{\tilde{t}\overline{c}}$	1000642	1500
$R^+_{\tilde{t}\overline{b}}$	1000652	4800
$R^0_{\tilde{t}dd_1}$	1006113	650
$R^+_{\tilde{t}ud_0}$	1006211	650
$R^+_{\tilde{t}ud_1}$	1006213	650
$R^{++}_{\tilde{t}uu_1}$	1006223	650
$R^0_{\tilde{t}sd_0}$	1006311	825
$R^0_{\tilde{t}sd_1}$	1006313	825
$R^+_{\tilde{t}su_0}$	1006321	825
$R^+_{\tilde{t}su_1}$	1006323	825
$R^0_{\tilde{t}ss_1}$	1006333	1000

Table 5.2: *Gluino and stop hadrons in the implemented model. The antiparticles have not been explicitly written in the table.*

expected to change the trajectory of an object with a mass of $\mathcal{O}$(100's of GeV/c^2) measurably and the resulting muons would be of low transverse momentum leading to absorption in the detector. Also the combinatorics in the above considerations become considerably more complicated when having to differ between d and s quarks. This is illustrated in equation 5.5.

$$R^0_{\tilde{g}uds} + uud \rightarrow R^0_{\tilde{g}uds} + uud \quad / \quad R^0_{\tilde{g}udd} + uus \tag{5.5}$$

Again this is not something that can be expected to change the phenomenology vastly. If we are anyway ignoring decays of the constituent quarks of the R-hadron the only difference would be in the energy depositions of low energy strange hadrons instead of purely protons, neutrons and pions. This is not estimated to impact the phenomenology significantly, so the solution to incorporating the heavier flavours has here been chosen to be duplicating the process list for all R-hadrons containing d quarks to the strange R-hadrons and simply turn the s quark into a d quark in the first hadronic reaction. PYTHIA never produces heavier flavours than this but they would be incorporated in the same manner.

Anti-R-baryons arise rarely in the hadronisation of a gluino event as this requires three anti-quarks. When they do appear they will interact primarily through elastic scattering and baryon annihilation. Baryon number conservation also implies that an anti-R-baryon will never be created in the nuclear interactions of an R-meson or R-baryon and they are thus to

be regarded as extremely rare. The possible processes look like

$$\begin{aligned} R^{-}_{\tilde{g}\overline{uud}} + p &\rightarrow R^{-}_{\tilde{g}\overline{uud}} + p \\ &\rightarrow R^{0}_{\tilde{g}u\overline{u}} + \pi^0 + \pi^0 \\ &\rightarrow R^{+}_{\tilde{g}u\overline{d}} + \pi^0 + \pi^- \\ &\rightarrow R^{-}_{\tilde{g}d\overline{u}} + \pi^0 + \pi^+. \end{aligned} \tag{5.6}$$

These processes are thus put into the simulation for anti-R-baryons. Strange anti-R-baryons are treated just like strange R-mesons and R-baryons by treating the $\overline{s}$ quark like a $\overline{d}$ quark and removing it in the first nuclear reaction.

5.4.2 Process Lists for Stop R-hadrons

Process lists for stop hadrons have not been described in [Kra04b], so some more detail will be given to the area. As a start we consider only hadrons consisting of u and d quarks just as was done for the gluino case. The particle contents thus consists of mesoninos ($R^{+}_{\tilde{t}\overline{d}}$, $R^{0}_{\tilde{t}\overline{u}}$, $R^{-}_{\bar{\tilde{t}}d}$ and $R^{0}_{\bar{\tilde{t}}u}$) as well as sbaryons ($R^{++}_{\tilde{t}uu}$, $R^{+}_{\tilde{t}ud}$ and $R^{0}_{\tilde{t}dd}$) and anti-sbaryons ($R^{--}_{\bar{\tilde{t}}\overline{uu}}$, $R^{-}_{\bar{\tilde{t}}\overline{ud}}$ and $R^{0}_{\bar{\tilde{t}}\overline{dd}}$).

The simplest case to treat is the $\bar{\tilde{t}}q$ states. Applying the quark counting of reggeon and pomeron exchange leads to the processes shown in table 5.3. Completing the description of

$2 \rightarrow 2$ processes:		
$R^{0}_{\bar{\tilde{t}}u} + p$	$\rightarrow$	$R^{0}_{\bar{\tilde{t}}u} + p$
$R^{-}_{\bar{\tilde{t}}d} + p$	$\rightarrow$	$R^{-}_{\bar{\tilde{t}}d} + p$
$R^{0}_{\bar{\tilde{t}}u} + n$	$\rightarrow$	$R^{0}_{\bar{\tilde{t}}u} + n$
$R^{-}_{\bar{\tilde{t}}d} + n$	$\rightarrow$	$R^{-}_{\bar{\tilde{t}}d} + n$
$R^{0}_{\bar{\tilde{t}}u} + n$	$\rightarrow$	$R^{-}_{\bar{\tilde{t}}d} + p$
$R^{-}_{\bar{\tilde{t}}d} + p$	$\rightarrow$	$R^{0}_{\bar{\tilde{t}}u} + n$

$2 \rightarrow 3$ processes:		
$R^{0}_{\bar{\tilde{t}}u} + n$	$\rightarrow$	$R^{-}_{\bar{\tilde{t}}d} + p + \pi^0$
	$\rightarrow$	$R^{0}_{\bar{\tilde{t}}u} + n + \pi^0$
	$\rightarrow$	$R^{-}_{\bar{\tilde{t}}d} + n + \pi^+$
	$\rightarrow$	$R^{0}_{\bar{\tilde{t}}u} + p + \pi^-$
$R^{0}_{\bar{\tilde{t}}u} + p$	$\rightarrow$	$R^{0}_{\bar{\tilde{t}}u} + n + \pi^+$
	$\rightarrow$	$R^{-}_{\bar{\tilde{t}}d} + p + \pi^+$
	$\rightarrow$	$R^{0}_{\bar{\tilde{t}}u} + p + \pi^0$
$R^{-}_{\bar{\tilde{t}}d} + n$	$\rightarrow$	$R^{-}_{\bar{\tilde{t}}d} + n + \pi^0$
	$\rightarrow$	$R^{-}_{\bar{\tilde{t}}d} + p + \pi^-$
	$\rightarrow$	$R^{0}_{\bar{\tilde{t}}u} + n + \pi^-$
$R^{-}_{\bar{\tilde{t}}d} + p$	$\rightarrow$	$R^{-}_{\bar{\tilde{t}}d} + p + \pi^0$
	$\rightarrow$	$R^{-}_{\bar{\tilde{t}}d} + n + \pi^+$
	$\rightarrow$	$R^{0}_{\bar{\tilde{t}}u} + n + \pi^0$
	$\rightarrow$	$R^{0}_{\bar{\tilde{t}}u} + p + \pi^-$

Table 5.3: *Process table for $\bar{\tilde{t}}u/d$ states.*

the mesoninos before progressing to the sbaryons and anti-sbaryons we now move to the $\tilde{t}\overline{q}$ states and their interactions with matter. As was the case for the gluino states these states only have anti-quarks available to react with the surrounding matter. Reactions therefore fall into three categories as shown for $2 \rightarrow 2$ processes in figure 5.8. Running through all permutations of quark contents and hadronic target particles the process list for mesoninos

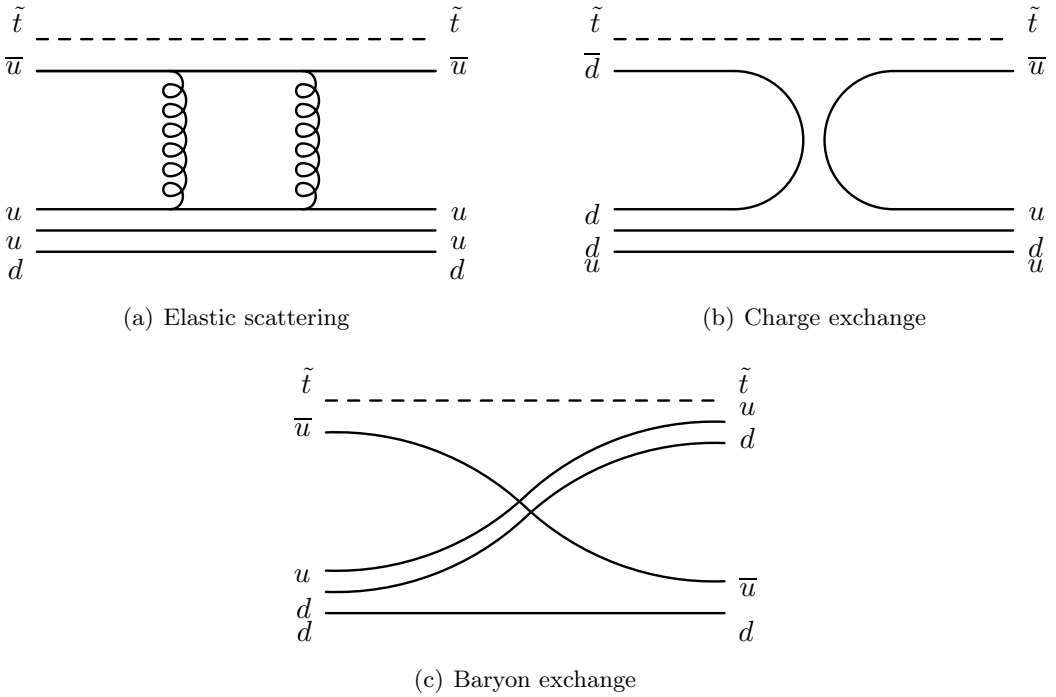

(a) Elastic scattering

(b) Charge exchange

(c) Baryon exchange

Figure 5.8: $2 \to 2$ *nuclear reactions of* $\tilde{t}\overline{q}$ *R-hadrons (stop-mesoninos). The stop remains a spectator to the nuclear reactions while the exchange of light quarks mediate charge and baryon number exchange.*

containing a $\tilde{t}$ is summarised in table 5.4. Note how mesoninos containing a $\tilde{t}$ rather than a $\overline{\tilde{t}}$ can acquire a baryon number in hadronic reactions.

The combinatorics of the processes increases in complexity when moving to sbaryons and anti-sbaryons. The governing principles remain the same, though. Process lists for sbaryons and anti-sbaryons are summarised in table 5.5

5.4.3 Preliminary Observations

The first observation that can be made from simply considering the possible processes of sections 5.4.1 and 5.4.2 is that a gluino meson or a stop mesonino undergoing nuclear reactions in matter may at some point acquire a baryon number, thus turning into a gluino baryon or a stop sbaryon respectively. In ordinary matter it is impossible for the heavy hadron to part with the acquired baryon number due to baryon number conservation. Conversely anti-stop sbaryons will tend to annihilate with nuclear matter leading to a conversion into mesoninos. Where not explicitly noted otherwise, the particles studied were gluino baryons and stop sbaryons. In the cases where anti-stops were explicitly studied the incident particle was chosen to be a anti-stop mesonino.

The focus in the following will be twofold. The compatibility of the results obtained with GEANT4 to the GEANT3 results will be demonstrated, and differences between the colour octet / colour singlet heavy parton cases exemplified by squarks and gluinos will be highlighted.

$2 \to 2$ processes:		
Elastic:		
$R^0_{\tilde{t}\overline{u}} + p$	$\to$	$R^0_{\tilde{t}\overline{u}} + p$
$R^0_{\tilde{t}\overline{u}} + n$	$\to$	$R^0_{\tilde{t}\overline{u}} + n$
$R^+_{\tilde{t}\overline{d}} + p$	$\to$	$R^+_{\tilde{t}\overline{d}} + p$
$R^+_{\tilde{t}\overline{d}} + n$	$\to$	$R^+_{\tilde{t}\overline{d}} + n$
Charge exchange:		
$R^0_{\tilde{t}\overline{u}} + p$	$\leftrightarrow$	$R^+_{\tilde{t}\overline{d}} + n$
Baryon exchange:		
$R^0_{\tilde{t}\overline{u}} + n$	$\to$	$R^+_{\tilde{t}ud} + \pi^-$
	$\to$	$R^0_{\tilde{t}dd} + \pi^0$
$R^0_{\tilde{t}\overline{u}} + p$	$\to$	$R^{++}_{\tilde{t}uu} + \pi^-$
	$\to$	$R^+_{\tilde{t}ud} + \pi^0$
$R^+_{\tilde{t}\overline{d}} + n$	$\to$	$R^+_{\tilde{t}ud} + \pi^0$
	$\to$	$R^0_{\tilde{t}dd} + \pi^+$
$R^+_{\tilde{t}\overline{d}} + p$	$\to$	$R^{++}_{\tilde{t}uu} + \pi^0$
	$\to$	$R^+_{\tilde{t}ud} + \pi^+$

$2 \to 3$ processes:		
Normal inelastic:		
$R^0_{\tilde{t}\overline{u}} + n$	$\to$	$R^+_{\tilde{t}\overline{d}} + n + \pi^-$
	$\to$	$R^0_{\tilde{t}\overline{u}} + n + \pi^0$
	$\to$	$R^0_{\tilde{t}\overline{u}} + p + \pi^-$
$R^0_{\tilde{t}\overline{u}} + p$	$\to$	$R^+_{\tilde{t}\overline{d}} + p + \pi^-$
	$\to$	$R^0_{\tilde{t}\overline{u}} + p + \pi^0$
	$\to$	$R^0_{\tilde{t}\overline{u}} + n + \pi^+$
	$\to$	$R^+_{\tilde{t}\overline{d}} + n + \pi^0$
$R^+_{\tilde{t}\overline{d}} + n$	$\to$	$R^0_{\tilde{t}\overline{u}} + n + \pi^+$
	$\to$	$R^+_{\tilde{t}\overline{d}} + n + \pi^0$
	$\to$	$R^0_{\tilde{t}\overline{u}} + p + \pi^0$
	$\to$	$R^+_{\tilde{t}\overline{d}} + p + \pi^-$
$R^+_{\tilde{t}\overline{d}} + p$	$\to$	$R^0_{\tilde{t}\overline{u}} + p + \pi^+$
	$\to$	$R^+_{\tilde{t}\overline{d}} + p + \pi^0$
	$\to$	$R^+_{\tilde{t}\overline{d}} + n + \pi^+$
Baryon exchange:		
$R^0_{\tilde{t}\overline{u}} + n$	$\to$	$R^+_{\tilde{t}ud} + \pi^- + \pi^0$
	$\to$	$R^0_{\tilde{t}dd} + \pi^- + \pi^+$
	$\to$	$R^0_{\tilde{t}dd} + \pi^0 + \pi^0$
$R^0_{\tilde{t}\overline{u}} + p$	$\to$	$R^{++}_{\tilde{t}uu} + \pi^- + \pi^0$
	$\to$	$R^+_{\tilde{t}ud} + \pi^- + \pi^+$
	$\to$	$R^+_{\tilde{t}ud} + \pi^0 + \pi^0$
	$\to$	$R^0_{\tilde{t}dd} + \pi^+ + \pi^0$
$R^+_{\tilde{t}\overline{d}} + n$	$\to$	$R^+_{\tilde{t}ud} + \pi^- + \pi^+$
	$\to$	$R^+_{\tilde{t}ud} + \pi^0 + \pi^0$
	$\to$	$R^0_{\tilde{t}dd} + \pi^+ + \pi^0$
$R^+_{\tilde{t}\overline{d}} + p$	$\to$	$R^{++}_{\tilde{t}uu} + \pi^- + \pi^+$
	$\to$	$R^{++}_{\tilde{t}uu} + \pi^0 + \pi^0$
	$\to$	$R^+_{\tilde{t}ud} + \pi^0 + \pi^+$

Table 5.4: *Process table for $\tilde{t}\overline{u}/\overline{d}$ states.*

(a) Sbaryon process list

$2 \to 2$ processes:		
Elastic:		
$R^{++}_{\tilde{t}uu} + n/p$	$\to$	$R^{++}_{\tilde{t}uu} + n/p$
$R^{+}_{\tilde{t}ud} + n/p$	$\to$	$R^{+}_{\tilde{t}ud} + n/p$
$R^{00}_{\tilde{t}dd} + n/p$	$\to$	$R^{00}_{\tilde{t}dd} + n/p$
Charge exchange:		
$R^{++}_{\tilde{t}uu} + n$	$\to$	$R^{+}_{\tilde{t}ud} + p$
$R^{+}_{\tilde{t}ud} + n$	$\to$	$R^{0}_{\tilde{t}dd} + p$
$R^{+}_{\tilde{t}ud} + p$	$\to$	$R^{++}_{\tilde{t}uu} + n$
$R^{0}_{\tilde{t}ud} + p$	$\to$	$R^{+}_{\tilde{t}ud} + n$
$2 \to 3$ processes:		
$R^{++}_{\tilde{t}uu} + n/p$	$\to$	$R^{++}_{\tilde{t}uu} + n/p + \pi^0$
$R^{+}_{\tilde{t}ud} + n/p$	$\to$	$R^{+}_{\tilde{t}ud} + n/p + \pi^0$
$R^{00}_{\tilde{t}dd} + n/p$	$\to$	$R^{00}_{\tilde{t}dd} + n/p + \pi^0$
Charge exchange:		
$R^{++}_{\tilde{t}uu} + n$	$\to$	$R^{+}_{\tilde{t}ud} + n + \pi^+$
	$\to$	$R^{+}_{\tilde{t}ud} + p + \pi^0$
	$\to$	$R^{++}_{\tilde{t}uu} + p + \pi^-$
$R^{++}_{\tilde{t}uu} + p$	$\to$	$R^{+}_{\tilde{t}ud} + p + \pi^+$
	$\to$	$R^{++}_{\tilde{t}uu} + n + \pi^+$
$R^{+}_{\tilde{t}ud} + n$	$\to$	$R^{0}_{\tilde{t}dd} + p + \pi^0$
	$\to$	$R^{0}_{\tilde{t}dd} + n + \pi^+$
	$\to$	$R^{+}_{\tilde{t}ud} + p + \pi^-$
$R^{+}_{\tilde{t}ud} + p$	$\to$	$R^{++}_{\tilde{t}uu} + n + \pi^0$
	$\to$	$R^{0}_{\tilde{t}dd} + p + \pi^+$
	$\to$	$R^{++}_{\tilde{t}uu} + p + \pi^-$
	$\to$	$R^{+}_{\tilde{t}ud} + n + \pi^+$
$R^{0}_{\tilde{t}dd} + n$	$\to$	$R^{0}_{\tilde{t}dd} + p + \pi^-$
	$\to$	$R^{+}_{\tilde{t}ud} + n + \pi^-$
$R^{0}_{\tilde{t}dd} + p$	$\to$	$R^{0}_{\tilde{t}dd} + n + \pi^+$
	$\to$	$R^{+}_{\tilde{t}ud} + n + \pi^0$
	$\to$	$R^{+}_{\tilde{t}ud} + p + \pi^-$
	$\to$	$R^{++}_{\tilde{t}uu} + n + \pi^-$

(b) Anti-sbaryon process list

$2 \to 2$ processes:		
Elastic:		
$R^{--}_{\bar{\tilde{t}}uu} + n/p$	$\to$	$R^{--}_{\bar{\tilde{t}}uu} + n/p$
$R^{-}_{\bar{\tilde{t}}ud} + n/p$	$\to$	$R^{-}_{\bar{\tilde{t}}ud} + n/p$
$R^{0}_{\bar{\tilde{t}}dd} + n/p$	$\to$	$R^{0}_{\bar{\tilde{t}}dd} + n/p$
Charge exchange:		
$R^{--}_{\bar{\tilde{t}}uu} + p$	$\to$	$R^{-}_{\bar{\tilde{t}}ud} + n$
$R^{-}_{\bar{\tilde{t}}ud} + p$	$\to$	$R^{0}_{\bar{\tilde{t}}dd} + n$
$R^{-}_{\bar{\tilde{t}}ud} + n$	$\to$	$R^{--}_{\bar{\tilde{t}}uu} + p$
$R^{0}_{\bar{\tilde{t}}dd} + n$	$\to$	$R^{-}_{\bar{\tilde{t}}ud} + p$
Annihilation:		
$R^{--}_{\bar{\tilde{t}}uu} + p$	$\to$	$R^{0}_{\bar{\tilde{t}}u} + \pi^-$
	$\to$	$R^{-}_{\bar{\tilde{t}}d} + \pi^0$
$R^{--}_{\bar{\tilde{t}}uu} + n$	$\to$	$R^{-}_{\bar{\tilde{t}}d} + \pi^-$
$R^{-}_{\bar{\tilde{t}}ud} + p$	$\to$	$R^{0}_{\bar{\tilde{t}}u} + \pi^0$
	$\to$	$R^{-}_{\bar{\tilde{t}}d} + \pi^+$
$R^{-}_{\bar{\tilde{t}}ud} + n$	$\to$	$R^{-}_{\bar{\tilde{t}}d} + \pi^0$
	$\to$	$R^{0}_{\bar{\tilde{t}}u} + \pi^-$
$R^{0}_{\bar{\tilde{t}}dd} + p$	$\to$	$R^{0}_{\bar{\tilde{t}}u} + \pi^+$
$R^{0}_{\bar{\tilde{t}}dd} + n$	$\to$	$R^{0}_{\bar{\tilde{t}}u} + \pi^0$
	$\to$	$R^{-}_{\bar{\tilde{t}}d} + \pi^+$
$2 \to 3$ processes:		
$R^{--}_{\bar{\tilde{t}}uu} + n/p$	$\to$	$R^{--}_{\bar{\tilde{t}}uu} + n/p + \pi^0$
$R^{-}_{\bar{\tilde{t}}ud} + n/p$	$\to$	$R^{-}_{\bar{\tilde{t}}ud} + n/p + \pi^0$
$R^{0}_{\bar{\tilde{t}}dd} + n/p$	$\to$	$R^{0}_{\bar{\tilde{t}}dd} + n/p + \pi^0$
Charge exchange:		
$R^{--}_{\bar{\tilde{t}}uu} + n$	$\to$	$R^{-}_{\bar{\tilde{t}}ud} + n + \pi^-$
	$\to$	$R^{--}_{\bar{\tilde{t}}uu} + p + \pi^-$
$R^{--}_{\bar{\tilde{t}}uu} + p$	$\to$	$R^{--}_{\bar{\tilde{t}}uu} + n + \pi^+$
	$\to$	$R^{-}_{\bar{\tilde{t}}ud} + n + \pi^0$
	$\to$	$R^{0}_{\bar{\tilde{t}}dd} + n + \pi^-$
	$\to$	$R^{-}_{\bar{\tilde{t}}ud} + p + \pi^-$
$R^{-}_{\bar{\tilde{t}}ud} + n$	$\to$	$R^{-}_{\bar{\tilde{t}}ud} + p + \pi^-$
	$\to$	$R^{--}_{\bar{\tilde{t}}uu} + p + \pi^0$
	$\to$	$R^{--}_{\bar{\tilde{t}}uu} + n + \pi^+$
	$\to$	$R^{0}_{\bar{\tilde{t}}dd} + n + \pi^-$
$R^{-}_{\bar{\tilde{t}}ud} + p$	$\to$	$R^{-}_{\bar{\tilde{t}}ud} + n + \pi^+$
	$\to$	$R^{--}_{\bar{\tilde{t}}uu} + p + \pi^+$
	$\to$	$R^{0}_{\bar{\tilde{t}}dd} + n + \pi^0$
	$\to$	$R^{0}_{\bar{\tilde{t}}dd} + p + \pi^-$

Table 5.5: *Process lists for stop sbaryons and anti-sbaryons*

5.4.4 Baryonisation

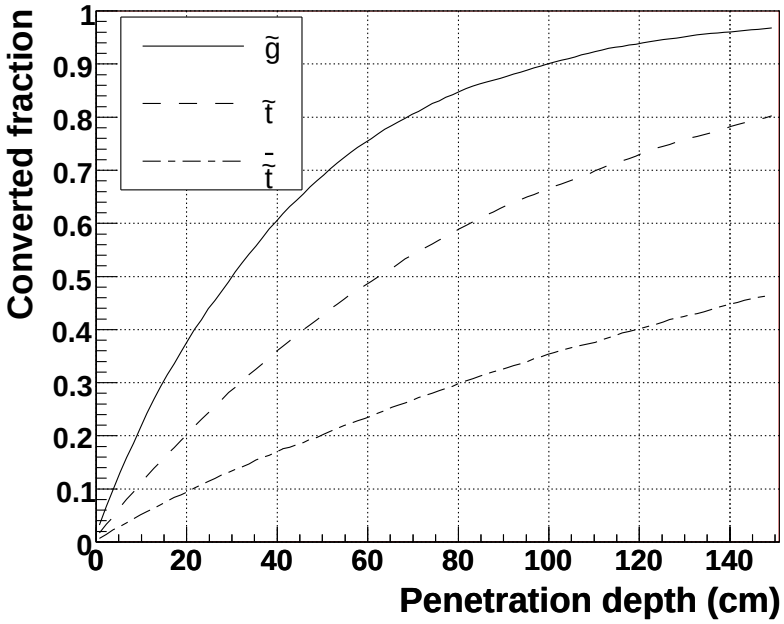

Figure 5.9: *Fraction of gluino baryons, stop sbaryons and anti-stop mesoninos as a function of the travelled distance in iron.*

To study the acquisition of baryon number figure 5.9 shows the fraction of gluino mesons, stop mesoninos and anti-stop sbaryons that have converted into gluino baryons, stop sbaryons or anti-stop mesoninos respectively as a function of the travelled distance in iron. The heavy parton has been given a mass of 300 GeV/c^2 but this has little influence as long as $M_{LQS} \ll M_{Tot}$ due to the nature of the cross section calculation. There is no discernible difference between the toy-model and the parametrised model, as this quantity exclusively relies on pure phase space considerations. Any difference would have to be induced by nuclear binding which is a small effect at the energies considered. The curve representing the gluino case is not completely identical to that of the previous work. In GEANT3 approximately 96% of the gluino mesons had converted into baryons after travelling through 1 m of iron [Kra04b] whereas the corresponding number for GEANT4 is 90%. There is, however a dependence of these curves on the kinematic input distributions. Running the programme at lower energies opens up the phase space for $2 \rightarrow 2$ processes relative to that for $2 \rightarrow 3$ processes. The $2 \rightarrow 2$ processes have a higher fraction of baryon number changing processes than the $2 \rightarrow 3$ processes leading to earlier conversions. In this context the GEANT4 curve can be considered to represent a high-energy asymptotic limit, while the GEANT3 curve is relevant at significantly lower energies. The GEANT4 curve was made for 300 GeV/c^2 gluino R-hadrons generated with a flat distribution of kinetic energies ranging from 0 to 2 TeV while the GEANT3 curve was made for a fixed incident momentum of 300 GeV/c for a 300 GeV/c^2 gluino [Kra]. Running the GEANT4 code at this energy reproduces the GEANT3 result.

Looking at the stop and anti-stop hadrons it is seen that the stop and anti-stop hadrons take, on average, a longer distance to change their baryon number due to the lower cross section of the smaller LQS.

5.4.5 Energy Loss

Another quantity influenced by the mass of the LQS of the stop-R-hadrons is the hadronic energy loss as can be seen in figure 5.10. The plot is for a HP mass of 300 GeV/c^2 in iron, but there is no discernible difference between different masses when parametrising in γ. The masses of the LQS are the same as in section 5.3.2. The LQS in the stop case carries a smaller fraction of kinetic energy and thus less energy is available in the collision than for the gluino case. This behaviour is clear from the plot. Considering the toy-model in comparison with the parametrised model, one observes that the energy loss grows approximately linearly with the γ-factor and hence with the energy. This is consistent with the LQS carrying a constant fraction of the total energy given the simplified treatment of the collision in this model. The parametrised model on the other hand shows an energy loss that is comparable in magnitude with an initial steep rise that flattens out with energy. As the main difference between the two models is the inclusion of the struck nucleus we can thus here directly see the effect of the nucleus on the energy loss.

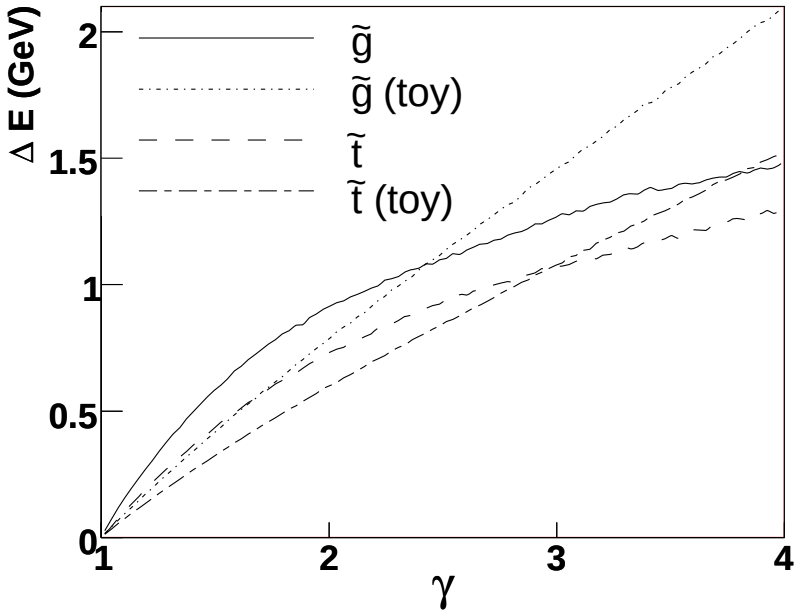

Figure 5.10: *Energy loss per hadronic interaction for 300 GeV/c^{2}gluino hadrons and stop hadrons in iron. The statistical uncertainty is on the level of one per mille and below which is why it has not been graphically shown.*

Turning to figure 5.11 which is a detailed comparison of the energy loss per hadronic interaction between the models in play, one sees immediately that the toy-model is not consistent with the previous work in neither a quantitative nor a qualitative sense, as is expected. It *does*, however, give numbers within the same order of magnitude. We thus see clearly for both distributions the changes in phenomenology induced by the treatment of the struck nucleus and the consequent changes in kinematics. Looking at the parametrised model the energy loss is closer, but not identical, to that predicted with the GEANT3 model. The difference is expected because the kinematics differs somewhat between the GEANT3 and GEANT4 versions of this model as discussed in section 5.3.2.

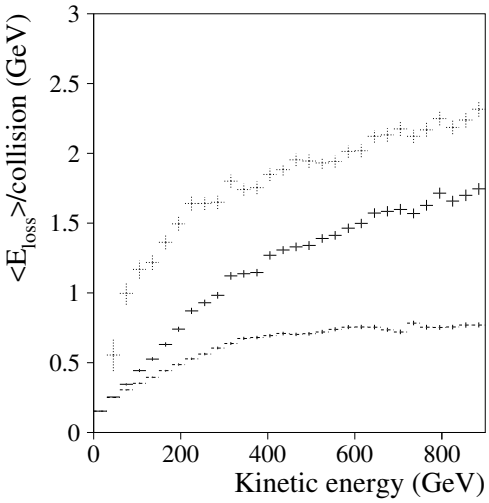

(a) GEANT3 [Kra04b]. The higher set of points is $2 \rightarrow 3$ processes, while the lower is $2 \rightarrow 2$. The central set of points is the combined one.

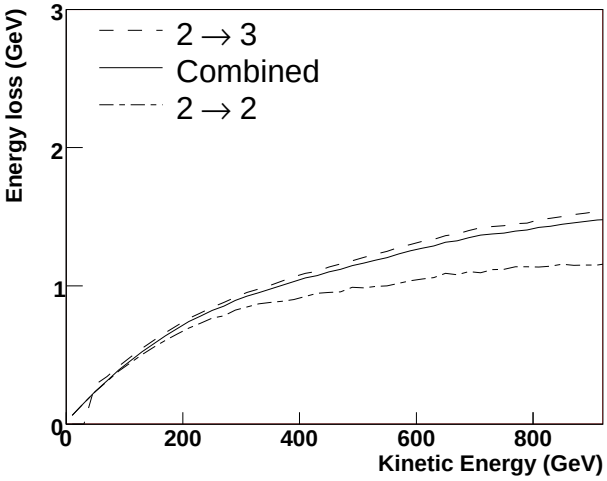

(b) GEANT4 - Parametrised model

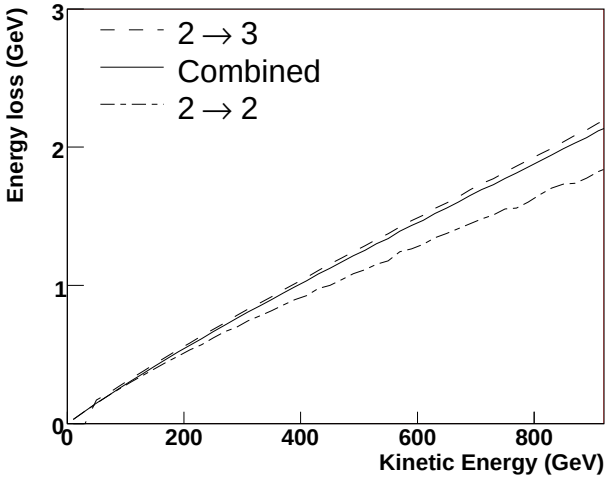

(c) GEANT4 - Toy model

Figure 5.11: *Mean energy loss per hadronic interaction for a 300 GeV/c^2 gluino hadron in iron. Both the GEANT3 and GEANT4 values are shown. The kinetic energy is that of the heavy hadron as seen from the rest-frame of the struck nucleus. The mass of the LQS is given as in section 5.3.2. The statistical uncertainty is below one per mille.*

The energy loss is seen to be somewhat higher for the $2 \rightarrow 2$ processes in GEANT4 relative to what is predicted in GEANT3 while the opposite is true for $2 \rightarrow 3$ processes. The two models are still roughly compatible, however, and nothing here suggests a drastic difference in phenomenology between the two models. To corroborate this observation the energy loss in 1 m of iron for a 300 GeV/c^2 heavy parton is shown in figure 5.12. The values were calculated using the parametrised model only. In the figure one can see both the ionisation

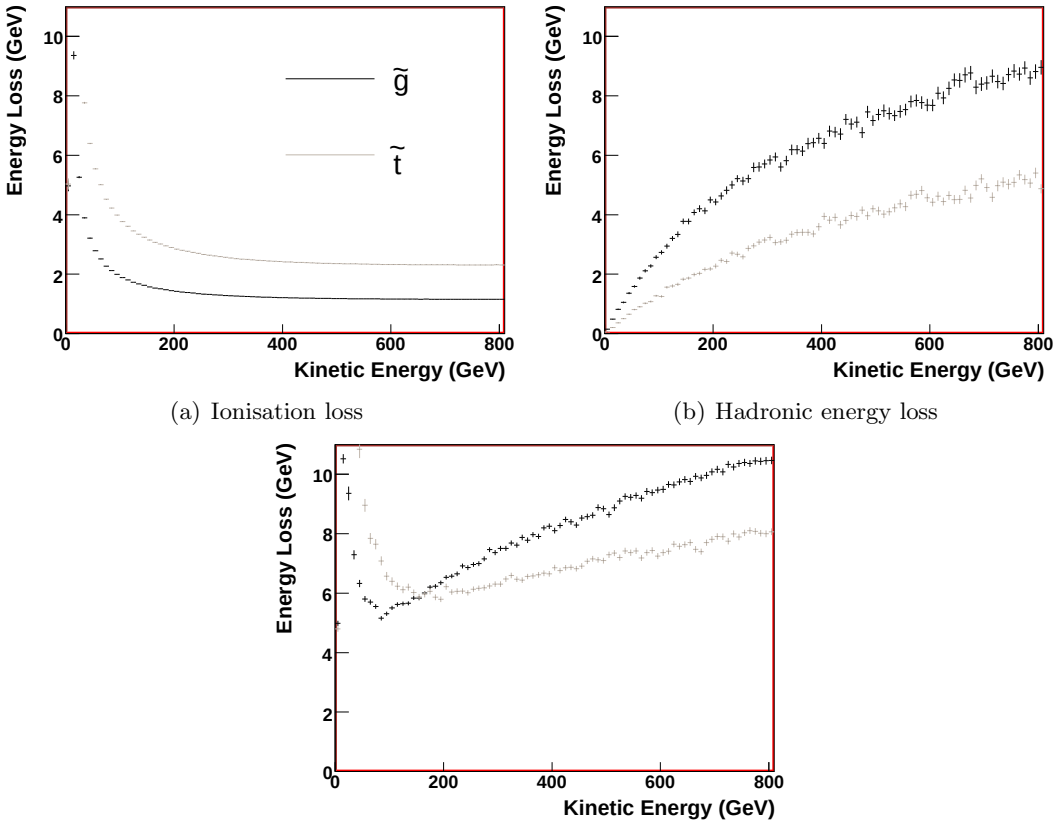

(a) Ionisation loss

(b) Hadronic energy loss

(c) Total energy loss

Figure 5.12: *Mean absolute energy loss in 1 m of iron for a 300 GeV/c^2 gluino / stop hadron as a function of kinetic energy as seen from the rest frame of the iron block. In the GEANT4 plots the numbers corresponding to gluino hadrons are represented by the fully drawn line whereas the stop hadrons are represented by a dotted line.*

and hadronic energy losses, and the combination for a 300 GeV/c^2 heavy parton. This is in comparison with the values from GEANT3 which are shown in figure 5.13. The values are seen to be compatible. The average kinetic energy carried by the LQS is smaller for the stop case than for the gluino case as previously mentioned. Also the interaction cross section is smaller. The hadronic energy loss per interaction is thus correspondingly smaller and the contribution from ionisation is clearly more visible for the stop case than for the gluino case. The effect is amplified by the fact that by simple quark counting a stop sbaryon will more often have double charge than what is the case for gluino baryons. The charge enters the Bethe Bloch formula squared [Leo93], leading to a substantially higher energy loss due to ionisation. This is indeed observed in figure 5.12(a).

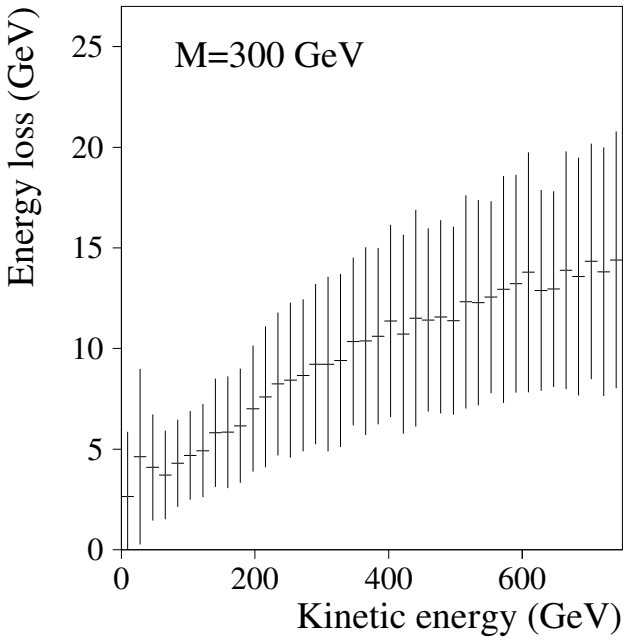

Figure 5.13: *GEANT3 hadronic energy loss in 1m of iron for a 300 GeV/c^2 gluino hadron.[Kra04b]*

We can thus conclude that the physics content of the GEANT3 and the GEANT4 models is the same, with one quantitative difference induced by a conceptual difference in the handling of the kinematics.

5.4.6 dE/dx

Turning to a classic observable, energy loss distributions were calculated as a function of distance crossed by the R-hadrons in iron. The simulations were produced in the case of gluino baryons, stop sbaryons and anti-stop mesoninos to simplify matters in relation to section 5.4.4.

As can be seen from figure 5.14 there is a difference in the shape of the distribution between the gluino and the stop/anti-stop case while the main difference between the stops and the anti-stops is the overall energy deposition. The difference in shape stems from the cross-over where the hadronic energy loss starts to dominate over the EM energy loss.

Figure 5.15 shows dE/dx for all three kinds of particles where the energy loss has been split into an EM contribution and a hadronic contribution. It is clear from the figure that stops and anti-stops are very similar apart from the overall size of the energy loss. Furthermore the onset of the hadronic energy loss is a lot sharper in the gluino case due to the larger cross section and energy loss per interaction as already discussed in section 5.4.5.

As R-hadrons are often produced in pairs, the difference in normalisation of the dE/dx distributions for squarks and anti-squarks could prove to be a powerful estimator to distinguish between a gluino and a squark signal. If dividing a sample of R-hadron candidates into a

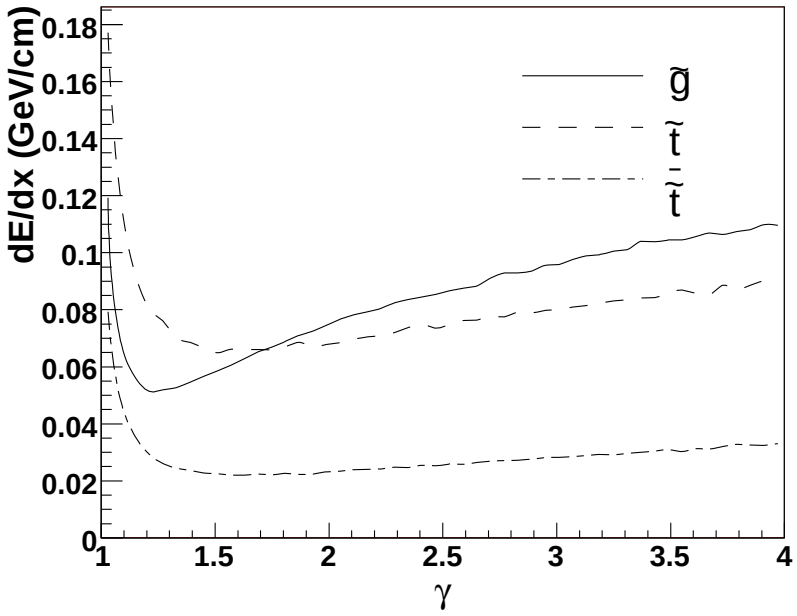

Figure 5.14: *dE/dx distributions for a sparticle mass of 600 GeV/c^2 in iron comparing the stop and anti-stop to the gluino case. Statistical errors are below one per mille.*

positively and negatively charged sample resulted in large differences in energy depositions, one would have a powerful argument for a charged colour triplet hypothesis. Conversely, if no difference was found or if the samples proved to be ill defined, one would be able to reject the squark R-hadron scenario for at least the case of no oscillations.

5.4.7 Shower Shapes

The electromagnetic and hadronic interactions of R-hadrons and their collision reaction products will give rise to showers of secondary and tertiary particles. The profiles of these showers might provide a handle on finding and identifying R-hadrons. Samples were generated in which beams of particles were shot into 10 m of iron. The particles were generated with a flat distribution in kinetic energy up to 1 TeV. Hadronic interactions of secondaries were treated using a standard GEANT4 physics list (QGSP).

Figure 5.16 sets the scale of the energy depositions. It is seen that hadrons will mostly deposit all their energy within the first 2-3 m at a scale that is two orders of magnitude beyond typical values for muons.

In figure 5.17 the various types of R-hadrons are compared to the average muon energy deposition for μ^+. It is seen that the level of energy deposition is comparable between the muons and the R-hadrons. A detailed comparison between the different species of R-hadrons shows little difference in dE/dx between gluino R-baryons generated with positive or negative charge. This is to be expected as after a few hadronic interactions the R-hadron will have no memory of its initial charge. Also the sign of the charge plays no role neither in the Bethe-Bloch formula or the hadronic interactions. As expected the lower cross section of the anti-stop states lead to a smaller overall energy deposition than for any of the other cases.

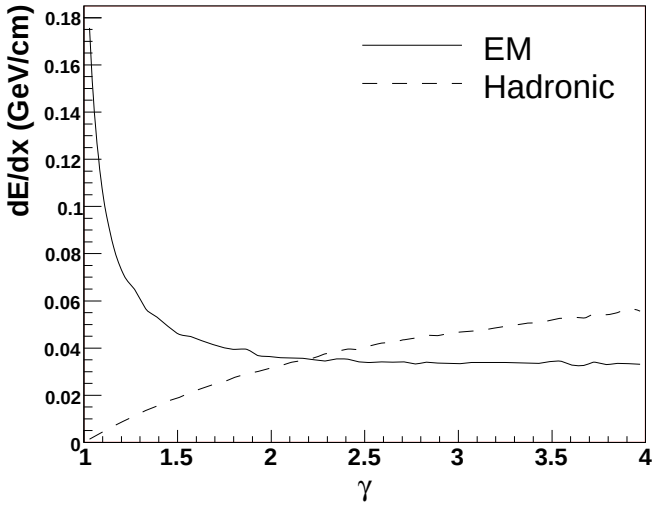

(a) Stop sbaryons ($\tilde{t}qq$)

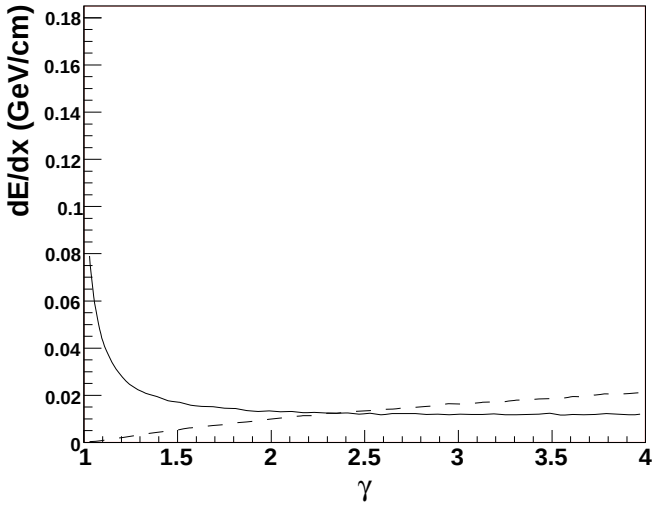

(b) Anti-stop mesoninos ($\bar{\tilde{t}}q$)

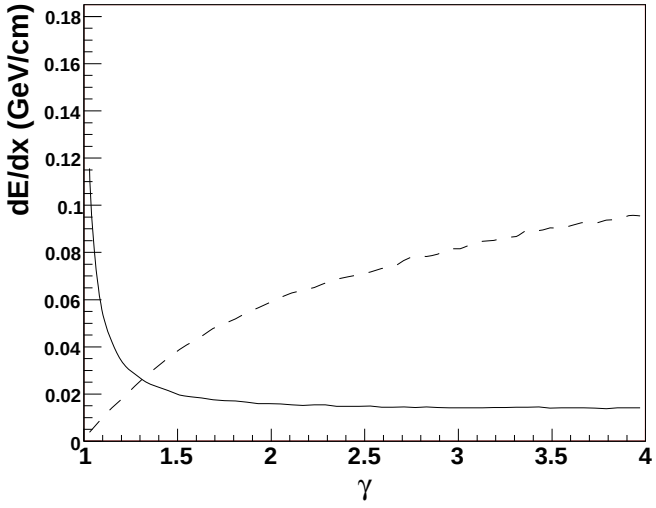

(c) Gluino baryons ($\tilde{g}qq$)

Figure 5.15: *Cross-over between EM and hadronic energy loss for stops and gluinos. Statistical errors are below one per mille. Note how the behaviour of the gluino differs from the stop cases by the onset of the hadronic contribution relative to the EM contribution.*

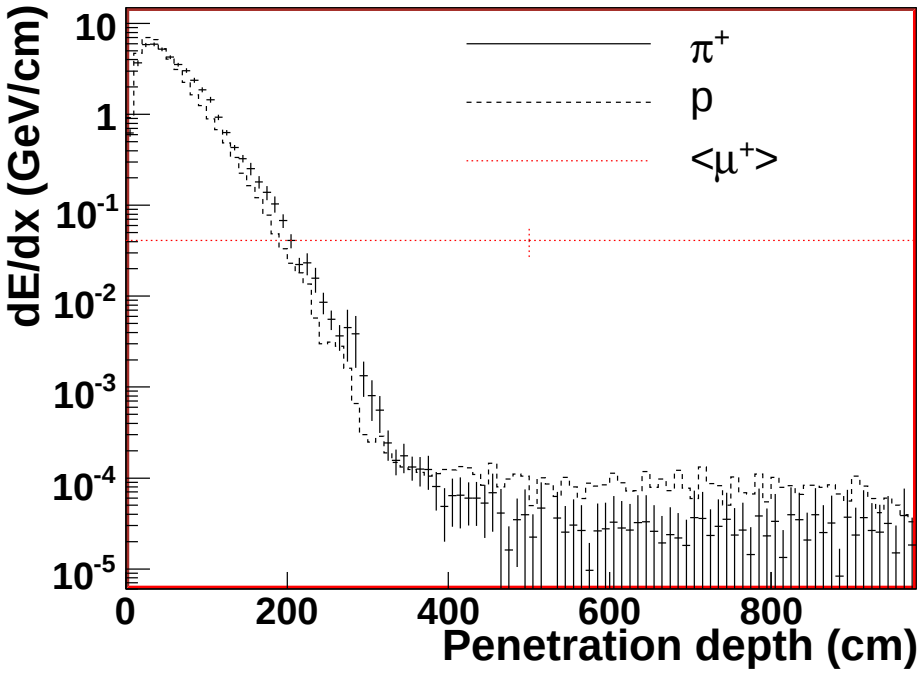

Figure 5.16: *Longitudinal shower profile of pions and protons compared to muons. Error bars have been omitted for protons in the interest of readability. Due to large fluctuations in the muon energy deposition from catastrophic energy loss, the value shown is the mean value with the error estimated by the RMS.*

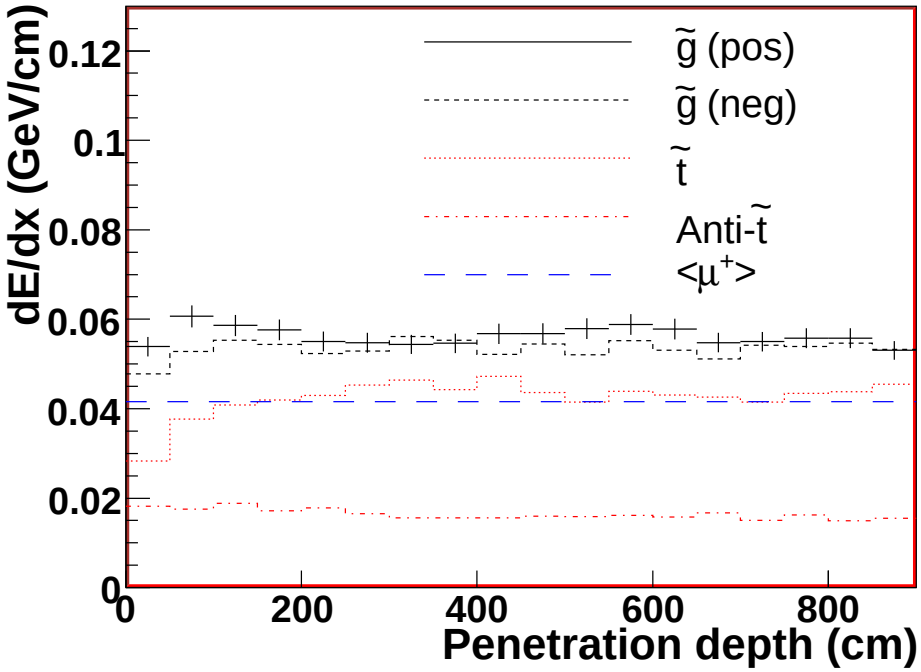

Figure 5.17: *Longitudinal shower profile of muons and 300 GeV/c^2 R-hadrons generated with the same flat kinetic energy distribution. Errors have been added to one of the histograms to illustrate the typical errors. The $\tilde{g}$(pos/neg) denotes gluino R-hadrons started with positive and negative charge respectively.*

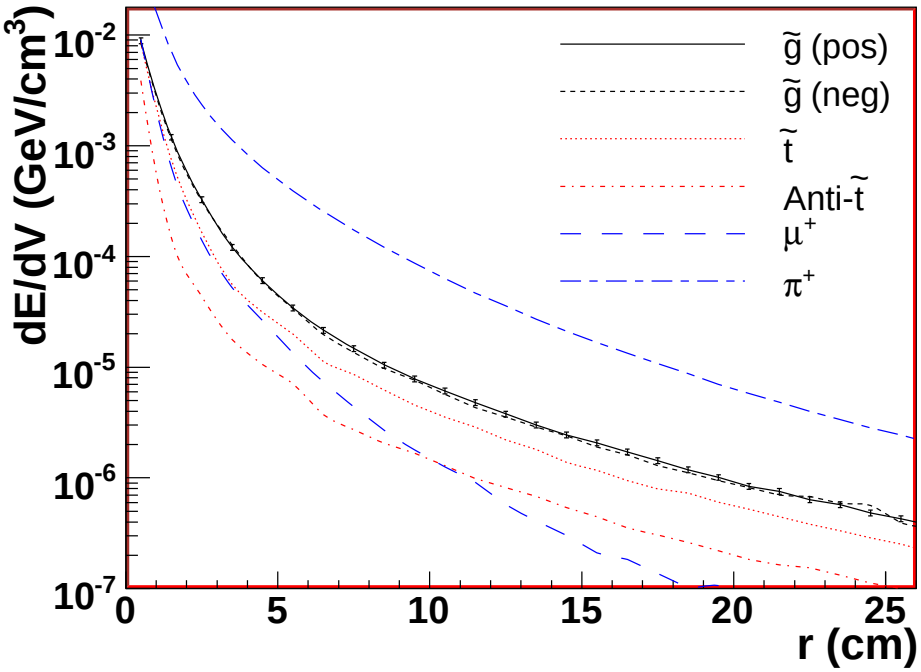

Figure 5.18: *Transverse shower profile for 300 GeV/c^2 R-hadrons compared with muons and pions. Statistical errors have been added to the $\tilde{g}(pos)$ line to illustrate the typical magnitude of the errors.*

Turning to the transverse shower profiles, figure 5.18 shows the energy deposition density at a distance r from the incident direction of the R-hadron. R-hadrons are compared to muons and pions in order to set a natural scale. From the figure one sees again the same differences between the different types of R-hadrons as was the case for the longitudinal profiles. The pions deposit substantially more energy than R-hadrons. This is due to the fact that they deposit all their energy, while the R-hadrons punch through as seen in figures 5.16 and 5.17. The muons tend to produce a narrower shower than the R-hadrons. This is consistent with the muons not having hadronic interactions. It thus appears that R-hadron showers deposit substantially less energy than ordinary hadrons and that the energy deposition is very much alike to that of muons apart from the fact that the shower is broader. We may add to this observation the fact that an R-hadron traversing a calorimeter may at times be neutral, leading to gaps in the energy deposition when looking at the longitudinal profile of the shower.

Part III
The Experimental Facility

Chapter 6

The Large Hadron Collider

The Large Hadron Collider is currently nearing completion at CERN near Geneva (Switzerland). It is a proton-proton collider being built in the LEP tunnel [LEP] and it is designed to deliver luminosities up to 10^{34} cm$^{-2}s^{-1}$ at a centre of mass energy of 14 TeV. The driving design consideration for the LHC as well as for the two general-purpose experiments installed, ATLAS and CMS, is to understand the origin of mass through electroweak symmetry breaking.

The primary references for this chapter are [B$^+$b] and [B$^+$a] to which the reader is referred for authoritative and exhaustive information.

6.1 Motivation and History

The design of the LHC is driven by the need to cover a large part of the possible parameter space for new physics. For this reason a hadron collider at a high luminosity was chosen as this gives the optimal conditions for discovery physics.

The LHC was approved by the CERN council in 1994, the year after the cancellation of the superconducting supercollider (SSC) project [SSC]. The SSC was to have been a 40 TeV pp-collider situated in Texas, USA with a circumference of 87 km. It was cancelled due to massive budget overruns. The role of the SSC and the LHC with respect to each other was that the SSC would reach high energies at low luminosity while the LHC was designed for comparatively smaller energies at much higher luminosities. Initially the LHC was envisioned to start operations in 2004 at an energy of 10 TeV with a later upgrade in 2008 to the full energy. In 1996 it was decided to push ahead for the full energy at start-up, though. The beginning of construction was delayed when in the summer of 2000 the four LEP experiments ALEPH, DELPHI, OPAL and L3 reported an excess consistent with a light Higgs boson at a mass of approximately 114 GeV/c^2[LEPH03].

6.2 Accelerator Overview

The LHC is designed as a two-ring circular collider with a circumference of 27 km. The physics aims require luminosities of up to 10^{34} cm$^{-2}s^{-1}$ to be reached excluding a $p\overline{p}$ collider with a

common ring/magnet system such as the one used at the TEVATRON collider at Fermilab [Gro]. The first three years of LHC operations will be at a luminosity of 10^{33} $\mathrm{cm}^{-2}s^{-1}$ (commonly referred to as *low luminosity*) leading to an expected amount of data of 10 fb^{-1}/year. The upgrade to 10^{34} $\mathrm{cm}^{-2}s^{-1}$ (*high luminosity*) in will result in a possible 100 fb^{-1}/year. In comparison, the numbers of the Tevatron are shown in figure 6.1. The entire integrated

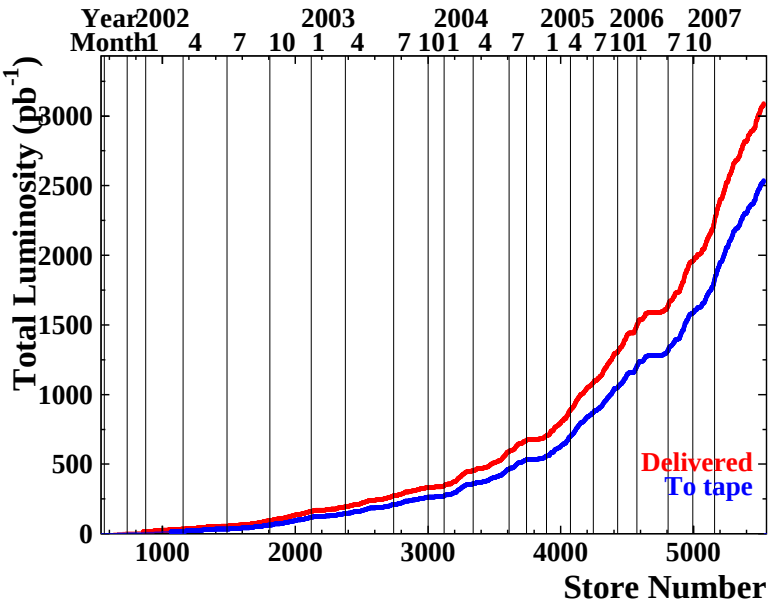

Figure 6.1: *Integrated luminosity delivered by the Tevatron accelerator as measured by the CDF experiment. Note that not all of the delivered luminosity is collected and written to tape. [CDF]*

luminosity collected by the CDF experiment [A^{+}] at the time of the writing of this thesis was only of the order of a few fb^{-1}. The key parameters of the collider at full luminosity are summarised in table 6.1. In the accelerator four experiments will be installed. These are

Ring circumference	26659 m
Proton energy	7 TeV
Particles per bunch	1.15×10^{11}
Stored energy per beam	362 MJ
Inelastic cross section	60 mb
Total cross section	100 mb
Bunch crossing rate	40 MHz
Events per bunch crossing	19.02
Number of collision points	4

Table 6.1: *A selection of parameters describing the LHC at a luminosity of* 10^{34} $cm^{-2}s^{-1}$.

ATLAS, CMS [CMS06], ALICE and LHCb. ALICE [AL] and LHCb [Lb] are special-purpose experiments targeted for ultra-relativistic heavy-ion physics and B-physics respectively. The layout of the accelerator with the four experiments is shown in figure 6.2. In the figure the locations of Geneva, Lac Leman and the French Swiss national border are also indicated.

To achieve a centre of mass energy of 14 TeV the magnets of the LHC are required to deliver

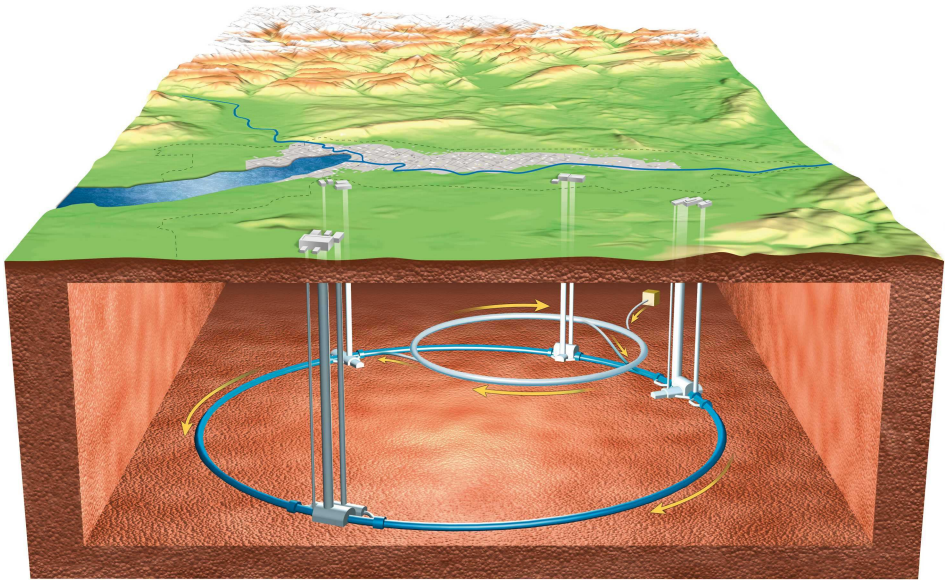

Figure 6.2: *An overview of the LHC with the four experiments shown [Off]. Geneva and Lac Leman are seen behind the accelerator and the Swiss-French border is shown as a dashed line.*

a nominal field of 8.33 T at full energy requiring the magnets to be superconducting. To ensure operation of the NbTi winded magnets they are immersed in superfluid helium at a maximum operating temperature of 1.9 K. Figure 6.3 shows a cross section of one of the LHC dipoles and cooling system with an illustration of how the magnetic field is formed around the coils.

6.3 The LHC Acceleration Chain

The high bunch crossing rates required for the LHC make demands not only on the LHC main ring but also on the entire injection chain. The accelerators feeding the LHC have thus had to be upgraded to live up the task of delivering the 2808 bunches per ring with an energy of 450 GeV per proton. A proton beam starts as a 50 MeV beam in the Linac2 accelerator. From here, it progresses into the Proton Synchrotron Booster where it is ramped up to an energy of 1.4 GeV. The Proton Synchrotron then takes over, accelerating the protons up to 25 GeV. The beam is then fed to the Super Proton Synchrotron, the SPS for acceleration up to 450 GeV. When this energy is reached the beam is moved into the LHC main ring. When all bunch slots are filled, the energy is ramped up to the full energy of 7 TeV, whereupon the accelerator is configured for collision. The LHC accelerator complex is shown in figure 6.4.

6.4 Experimental Challenges

The environment of the LHC is going to be extreme in many respects compared to the situations found at earlier collider experiments. The luminosity has been touched on briefly in section 6.2 but in addition to this number the experimental difficulties are quickly realised by considering the fact that according to table 6.1 there will be $\mathcal{O}(20)$ collisions occurring

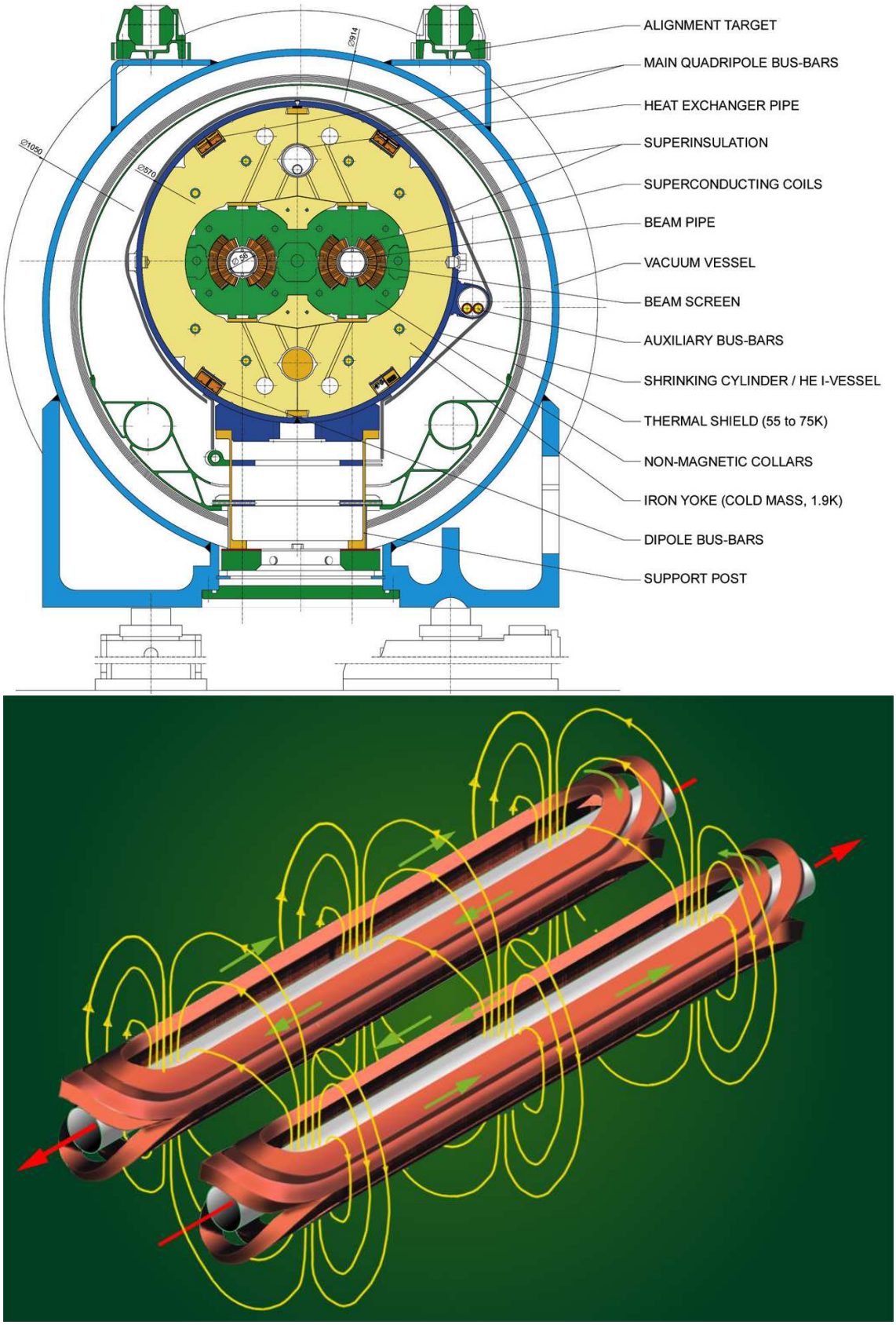

Figure 6.3: *The LHC dipole magnets and the resulting magnetic field [Off]. While the complete design of the LHC magnets is immensely complicated, these pictures do provide a conceptual overview of their function and structure.*

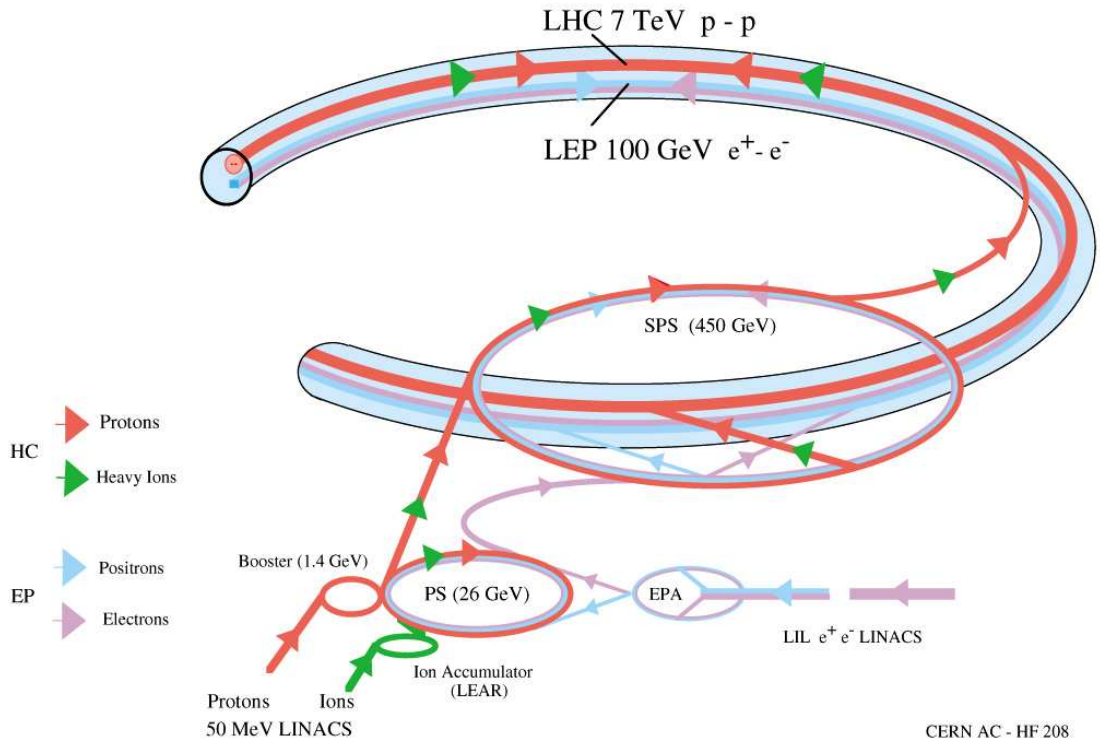

Figure 6.4: *The LHC Injection Chain [Off]. Many accelerators contribute in the creation of the two 7 TeV proton beams.*

40 million times per seconds leading to charged multiplicities of $\mathcal{O}(100)$ per bunch crossing [HLT]. Not all of these particles will of course be within the acceptance of a high energy physics detector. Figure 6.5 shows the range of cross sections that a general-purpose experiment must be able to target. The rates of different signals range for instance from the inclusive b-rate of 6 MHz to a rate of 0.001 Hz for the $H \rightarrow \gamma\gamma$ at high luminosity for a Higgs mass of 120 GeV/c^2. This is done through a comprehensive list of triggers implemented utilising a variety of different technologies.

One further central point is that even though the centre of mass energy of the two colliding protons in an event is 14 TeV the collision energy of the individual partons colliding is not. The momentum fractions carried by different types of partons are parametrised in the so-called *parton distribution functions* (PDFs). Due to the non-perturbative properties of the binding of partons in hadrons the PDFs of for instance the proton are not calculable from first principle. Instead they are found from performing fits to data. The HERA collider has played a large role in providing the data and measurements for these fits. HERA is an ep collider situated at DESY in Hamburg, Germany. The combination of the composite proton with the electron provides a clean testing ground for the structure of the proton. A current list of fits to the global body of data in the field is found at [PDF]. The CTEQ6M fit to $xf(x)$ where $f(x)$ is the probability density for a parton to be carrying the fraction x of the total proton momentum is shown in figure 6.6. A couple of features of this figure bears mentioning. First of all the distributions shown are $xf(x)$. The distribution functions themselves are consequently sharply peaked at zero. Also the PDFs are not universal at different energy scales Q. The left plot shows the PDFs at an energy scale $Q = 2$ GeV while the energy scale to the right is $Q = 100$ GeV. The non-universality of the PDFs at different energy scale expresses the so-called *scaling violation* which is due to higher order corrections made possible through the enlarged phase space at higher energies. The physical consequence for the PDFs of moving to higher energies is that the difference between the contributions from the different quark flavours go down, as $\frac{m_q}{Q}$ diminishes.

The PDFs introduce a systematic error on most measurements at the LHC due to the simple fact that the energies achievable a the LHC constitute a whole new frontier opening up the low-x regime. Extrapolations exist from the HERA energies but these have large errors due to the lack of data on the subject. In fact the PDF uncertainties are expected initially to be among the key contributing factors to the uncertainty of cross section measurements of benchmark processes [TCSG05].

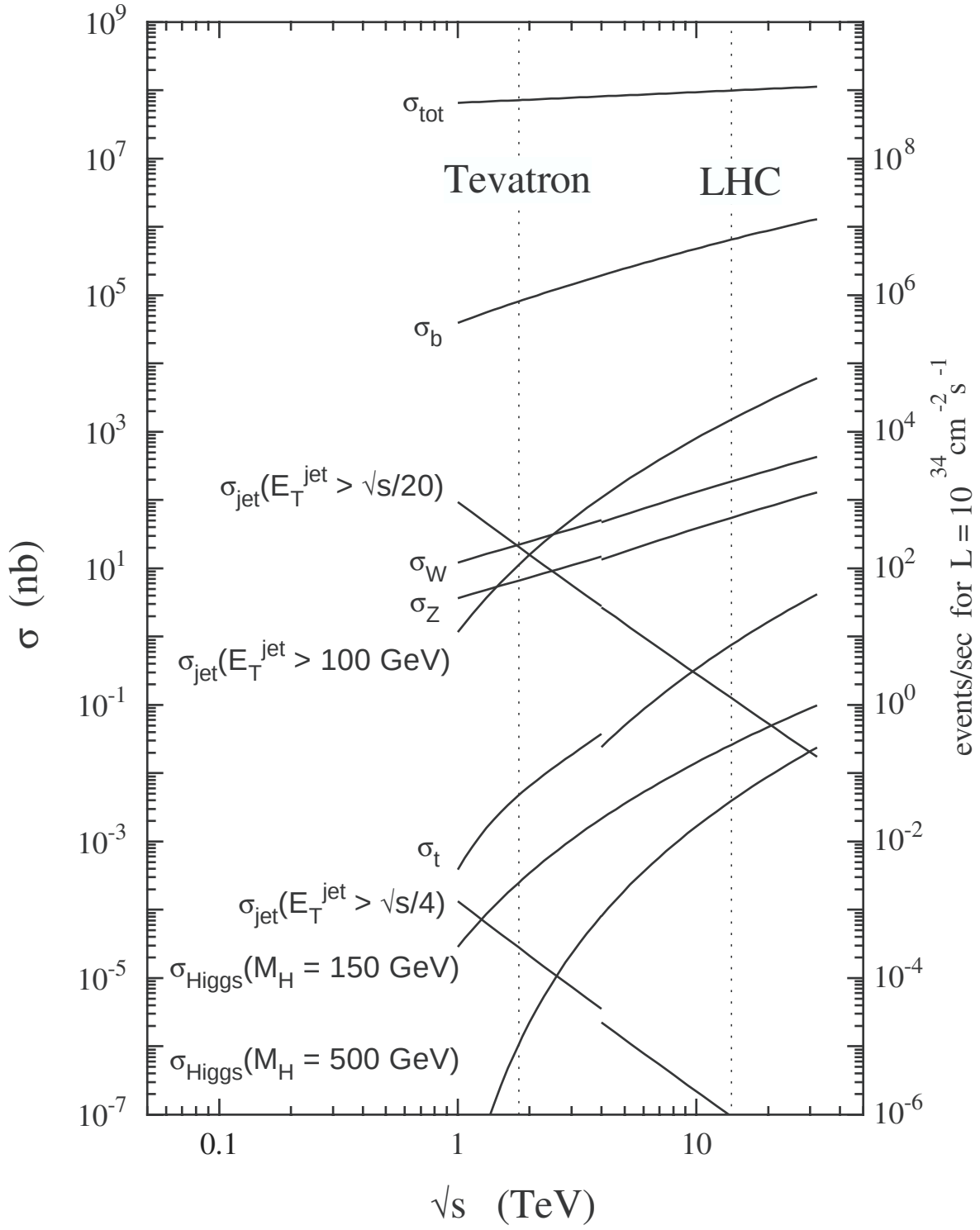

Figure 6.5: *The total cross section for a number of SM processes at the LHC [HLT]. Note that the potentially interesting cross sections shown span 15 orders of magnitude. This fact in conjunction with the high luminosities expected at the LHC creates a huge challenge in the design and implementation of trigger strategies for the LHC experiments.*

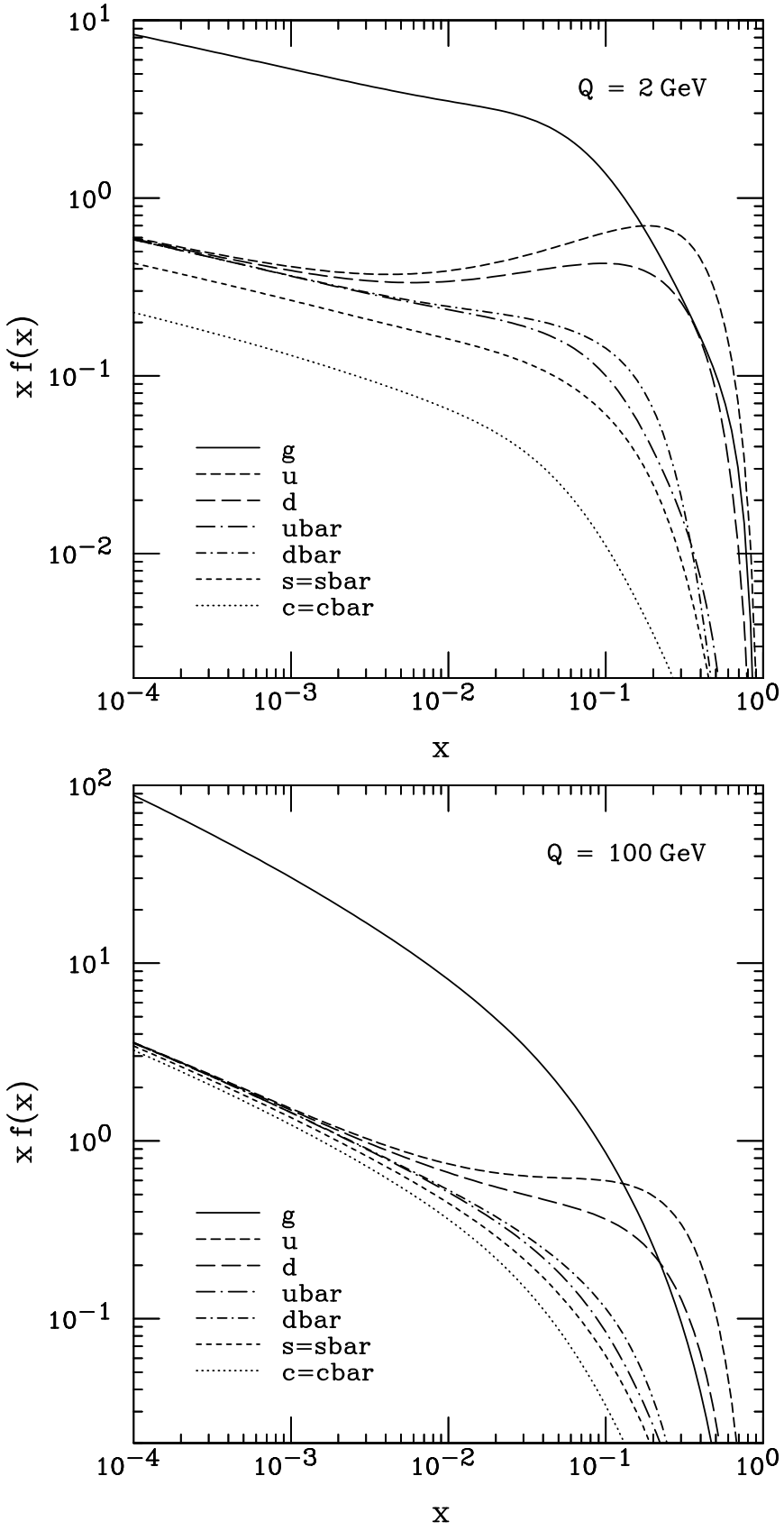

Figure 6.6: *The CTEQ6M PDFs as calculated in [P+02].*

Chapter 7

The ATLAS Experiment

The ATLAS experiment is one of the two general-purpose detectors being installed at the LHC. It is the largest particle detector ever built for a collider experiment. It is 46 m long with a height of 22 m. The design utilises a number of conceptually very different technologies to minimise the risk of the detector not working properly. The principal references for this chapter are [TDRa] and [TDRb].

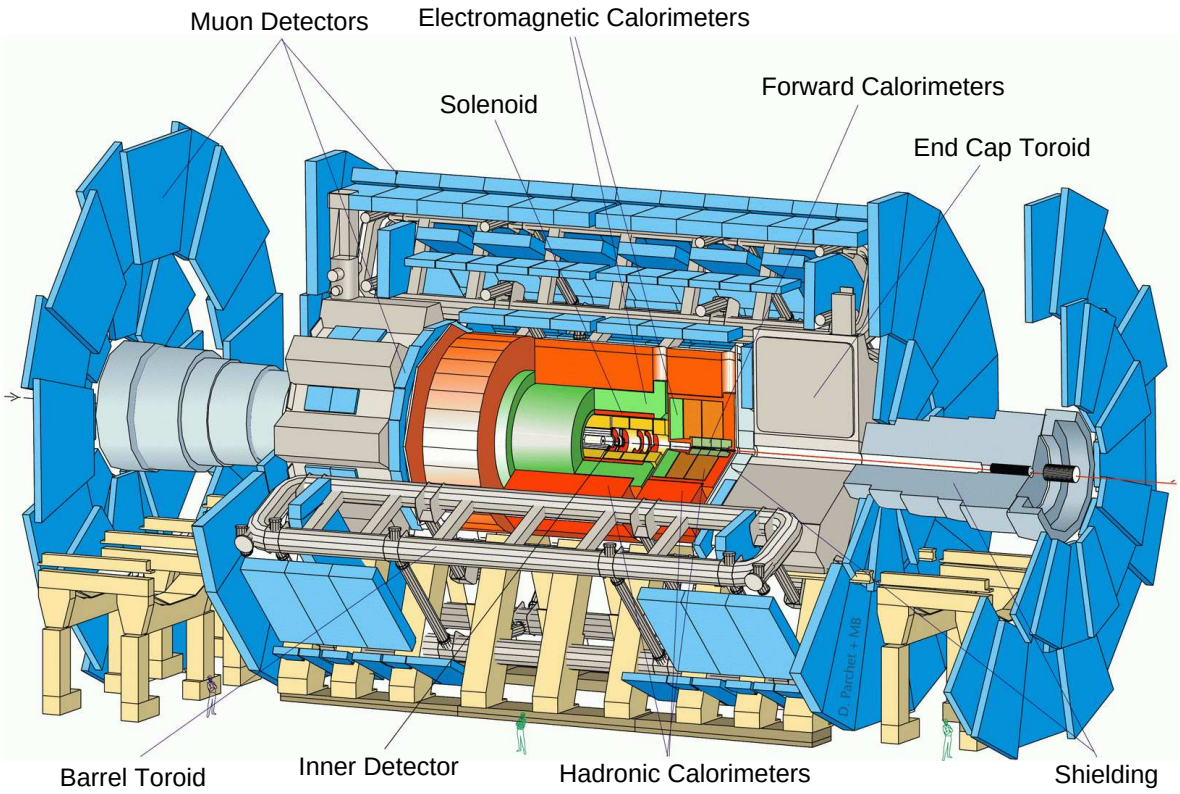

Figure 7.1: *The ATLAS detector is the Worlds largest accelerator based particle physics detector.*

7.1 Design Philosophy of the ATLAS Detector

The ATLAS experiment is shown in figure 7.1. It is designed to cover a vast aspect of physics scenarios through a multitude of different detector technologies. The Inner Detector (ID) performing tracking is enclosed in a superconducting solenoid magnet as shown on the figure. The calorimeters are placed outside the solenoid volume. This is all very commonplace in particle physics detectors. The hallmark of ATLAS is the huge air-core toroidal magnets surrounding the calorimeters in an eight-fold structure. These magnets deliver a magnetic field of up to 4.1 T with a bending power of 2-8 Tm (hence the size of the detector) allowing for ultra-precise muon reconstruction.

The main performance parameters of ATLAS are:

- The electromagnetic calorimetry should allow for efficient reconstruction and identification of electrons and photons, while the coverage and precision of the hadronic calorimeters should allow for a good resolution in missing transverse energy, E_T^{miss}.
- A high precision on the muon reconstruction should be obtainable using the muon spectrometer alone, as high-luminosity running might infer occupancy-related problems in the ID tracking.
- The full tracking chain should be precise enough to efficiently reconstruct high-p_t leptons and to assist in the b-tagging and the τ-reconstruction.
- High coverage in the η/φ plane is desirable as pp events will often be boosted leading to a need for a large acceptance in η.
- The trigger chain should be capable of handling not only objects with high values of transverse momentum. Lower energy objects should also be treated to ensure a high efficiency for all potentially interesting physics channels.

The key dimensions and over-all structure of the detector is summarised below:

Inner Detector: The ID is enclosed within a cylinder of length 7 m and radius 1.5 m. It contains two varieties om semi-conductor trackers as well a a continuous tracking detector capable of measuring transition radiation. The combined tracking has an acceptance $|\eta| < 2.5$.

Calorimeters: Electromagnetic calorimetry is supplied by a liquid Ar calorimeter (LAr) covering an η-range of $|\eta| < 3.2$ extended by the LAr forward calorimeters to $|\eta| = 4.9$ corresponding to a polar angle of 0.85 degrees. The hadronic calorimeters consist of a scintillator-tile barrel calorimeter and two so-called *extended barrel* cylinders. The calorimeters are contained within a cylinder of radius 4.25 m and length 13.30 m.

Muon Spectrometer: The muon spectrometer consists of the barrel toroids with a length of 25 m. The outer barrel chambers extend to a radius of 11 m from the beam-line, and the outermost muon end-caps are situated 23 m from the interaction point.

7.2 Subdetectors

After the brief overview of the ATLAS detector given in the previous section a more detailed description of the individual detector components will be given here.

7.2.1 The Inner Detector

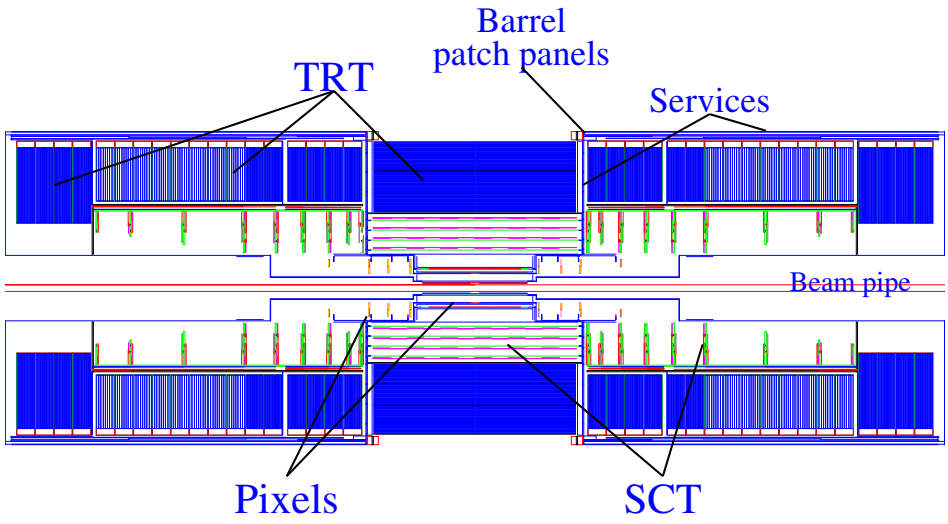

Figure 7.2: *A cut-through view of the Inner Detector of the ATLAS experiment. The three subdetectors of the ID are shown together, illustrating how they will complement each other. [TDRa]*

The ID shown in figure 7.2 is comprised of the tracking detectors as shown in the figure. These are two silicon-based tracking detectors, namely the Pixel and Semi Conductor Trackers which are surrounded in turn by the Transition Radiation Tracker, a straw detector providing continuous tracking and particle identification. The ID is placed inside the superconducting solenoid delivering a magnetic field of 2 T. Typical tracks cross three pixel layers and eight SCT layers. When $\mathcal{O}(36)$ points from the TRT are added, there is basis for robust reconstruction with accurate spatial and momentum resolution. Table 7.1 gives a recap of the

Subdetector:	Position:	Area (m^2)	Resolution: (μm)	Channels:	η coverage:
Pixels	1 removable barrel layer (B-layer)	0.2	$R\varphi = 12$, $z = 66$	1.6×10^7	± 2.5
	2 barrel layers	1.4	$R\varphi = 12$, $z = 66$	8.1×10^7	± 1.7
	2×5 end-cap disks	0.7	$R\varphi = 12$, $R = 77$	4.3×10^7	1.7 -2.5
SCT	4 barrel layers	34.4	$R\varphi = 16$, $z = 580$	3.2×10^6	± 1.4
	2×9 end-cap wheels	26.7	$R\varphi = 16$, $R = 580$	3.0×10^6	1.4 -2.5
TRT	Axial barrel straws		170 (per straw)	1×10^5	± 0.7
	Radial end-cap straws		170 (per straw)	3.2×10^5	0.7-2.5

Table 7.1: *Design parameters for the Inner Detector.*

design parameters for the tracking detectors as they are given in [TDRa]. The performance part of these numbers are to a some degree obsolete but they have been used extensively as benchmarks.

The Pixel Detector

The Pixel detector is the innermost part of the ATLAS tracking system. It is designed to provide high-precision measurements of 3D space points in the high-luminosity environment of ATLAS at pseudorapidities of up to $\eta = 2.5$. The goals of the detector is to have a precision that provides low occupancy even in events with very high multiplicity and to do so using technology that will withstand the radiation damage induced by a collision rate of 40 MHz 14 TeV pp collisions. The Pixel design was first used in a collider experiment in DELPHI at LEP [B$^+$97], but the technology has been developed extensively since then.

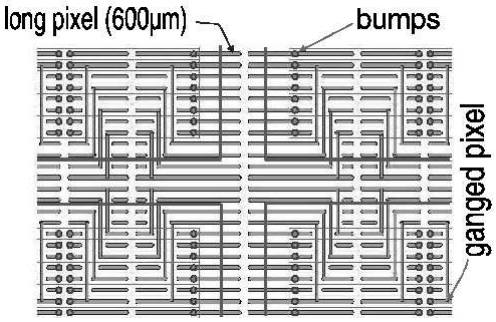

Figure 7.3: *The layout of a silicon Pixel sensor.*

The basic design of a Pixel sensor is shown in figure 7.3. The pixel size of the detector is 50 μm$\times$ 400 μm.allowing for a spatial resolution of 10 μm in the $R\varphi$-plane [Px07]. The detector is comprised of three cylindrical barrel layers located at r = 5.1 cm, 8.9 cm and 12.1 cm respectively while each end-cap is instrumented with three disks (as opposed to the original plan of five) positioned in the region of $|z|$ = 50-60 cm. The total area of the Pixel detector is approximately 1.7 m^2 and it supplies approximately 80×10^6 channels for read-out. The final design of the Pixel detector can be seen in figure 7.4.

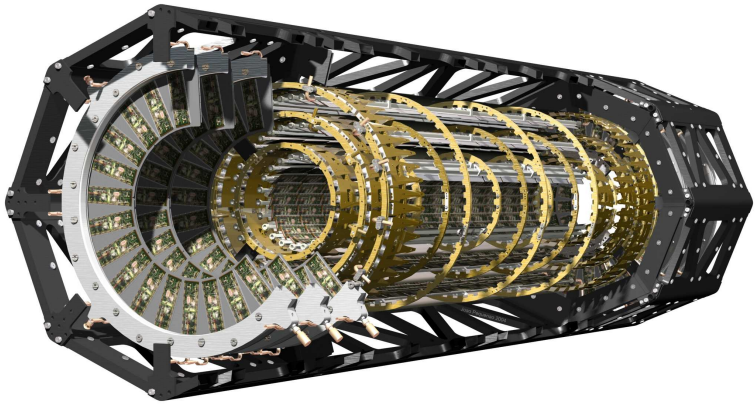

Figure 7.4: *A 3D cut-out view of the Pixel detector and its support structure [Off].*

The Semi Conductor Tracker (SCT)

The next layer in the Inner Detector is the SCT. This subdetector is a silicon strip detector. The barrel part of the detector consists of four layers of silicon strip modules placed around the beamline at radii 30.0, 37.3, 44.7 and 52.0 cm. Each module is 6.36 cm × 6.40 cm and they accommodate each 768 read-out strips with a pitch of 80 μm. Two such modules are

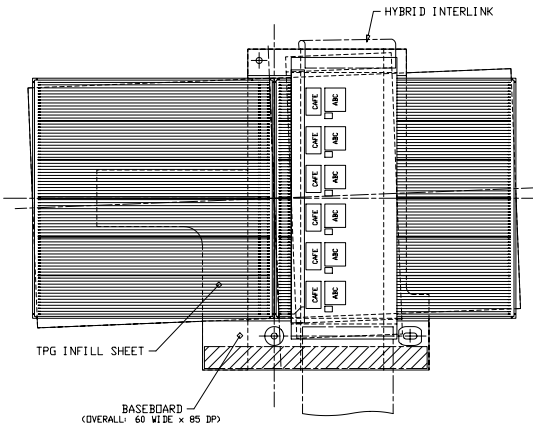

Figure 7.5: *Two SCT modules joined with an illustration of the stereo angle principle. The two modules are aligned at an angle of 40 mrad with respect to each other. Correlations between the hit strips in the two modules can be used to measure the z coordinate.*

seen joined in figure 7.5. As is hinted on the figure the layers are arranged with a stereo angle of ±20 mrad allowing for a measurement of z as well as $R\varphi$. Consequently a particle leaving the interaction point will cross 4×2 strip layers in the barrel SCT. The end-cap part of the detector rely on nine wheels of radially aligned strips extending out to $z = 2.8$ m. The space-point resolutions of the SCT are $\sigma(R\varphi) = 16\mu$m and $\sigma(z) = \sigma(R) = 580\mu$m. The SCT

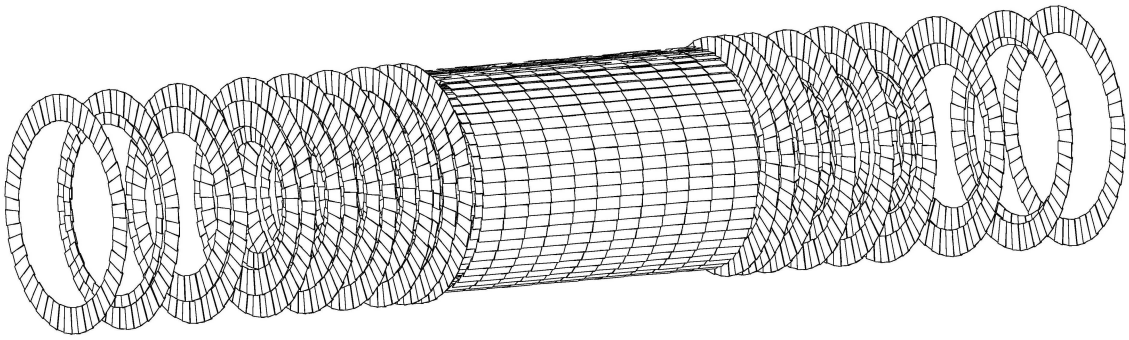

Figure 7.6: *A view of the SCT structure.*

comprises all-in-all 61 m^2 of detector material with 6.2×10^6 read-out channels.

The Transition Radiation Tracker (TRT)

The Transition Radiation Tracker is in its design a continuous tracking detector consisting of gas-filled drift tubes ("straws") with a diameter of 4 mm. In addition to being a tracking detector it also provides a method for particle identification (PID) through measuring the occurrence of transition radiation in the detector.

The straws of the TRT are made from kapton with a protective mylar film yielding a wall thickness of 72 μm. The inner surface of the straw is conducting. Inside the straw a gold-plated tungsten wire is strung. The wire then serves as the anode for the straw as a Xenon-CO_2-filled drift chamber as illustrated in figure 7.7. The drift time t is measured and converted into

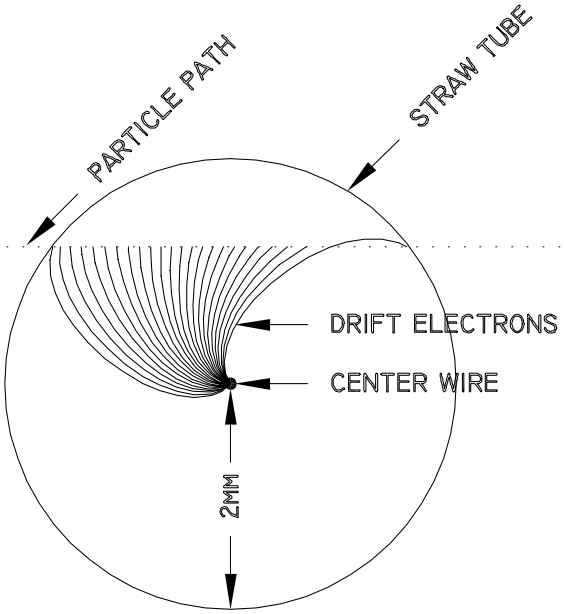

Figure 7.7: *Ionisation deposited by a traversing particle is collected on the wire of a drift tube. The drift path is seen to bend in the ambient magnetic field.*

a drift distance R using an R-t relation such as the one illustrated in figure 7.8. This has in test-beams and simulations been shown to be possible with a resolution of 130 - 140 μm [Kit07] as opposed to the 170 μm that was the original design goal as outlined in table 7.1.

The TRT derives its name from the fact that the drift tubes of the detector are immersed in a material with rapidly changing refractive index. This enhances the probability of transition radiation to occur for highly relativistic charged particles traversing the material. The intensity of the emitted radiation for a particle crossing one boundary between domains of different refractive index is proportional to the boost, γ of the particle. The configuration of the ATLAS TRT results in particles with γ-factors of about 10^3 radiating X-ray photons with an energy of $\mathcal{O}(5\text{ keV})$ collinearly with the particle line of flight [AYM75, Ege]. The Xenon-CO_2 gas in the drift tubes is aimed at absorbing these photons leading to enhanced energy deposition in the individual straw traversed by the particle. The read-out of the TRT handles this by applying two thresholds to the collected ionisation. The low-threshold (LT) time is used for drift distance reconstruction as previously described while the high-threshold (HT) which is higher by a factor of ~ 20 can be used for PID. The potential for PID using HT

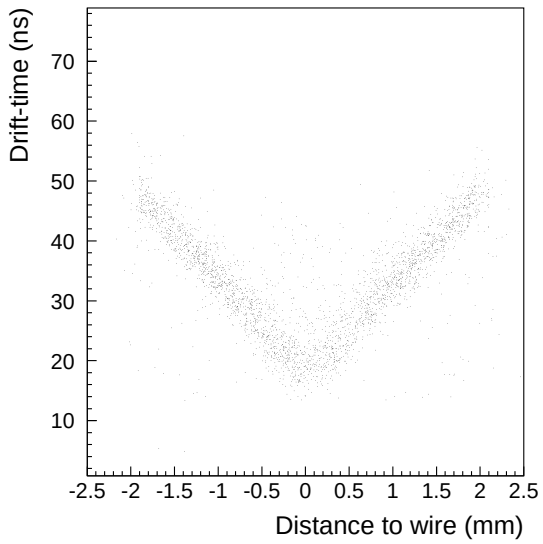

Figure 7.8: *An example of a TRT R-t relation [ID]. The two sides of the "V"-plot show the relation between the track/wire distance and the measured drift time. The latency of the straw is referred to as t_0. It is visible as the minimum measured drift time corresponding to low radii.*

information is illustrated in figure 7.9. The figure shows a measurement carried out during

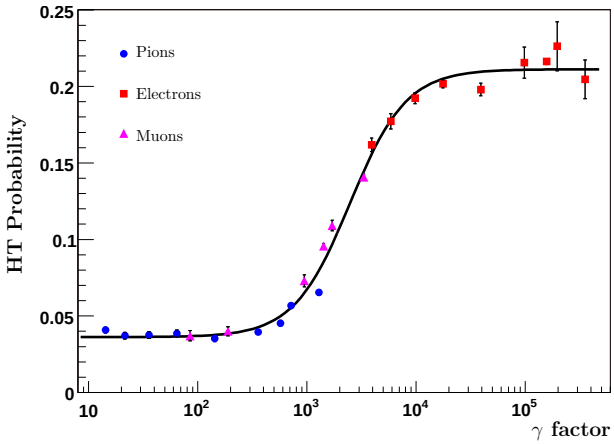

Figure 7.9: *Probability for getting a HT hit in a straw as a function of the γ-factor [MP06]. Notice how different beams have been used to cover a range of fiver orders of magnitude in γ.*

the 2004 combined test-beam of ATLAS where a full slice of detector elements were tested in combination. As the setup of the test-beam was such that the identity and energy of the incident particles were known this probability could be measured.

The basic lay-out of the TRT is two-fold. One part is a barrel detector consisting of axially aligned straws. The straws are organised in 96 modules in three layers as illustrated in figure 7.10(a)-7.10(b). The radiator material in the barrel TRT consists of a fiber material which is worked into mats with a thickness of 3 mm and then cut to fit the modules and accommodate the straws. Each module contains $\mathcal{O}(500)$ of such mats. The barrel radiator material is shown in figure 7.10(c) - 7.10(d). The physical dimensions of the barrel TRT is a cylindrical shell with an length of 150 cm, an inner radius of 56 cm and an outer radius of 107 cm. It contains

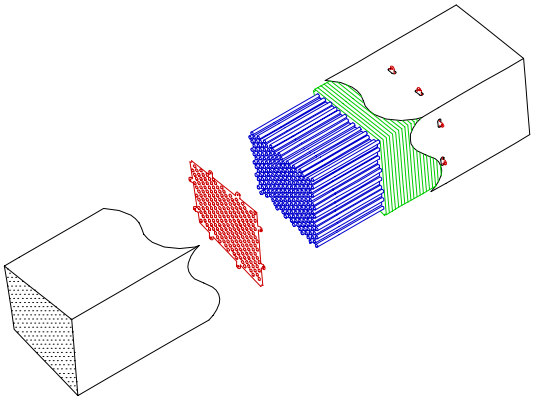

(a) An exploded view of a TRT barrel module.

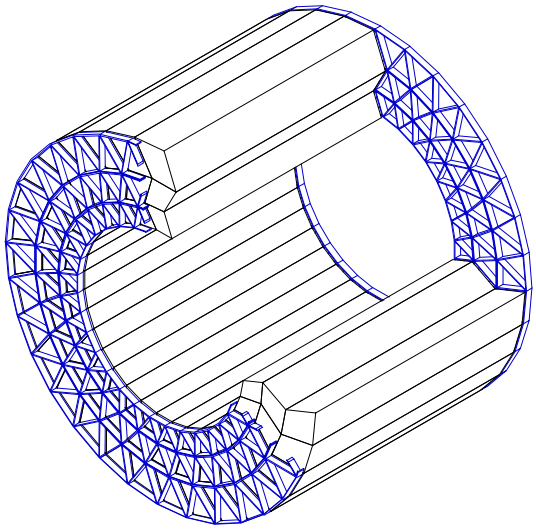

(b) The TRT barrel put together

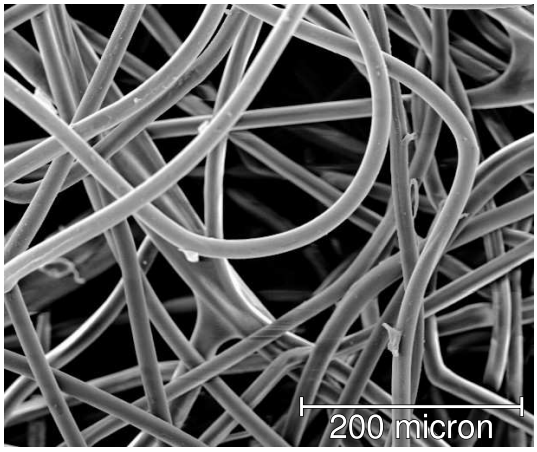

(c) A microscopy of the barrel radiator material

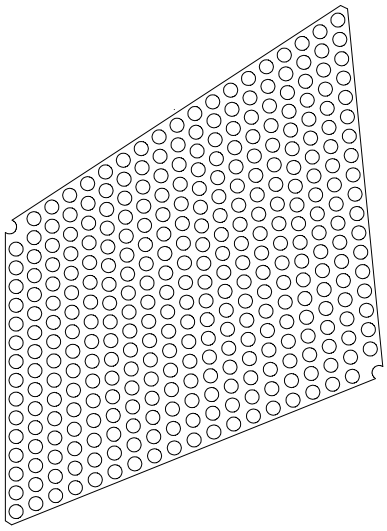

(d) A fibrous mat of radiator material for the barrel TRT

Figure 7.10: *The structure of the TRT barrel.[ID]*

52544 straws. Each straw is divided by a glass pearl at $z = 0$ providing for two read-out channels per straw.

The TRT end-cap is build up of wheels of radially oriented straws organised in layers interspersed with 16 layers of polypropylene with a thickness of 15 μmspaced by 200 μm. Each end-cap consists of 18 wheels totalling 122880 straws. Of the 18 wheels the outer four are at this time staged with no guarantee of being built. The remaining 14 wheels covers a radius of 64 to 103 cm and extend out to the $z = 2.8$ m.

7.2.2 Calorimetry in ATLAS

While the tracking system of a particle physics detector is perfectly adequate in measuring in great detail the properties of the charged particles traversing the detector after a collision it wins by being supplemented by electromagnetic calorimetry for electron tagging and it is naturally unable to handle neutral particles such as photons or neutral hadrons. The latter need heavy hadronic calorimeters to encapsulate the large showers arising from an incident high-energy hadron.

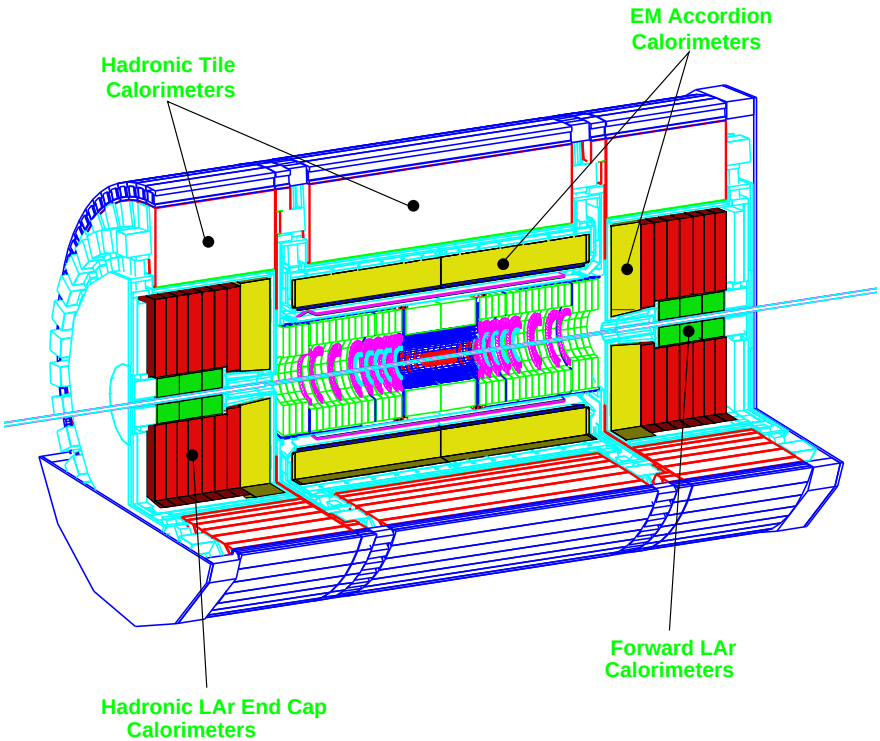

Figure 7.11: *An overview of the calorimeters of ATLAS [TDRa].*

The calorimeters of ATLAS are outlined in figure 7.11. The EM liquid argon calorimeter is seen closest to the interaction point where rates and densities are high such that energy resolution and segmentation are extremely important. Further out an iron/scintillator calorimeter is used which has a somewhat coarser segmentation.

The Liquid Argon Calorimeter

Electromagnetic calorimetry in ATLAS in handled with a liquid argon calorimeter (LAr). The basic idea of a LAr calorimeter is alternating shower material such as lead or iron with liquid argon in a strong electric field. The individual cells of the calorimeter now essentially works as drift chambers where ionisation in the argon is picked up on the electrodes generating the electric field. This technology is extremely radiation hard as the liquid argon can be flushed out and changed more or less continuously if need be.

Several calorimeters in ATLAS use the LAr technology. The structure in the ATLAS incarnation consists of iron plates sandwiched in a so-called *accordion structure* structure with the LAr electrodes as shown in figure 7.12. The barrel EM calorimeter covers a pseudorapidity

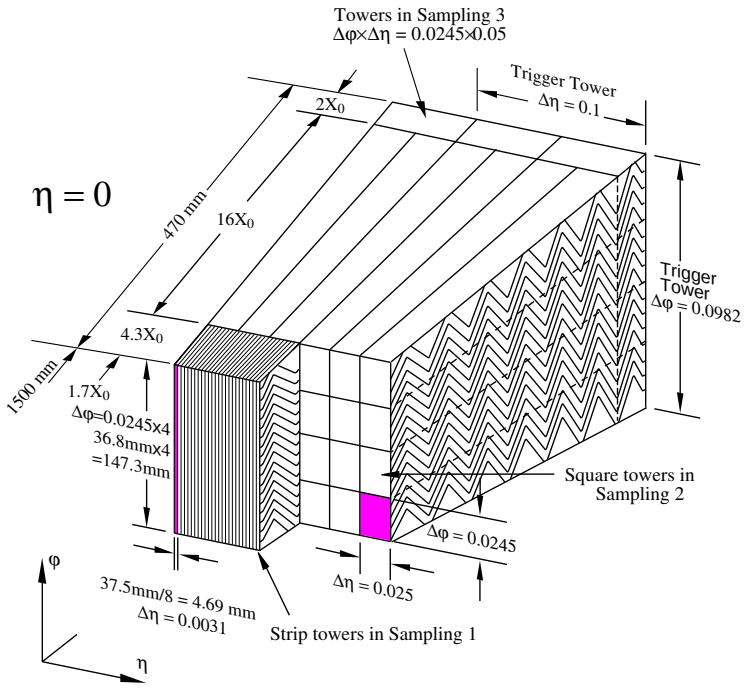

Figure 7.12: *The accordion structure of the ATLAS LAr calorimeter ensures a good azimuthal coverage of the calorimeter. [LAr]*

range of $|\eta| < 1.475$ and consists of two half-barrels with a gap in between of ~ 6 mm at $z = 0$. The virtue of the accordion shape in this context is apparent in the fact that each half-barrel is continuous in φ even though it is segmented in cells keeping the dead areas to an absolute minimum. Each half-barrel contains 1024 converter plates folded in the shown accordion geometry and stacked in φ. Between these absorber plates are the electrodes and read-out boards collecting the ionisation of the shower products. Four plates form one read-out cell as shown while the calorimeter is divided into three samplings. The geometry of the

end-cap EM calorimeters is slightly more complicated. Each end-cap calorimeter is divided into two wheels. The outer wheel covers an η-range of $1.375 < \eta < 2.5$ while the inner wheel covers the range of $2.5 < \eta < 3.2$. The forward detectors installed closest to the beampipe extend the coverage of the calorimeter down to $\eta = 4.9$ which corresponds to a polar angle of 0.85 degrees. The geometry of the forward detectors differ somewhat from the rest, though. They consist of a metal matrix made of copper or tungsten depending on the position. The matrix is then filled with axially aligned channels in each of this a metal rod is placed. The metal rod is kept isolated from the matrix by a quartz wire, and the space is filled up with liquid argon. This dense structure with its ultra-thin drift gaps of 250 μm ensure operation of the detector even in an environment of extreme rates and densities such as the forward region. The structure of the forward calorimeters is depicted in figure 7.13.

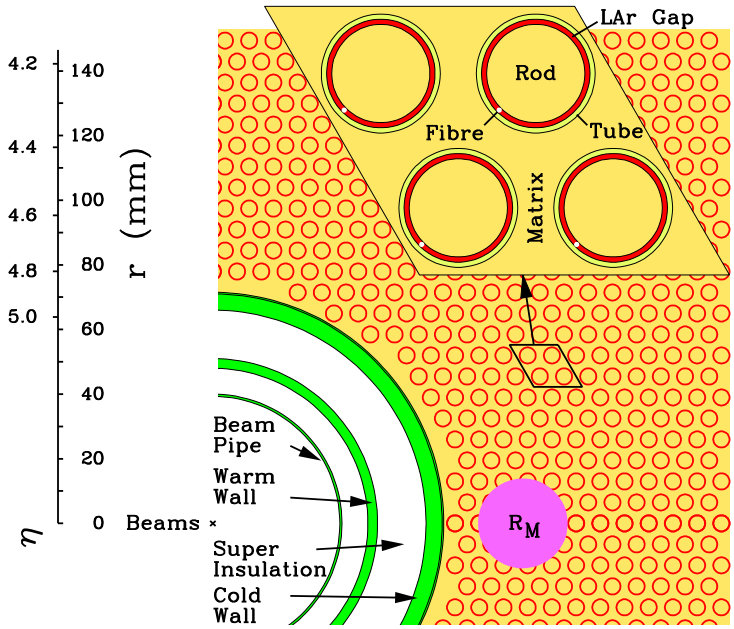

Figure 7.13: *Metal matrix with rods in the forward detector. This is a structure designed for the extremely high rates expected close to the beam pipe.*

The physical dimensions of the barrel EM calorimeter are such that the thickness of the calorimeter in the barrel is at least 24 radiation lengths (X_0) in the barrel and 26 X_0 in the end-cap. While the geometry of the calorimeter varies a little in the different parts of the detector due to the geometric properties of the accordion shape, the fundamental principle of a calorimeter segmented in the three samplings remains as illustrated in figure 7.12.

To correct for energy lost in material in front of the calorimeter the presence of a presampler is required. The presampler in the barrel and end-cap is designed as a thin (5-10 mm) layer of liquid argon with electrodes positioned perpendicular to the beam axis for the barrel and parallel to the beam axis for the end-cap.

The energy resolution of the calorimeter is estimated by the results obtained in test-beam for a part of the barrel calorimeter: [AEBC06].

$$\frac{\sigma(E)}{E} = \frac{10.1\%}{\sqrt{E}} \oplus 0.17\%, \tag{7.1}$$

where E is assumed measured in GeV. The first term is the sampling uncertainty while the second term is an estimation of imperfections and miscalibrations of the detector. Both errors are statistical and may be added in quadrature. The uncertainty furthermore has a systematic contribution of up to 0.1%.

The Tile Calorimeter

The Tile Calorimeter of ATLAS is the outermost part of the calorimeter. It encloses and supports the weight of the ID and the LAr calorimeter. The calorimeter is a sampling structure consisting of iron absorbers and scintillating tiles. The detector has an inner radius of 2280 mm and an outer radius 4230 mm. It is divided into a barrel region of length 5640 mm covering $|\eta| < 1$ and two *extended barrels* each with a length of 2910 mm providing coverage in the region $0.8 < |\eta| < 1.7$. Each of these cylinder is comprised of 64 independent parts stacked in the azimuthal direction.

The tiles are placed in planes perpendicular to the beam axis in a structure that is periodic in z. Each scintillating tile is 3 mm in thickness and the total amount of iron absorber per period is 14 mm. Radially, the cylinders are segmented into three layers with thicknesses of approximately 1.4, 3.9 and 1.8 interaction lengths at $\eta = 0$. The $\Delta\eta \times \Delta\phi$ segmentation is 0.1×0.1 in the two first layers and 0.2×0.1 in the last layer called the *tail catcher* layer. The combined hadronic energy resolution of ATLAS is expected to meet the design goal of having jet resolutions of: [ATLa]

$$\begin{aligned} \frac{\Delta E}{E} &= \frac{50\%}{\sqrt{E}} \oplus 3\% \qquad (\text{for} |\eta| < 3) \\ \frac{\Delta E_t}{E_t} &= \frac{100\%}{\sqrt{E}} \oplus 10\% \qquad (\text{for} 3 < |\eta| < 4.9). \end{aligned} \tag{7.2}$$

Material Distribution in ATLAS

The objective of the calorimeters is to measure the energy deposited by electromagnetic showers. To do this a certain thickness is required to ensure that hadronic showers are properly contained and that punch-through to the muon chambers is reduced. The total thickness of the calorimeters range between 10 and 21 interaction lengths with 11 interaction lengths at $\eta = 0$ as shown in figure 7.14. One interaction length equates approximately 17 cm in iron (high energy limit, [PDG06]). Any particle reaching the muon system has thus traversed the equivalent of 1.7 - 3.5 m of iron.

To see what this means we consider the nuclear interaction length for an R-hadron in iron. This is [BV]

$$\lambda_{Fe} = \frac{A_{Fe}}{\sigma_{Fe} N_A \rho_{Fe}}, \tag{7.3}$$

where N_A is Avogadro's number, ρ_{Fe} is the density of iron and A_{Fe} is the atomic weight in $g/mole$. Using the flat cross section defined in section 5.1 to calculate σ_{Fe} the nuclear interaction length becomes (considering only u and d quarks)

$$\lambda_{Fe} = \frac{47 \text{ cm}}{n_q}, \tag{7.4}$$

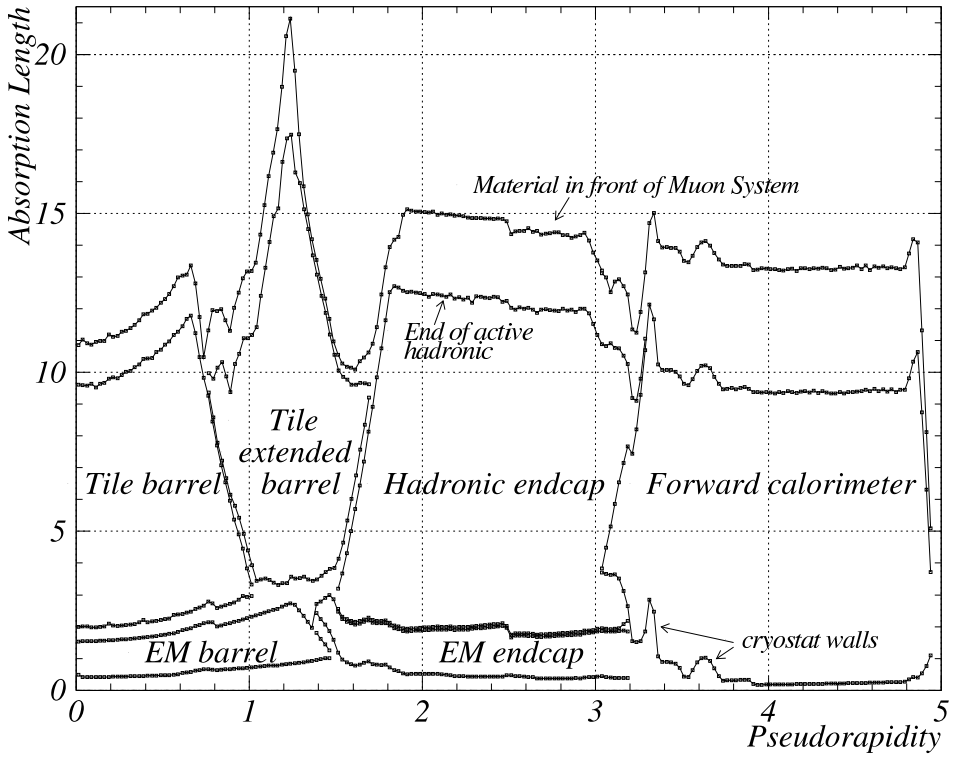

Figure 7.14: *The material distribution in ATLAS as a function of pseudorapidity [ATLa].*

where n_q is the number of light quarks in the R-hadron. This means that for instance a gluino R-baryon will undergo typically 10-20 nuclear interactions before reaching the muon system in ATLAS. Correspondingly a stop sbaryon will on average interact hadronically 7-15 times before exiting the calorimeters.

7.2.3 The Muon Spectrometer

The muon system of ATLAS is the single part of the detector that defines the outer geometry and sheer size of the detector. The governing principle of the design is to deflect muons in the $R-z$ plane using the large air-core toroidal magnets that are seen in figure 7.1. The magnets deliver a field integral of $\int \vec{B} \cdot d\vec{\ell} = 2-6$ Tm for the barrel toroids and 4-8 Tm for the end-cap toroids. Two views of the muon spectrometer are shown in figure 7.15. The bending direction outside the solenoid is in the $R-z$ plane of figure 7.15(b).

Several technologies are utilised in the combined spectrometer. These are the *Monitored Drift Tubes* (MDTs), the *Thin Gap Chambers* (TGCs), the *Resistive Plate Chambers* (RPCs) and the *Cathode Strip Chambers* (CSCs). The different types of detectors are placed in layers (*stations*) such that particles originating at the nominal interaction point will encounter three stations while traversing the detector.

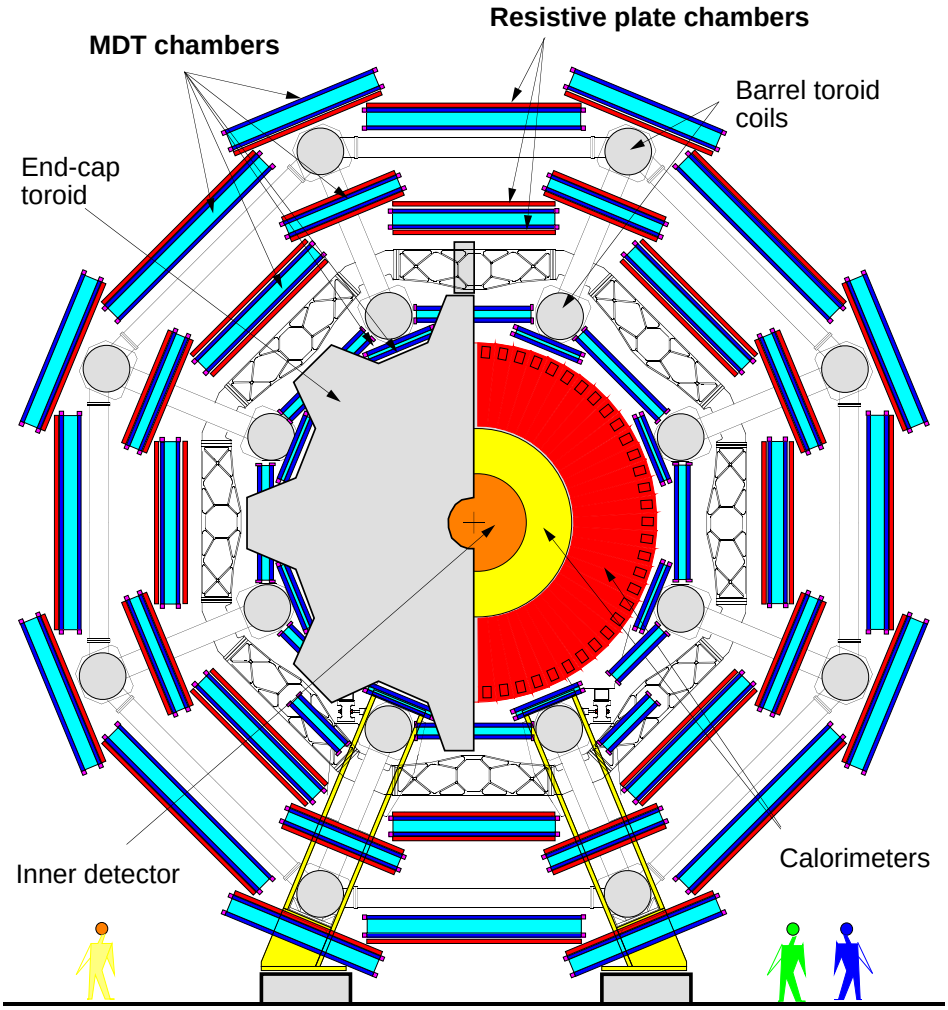

(a) End view

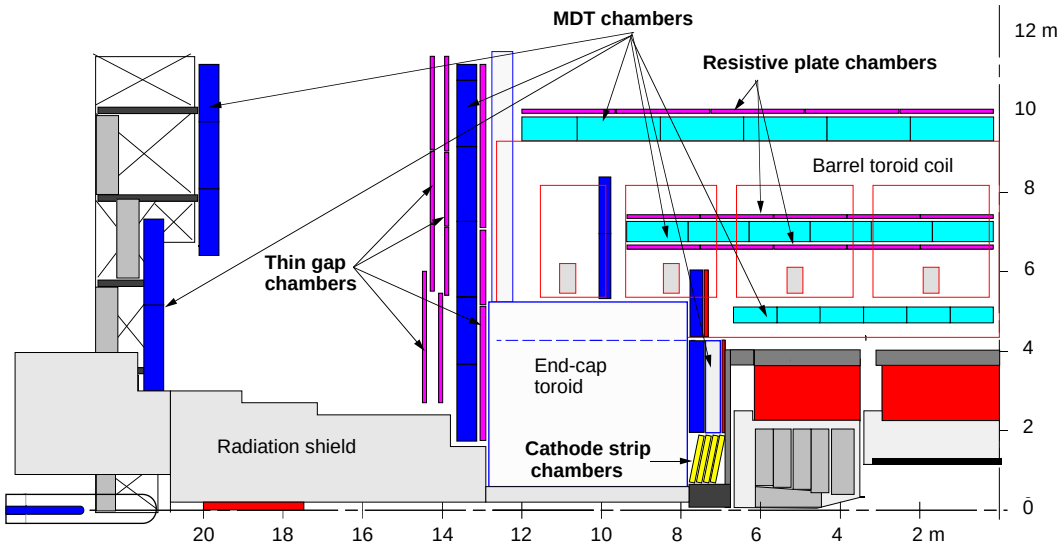

(b) Side view

Figure 7.15: *Two projections of the ATLAS muon system [mTD]. As can be readily seen the Muon Spectrometer defines the outer geometry of ATLAS.*

Monitored Drift Tubes

The MDT chambers are straw detectors much in analogy with the TRT. The individual drift tube is 30 mm in diameter with a length between 70 cm and 630 cm. It has a 50 μm W-Re wire strung along its axis. The gas is an Ar-CH_4-N_2 mixture and the drift tubes are operated at a pressure of 3 bar giving a maximum drift time for the deposited ionisation of 500 ns and an expected spatial resolution of 80 μm. Figure 7.16 shows a view of a barrel MDT chamber.

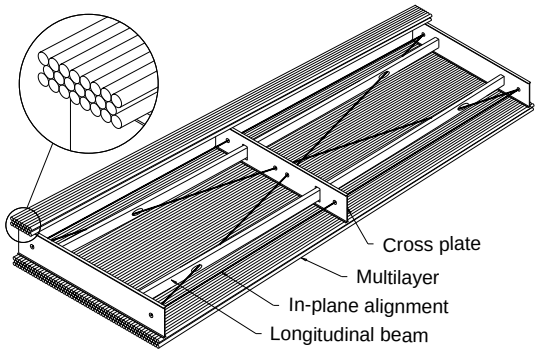

Figure 7.16: *A rectangular barrel MDT chamber. The two multilayers provide detailed input to the reconstruction by combining the measurements of individual tubes to form "super points" for the reconstruction.*

As can be seen the drift tubes are arranged in 2×3 layers for redundancy. The inner stations in contrast are equipped with 2×4 layers. The end-cap chambers are trapezoidal in shape but are otherwise similarly designed.

Cathode Strip Chambers

The CSCs are constructed as multi-wire proportional chambers [Leo93] with a distance between the cathode and the anode equal to the anode wire pitch. The cathode is segmented into strips that read out the charge induced through the formation of avalanches on the anode wires. The spatial resolution is optimised by using charge interpolation between neighbouring strips and by having the strips aligned orthogonally as well as parallel with the wires.

Figure 7.17 shows the design of the CSC. Figure 7.17(a) shows the conceptual design of the chamber while 7.17(b) shows how the modules are built. The CSCs are arranged in 2×4 layers where each layer is made out of the nomex honeycomb structure shown in figure 7.17(b). The performance of the CSCs is inherently dependent on crossing angle of the incident particle but resolutions better than 60 μm have been measured in test-beams.

Resistive Plate Chambers

The RPCs are thin gaseous detectors consisting of two resistive bakelite plates with a gap of 2 mm in between. The gap is filled with a $C_2H_2F_4$ mixture, and a 4.5 kV/mm electric field is applied across the gap. Ionisation avalanches are detected by a capacitive coupling to electrodes on both sides of the detector. The RPCs provide a space-time resolution of 1 cm $\times$ 1 ns and they are therefore prime candidates to be used for triggering purposes, as they can give a rough estimate of a track position very quickly. Figure 7.18 shows a cross section of an RPC chamber. Note, how two chambers overlap to eliminate dead areas.

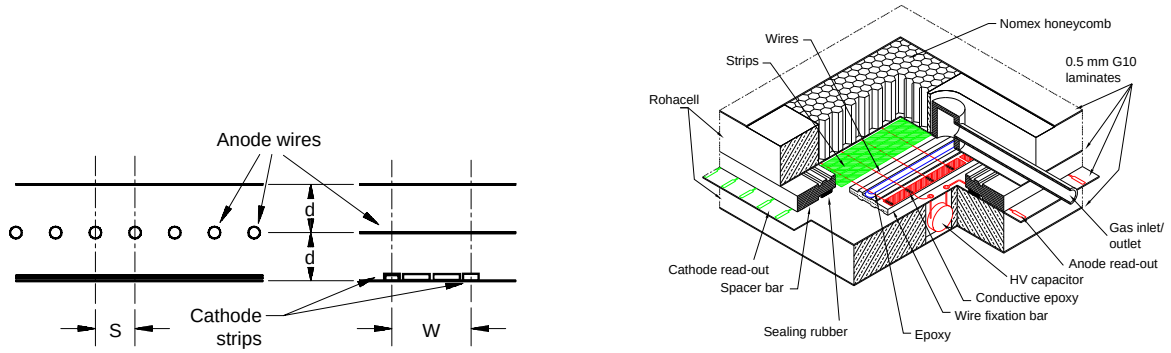

(a) An illustration of the CSC as a MWPC

(b) A view of CSC module

Figure 7.17: *The design and concept of the CSCs.*

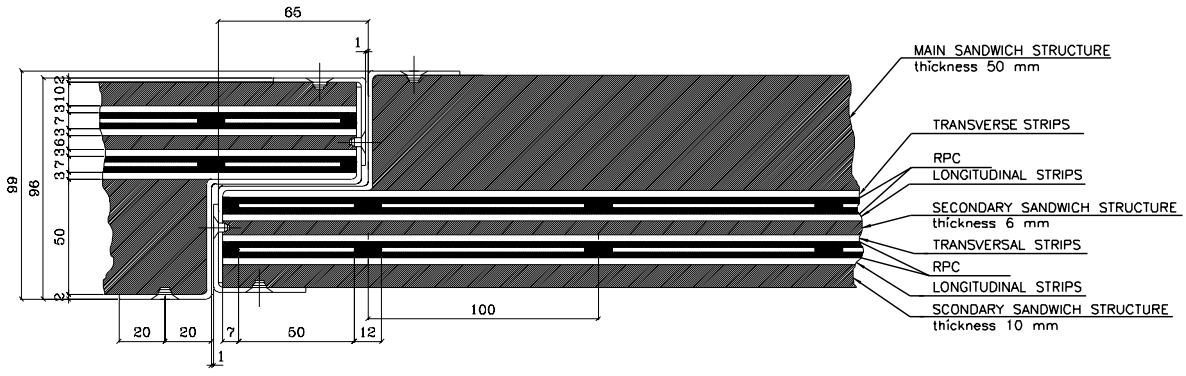

Figure 7.18: *Cross section of an RPC chamber.*

Thin Gap Chambers

The TGCs are similar to the CSCs in the sense that they are MWPCs. In contrast with the CSC, though, they have a cathode-anode distance smaller than the wire pitch as illustrated in figure 7.19. The gas mixture of the TGCc is highly quenching ($CO_2/n - c_5H_{12}$ preventing

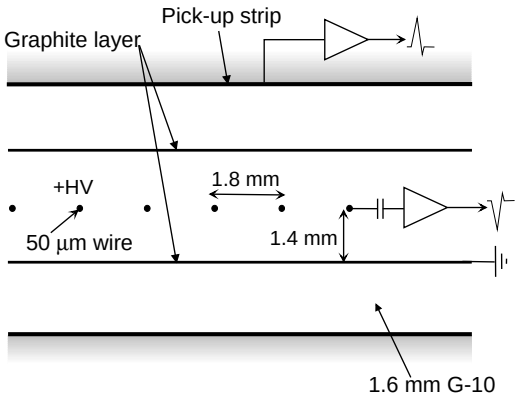

Figure 7.19: *An illustration of the TGC layout.*

the chamber from streaming. This allows for running in so-called saturated mode [MCBM83, B^+90] which is characterised by a low sensitivity to mechanical deformations that easily pose a problem in a detector the size of ATLAS. Also, the energy deposition is Gaussian in nature and there is little dependence of the signal on the incident angle of the particle traversing the chamber.

7.3 The Trigger/DAQ of ATLAS

The ATLAS physics programme covers a wide variety of phenomenologies. The detector must be able to handle with great accuracy the reconstruction of leptons, hadrons, photons, jets and missing energy. Furthermore the phenomenologies in question span $\mathcal{O}(8)$ orders of magnitude at the LHC energies as seen in figure 6.5. This is precisely the rationale for the construction of the LHC as a high-luminosity machine. It *does*, however, pose a requirement of an extremely efficient trigger that rejects minimum-bias events while conserving rare signal with a high-efficiency. To illustrate the problem one merely needs to consider that the total output of the ATLAS detector at full luminosity will be $\mathcal{O}(80$ TB/s). This is merely the product of an estimated event size of 2 MB and an event rate of 40 MHz. This data rate is not only outside the realm of the possible with respect to storage, but also it prohibits transporting all data away from the detector.

The trigger system of ATLAS is outlined in figure 7.20. The trigger is subdivided into three levels and while the precise contents of the trigger menus is not finalised, the basic structure is well established. Level 1 is responsible for providing fast decisions using specialised hardware, while the level 2 and event filter stages utilise software algorithms. The combined trigger is expected to provide a downsampling from the bunch crossing rate of 40 MHz down to $\mathcal{O}(100$ Hz). Design considerations are to use a modular design with standard components across the different trigger slices and to perform parallel data processing on the front-end to reduce the need for bandwidth.

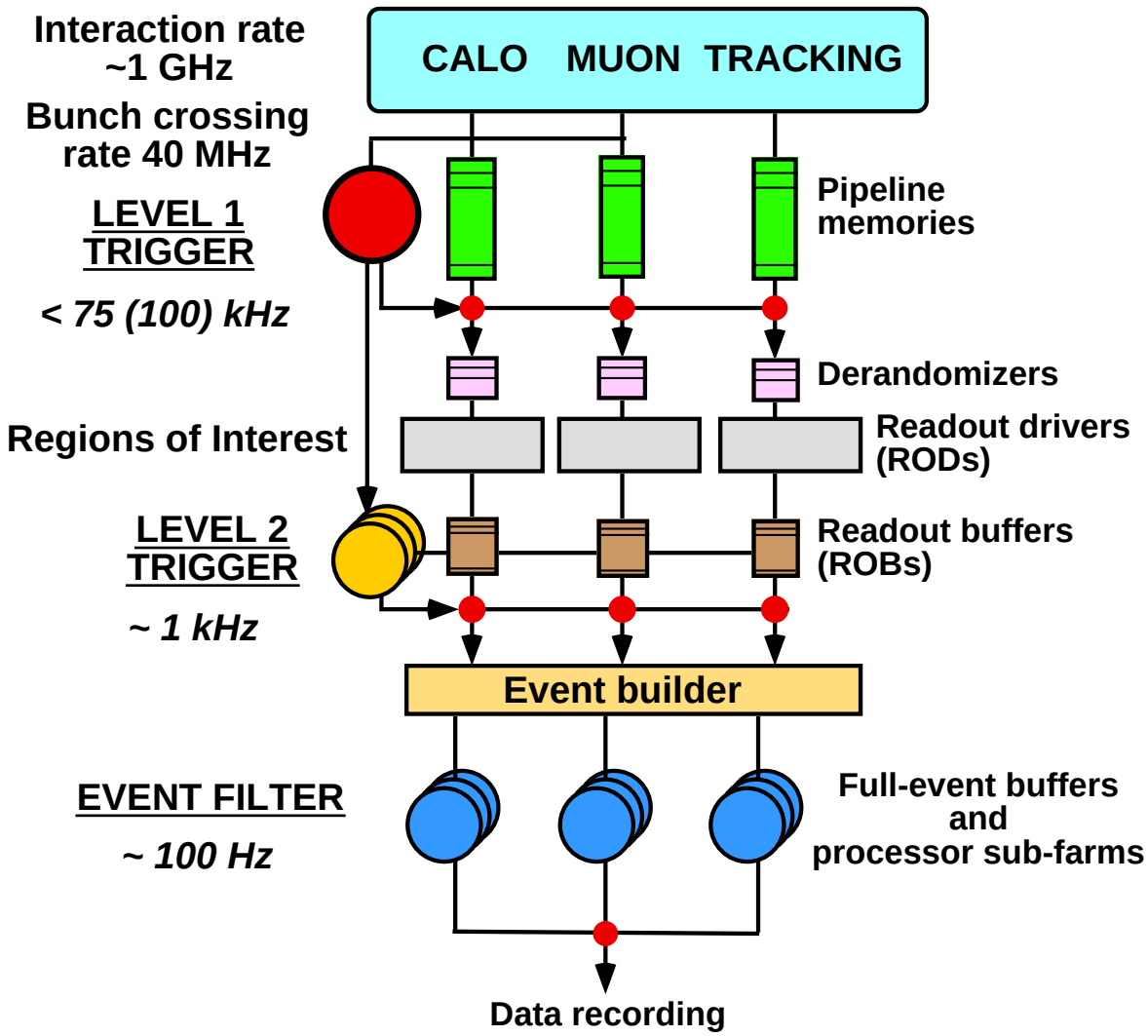

Figure 7.20: *A diagram of the ATLAS trigger system. The trigger system consists of three trigger levels.*

7.3.1 Level-1

The Level-1 trigger (often abbreviated LVL1 or simply L1) receives data at each bunch crossing and it is charged with reducing the event rate to $\mathcal{O}(75$ kHz). Decisions are made with a latency time of $\mathcal{O}(2.5$ μs). At a bunch crossing rate of 40 MHz this amounts to 100 events that need to be fully stored in pipeline memories. The LVL1 trigger relies on fast though somewhat coarse detector hardware and simple pattern recognition performed by dedicated hardware at the detector front-end. The LVL1 trigger decision is issued based on the multiplicities of a number of objects with varying p_t-thresholds. The objects are grouped into different areas. These are: muon, EM clusters, narrow jets (hadronic τs / single hadrons) and missing transverse energy.

As part of a positive LVL1 trigger decision *Regions of Interest* (RoIs) are formed. These RoIs are passed on to LVL2. Also the LVL1 pipeline memories are read out and stored in *readout buffers* (ROBs) for use by LVL2.

7.3.2 Level-2

The LVL2 trigger is a software trigger that utilises the RoIs formed in the LVL1 decision. Also, global information such as the components of the missing-E_t vector as calculated at LVL1 is used as input for LVL2. Each RoI is examined by the LVL2 trigger in the detector system in which it originated to confirm or reject the LVL1 decision. The individual RoI may be cross-referenced with information from other sub-detectors. For instance ID information such as SCT/TRT hits may be used in the evaluation of a muon RoI. The LVL2 trigger is expected to consume $\mathcal{O}(10$ ms) to issue a trigger decision and the output design rate is 1 kHz.

7.3.3 Event-Filter

The final stage in the trigger selection is in ATLAS referred to as the Event-Filter (EF). The EF selection is performed using computer farms and the entire detector is therefore read out at this stage and the data is transferred above ground. The EF does not perform a full reconstruction but it does use all information in the detector and the full granularity of all detector elements though calibration and alignment constants are not the final ones. The EF is thus capable of reconstructing for instance γ conversions or doing bremsstrahlung recovery. The output rate of the EF is expected to be ~ 100 Hz.

7.3.4 The ATLAS Muon Trigger

The analysis presented in part IV of this thesis utilises the muon trigger of ATLAS. It is therefore prudent at this stage to go into a little more detail with the structure and performance of this trigger slice. The muon trigger is presented in detail in [mTD, TDRa].

The Level-1 muon trigger exploits the fast response time of the TGCs and the RPCs of the Muon Spectrometer (section 7.2.3) to look for muons above a p_t threshold pointing to the interaction vertex. The trigger is subdivided into a barrel ($|\eta| < 1.05$) and an end-cap ($1.05 < |\eta| < 2.2$). Figure 7.21 depicts the muon barrel trigger strategy. As mentioned in

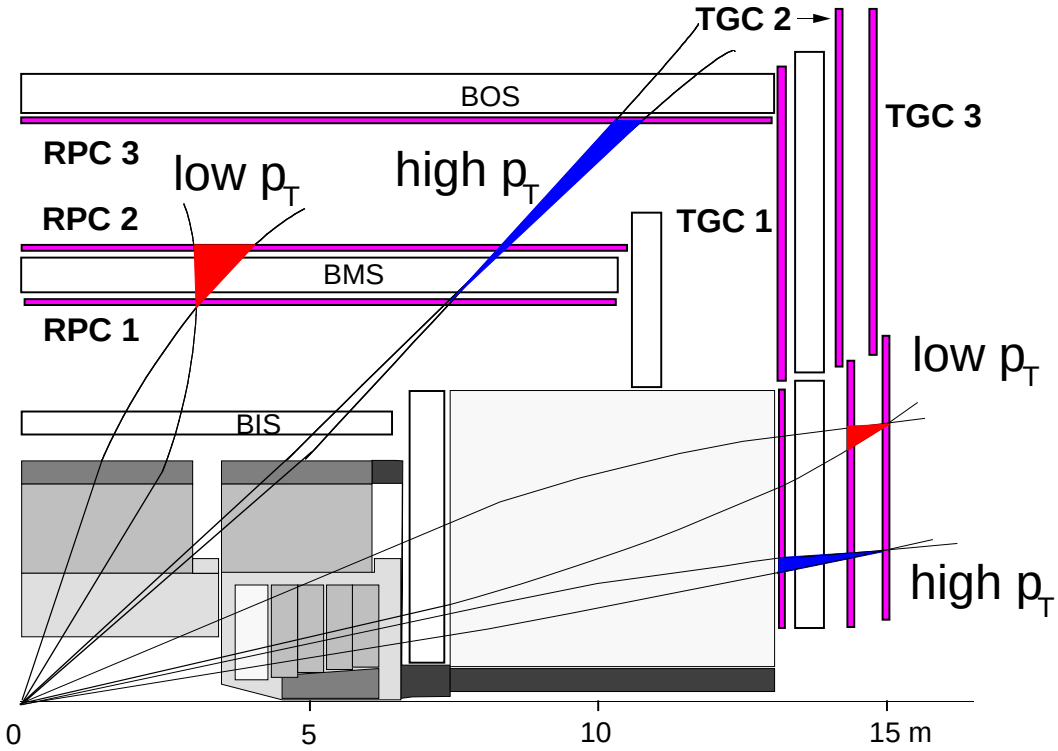

Figure 7.21: *An illustration of the ATLAS muon trigger. The low-p_t trigger requires a coincidence between the pivot (middle) layer and one other layer, while the high-p_t trigger requires a coincidence between all three traversed layers.*

section 7.2.3, there are three RPC layers. The coincidence finding is based on the second RPC station, the *pivot* layer. Strips in the pivot layer are related via a look-up table to strips in the other layers as indicated in the figure. At LVL1 a coincidence is valid when matching strips have hits in the same trigger window. As the p_t-range of the physics signatures involving muons is very large the trigger logic is divided into low-p_t and high-p_t types. The low-p_t trigger requires a coincidence in the two first trigger stations while the high-p_t trigger requires an *additional* coincidence with one layer of the third RPC station. The end-cap trigger is similar in logic even though the TGCs are used in place of the RPCs.

The first task of the Level-2 muon trigger is to confirm the LVL1 RoIs. There are typically of the order five RoIs in a positive LVL1 decision [Mat00]. This is done by reading out the data from the MDTs in combination with the RPC and TGC information. This requires a few percent of the event data to be read out. However, at LVL2 some b-physics triggering also takes place. This requires analysis of ID data such as the TRT and the SCT. Upon RoI confirmation the muon tracks are extrapolated back to the interaction vertex and combined with the ID information to obtain refined estimates of the track parameters.

The Event-Filter has access to the the full event information of all the sub-detectors of ATLAS. At this stage of the triggering process specialised versions of the offline reconstruction software are wrapped into the online software to ensure that there are no offline dependencies in the online data-taking software.

Figure 7.22 shows the expected trigger efficiencies of the ATLAS muon trigger as evaluated in [mTD]. The structure of the ATLAS detector along z is visible in the trigger efficiency vs η while the eight-fold azimuthal structure of the detector is seen in the ϕ plot. A common variable in which to study the trigger efficiency is the transverse momentum. This is shown in figure 7.23.

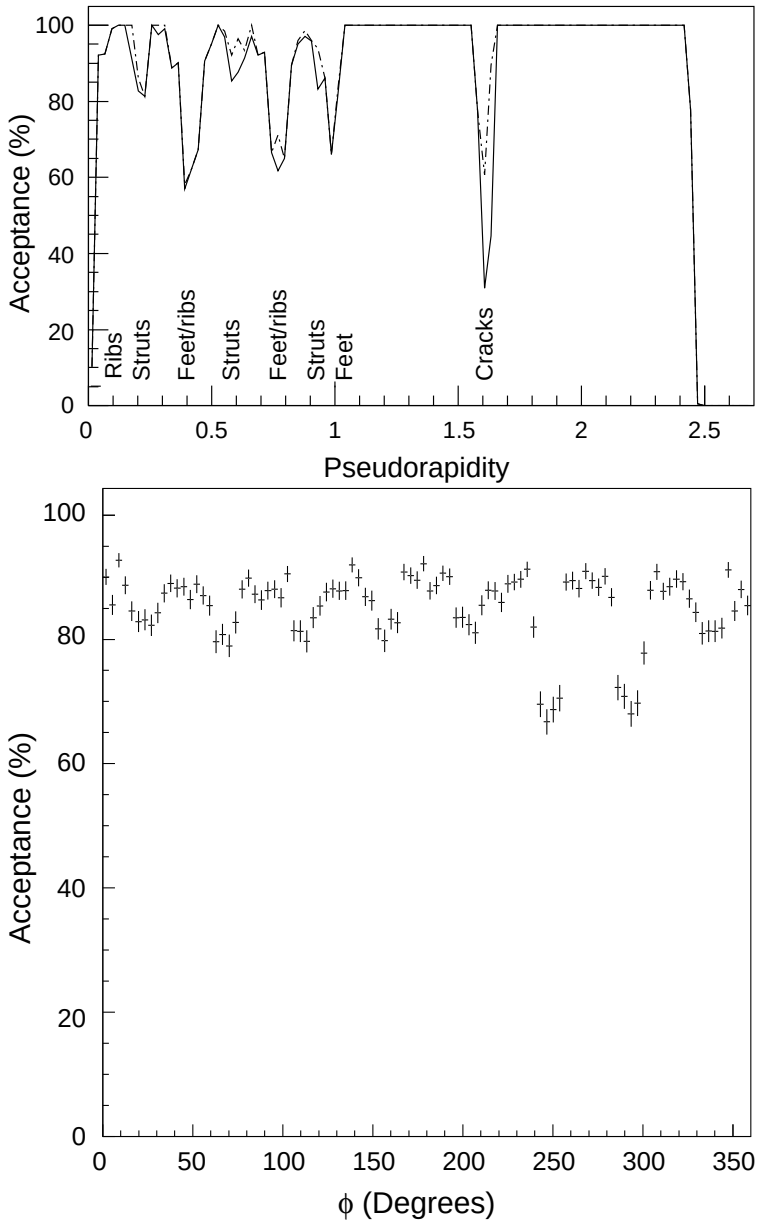

Figure 7.22: *Muon trigger acceptance as a function of $|\eta|$ and φ [mTD]. The dash-dotted line of the top plot represents the low-p_t trigger, while the solid line is the high-p_t trigger. The azimuthal acceptance plot is averaged over both triggers. The structure of the ATLAS detector can be related to the features of these plots as indicated on the η parametrisation. On the azimuthal parametrisation the eight toroid magnets can be seen with additional drops in efficiency where the legs of the detector are located.*

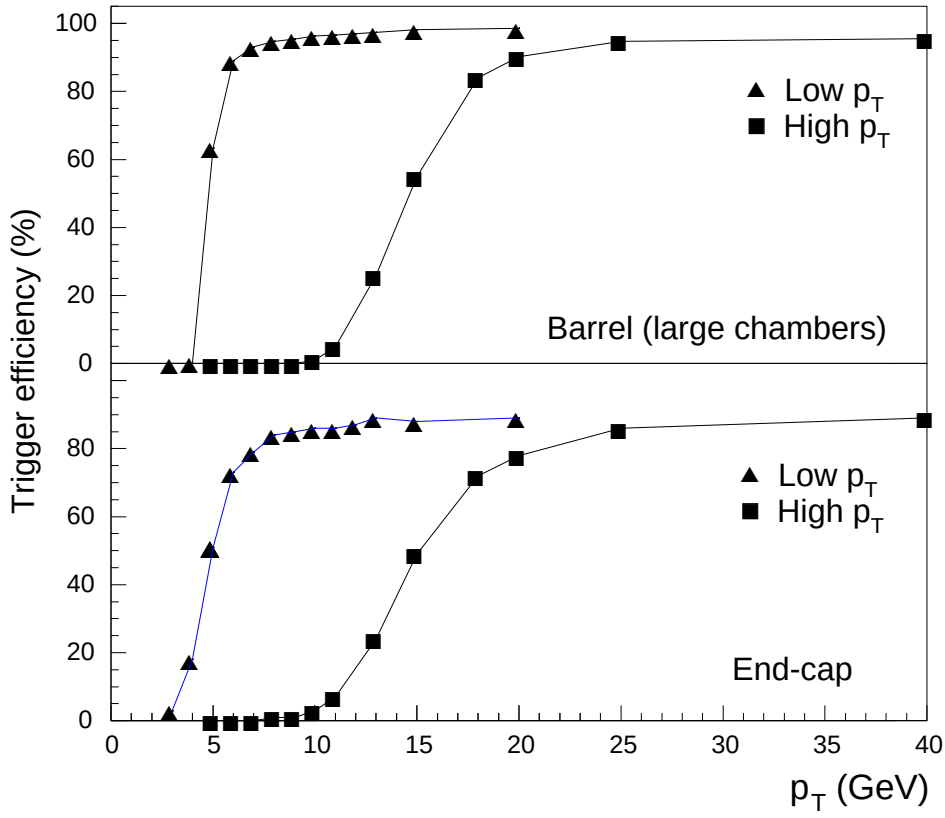

Figure 7.23: *The muon trigger efficiency in the barrel (top) and end-cap (bottom) as a function of p_t. The low- and high-p_t triggers are shown separately.*

Part IV
ATLAS analysis

An elementary particle is not an independently existing, analyzable entity. It is, in essence, a set of relationships that reach outward to other things.

[Henry P. Stapp]

Chapter 8

Event Generation and Detector Response

The analysis presented in this part of the thesis is a Monte Carlo study outlining the discovery potential of exotic heavy hadrons described in the models presented in part II. As such it is important to establish exactly what is studied so that the conclusions in the end are firm. This chapter will concern itself with the PYTHIA setup used for the study as well as check plots of the ATLAS detector response as it is described by the ATLAS software. For details on the ATLAS software releases used the reader is referred to appendix A.

8.1 A First Look at Split-SUSY

Split-SUSY was described in section 3.1. We will here deal with the situation where the gluino is long-lived enough to always exit the detector. The LSP in this context becomes irrelevant except for the cases of direct weak pair-production. Looking for direct neutralino pair-production through for instance Higgs decays would be a fundamentally different signature. Also it would require some assumptions to be made on the specifics of the models in question thus reducing the generality of the study. Squark production is in general *not* possible at the LHC and any diagrams containing a virtual squark will be strongly suppressed.

The approach taken here is to set the gluino to be absolutely stable in PYTHIA and push all other SUSY particles significantly above the TeV scale. We thus ensure that we only produce on-shell gluinos that can then be hadronised and studied.

8.1.1 Setup of the Monte Carlo Event Generator

Events were produced using PYTHIA 6.403 [Sjo94, SMS06] as integrated into the ATLAS software framework at the time of release 12.0.31. All sparticle masses except for $m_{\tilde{g}}$ were set to 4 TeV and direct gluino pair-production through the process $gg \rightarrow \tilde{g}\tilde{g}$ was enabled (Subprocess 244, [SMS06]). PYTHIA also contains the option of generating $f\overline{f} \rightarrow \tilde{g}\tilde{g}$ (Subprocess 243). This process takes place through the diagrams shown in figure 8.1. The two diagrams interfere destructively [KHN07] so high squark masses tend to increase the total cross section

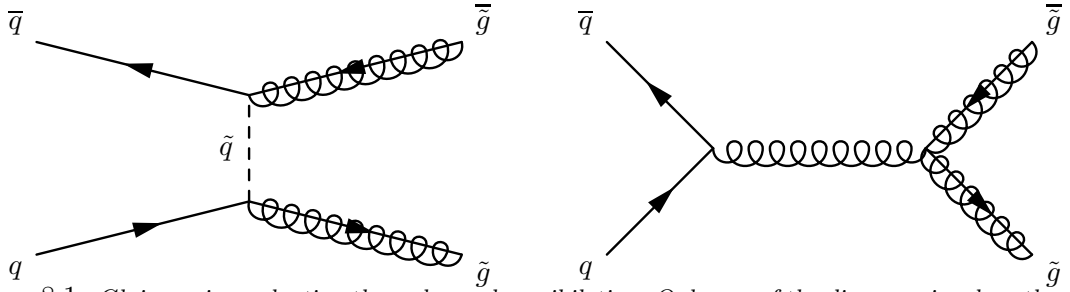

Figure 8.1: *Gluino pair production through quark annihilation. Only one of the diagrams involve other BSM particles than the gluino itself but the two diagrams interfere destructively rendering this production channel sensitive to model dependence.*

for $f\overline{f} \rightarrow \tilde{g}\tilde{g}$. In other words the process is heavily dependent on the squark mass in contrast to the $gg \rightarrow \tilde{g}\tilde{g}$ process which does not involve the rest of the SUSY spectrum. The $f\overline{f} \rightarrow \tilde{g}\tilde{g}$ process was therefore kept disabled in order to keep down model dependence. It should be mentioned for completeness that the processes allowing for $f\overline{f} \rightarrow \tilde{g}\tilde{\chi}_n$ (Subprocesses 237-242) were disabled for the same reasons.

After creation of the gluinos they were hadronised using custom code adapted from the example R-hadron program on the PYTHIA homepage [PPA]. The probability for a gluino to form a gluino ball with a gluon was set to 0.1 from colour considerations.

Samples were generated at gluino masses of 100, 300, 600, 1000, 1300, 1600 and 2000 GeV/c^2. Each sample contained 10000 events to ensure high statistics on the study of the detector response.

8.1.2 Cross Section

At event generation PYTHIA calculates a LO cross section for the processes generated. This cross section is shown in figure 8.2 as a function of the gluino mass. For comparison the reader is reminded of figure 6.5 which depicts the total cross section at the LHC for a number of SM processes.

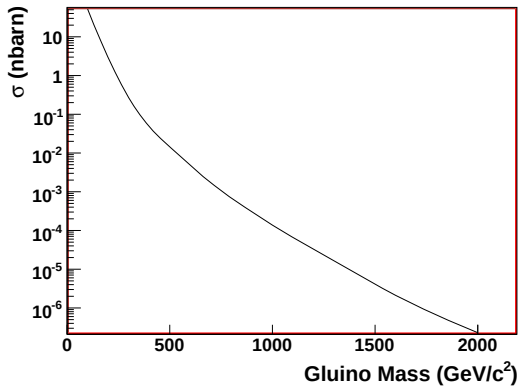

Figure 8.2: *Total cross section for gluino pair-production at the LHC as a function of gluino mass. The cross section shown is the LO calculation used in PYTHIA.*

Table 8.1 shows the expected number of events per inverse femtobarn at the different mass points generated as well as the corresponding integrated luminosity of the generated MC

sample at the given mass point. As can be readily seen the cross section spans eight orders of magnitude and the challenge is to construct an analysis that retains the relatively low event counts in the higher mass range while keeping the background down.

Gluino mass: (GeV/c^2)	**σ (nbarn)**	**Events/fb^{-1}:**	**$\mathcal{L}$ of MC sample: (fb^{-1})**
100	52.3	5.23×10^7	1.91×10^{-4}
300	0.269	2.69×10^5	3.72×10^{-2}
600	4.84×10^{-3}	4.84×10^3	2.07
1000	1.38×10^{-4}	138	72.5
1300	1.64×10^{-5}	16.4	610
1600	2.12×10^{-6}	2.12	4.72×10^3
2000	2.30×10^{-7}	0.230	4.35×10^4

Table 8.1: *Expected number of pair-production events per integrated luminosity of fb^{-1} and $\mathcal{L}$ of signal samples. Each sample consists of 10000 events. Numbers are not corrected for detector acceptance.*

8.1.3 Kinematics

In order to motivate the cuts and methods of chapter 9 it is instructive to take a look at the kinematics of the physics processes generated. Heavy stable particles tend to be slow-moving due to the limited energy of the accelerator. This fact has been previously exploited in analyses and feasibility studies looking for heavy stable particles where the Time-of-Flight (ToF) has been an important parameter [A+00]. Figure 8.3 shows the velocity (β) distributions for gluino R-hadrons as a function of the gluino mass. The colour coding used is the same throughout this section. To the right in the figure the mean β is parametrised in $m_{\tilde{g}}$ with the RMS shown to illustrate the spread. As can be seen from the figure the reduction in

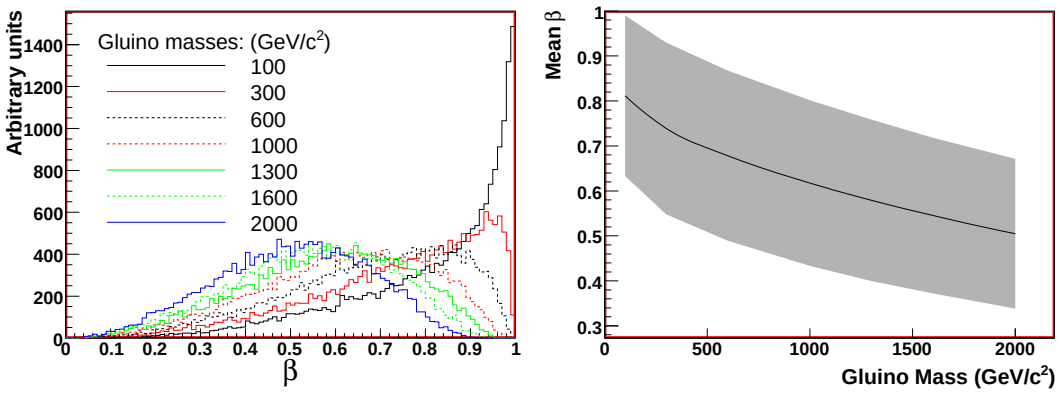

Figure 8.3: *Velocity (β) distributions for gluino R-hadrons for different values of $m_{\tilde{g}}$. There is a significant reduction in mean velocity with increasing gluino mass.*

available phase space, as the gluino mass approaches a significant fraction of $\sqrt{s}$, results in slower moving particles. This is potentially a problem for the trigger, as the bunch spacing at the LHC is 25 ns. If the particles arrive too late at the muon trigger chambers the trigger will be assigned to the wrong event and both events will most likely be lost. The traditional assumption[Kra04a] on which value of β is necessary for the trigger to be assigned to the

correct bunch crossing is based on simple geometric considerations of the distance from the nominal interaction point to the muon trigger stations. It was found that the condition for a particle to arrive within the correct bunch crossing throughout the detector was $\beta \geq 0.7$.

Turning now instead to the p_t distributions we see that the mean p_t as well as the RMS grows with $m_{\tilde{g}}$. What can be inferred from this is that tracks in the muon chambers coming from

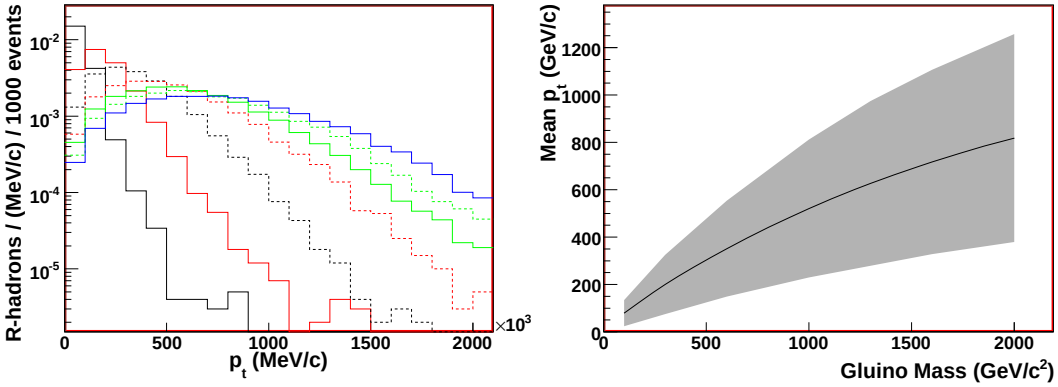

Figure 8.4: *Transverse momentum distributions for gluino R-hadrons for different values of $m_{\tilde{g}}$. Line styles and colours are identical to figure 8.3. The mean p_t as well as the RMS of the distribution grows with the gluino mass.*

charged R-hadrons will be seen as very high-p_t muons that would be found to have a low value of β if one were to measure the ToF of the particles.

Finally, one of course wishes to know if the R-hadrons will be within the geometrical acceptance of the ATLAS detector. As any analysis will be relying on tracking it is interesting to see how many of the R-hadrons fall within the tracking acceptance of $|\eta| \leq 2.5$. Figure 8.5

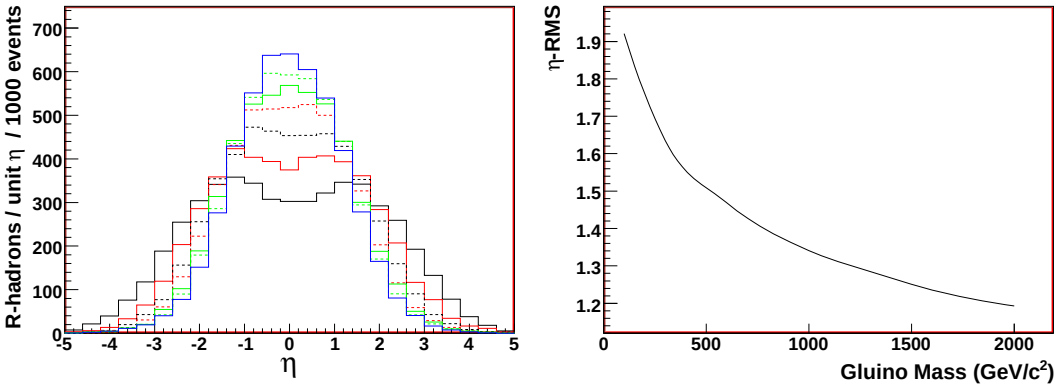

Figure 8.5: *Pseudo-rapidity distributions for gluino R-hadrons for different values of $m_{\tilde{g}}$. Line styles and colours are identical to figure 8.3. The events are seen to be more central for higher gluino masses as is shown by the narrowing of the η distribution as a function of $m_{\tilde{g}}$.*

shows that there is a significant narrowing of the η-distribution for increasing values of $m_{\tilde{g}}$ which follows logically as the energy available to boost the event decreases for higher masses. The RMS of the distributions is shown to the right as a function of $m_{\tilde{g}}$.

Introducing an η acceptance cut of $|\eta| < 2.5$ on the Monte Carlo truth information together with the requirement that $\beta > 0.7$ for an R-hadron to be "visible" the fractions of events that have at least one visible or two visible R-hadrons are listed in table 8.2. The low fraction of

Gluino Mass: (GeV/c^2)	**One visible:**	**Two visible:**
100	0.75	0.37
300	0.71	0.35
600	0.64	0.25
1000	0.51	0.16
1300	0.41	0.1
1600	0.31	0.06
2000	0.21	0.03

Table 8.2: *Fraction of events with at least one or two "visible" R-hadrons ($|\eta| < 2.5$, $\beta > 0.7$). One sees clearly the effect of the slowness of R-hadrons at higher gluino masses.*

events containing two visible R-hadrons shows that one cannot rely exclusively on correlations between the two R-hadrons to select an event through global event variables. An analysis must also select events based on single objects.

Having established the kinematical properties of the individual R-hadron, it is also of interest to study correlations between the two R-hadrons in the event. We know that they are pair-

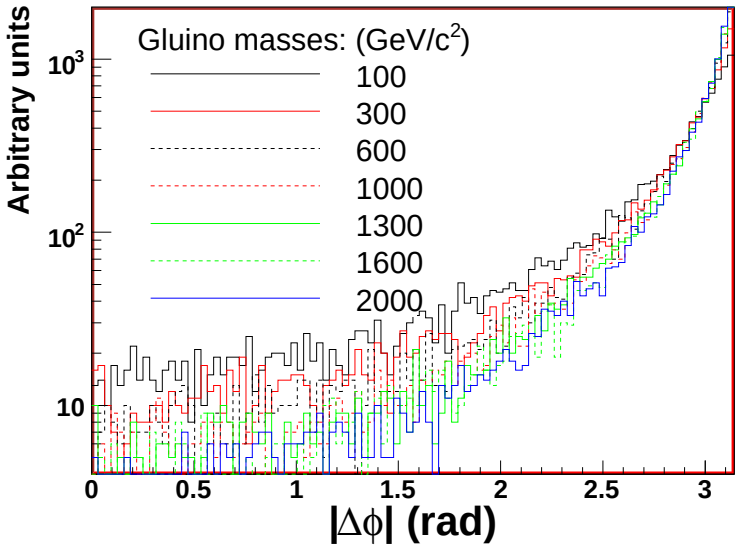

Figure 8.6: *Distributions of $|\Delta\phi|$ for gluino R-hadron pairs for different values of $m_{\tilde{g}}$. It is seen that the typical events for all masses feature back-to-back R-hadrons. Some events appear to have a transversely boosted $\tilde{g}\overline{\tilde{g}}$ system leading to R-hadrons appearing with smaller azimuthal separations. This fraction reduces significantly with increasing gluino mass due to the reduced phase space available for such boosts.*

produced and it is thus reasonable to use correlations between objects in an event selection. Figure 8.6 shows the separation in azimuthal angle between R-hadrons for varying gluino masses. The curve is seen to show little dependence on $m_{\tilde{g}}$ with a slight tendency for higher masses to be more back-to-back.

To complete this exercise we now classify the events according to table 8.3. In this table only events with two visible R-hadrons are shown. The columns are from left to right (excluding the first one):

- Two neutral R-hadrons.
- One positively charged and one neutral.
- One negatively charged and one neutral.
- One positive and one negative.
- Two positive.
- Two negative.

Gluino Mass: (GeV/c^2)	00	$+0$	-0	$+-$	$++$	$--$
100	0.31	0.22	0.26	0.10	0.04	0.06
300	0.30	0.23	0.27	0.09	0.04	0.06
600	0.31	0.21	0.26	0.10	0.04	0.06
1000	0.31	0.22	0.27	0.10	0.04	0.06
1300	0.32	0.22	0.26	0.10	0.05	0.06
1600	0.31	0.22	0.29	0.10	0.03	0.05
2000	0.33	0.24	0.23	0.09	0.04	0.07

Table 8.3: *Event topologies with two "visible" R-hadrons. There is little discernible variation in the fractions of different event topologies for the different gluino masses.*

It is immediately apparent from table 8.3 that there is little variation in the hadronisation of the R-hadrons for different values of $m_{\tilde{g}}$ as the fractions of different event topologies practically do not vary. Also it is seen that many events will have no tracks in the Inner Detector while one can hope for the R-hadron to have acquired charge when reaching the outer layers of the detector.

8.2 Single Particles in ATLAS

Many BSM physics scenarios (including most SUSY scenarios) contain a variety of heavy particles. These are most often highly unstable. The normal approach to such analyses is to reconstruct peaks and edges in combinations of kinematical properties such as lepton transverse momenta and missing transverse energy in the event [TDRb]. The analysis presented here, however, concerns itself with the case of stable particles escaping the detector. It is consequently very much of interest to understand the performance of ATLAS for these particles. Single particle samples is a very efficient tool to do this, as the event contents is fully known in every event.

A number of single particle samples have been simulated, digitized and reconstructed in ATLAS. To continue the discussions in part II of the thesis this was done for stable stops as well as gluinos, even though the rest of the analysis will primarily concern itself with stable

gluinos. The simulation software used was the standard ATLAS setup modified to encompass the FullModelHadronicProcess described in 5.3.2.

As discussed previously in section 8.1.3 the velocity of the R-hadrons can be expected to play a key role in the evaluation of the trigger performance. For this reason the samples were generated at fixed velocities chosen as the central points of 100 bins in β between 0.5 and 1.0. Pseudorapidity and azimuthal angle were chosen according to a flat distribution in the standard tracking acceptance of $|\eta| < 2.5$ and $\varphi \in [0, 2\pi]$. The flavours studied were for the gluino case $R^0_{\tilde{g}udd}, R^+_{\tilde{g}uud}$ and $R^-_{\tilde{g}ddd}$ while the stop cases chosen were $R^0_{\tilde{t}dd_1}$, $R^+_{\tilde{t}ud_1}$ and $R^-_{\overline{\tilde{t}ud_1}}$. These were chosen as meson states will anyway convert into baryon states as shown in section 5.4.4. The mass range for the gluino case was 100 - 2000 GeV/c^2 as in section 8.1.1 while the stops were for reasons of CPU time limited to a 100 - 1000 GeV/c^2 mass range.

8.2.1 Basic Performance of ATLAS

In this section the basic performance of the ATLAS detector is checked using single particle samples. Where appropriate the numbers will be compared to single muon samples as well as full signal and background events.

Tracking performance

As demonstrated in section 8.1.3 it will be necessary to study tracks with transverse momenta in excess of 1 TeV/c. This requires that the tracking resolution be checked for the muon system as well as for the Inner Detector. If we are to identify charge-changing particles it is crucial that we know the expected performance of the detector and the tracking software.

The primary parameter of interest is the transverse momentum resolution and hence the accuracy with which charge is reconstructed. The technical design report of the ATLAS muon spectrometer [mTD] quotes the resolutions shown in figure 8.7. The dashed lines show the resolution if only the Inner Detector is used for the measurement. From the figure one is tempted to draw the conclusion that the probability of misreconstructing the charge of a muon is absolutely vanishing as a Gaussian error of the magnitudes shown in the figure will practically never lead to a mismeasurement of more than 100 %. This observation turns out not to be the true, however. Simulating, digitizing and reconstructing a sample of single muons in ATLAS one has access to the truth information. It is thus a simple task to count the number of times a muon track is reconstructed with the wrong charge by the software. The result of such a test is shown in figure 8.8. As is seen in the figure the probability ranges from approximately 0.1% up to $\sim 4\%$ indicating that muons may indeed appear to change charge in the muon system. A contamination of an R-hadron charge-flip signal by muons can not be completely disregarded as a possibility.

Turning to charged R-hadron samples the picture is a little more complicated. Keeping in mind that the energy loss in the ATLAS detector is small compared to typical energies of R-hadrons (figures 5.14 and 8.4) the resolutions are estimated using the quantity

$$\frac{q_{Rec}\ p_t(\text{Rec}) - q_{Truth}\ p_t(\text{Truth})}{q_{Truth}\ p_t(\text{Truth})}, \tag{8.1}$$

where p_t is the transverse momentum and q is the measured charge. "Rec" and "Truth"

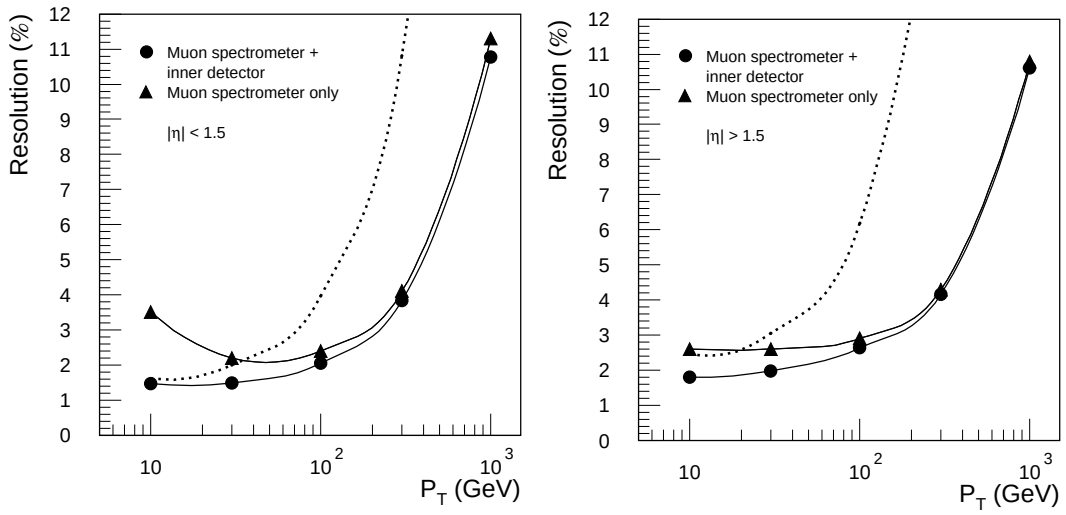

(a) $|\eta| < 1.5$ (b) $|\eta| > 1.5$

Figure 8.7: *ATLAS transverse muon momentum resolution. The two solid lines show the resolution obtained using the Muon Spectrometer alone or in conjunction with the Inner Detector while the dotted line shows the resolution obtained by using ID information only. The effect of the dimensions of ATLAS on the p_t resolution is clear.*

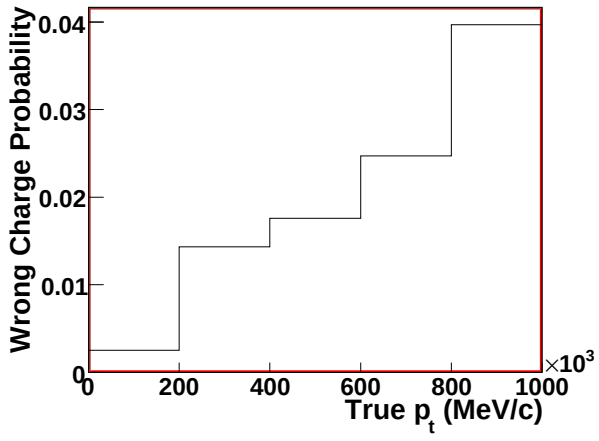

Figure 8.8: *Probability of misreconstructing the charge of a muon as a function of p_t. The muons have here been restricted to be within $|\eta| < 1.5$ to ensure that we are well within the barrel. The plot was made using the muon system exclusively. No Inner Detector information was used.*

refers to reconstructed quantities and truth quantities respectively. We will be looking at the resolution in the Inner Detector and in the muon system separately. As a match between the truth track and the reconstructed track we will be using a simple cut stating that any reconstructed track fulfilling the condition that $\sqrt{(\eta_{Rec} - \eta_{Truth})^2 + (\varphi_{Rec} - \varphi_{Truth})^2} < 0.1$ is considered a match. To study the p_t dependence of the resolution we divide the samples of R-hadrons into three bins in p_t(Truth). This yields the distributions shown in 8.9. Four

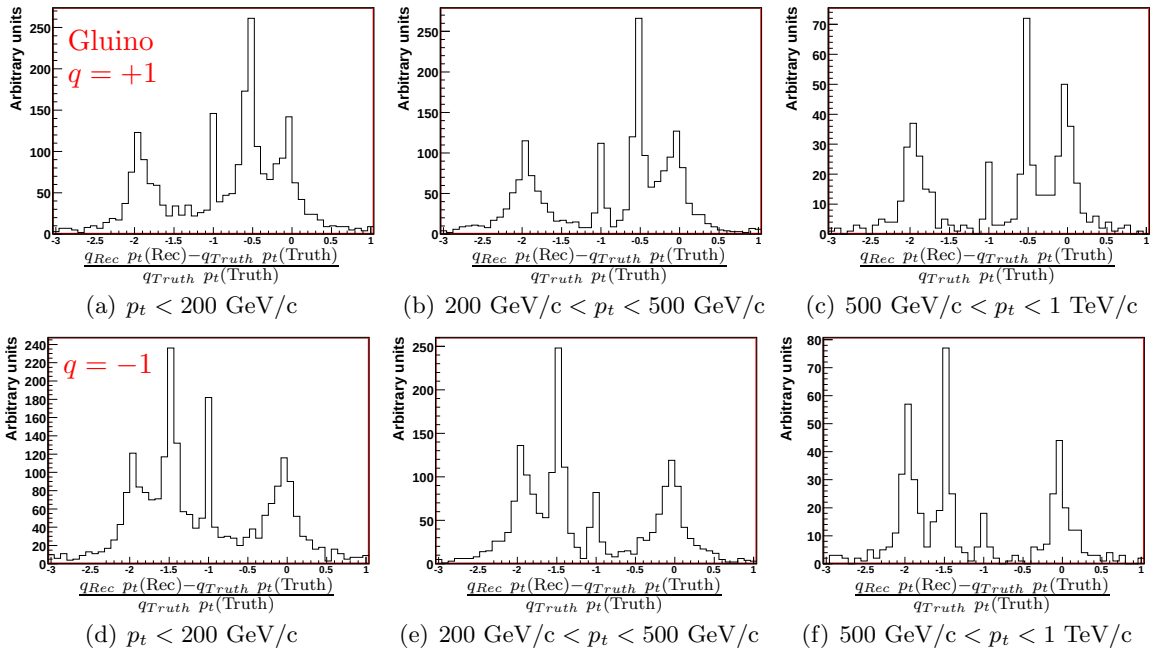

(a) $p_t < 200$ GeV/c (b) 200 GeV/c $< p_t <$ 500 GeV/c (c) 500 GeV/c $< p_t <$ 1 TeV/c

(d) $p_t < 200$ GeV/c (e) 200 GeV/c $< p_t <$ 500 GeV/c (f) 500 GeV/c $< p_t <$ 1 TeV/c

Figure 8.9: *Resolution plots for gluinos of mass 300 GeV/c^2 in the muon system for initial charge +1 (top) and -1 (bottom).*

distinct peaks are visible in the plots. For positive initial charge they are seen at values of -2, -1, -0.5 and 0 while negative initial charge results in peaks at -2, -1.5, -1 and 0. The interpretation of these peaks is:

- The peak at 0 is particles reaching the muon system with the same charge as they had in the Inner Detector.
- The peak at -2 represents particles flipping charge $+1 \leftrightarrow -1$.
- The peak at -1 is noise from secondary particles from hadronic interactions. This is corroborated by the position and the diminutive width of the peak. This peak is an expected feature of this rather loose truth matching and it illustrates the need for a noise cut in any event selection involving tracks.
- The "half-integral" peak (-1.5 / -0.5) represents particles changing into doubly-charged states. The reconstruction software assumes a charge of ± 1 and a doubly-charged particle will therefore appear with half the momentum. Note that this is peak is high and narrow. This is due to the improved momentum resolution stemming from the larger sagitta of a doubly-charged particle.

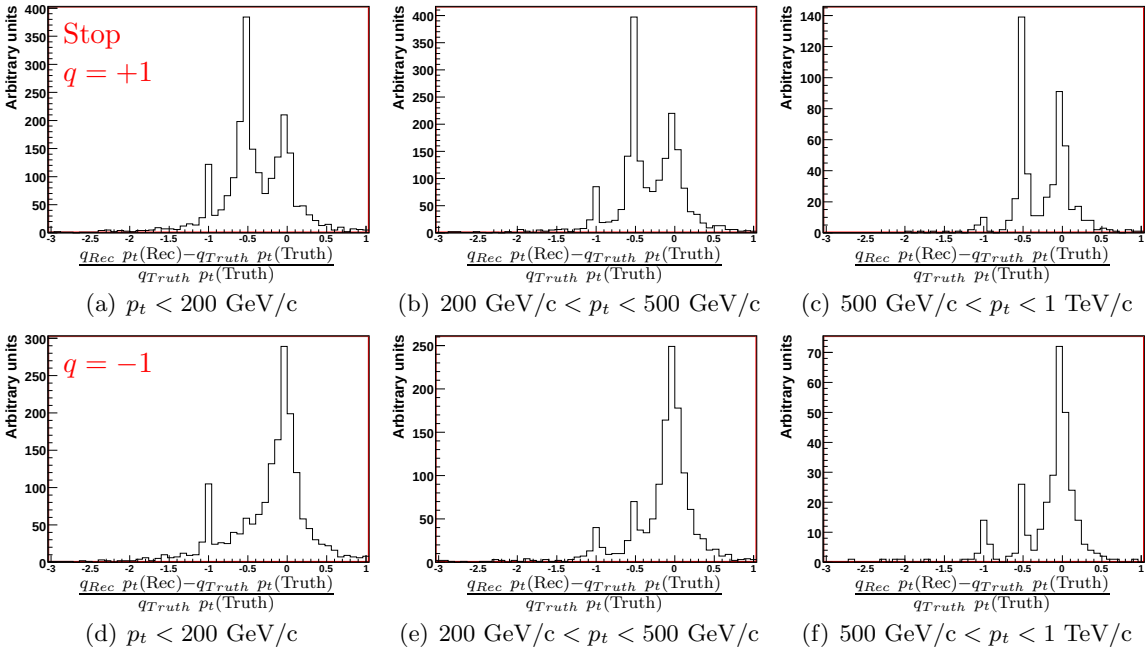

(a) $p_t < 200$ GeV/c (b) 200 GeV/c $< p_t <$ 500 GeV/c (c) 500 GeV/c $< p_t <$ 1 TeV/c

(d) $p_t < 200$ GeV/c (e) 200 GeV/c $< p_t <$ 500 GeV/c (f) 500 GeV/c $< p_t <$ 1 TeV/c

Figure 8.10: *Resolution plots for stops of mass 300 GeV/c^2 in the muon system for initial charge +1 (top) and -1 (bottom).*

Corresponding plots for 300 GeV/c^2 stop hadrons are shown in figure 8.10. These plots show significantly less structure due to the fact that a positively charged stop may *not* flip charge to a negatively charged state and vice versa. The noise peak at -1 is still there, though. The "$+1 \rightarrow +2$" peak is seen in 8.10(a) - 8.10(c). A feature that is evident at this particular mass is also the non-vanishing probability for a negatively charged antistop-state to acquire charge -2. This is shown by the peak at -0.5 in 8.10(d)-8.10(f).

$m_{\tilde{g}}$ (GeV/c^2)	σ_{p_t}/p_t $(q = -1)$	σ_{p_t}/p_t $(q = +1)$
100	8%	9%
300	14%	15%
600	27%	21%
$m_{\tilde{t}}$: 100	8%	8%
300	13%	15%
600	13%	Insuff. stat.

Table 8.4: *Muon system p_t resolution for gluino and stop R-hadrons. The transverse momentum is restricted to 200 GeV/$c < p_t <$ 500 GeV/c.*

Table 8.4 contains an estimate of the transverse momentum resolution of the ATLAS muon system for R-hadrons. The resolutions quoted are the spreads of Gaussian fits made to either the 0 or the -2 peak depending on which was the most isolated one. For R-hadrons with initial positive charge the -2 peak was chosen while the 0 peak was the choice for an initial charge of -1. The fits were performed iteratively to obtain a fit from -1.5σ to 1.5σ relative to the peak position with the condition that any fit involve at least six bins at a binwidth of 1%. Where an entry has been left empty the reason is that there were too few entries in the

histogram or the peaks were too smeared to obtain a meaningful fit. Only the central p_t-bin of 200-500 GeV/c is studied as this is the p_t-bin that is most often highly populated for the different masses.

We are not at this point interested in the actual resolution of the detector. We merely wish to have a consistent parameter that we may study to emphasise similarities and differences between the different particle species and masses.

The main lesson from this study is that the p_t resolution gets worse as the mass increases *even when the particles are restricted in* p_t. As we have no reason to assume that heavier particles should suffer larger deflections along their trajectory this is attributed to the fact that heavier R-hadrons arrive late at the MDTs. The velocity of particles in the muon system is assumed to be $\beta = 1$ and the corresponding time-of-flight enters the track fit. For the heavier and slower R-hadrons the ToF estimate is wrong leading to a reduced fit quality and a corresponding diminished p_t resolution.

Tracking in the Inner Detector is less dependent on drift time measurements. The only exception from this being the TRT. The drift tubes used here are a lot smaller than the MDTs though. The effect of the slowness of the R-hadrons is thus expected to be less evident when looking at the ID p_t resolution. Figures 8.11 and 8.12 show the resolution for 300 GeV/c^2 stops in the Inner Detector. As can be readily seen from the plots hadronic reactions *do* take place in the Inner Detector although they are exceedingly rare. This leads to hints of the charge-change peaks from figures 8.9 and 8.10. Fitting the central peaks of the resolution

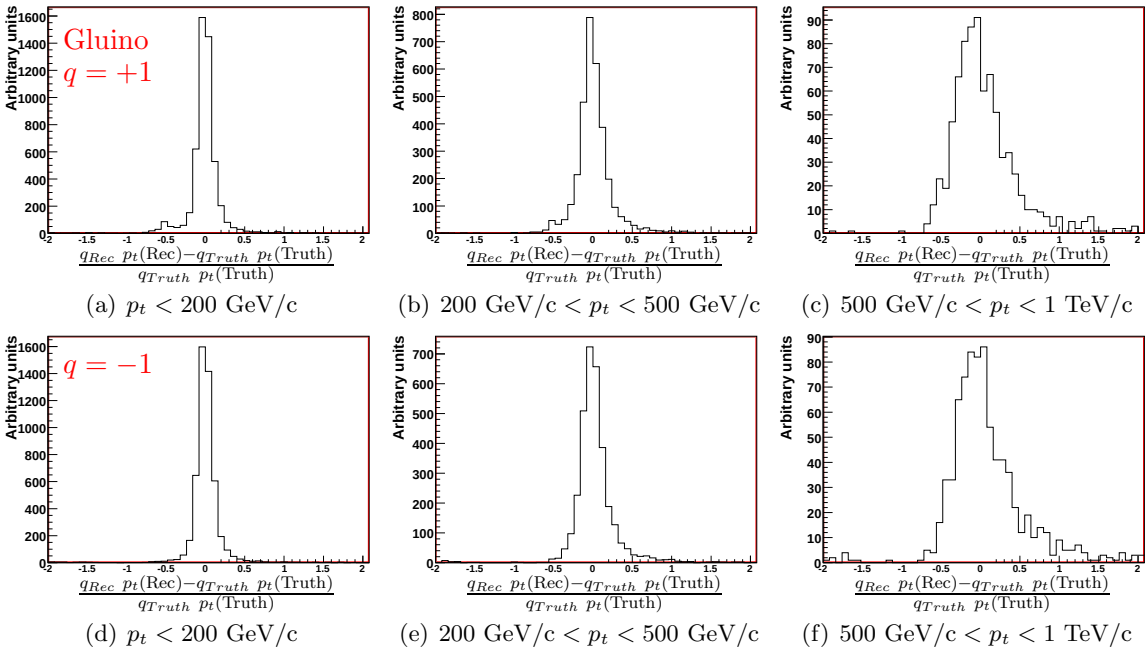

(a) $p_t < 200$ GeV/c (b) 200 GeV/c $< p_t <$ 500 GeV/c (c) 500 GeV/c $< p_t <$ 1 TeV/c

(d) $p_t < 200$ GeV/c (e) 200 GeV/c $< p_t <$ 500 GeV/c (f) 500 GeV/c $< p_t <$ 1 TeV/c

Figure 8.11: *Resolution plots for gluinos of mass 300 GeV/c^2 in the Inner Detector for initial charge +1 (top) and -1 (bottom).*

distributions with the same procedure as was used for the gluinos one obtains the resolutions shown in table 8.5. The resolution *does* indeed appear to be less sensitive to the mass. Only a moderate change in resolution occurs for masses below 1 TeV/c^2.

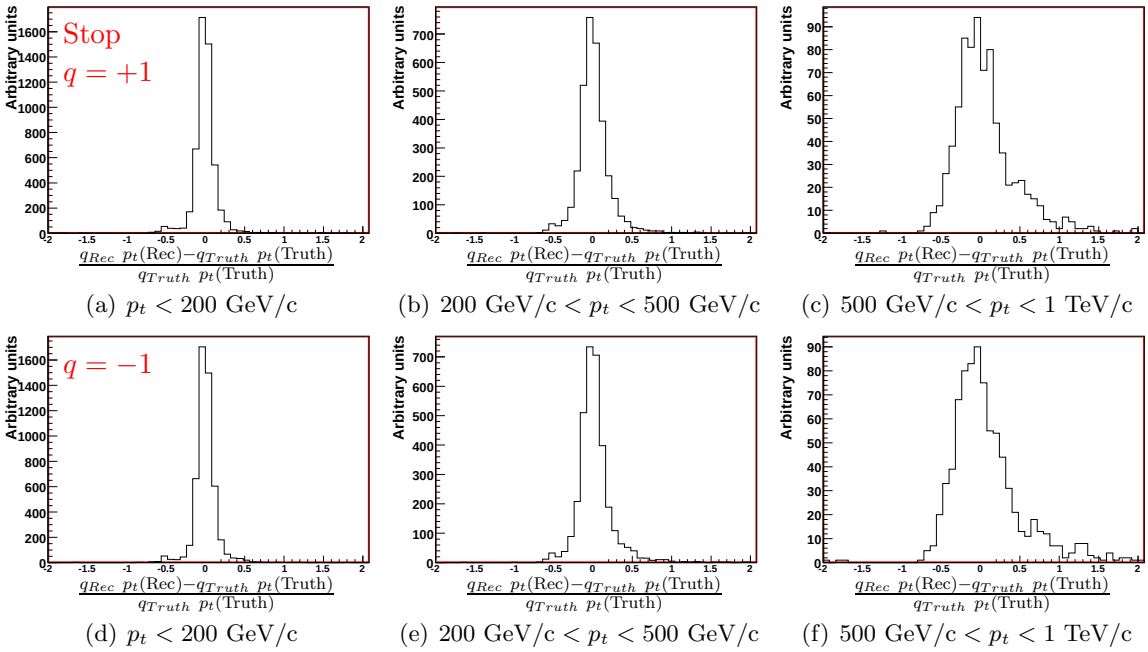

(a) $p_t < 200$ GeV/c (b) 200 GeV/c $< p_t <$ 500 GeV/c (c) 500 GeV/c $< p_t <$ 1 TeV/c

(d) $p_t < 200$ GeV/c (e) 200 GeV/c $< p_t <$ 500 GeV/c (f) 500 GeV/c $< p_t <$ 1 TeV/c

Figure 8.12: *Resolution plots for stops of mass 300 GeV/c^2 in the Inner Detector for initial charge +1 (top) and -1 (bottom).*

$m_{\tilde{g}}$ (GeV/c^2)	σ_{p_t}/p_t $(q = -1)$	σ_{p_t}/p_t $(q = +1)$
100	13%	13%
300	13%	12%
600	13%	14%
1000	17%	16%
1300	19%	20%
1600	21%	25%
2000	33%	32%
$m_{\tilde{t}}$: 100	14%	13%
300	12%	12%
600	14%	13%
1000	16%	16%

Table 8.5: *Inner Detector p_t resolution for gluinos and stops. The transverse momentum is restricted to 200 GeV/c $< p_t <$ 500 GeV/c and the same adaptive fitting procedure is used as for the muon resolution estimates in table 8.4.*

Utilising the TRT

Part II of this thesis deals among other things with the energy deposition properties of R-hadrons in matter. It thus seems a valid point to consider if the high-threshold information provided by the TRT can provide a parameter suited to distinguish R-hadrons from the background. However, as mentioned in section 8.2.1 there is little probability for hadronic interactions to occur in the tracker. We need therefore only study the electromagnetic interactions of R-hadrons. To estimate this the charged initial-state single-particle samples were used. Figure 8.13 is a profile histogram showing the number of high-threshold hits divided by the number of low-threshold hits on a per-track basis as a function of the transverse momentum of the individual track. For comparison the plot also contains the same quantity for

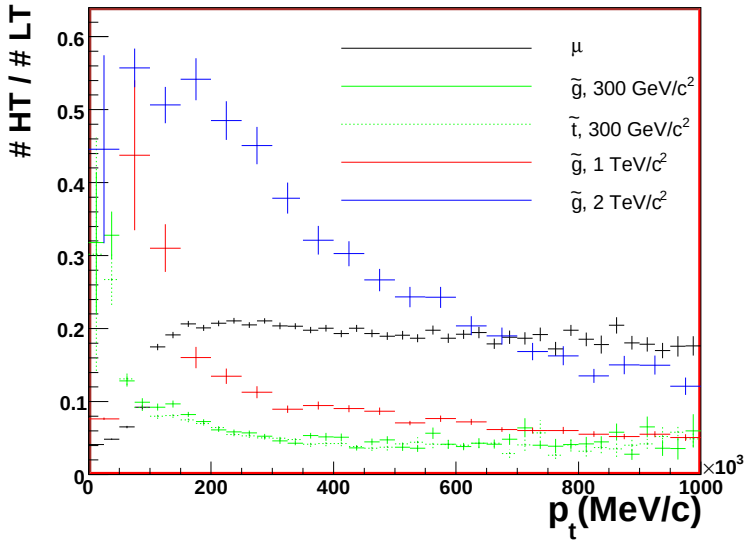

Figure 8.13: *Fraction of high-threshold over low-threshold hits for varying species of R-hadrons as a function of p_t. The distributions are compared to that for muons.*

muons. What is seen in the plot is that the low-end of the Bethe-Bloch formula is clearly visible for the R-hadrons, due to their masses. They move slowly (i.e. with a low value of $\beta\gamma$) thus depositing much energy as ionisation along their path. Also we note that relative to even ultra-relativistic muons, R-hadrons can be considered to be minimum-ionising for most masses. They have on average a significantly lower HT/LT fraction indicating a lower value of dE/dx. At higher masses, however, the difference between R-hadrons and muons is washed out and even reversed up to very high values of p_t due to the slowness of the very heavy R-hadrons.

Figure 8.14 shows the #HT/#LT distributions for the same samples in linear and logarithmic scale to emphasise the peak and the tail regions respectively. To cut away the left part of figure 8.13 a p_t cut of 100 GeV/c has been applied to the samples. Little quantitative information can be deduced from this distribution as-is due to the fact that its shape rely extensively on the underlying kinematic distributions. One must therefore compare specific signal and background samples to construct parameters and cuts for analysis.

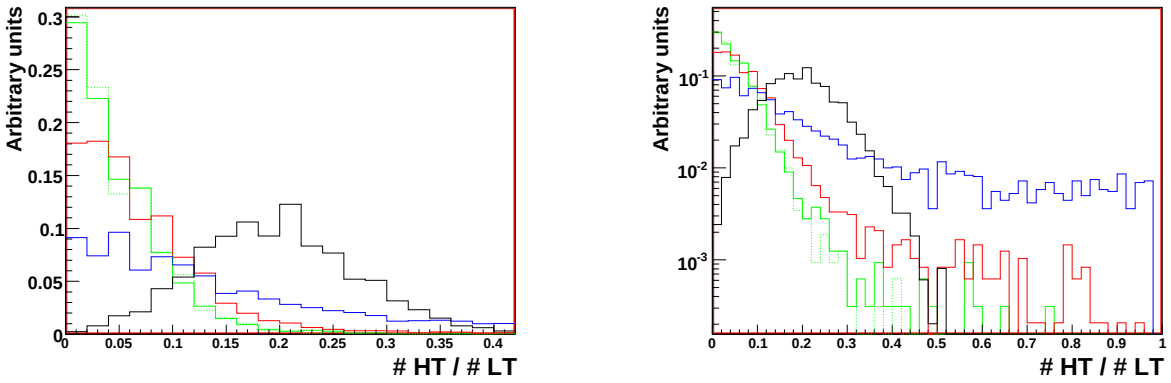

Figure 8.14: *Fraction of high-threshold over low-threshold hit distributions for a 100 GeV/c cut in p_t of the tracks. Line styles and colours are identical to figure 8.13.*

Jet Information

As the samples considered here are single-particle samples there are of course no jets to be found from the fragmentation of a gluino-production event. It is still of interest, though, to see whether the ATLAS jet clustering schemes identify jets from the interactions of R-hadrons with the calorimeters of ATLAS. This turned out not to be the case. The number of events with jets in them varied in the range 20 - 30 % for the different samples but no jet in any sample exceeded an energy of 110 GeV. This result was obtained using the k_t algorithm [BCCW03] on topological clusters with the distance parameter set to 0.4 which is one of the eight jet algorithm setups implemented as a standard in the ATLAS reconstruction software [Jet]. It did not vary discernibly when changing the jet algorithm or parameters within standard values.

From the above, one can conclude that since the very formation of two gluinos take up most of the available energy in a pair-production event, the occurrence of hard jets at the order of hundreds of GeV is a rare occurrence. This indicates that hard-jet activity may be used as a veto to filter out ordinary QCD events faking for instance an R-hadron changing sign between the Inner Detector and the muon system by track-mismatching.

8.2.2 R-hadron Specific Performance

Trigger Response

The events studied here are not full events and we are therefore excluded from making strong statements about the trigger efficiencies for signal events as a whole. We *can*, however, evaluate the trigger response to the R-hadron itself. As mentioned in section 8.1.3 previous studies found that the trigger should start to die out at R-hadron velocities below 0.7 c. Figure 8.15 shows the response of the 6 GeV/c Event Filter muon trigger called EF_mu6 for a variety of gluino massed as a function of β of the generated R-hadron. This trigger is a low-p_t muon trigger as defined in section 7.3.4. From the figure one observes an onset at $\beta \approx 0.5$ which is a bit lower than estimated by previous studies. These studies, however, did not include the full trigger simulation of ATLAS. One also observes how the matching requirement between the Inner Detector and the muon system kills off practically all R-

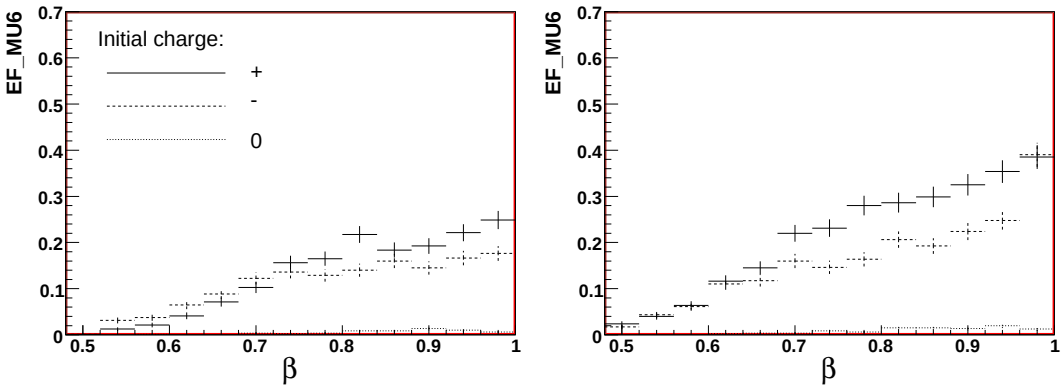

(a) $m_{\tilde{g}} = 100$ GeV/c^2 (b) $m_{\tilde{g}} = 600$ GeV/c^2

(c) $m_{\tilde{g}} = 1300$ GeV/c^2 (d) $m_{\tilde{g}} = 2000$ GeV/c^2

Figure 8.15: *EF_mu6 trigger efficiency as a function of the true velocity (β_{true}) for single-particle samples. The trigger is seen to effectively veto R-hadrons with no associated ID track.*

hadrons with neutral initial charge for this reason only charged initial states are considered for the remainder of this section. To understand the differences in trigger efficiencies between the masses we turn to the second level trigger. Figure 8.16 shows the L2_mu6 trigger. It

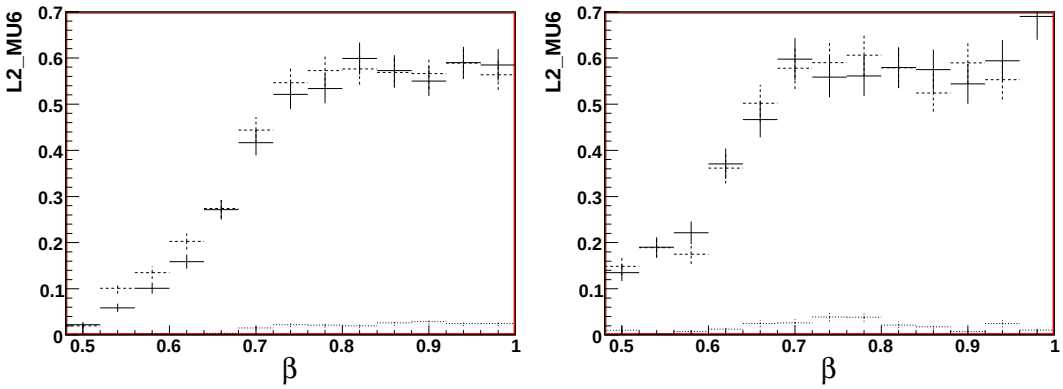

(a) $m_{\tilde{g}} = 100$ GeV/c^2 (b) $m_{\tilde{g}} = 2000$ GeV/c^2

Figure 8.16: *L2_mu6 trigger efficiency as a function of the true (β_{true}) for selected single-particle samples. The attenuation of the signal for the samples with initially neutral R-hadrons is also present at this trigger level.*

is seen that at this trigger level the trigger efficiency really appears to be a function of β that is universal for all masses and (non-zero) charges. To illustrate this, figure 8.17 shows a comparison of the L2_mu6 trigger efficiency for 100 GeV/c^2 and 2 TeV/c^2 R-hadrons started with opposite initial charge. The rise of the curve is seen to be slightly different while the plateau efficiencies are very similar.

For all samples the L2 trigger reaches a plateau efficiency of approximately 60% for $\beta \approx 0.7$. The efficiency on the plateau is understood by running a stand-alone simulation of a beam of gluino R-hadrons traversing an iron block. After a few hadronic interactions approximately 68% of the R-hadrons will be charged with no memory of the initial charge. Assuming the same percentage of charged R-hadrons in the ATLAS muon system this shows that a charged R-hadron arriving in time to the muon trigger stations will have a probability of approximately $60/68 \approx 0.88$ of passing the Level-2 trigger (We are here ignoring R-hadrons stopping in the detector). This behaviour is somewhat suppressed at the Event Filter stage. The plateau disappears and is replaced by a flattening out of the curve from around $\beta = 0.7$. Also the total efficiency drops. This is attributed to quality cuts applied to track fits at the Event Filter stage.

Figure 8.18 shows the muon trigger response parametrised in the true p_t of the generated R-hadron. There are indications of a plateau in the response curve with an onset around $p_t \approx m_{\tilde{g}}c$. This is a remnant of the plateau in the β-parametrisation, as $\beta_{\tilde{g}} \approx 0.7 \Rightarrow p_{\tilde{g}} = m_{\tilde{g}}c\beta\gamma \approx m_{\tilde{g}}c$. As the plateau onset rises with the mass there is obviously no hope to find a cut in p_t that will allow for a uniform trigger response for all masses. It would appear, though, that one can make severe cuts on the p_t of the muon track without affecting the signal for the higher masses. The trade-off in the analysis is now, to conserve enough of the low-mass signal while using the p_t cut to remove background.

A complete description of the trigger efficiency also includes the efficiency in varying parts of the detector. The sheer geometry of the detector has influence on the trigger for timing-

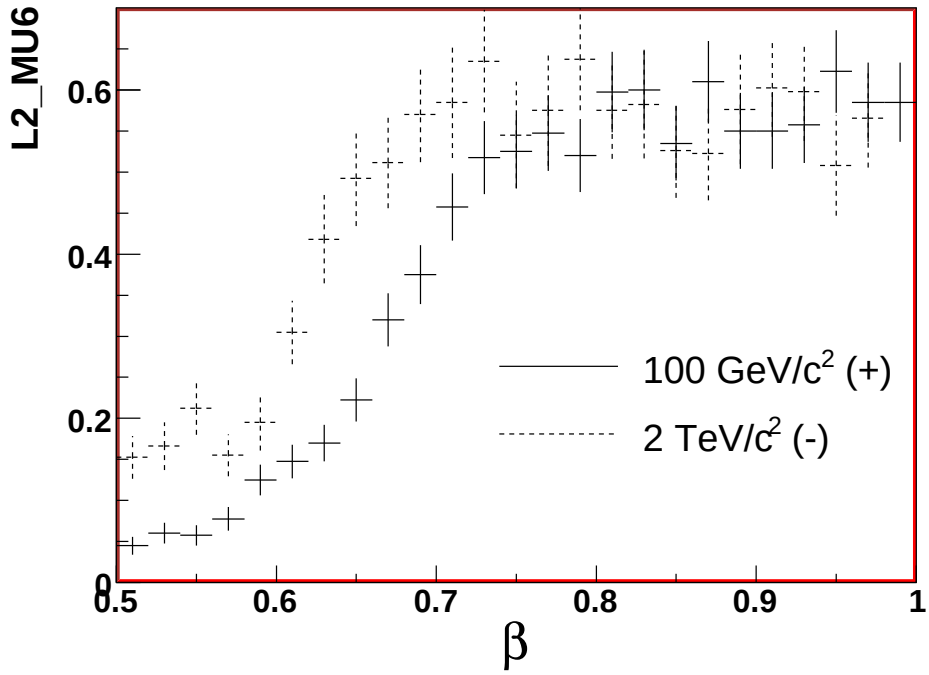

Figure 8.17: *A comparison of the L2 trigger response curve for initially positive R-hadrons with* $m_{\tilde{g}} = 100$ *GeV*$/c^2$ *and initially negative R-hadrons with* $m_{\tilde{g}} = 2$ *TeV*$/c^2$*. The onset is seen to be slightly different while the plateau efficiencies are very close.*

related reasons, while the amount of material traversed also is expected to play a role due to quality cuts made at the higher trigger levels. Hadronic interactions in the muon system might cause a muon track fit to fail leading to a rejection of the event. Figure 8.19 shows the trigger efficiency as a function of η and φ for 600 GeV/c^2 gluino hadrons with positive initial charge. These plots agree qualitatively with the muon trigger acceptance referred to in figure 7.22 although the statistical precision from those plots has not been replicated. One can identify the various support structures of the ATLAS detector in the left plot, while the right plot reveals the eight-fold azimuthal structure of ATLAS with dips in the trigger efficiency where the legs are placed.

Track Matching

When comparing tracks in the Inner Detector with tracks in the muon system it is imperative to have an understanding of how to correctly match them. To do this we consider the distance distribution in $R = \sqrt{\Delta\eta^2 + \Delta\phi^2}$ of hard Inner Detector tracks relative to hard muon tracks. A track is considered *hard* if it has a transverse momentum exceeding 200 GeV/c. As can be seen from figure 8.20 an adequate matching criterion may be set by requiring $R < 0.1$. Depending on the characteristics of the background and the underlying event in the signal events there may of course still be be advantages to tightening the matching cut.

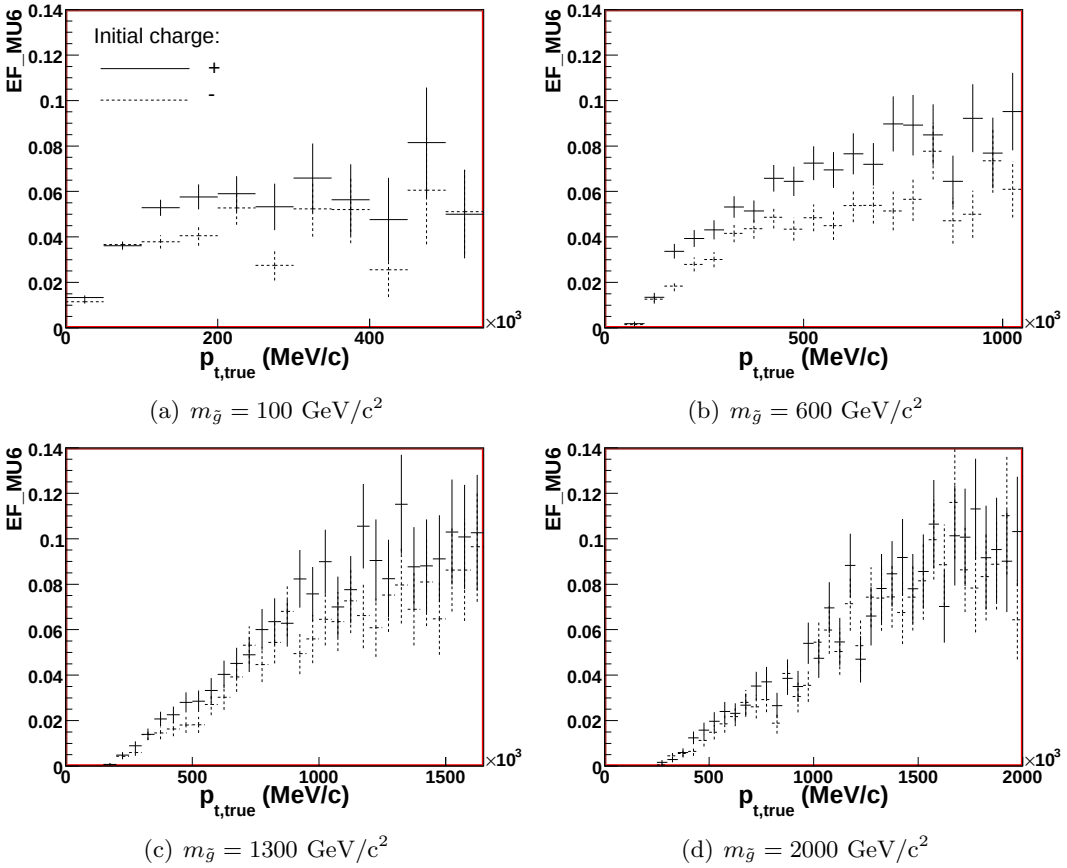

(a) $m_{\tilde{g}} = 100$ GeV/c^2

(b) $m_{\tilde{g}} = 600$ GeV/c^2

(c) $m_{\tilde{g}} = 1300$ GeV/c^2

(d) $m_{\tilde{g}} = 2000$ GeV/c^2

Figure 8.18: *EF_mu6 trigger response as a function of $p_{t,true}$ for single-particle samples.*

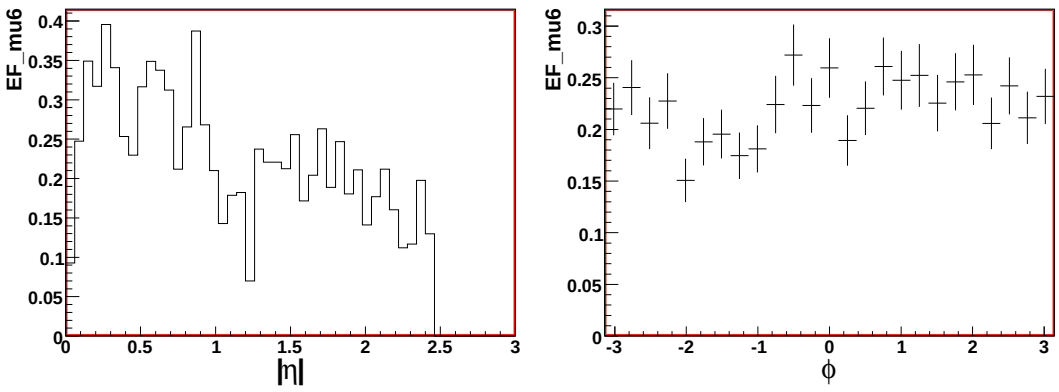

Figure 8.19: *EF_mu6 trigger response vs. η and φ for a gluino mass of 600 GeV/c^2. The same elements of the structure of the ATLAS detector are seen here as is the case in figure 7.22. Note that $\varphi \in [-\pi, \pi]$ here as opposed $\varphi \in [0, 2\pi]$ in figure 7.22.*

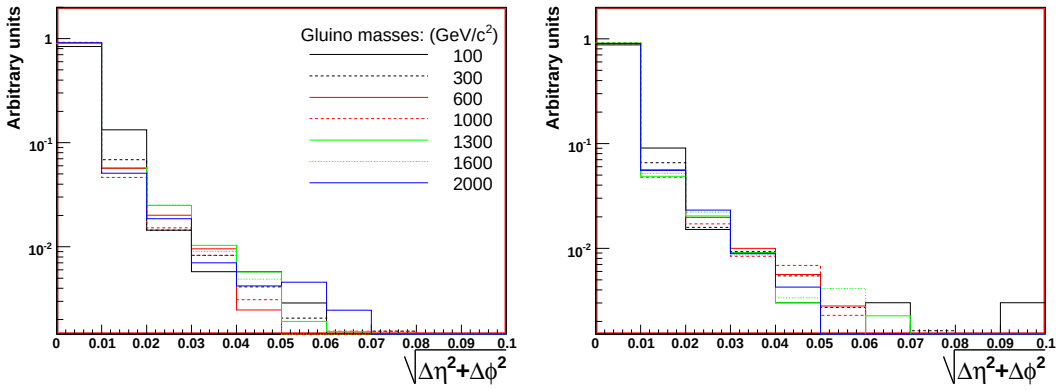

(a) R-hadrons started with a negative charge (b) R-hadrons started with a positive charge

Figure 8.20: $\sqrt{\Delta\eta^2 + \Delta\phi^2}$*-distribution of hard ID tracks relative to hard muon tracks. As we know the contents of the event to be limited to the R-hadron alone this provides information on the matching of ID tracks with muon tracks for R-hadrons.*

Charge Flipping

Having studied the resolutions in the different parts of the detector as well as the track matching it seems prudent to study whether the charge flipping of the R-hadrons is easily turned into cuts in measurable parameters. In figure 8.21 the Inner Detector transverse momentum ($p_t(ID)$) is compared to the muon system signed transverse momentum ($q_\mu p_t(\mu)$). The comparison is made for tracks with a transverse momentum larger than 200 GeV/c and a $R < 0.1$. To stay within the realm of the physically plausible at a 14 TeV centre-of-mass energy collider a cut has been made that both tracks have a transverse momentum *smaller* than 5 TeV/c. The parameter plotted in the figure is independent of the initial charge of the R-hadron and indeed it appears from 8.21(a) (R-hadrons with negative initial charge) and 8.21(b) (positive initial charge) that an R-hadron reaching the muon system has no "memory" of its initial charge. This is consistent with the observations made in section 7.2.2 on the typical number of nuclear interactions for R-hadrons in ATLAS. Furthermore we see from the figure that approximately half of the track matches found exhibit the charge flipping property. The coarse resolution evident in the high-mass plots stems from the fact that transverse momenta in the multi-TeV range are prevalent for these samples as per section 8.2. When considering full events the high p_t region is expected to be strongly suppressed.

8.3 Signal and Background Samples

The samples of full events generated for section 8.1 were also run through the ATLAS full chain of detector simulation, digitization and reconstruction with the same modifications as were used for the single-particle samples. Table 8.6 shows the signal samples used for analysis. To complement the signal samples various background samples were generated; each corresponding to an integrated luminosity of at least $\mathcal{O}(1\ \text{fb}^{-1})$. As the trigger used for this analysis will be a muon trigger, only types of background was considered that might give rise to a muon signal. The muon background was estimated in the technical design report of the ATLAS muon system [mTD] as shown in figure 8.22. As can be seen from the figure

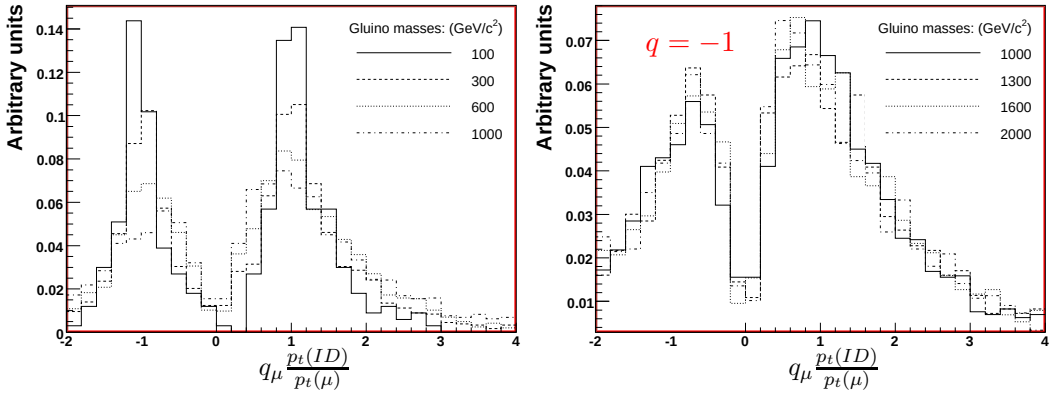

(a) Negative initial charge

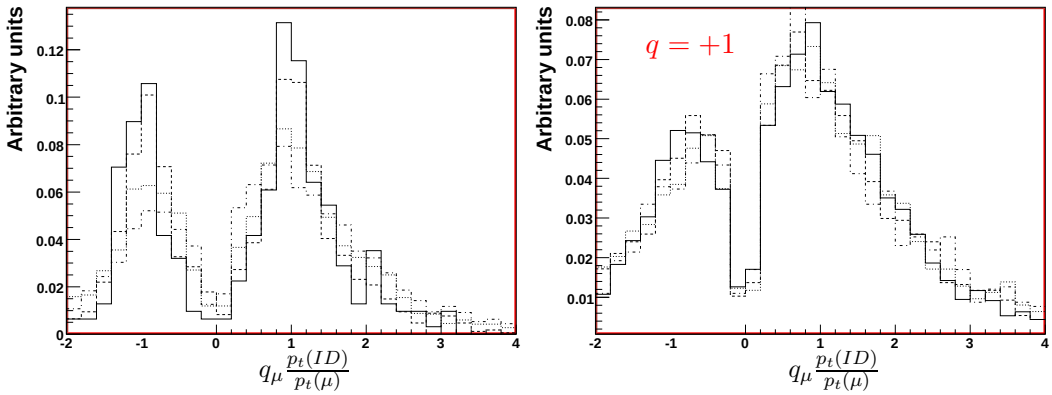

(b) Positive initial charge

Figure 8.21: $q_\mu \frac{p_t(ID)}{p_t(\mu)}$ *for different gluino masses.*

Gluino mass: (GeV/c^2)	**No. of Events:**	**$\mathcal{L}$ of sample: (fb^{-1})**
100	9890	1.89×10^{-4}
300	9810	3.65×10^{-2}
600	9880	2.04
1000	10000	72.5
1300	10000	610
1600	9900	4.67×10^{3}
2000	10000	4.35×10^{4}

Table 8.6: *Signal samples for analysis. Not all samples contain 10000 events due to software crashes.*

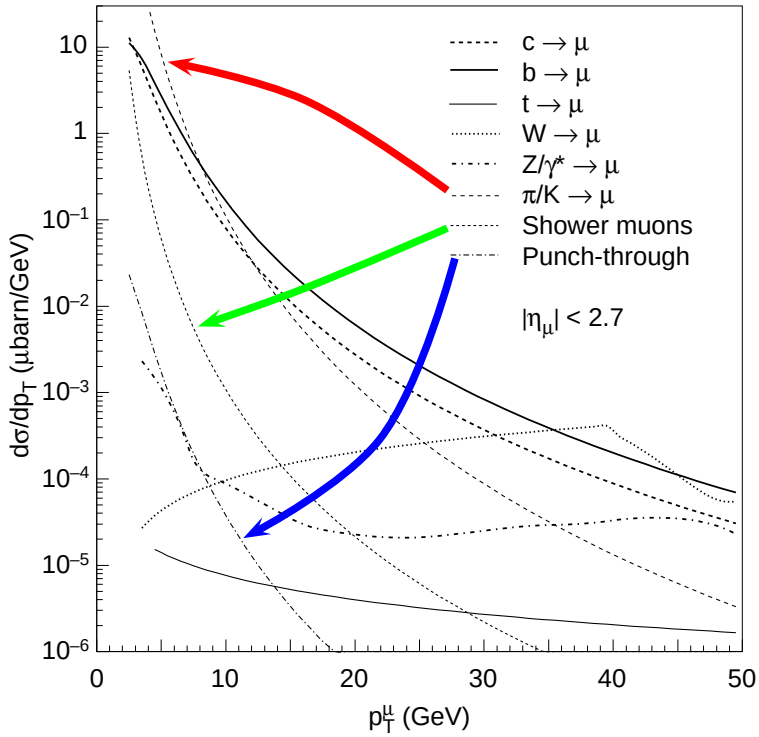

Figure 8.22: *Muon rates as estimated in [mTD]. The three highlighted contributions are not included in the background simulation.*

there are many sources of muon signals, some of which fall off with p_t more rapidly than others. Luckily the ones falling most rapidly (highlighted in the figure) are also the most CPU intensive to simulate. These are $\pi/\mathrm{K} \rightarrow \mu$, shower muons and punch-through particles. To keep down the requirements on CPU time in the simulation of background samples it was decided to ignore these three background sources and institute a generator level filter in the background generation demanding a muon with a transverse momentum in excess of 150 GeV/c at this stage. Figure 8.7 indicates a momentum resolution of approximately 3% corresponding 4.5 GeV/c at this transverse momentum, so it was at the same time decided to not consider reconstructed muons with $p_t < 200$ GeV/c in the analysis. The generator level filtering allowed to treat the following sources of muons with full simulation:

- $\mathrm{b} \rightarrow \mu$
- $\mathrm{c} \rightarrow \mu$
- $\mathrm{W/Z}/\gamma \rightarrow \mu$
- $\mathrm{t} \rightarrow \mu$

At $p_t > 200$ GeV/c figure 8.22 indicates that if the trends continue for higher transverse momenta, the three highlighted muon signal sources should be orders of magnitude below the sources considered. Applying the before-mentioned filter in the generation, samples were produced using the full chain of the ATLAS software. The background samples available for analysis are listed in table 8.7.

CSC no.	Sample	Gen. Events	Rec. Events	$\mathcal{L}(\text{fb}^{-1})$
	QCD: (PYTHIA)			
5013	J4 (140 GeV/c $< p_t <$ 280 GeV/c)	3.125×10^8	2572	0.98
5014	J5 (280 GeV/c $< p_t <$ 560 GeV/c)	2.5×10^7	4800	1.12
5015	J6 (560 GeV/c $< p_t <$ 1120 GeV/c)	3.5×10^5	738	1.01
5016	J7 (1120 GeV/c $< p_t <$ 2240 GeV/c)	5×10^4	241	9.46
5017	J8 (2240 GeV/c $< p_t$	1×10^4	42	442.29
	Di-boson: (HERWIG)			
5985	ZZ	2.5×10^4	53	9.82
5986	WW	2×10^4	50	1.21
5987	WZ	1.5×10^4	29	2.32
	Single-boson: (PYTHIA)			
5105	$Z \to \mu\mu$	1.3×10^4	600	1.29
5106	$Z \to \tau\tau$	3×10^3	108	9.94
5145	$W \to \mu\nu$	3×10^4	600	0.94
5146	$W \to \tau\nu$	3×10^4	120	7.82
5200	$t\bar{t}$: (MC@NLO)	1×10^6	4065.08	0.98

Table 8.7: *Background samples for analysis. The column listing the number of generated events use unweighted events while the reconstructed events are counted with weights.*

A few comments need to be made on the samples listed and generators used. A central concept in the background generation has been to use standard ATLAS samples as templates for event generation. The samples shown in table 8.7 rely on the standard sample definitions (so-called CSC definitions) defined by the numbers in the left column. Some sample definitions have been modified to impose a hardness cut on the matrix element. The decision to use the ATLAS standard setups for these samples has the consequence that not all background samples were made with the same Monte Carlo generator. The generators used were PYTHIA [Sjo94], HERWIG [C$^+$01] and MC@NLO [FW02].

The $t\bar{t}$ sample especially needs a few comments. The sample is described in detail in [VvV07]. The generator used, called MC@NLO calculates the hard process at next-to leading order (as per the name of the generator). It then relies on HERWIG to generate the actual event. Events in MC@NLO are weighted and negative weights occur in 13.4% of all events. When referring to the sample in this thesis the numbers used will be *weighted* numbers. For instance the actual number of unweighted events reconstructed were 5314, but adding up the event weights yielded the number shown in table 8.7. Herein lies the explanation for the fractional event counts that are common with this generator.

Chapter 9

Event Selection and triggers

In this chapter an event selection will be presented based on the preceding chapters. The trigger efficiency will be evaluated on the signal samples using the ATLAS trigger simulation. The different R-hadron event topologies will be explored, compared to background and combined.

9.1 Triggers

When choosing a trigger strategy for an R-hadron study several approaches can be considered. Indeed in a situation where the discovery *has* been made, dedicated triggers might conceivably be developed utilising the event topologies of R-hadron events. For now, however, we are relegated to triggering on the R-hadron itself. For this reason this analysis has chosen to rely on the muon trigger. Specifically the EF_mu6 trigger that was also studied in section 8.2.2 has been used for this analysis.

Table 9.1 shows the trigger efficiency and the expected trigger rates per fb^{-1} for the generated samples of R-hadrons. One notices that these efficiencies are considerably smaller than the

$m_{\tilde{g}}$ (GeV/c^2)	L2_mu6 eff.	EF_mu6 Eff.	L2_mu6 per fb^{-1}	EF_mu6 per fb^{-1}
100	0.32	0.11	1.7×10^7	5.7×10^6
300	0.36	0.14	9.7×10^4	3.9×10^4
600	0.35	0.16	1.7×10^4	7.7×10^3
1000	0.32	0.17	44	23
1300	0.29	0.16	4.8	2.6
1600	0.27	0.15	0.57	0.31
2000	0.23	0.12	0.052	0.028

Table 9.1: *Trigger efficiencies and rates for signal samples.*

"visible" numbers quoted in table 8.2. Also it is noted that the naïve notion that the fraction of visible events should diminish as strongly as indicated in table 8.2 is not true. There *is* a variation but it is a lot smaller. The variation of the L2 trigger is understood as the effect of the decreasing mean velocity of the R-hadrons with increasing mass. The EF trigger is more

complex as it is a convolution of the L2 efficiency with the evolution of track fit quality with increasing mass.

Sample	L2_mu6 eff.	EF_mu6 Eff.	L2_mu6 per fb^{-1}	EF_mu6 per fb^{-1}
J4	0.85	0.72	2.2×10^3	1.9×10^3
J5	0.86	0.72	3.7×10^3	3.1×10^3
J6	0.86	0.64	6.3×10^2	4.6×10^2
J7	0.87	0.60	22	15
J8	0.86	0.50	0.081	0.048
$Z \to \mu\mu$	0.93	0.90	4.3×10^2	4.2×10^2
$W \to \mu\nu$	0.78	0.74	5.0×10^2	4.7×10^2
$Z \to \tau\tau$	0.77	0.73	8.3	7.8
$W \to \tau\nu$	0.78	0.74	12	11
WW	0.76	0.74	31	31
WZ	0.83	0.79	10	9.9
ZZ	0.92	0.92	5.0	5.0
$t\bar{t}$	0.83	0.79	3.4×10^3	3.3×10^3

Table 9.2: *Trigger efficiencies and rates for background samples.*

In preparation for the analysis we consider table 9.2. Note that the samples are named according to the shorthand convention adopted in table 8.7. It is seen that QCD including $t\bar{t}$ contributes with quite a large number of muons due to the large total cross section. Also Z and W events are expected to be prime sources of background.

9.2 A Cursory Look

Section 8.2 helped quantify which cuts might be effective in isolating the R-hadron objects. To develop an event selection, however, we have to take a deeper look at the full events for both signal and background. A sensible starting point is to take a look at an event display. Figure 9.1 shows a gluino pair-production event in ATLAS. The two top views have no cuts applied. There is some soft activity in the Inner Detector and the calorimeters. Also there are back-to-back signals in the muon chambers. Applying a 10 GeV/c track cut to the event shows only one ID track in the event. This track links with the signals in the calorimeters and in the muon chambers. On the opposite side there is a signal in the calorimeter and a muon track with no associated Inner Detector track. Given complete trust in the reconstruction software this is thus a very R-hadron-like event. The immediate lesson drawn from this is that it seems a reasonable strategy to apply some hardness cuts to the track activity and then look for the different possible topologies.

9.2.1 Transverse Momentum Cut

All events at the LHC (will) have an underlying event containing a lot of soft tracks. These we naturally wish to cut away from the signal samples to facilitate the study of the R-hadron themselves. Also it is apparent from figure 8.4 and section 8.2.2 that we expect triggered R-hadrons to have very high transverse momenta allowing us to obtain a very high purity of

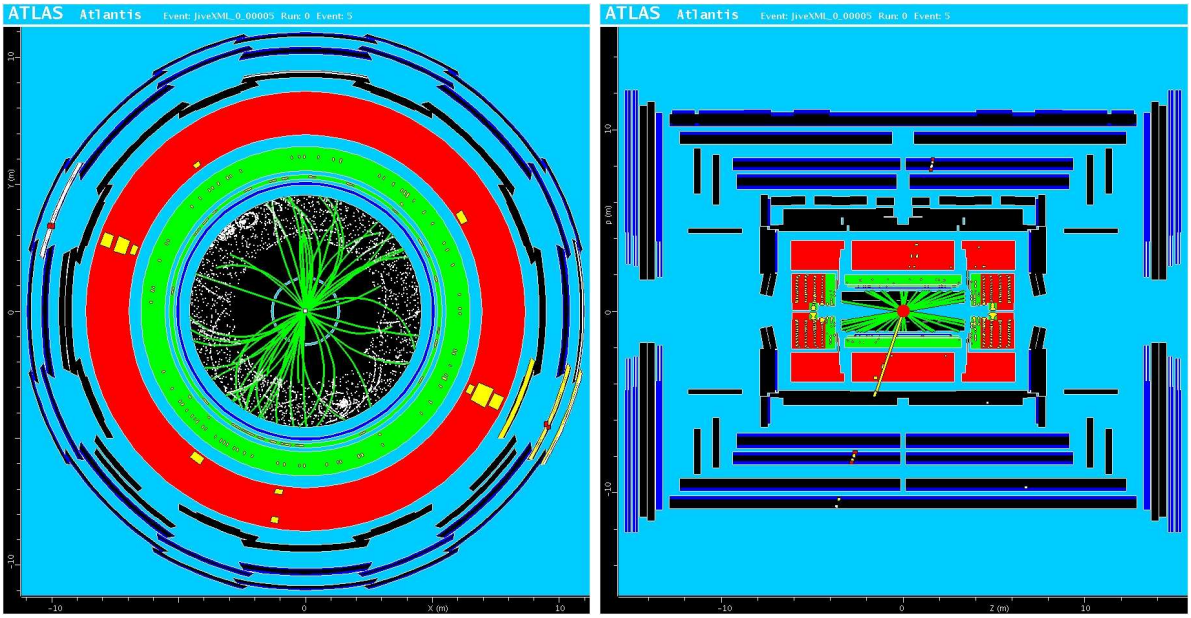

(a) No cuts applied

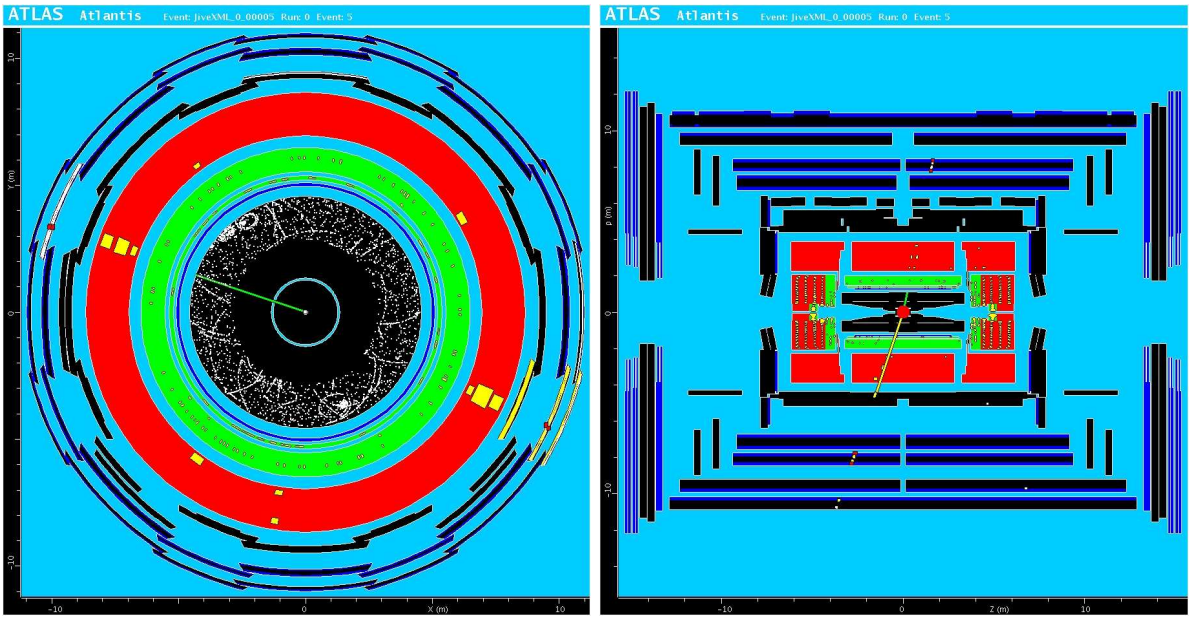

(b) 10 GeV/c track cut applied

Figure 9.1: *An event display of a gluino pair-production event.*

our event selection simply by putting in a cut on the transverse momentum of the objects studied.

Figure 9.2 shows a comparison of the p_t spectra for the signal samples for all events passing the EF_mu6 trigger. A cut-off is made at $p_t = 50$ GeV/c to eliminate the worst of the soft tracks.

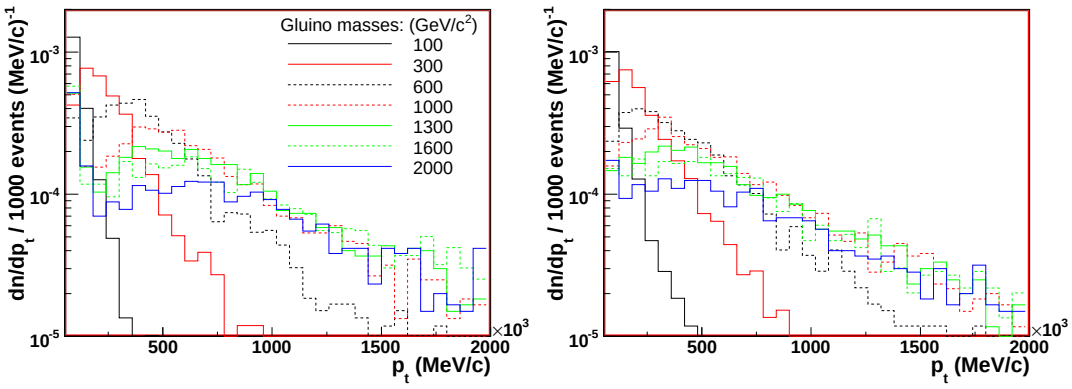

(a) Inner Detector tracks (b) Muon tracks

Figure 9.2: *p_t spectrum for signal samples.*

As mentioned previously the background samples have all been generated using heavy filtering at the matrix element stage. It is therefore not a simple task to renormalise the spectra in the same way as was done for the signal samples. Furthermore there are expected to be large differences in the absolute scale of the distributions. Figure 9.3 shows the p_t spectra for the individual background samples of ID tracks passing the EF_mu6 trigger while figure 9.4 shows the muon track spectra. The spectra are shown in arbitrary units. The reader is reminded that the background samples have been filtered at generator level for a muon with a transverse momentum of at least 150 GeV/c. For this reasons the numbers are *not* representative for the entire cross section for the processes listed. They *do*, however, provide an estimate of the possible signal-to-background ratios in the triggered samples given a cut on the transverse momentum of muon tracks.

The immediate observation is that there is nearly no background present containing muons with p_t above 500 GeV/c. A comparison with figure 9.2, however, shows that putting a p_t-cut that high would have severe consequences on the low-mass signal. As the cross section at low mass is very high and the benefit on the background rejection is large, a central part of the analysis will be establish the optimal value of the p_t-cut on the muons in order to maximise the significance over a large mass range.

Considering again the signal events, we know that we expect no more than two hard muon tracks for a suitable definition of "hard". Figure 9.5 shows the effect of p_t-cut in this context. From the figure and from figure 9.2, it is observed how a cut on p_t of 200 GeV/c (considerable lower than discussed above) creates the situation in which we are interested. All signal samples contribute (although the low mass samples are severely attenuated), and the signal events reduce to a few hard muon tracks that we can then study for R-hadron signatures.

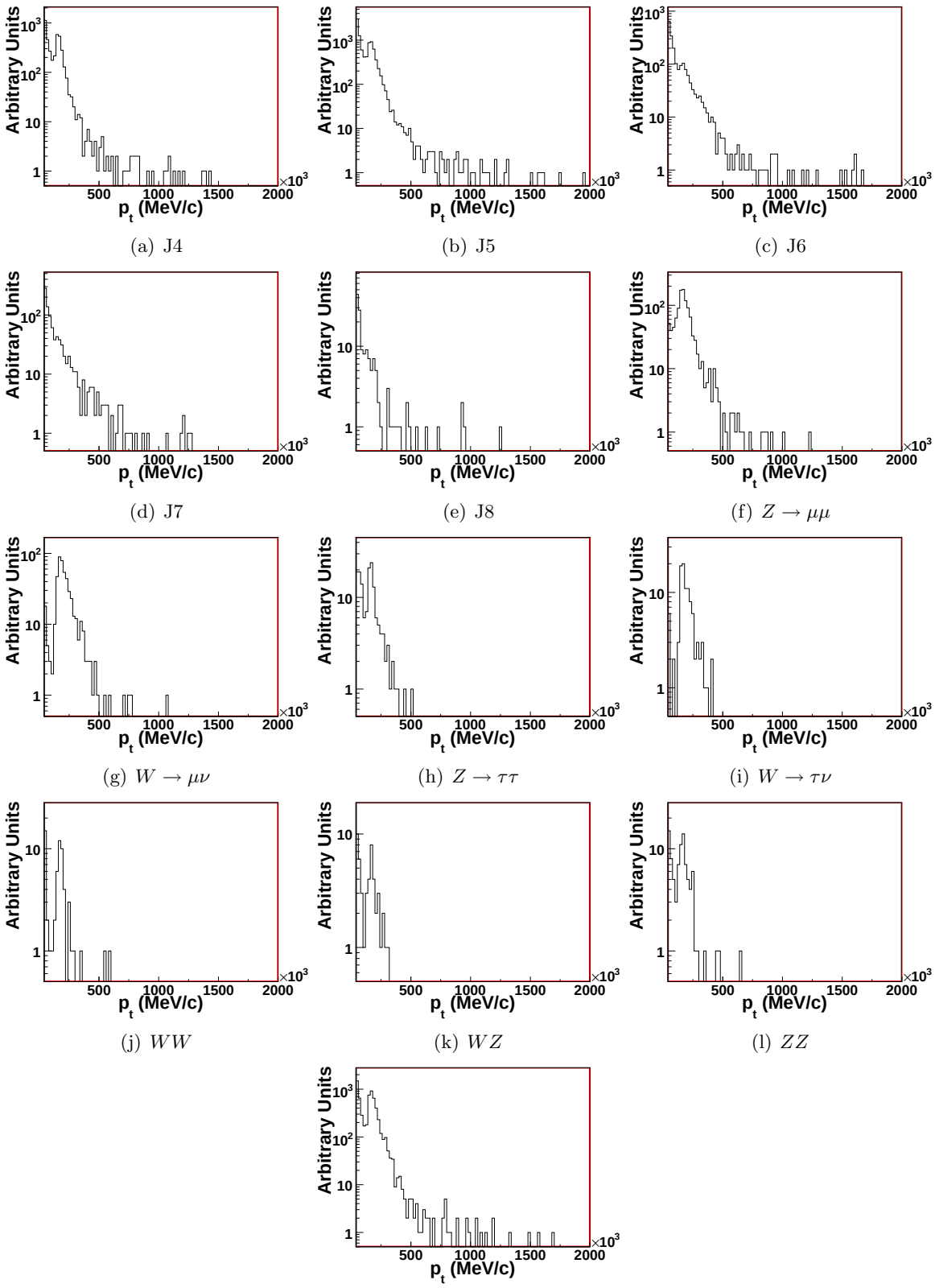

(a) J4 (b) J5 (c) J6

(d) J7 (e) J8 (f) $Z \to \mu\mu$

(g) $W \to \mu\nu$ (h) $Z \to \tau\tau$ (i) $W \to \tau\nu$

(j) WW (k) WZ (l) ZZ

(m) $t\bar{t}$

Figure 9.3: *p_t spectra for ID tracks in background samples.*

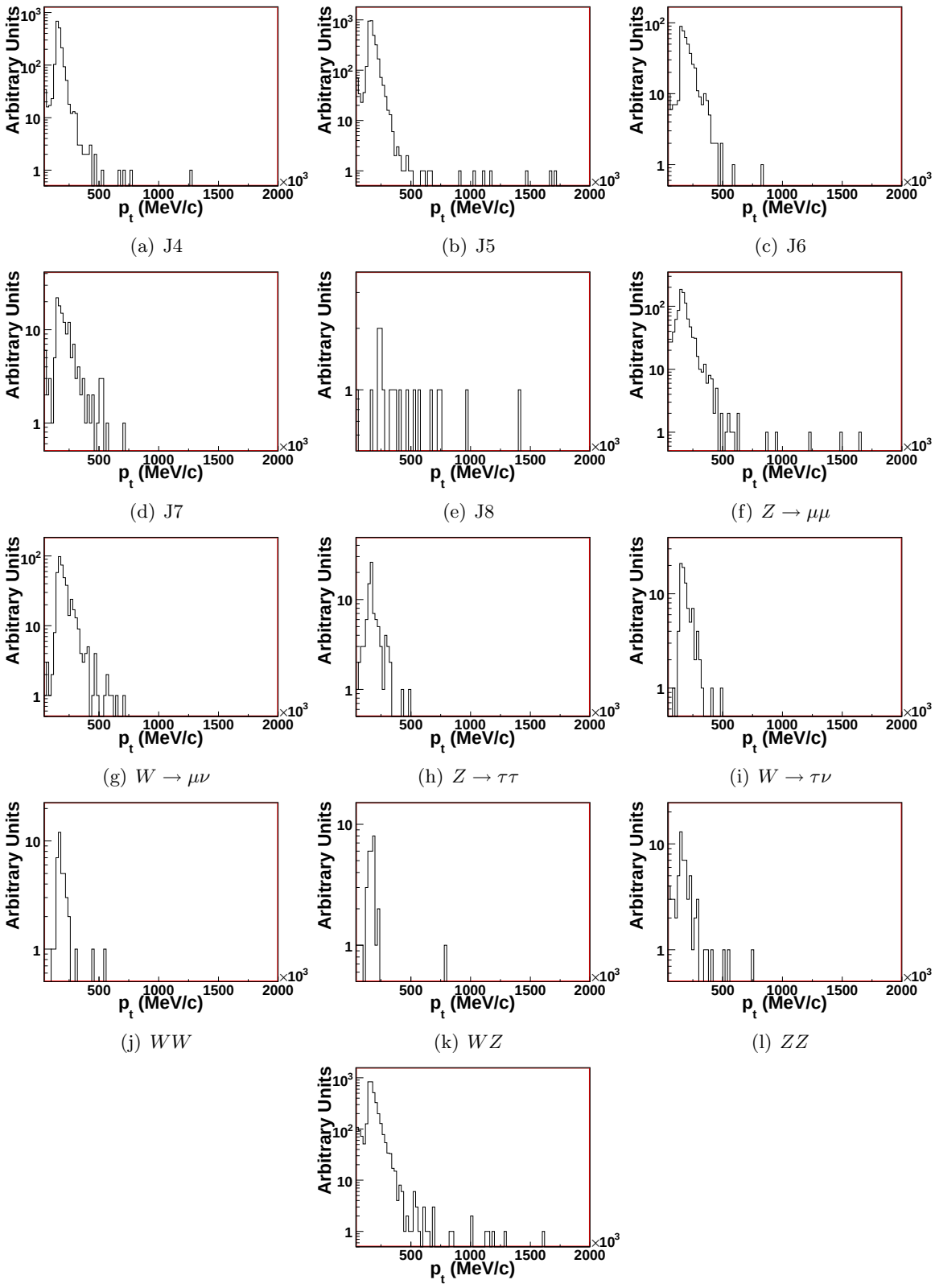

(a) J4 (b) J5 (c) J6

(d) J7 (e) J8 (f) $Z \to \mu\mu$

(g) $W \to \mu\nu$ (h) $Z \to \tau\tau$ (i) $W \to \tau\nu$

(j) WW (k) WZ (l) ZZ

(m) $t\bar{t}$

Figure 9.4: *p_t spectra for muon tracks in background samples.*

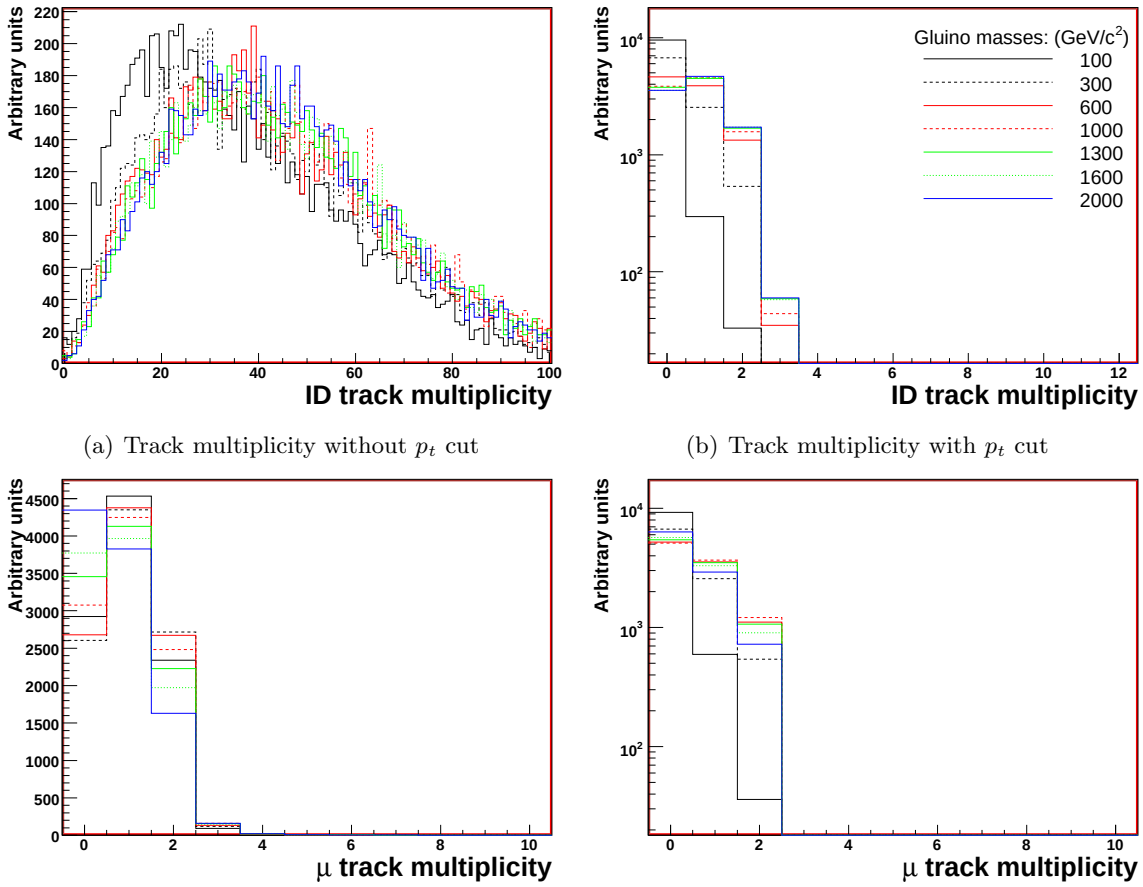

(a) Track multiplicity without p_t cut

(b) Track multiplicity with p_t cut

(c) Muon track multiplicity without p_t cut

(d) Muon track multiplicity with p_t cut

Figure 9.5: *Charged multiplicity in the Inner Detector and the muon system with and without a cut in p_t of 200 GeV/c.*

9.2.2 Link Properties of Hard Muon Tracks.

We have now established that the presence of a hard muon track in an event will be a prerequisite for any further event selection. To look for R-hadron behaviour we now study the following for signal and background samples alike:

- What is the probability for a hard muon track to have no ID link? This specific signature will be somewhat suppressed by the trigger as demonstrated in section 8.2.2 as an R-hadron with no ID track *cannot* trigger the event. The trigger object will therefore in most cases be the other R-hadron.
- What is the probability for a hard muon track to be linked to an Inner Detector track of same or opposite charge? Track matches with opposite charge are expected to be a prime signal source for gluino R-hadrons.
- What is the probability that a hard muons track matches ID tracks of both charges?

With respect to these items we may express the relevant probabilities as a function of the p_t-cut for the muons. Figure 9.6 shows these parametrisations for events passing the trigger. Due to the p_t spectra shown in figure 9.2, the 100 GeV/c^2 point has been excluded. The plot

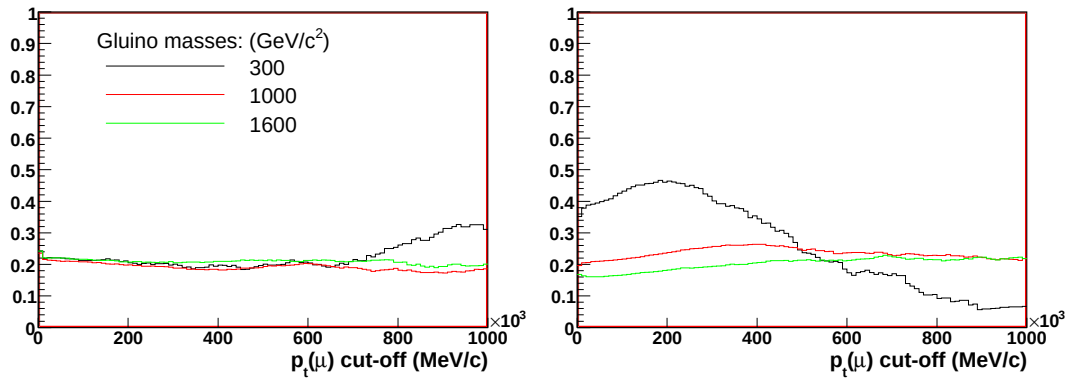

(a) No link (b) Same-sign link

(c) Opposite-sign link (d) Two sign matches

Figure 9.6: *Link probabilities for muon tracks in signal events as a function of the p_t cut on the muon track. No p_t cut is applied on the ID track.*

in figure 9.6(a) is the probability that a muon track above the given threshold does not have an ID link within an R-cone of 0.1. No p_t-cut is applied on the ID track.

Figures 9.6(b) and 9.6(c) are the probabilities for an above-threshold muon track to have an R-matching ID track with the same or opposite charge respectively. The ID track is required to be in a $p_t$window of 0.5 $p_t(\mu) - 1.5$ $p_t(\mu)$.

To evaluate if there is contamination from the rest of the event taking place figure 9.6(d) summarises the probability that a muon track has tracks of both signs matching. This is expected to fall off rapidly with the p_t-cut and indeed one may safely assume that the track matching is unique for muon tracks with a transverse momentum above 150 GeV/c.

Making plots in analogy to figure 9.6 for background is not as easily accomplished. Figure 9.7 tries to summarise the available information. Figures 9.7(a) to 9.7(d) represent the QCD samples samples as defined in table 8.7 while figures 9.7(e) to 9.7(h) represent electroweak samples. As there are many samples the plot axes have not been kept identical. The p_t range has been allowed to vary. Also the probability scale has been set logarithmic to maintain an overview of the many samples spanning several orders of magnitude in some of the plots. Where graphs appear to be missing (e.g. 9.7(e), 9.7(g), 9.7(h)) the samples in question simply do not contribute.

Little quantitative information can be extracted from plots of this complexity. The primary point of these plots is to give a visual indication of where sensible thresholds might be applied in analysis. A couple of observations *can* be made from this figure, though.

- Muon tracks at very high p_t are not very common among the Standard Model processes. Many of the plots shown here exhibit peculiar jumps due to very low statistics.
- The QCD samples are inherently jet-rich and muons in these samples are liable to be found within a jet. This fact is immediately apparent in figure 9.7(d) that shows a high probability for several tracks to match the same muon track. We thus see directly here, how a jet veto is going to be an important factor in suppressing noise.
- Muon tracks have a very high probability of being matched with an ID track of the same charge (figures 9.7(b) + 9.7(f)) as well they should given the fact that they most likely are muons.
- Mismatching of charge is at the percent level for the $Z \rightarrow \mu\mu$ sample. The only reason that the p_t cut remedies this is that the cross section itself dies out.

9.2.3 #HT/#LT Distributions

As was noted in section 8.2.1 there is a possibility that the TRT high-threshold information may be used to discriminate between signal and background. We therefore turn to the distributions of #HT/#LT for all Inner Detector tracks with a transverse momentum exceeding 200 GeV/c for all triggered events. Figure 9.8 shows the distributions for all signal samples. At this transverse momentum there is little of the 100 GeV/c^2 signal that contributes with any information as would be expected from figure 9.2(b). The other samples are seen to have their bulk below a fraction of 0.2. The background samples are checked in two groups as shown in figure 9.9.

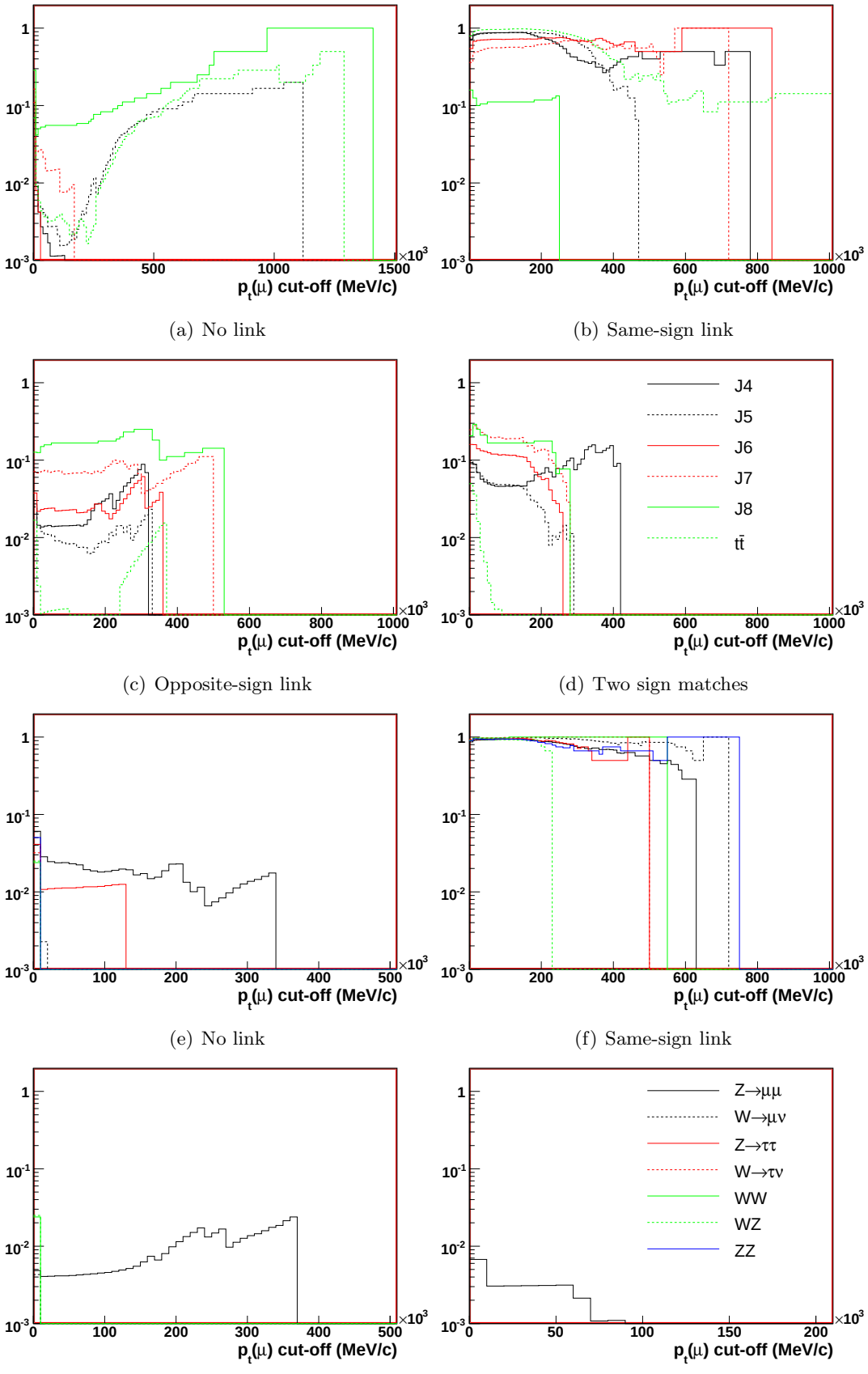

(a) No link (b) Same-sign link

(c) Opposite-sign link (d) Two sign matches

(e) No link (f) Same-sign link

(g) Opposite-sign link (h) Two sign matches

Figure 9.7: *Link probabilities for muon tracks in the background samples. The probabilities are expressed as a function of the p_t cut applied to the muon tracks. No p_t cut is applied to the ID tracks. Note that the p_t axis does not cover the same range in all plots.*

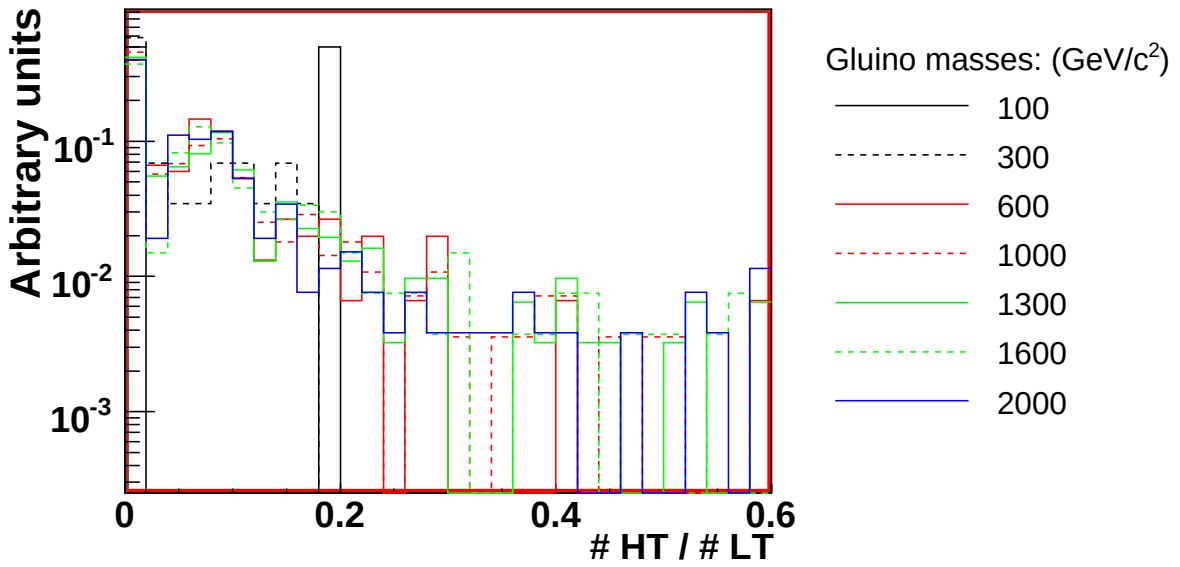

Figure 9.8: *Number of high-threshold hits divided by number of low-threshold hits at a p_t cut of 200 GeV/c for signal samples. The distributions are seen to have their bulk below 0.2.*

As is already known from figure 9.3 there are few background tracks surviving a 200 GeV/c cut on p_t so the statistics are necessarily low in these plots. One does notice, however, that the bulk of practically all the background is above a fraction of 0.1. It thus appears that there is basis for either a selection or a rejection criterion based on the TRT-high-threshold information.

9.2.4 Jet Information

We now move focus away from the R-hadrons themselves and consider the rest of the elements in the event. Sections 8.2.1 and 9.2.2 high-lighted the potential gain by applying a veto on jet activity. The origin of this gain is apparent from the fact that the sheer mass of the R-hadron uses up most of the available energy in events passing the trigger. There is very little probability for any hard jets to form in the event. High p_t QCD samples on the other hand will most likely produce large numbers of highly energetic hadrons that will lead to high-energy jets. To check this naïve assumption we consider figure 9.10. The distributions have all been normalised to unity as it is the distributions that are of interest and not their absolute scales. It is seen that the average number of jets in the QCD events including $t\bar{t}$ is slightly higher than for the signal samples although the statistics in the high p_t QCD sample (J8) is low. The jet energy distributions also show a larger fraction of high-energy jets for the QCD samples (this time excluding $t\bar{t}$). It does appear, however, that an effective jet veto will have to rely on more event information than simply the presence of high-energy jets in the event. To study this in detail distributions were studied of distances in η, φ and $R = \sqrt{\Delta\eta^2 + \Delta\varphi^2}$ for hard jets relative to hard muon tracks. A hard jet and muon in this case was set to have a transverse momentum in excess of 200 GeV/c.

Figure 9.11 depicts these distributions for a selection of signal samples while 9.12 shows them for a selection of background samples compared to one signal sample. As the aim is to develop

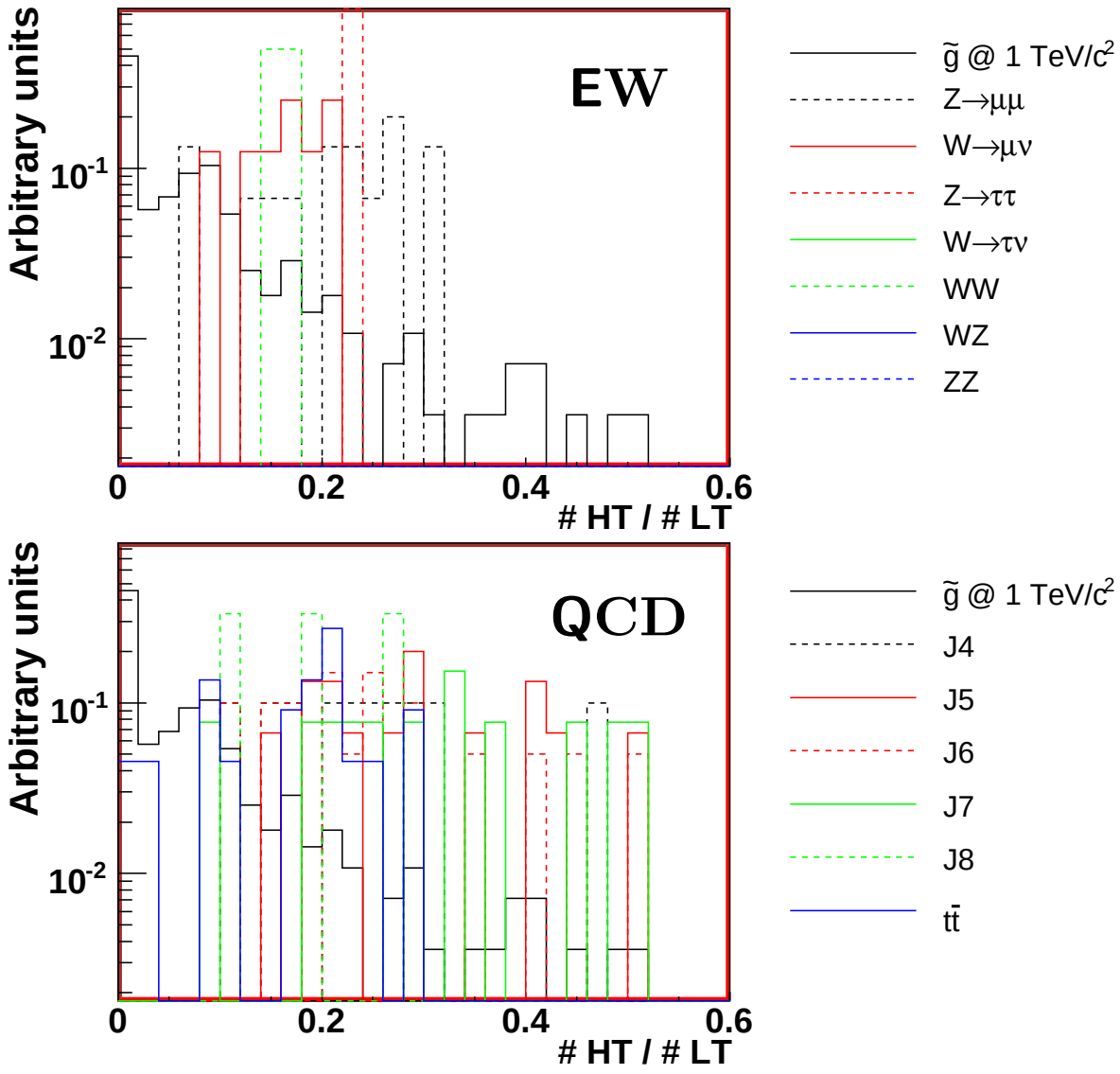

Figure 9.9: *Number of high-threshold hits divided by number of low-threshold hits at a p_t cut of 200 GeV/c. The background samples are compared to the 1 TeV/c^2 SSUSY sample for reference. The background distributions (excluding $t\bar{t}$) appear to have their bulk above 0.1.*

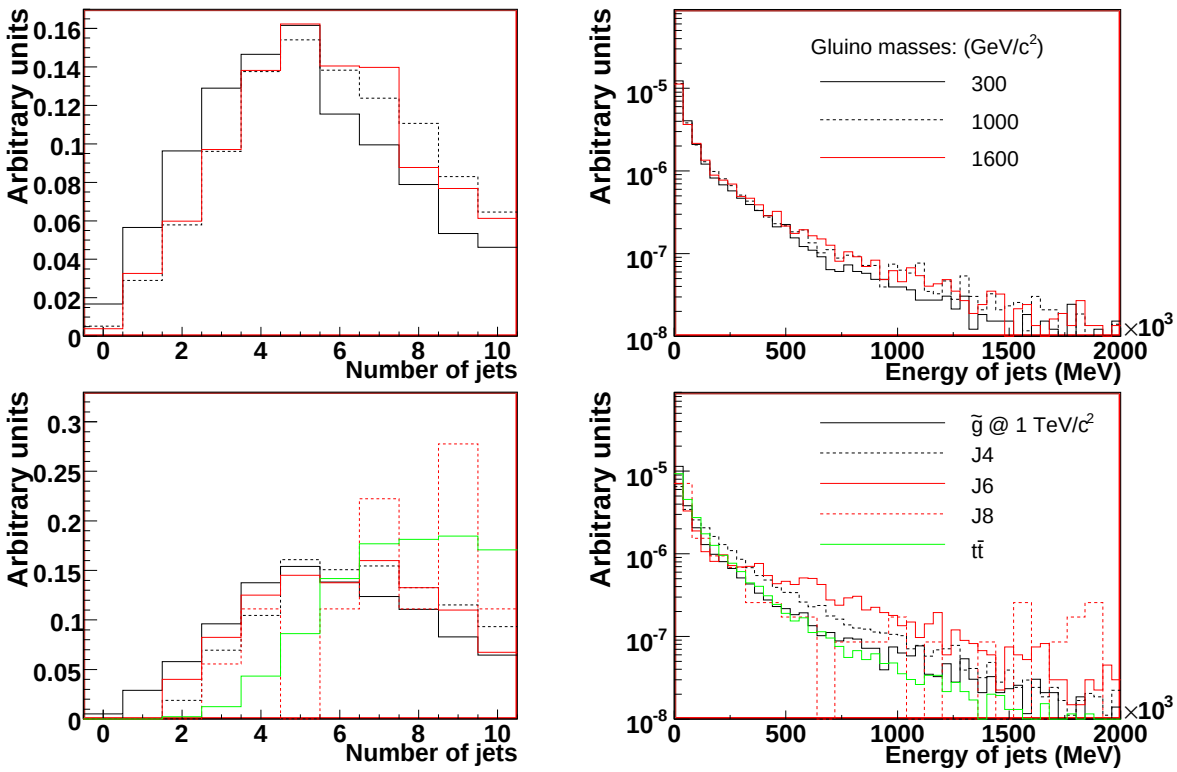

Figure 9.10: *Jet distributions for signal and QCD events passing the trigger. The background events are compared to the 1 TeV/c^2 gluino case.*

a jet veto, QCD samples including $t\bar{t}$ have been selected for study. The figures show that

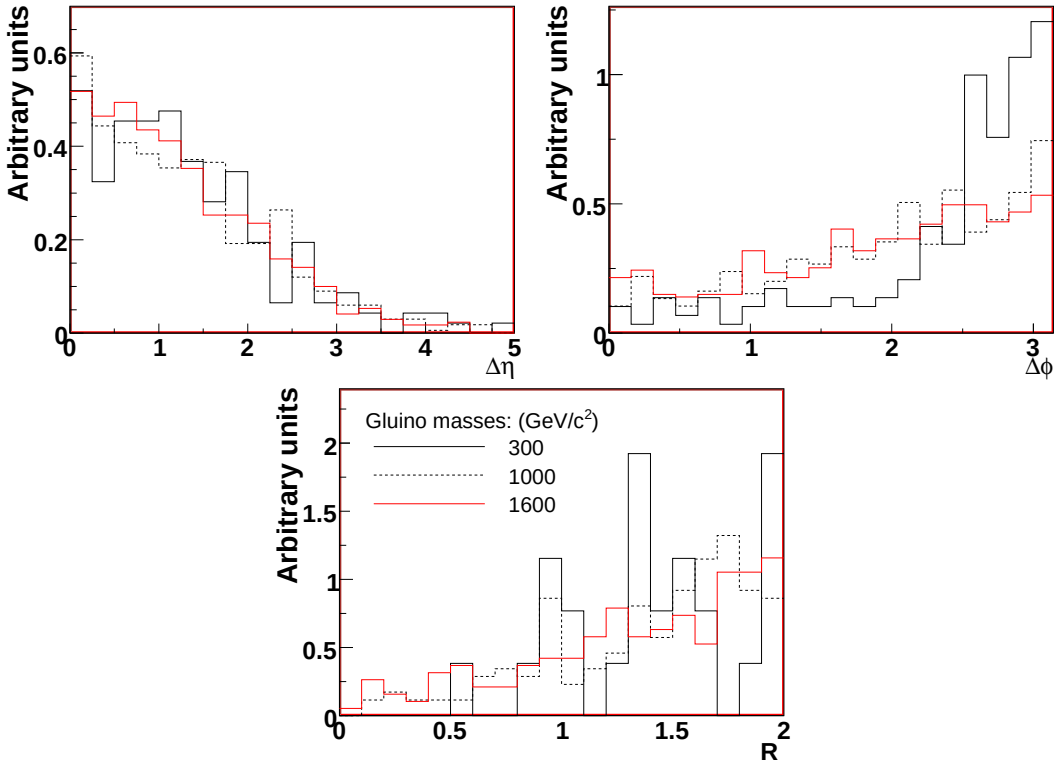

Figure 9.11: *Distance distributions between hard jets and hard muon tracks for signal samples. The distances are parametrised in η, φ and R.*

as expected many background muons are affiliated with a jet in contrast to the situation for signal samples for which a distance of R smaller than ~ 0.5 is rare. It thus seems sensible to use a jet veto on the proximity of hard jets to candidate muon tracks in the final event selection.

9.3 An Example Event Selection

The present analysis has in its aim to scan a wide part of parameter space for the gluino phenomenology. In order to do this the results of the preceding sections will be used to motivate an event selection. This event selection will then be evaluated in terms of signal significance at different integrated luminosities. When the methods are thus established the cuts will be optimised by scanning the cut parameters and maximising the signal significance.

In the following description of the selection criteria a *hard* track/jet has a transverse momentum larger than 200 GeV/c. A track *match* or *link* is characterised by an R-distance smaller than 0.1. For two objects to be *back-to-back* they are required to have $\cos\Delta\varphi < -0.9$.

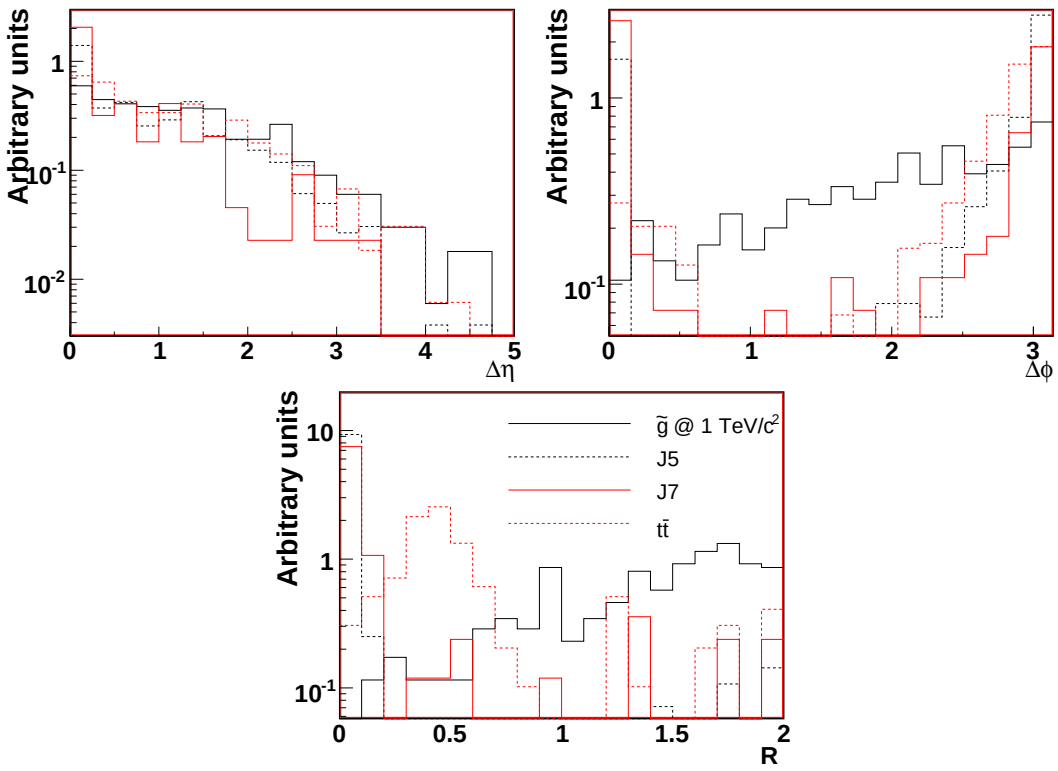

Figure 9.12: *Distance distributions between hard jets and hard muon tracks for background samples compared to the 1 TeV/c^2 gluino case. The distances are parametrised in η, φ and R.*

The selection criteria are as follows:

- The event passes the EF_mu6 trigger.
- No hard muon track has a hard jet closer than $R = 0.5$.
- One or more of the following conditions should be met:

  I The event contains at least one hard muon track with no Inner Detector link.

  II The event contains at least one hard muon track with a hard matching Inner Detector track of opposite charge fulfilling the condition $p_{t,Trk} > 0.5\ p_{t,\mu}$.

  III The event contains at least one hard muon track with a hard ID track with TRT hits and a #HT/#LT fraction smaller than 0.1. The track must either be a link or be back-to-back with the muon track.

  IV The event contains two hard back-to-back ID tracks with TRT hits and #HT/#LT fractions smaller than 0.1.

  V The event contains two back-to-back like sign muon tracks.

These cuts are with near absolute certainty not optimal in terms of signal significance but this will be investigated throughout the remainder of this chapter. Some cuts might have to be loosened or tightened and some selection criteria might have to be abandoned all together due to background contamination. As an ansatz, though, this set of selection criteria combines all our knowledge of the signal and the background samples respectively.

The trigger rates have been discussed previously in section 9.1, specifically tables 9.1 and 9.2. Selection efficiencies for the different parts of the event selection outlined above will be evaluated using events passing the trigger. Table 9.3 shows the individual selections separately and combined with the jet veto. Comparing these numbers to those in table 9.1 (p. 114) it is

Sample	I	II	III	IV	V	Combined + Veto	per fb^{-1}
100	28	7	7	0	8	38	2.0×10^5
300	207	106	100	4	92	384	1.1×10^4
600	319	306	302	26	193	790	3.9×10^3
1000	398	490	390	37	253	1028	14
1300	379	419	411	40	271	959	1.6
1600	346	439	386	44	221	893	0.19
2000	256	366	396	65	167	778	0.018

Table 9.3: *Selection rates for the example event selection on the signal samples. The selection channels are listed in individual columns. The* "Combined + Veto" *column counts events where one or more of the conditions I-V are fulfilled and applies the jet veto.*

observed that a fair percentage of the triggered events are selected. As expected most of the 100 GeV/c^2 signal is killed by the p_t-cut made. However, not much needs to pass the selection

criteria for the high cross section to save the signal. In particular the selection efficiency is consistently above 50% for the four highest masses.

Using the same numbers for the background samples one gets the numbers in table 9.4. One

Sample	I	II	III	IV	V	Combined + Veto	per fb^{-1}
J4	1	11	7	1	0	6	6.1
J5	3	16	39	1	0	31	28
J6	0	11	10	3	0	2	2.0
J7	0	11	3	0	1	0	0.00
J8	1	4	1	0	0	1	2.3×10^{-3}
$Z \to \mu\mu$	1	3	22	0	2	27	21
$Z \to \tau\tau$	0	0	2	0	0	2	0.20
$W \to \mu\nu$	0	0	21	0	0	21	22
$W \to \tau\nu$	0	0	1	0	0	1	0.13
WW	0	0	1	0	0	1	0.82
WZ	0	0	0	0	0	0	0.00
ZZ	0	0	2	0	0	2	0.20
$t\bar{t}$	0	0	90	0	0	86	88
Total:							1.7×10^2

Table 9.4: *Selection rates for background samples*

immediately concludes from this, that the high threshold information (cut number III) is too easily polluted by background. It is by no means the strongest cut in the signal selection and it provides for nearly all the background. Removing cut III from the selection we obtain the results shown in tables 9.5 and 9.6. In these tables the jet veto has also been directly

Sample	I	II	III	IV	V	Combined	per fb^{-1}
100	28	7	7	0	8	34	1.8×10^5
300	207	106	100	4	92	325	8.9×10^3
600	318	306	299	25	191	639	3.1×10^3
1000	397	487	389	37	250	849	12
1300	377	416	411	40	270	780	1.3
1600	340	429	382	43	214	725	0.16
2000	247	362	393	65	163	600	0.014

Table 9.5: *Selection rates without using cut III and with jet veto applied directly at each channel. The effect of the jet veto can be seen by comparing the individual columns to table 9.3. Cut III remains listed so the effect of the jet veto can be seen but it is not used in the combination in the right-most column.*

applied to each channel to see the influence of the veto cut on the individual samples. Direct comparison can thus be made between tables 9.3 / 9.5 and 9.4 / 9.6. As expected the jet veto is particularly effective in weeding out fake charge flips. One peculiar feature of the $t\bar{t}$ samples deserves mention here. One will note that channel II of the sample has 0 entries in table 9.4 while 1 entry *appears* when applying the jet veto directly to the channel. This is a consequence of the negative weights occurring in the sample.

Sample	I	II	III	IV	V	Combined	per fb^{-1}
J4	0	2	3	1	0	3	3.1
J5	3	3	25	1	0	7	6.3
J6	0	1	0	1	0	2	2.0
J7	0	0	0	0	0	0	0.0
J8	1	0	0	0	0	1	2.3×10^{-3}
$Z \to \mu\mu$	1	3	22	0	2	5	3.9
$Z \to \tau\tau$	0	0	2	0	0	0	0.0
$W \to \mu\nu$	0	0	21	0	0	0	0.0
$W \to \tau\nu$	0	0	1	0	0	0	0.0
WW	0	0	1	0	0	0	0.0
WZ	0	0	0	0	0	0	0.0
ZZ	0	0	2	0	0	0	0.0
$t\bar{t}$	0	1	85	0	0	1	1.0
Total:							16.2

Table 9.6: *Selection rates for background samples without using cut III and with jet veto applied directly at each channel.*

9.4 Estimating Signal Significance

A claim for discovery can traditionally be made when the *"signal significance is above 5σ"*. In the present analysis this is quantified by estimating the probability that the expected background event count will fluctuate up to the expected combined signal + background count. This probability can then be translated to the corresponding numbers of standard deviations of a Gaussian distribution. This section is about the details on how this is done.

9.4.1 A Method For Background Estimation

As shown in section 9.3 the background count at a given integrated luminosity is estimated by running the various background samples through the event selection and normalising the event counts to the relevant luminosity. In the limit of infinitely high background statistics the event count at a given integrated luminosity would then be expected to follow a Poisson distribution around the given estimate. The background samples as it turns out do *not* have infinitely high statistics and the background estimate must consequently take into account the uncertainty of the estimate provided by the samples. Also the background samples do not represent the *same* amount of integrated luminosity.

To understand how to correctly combine the background samples we consider two background samples representing different parts of the total cross section. The samples measure the event counts N_1 and N_2 at *different* integrated luminosities $\mathcal{L}_1$ and $\mathcal{L}_2$. These numbers can be expected to follow Poisson distributions f_1 and f_2 where N_1 and N_2 are used as estimators of the means at their respective integrated luminosities. For the example we consider the case where

$$N_1 = 2, \qquad \mathcal{L}_1 = 2 \text{ fb}^{-1}, \qquad N_2 = 4, \qquad \mathcal{L}_2 = 3 \text{ fb}^{-1}. \tag{9.1}$$

These distributions are depicted in figure 9.13.

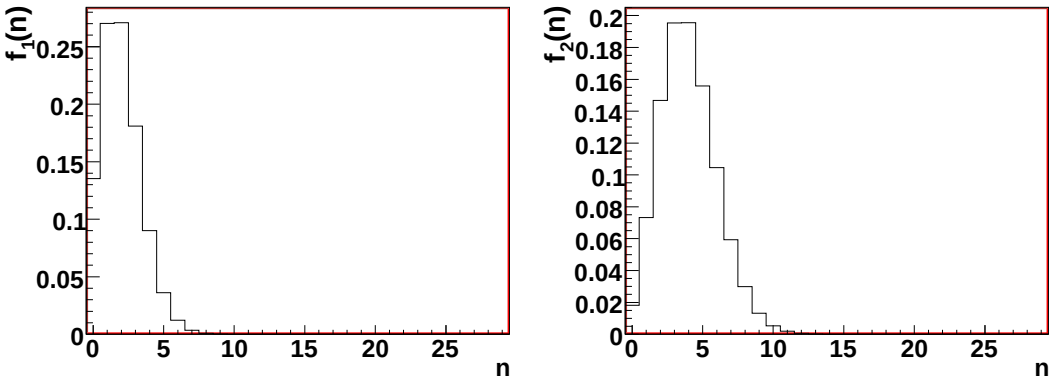

Figure 9.13: *Example Poisson distributions f_1 and f_2.*

We now estimate the *mean* background count at a reference luminosity $\mathcal{L}_0 = 1$ fb^{-1}. The probability that the combination of the two backgrounds give an event count $n \leq N$ is

$$p(n \leq N) = \sum_i \sum_j f_1(i) \times f_2(j) \Big|_{\left(\frac{i}{\mathcal{L}_1} + \frac{j}{\mathcal{L}2}\right)\mathcal{L}_0 \leq N}. \tag{9.2}$$

This cumulated distribution is shown in figure 9.14(a). The distribution is then differentiated

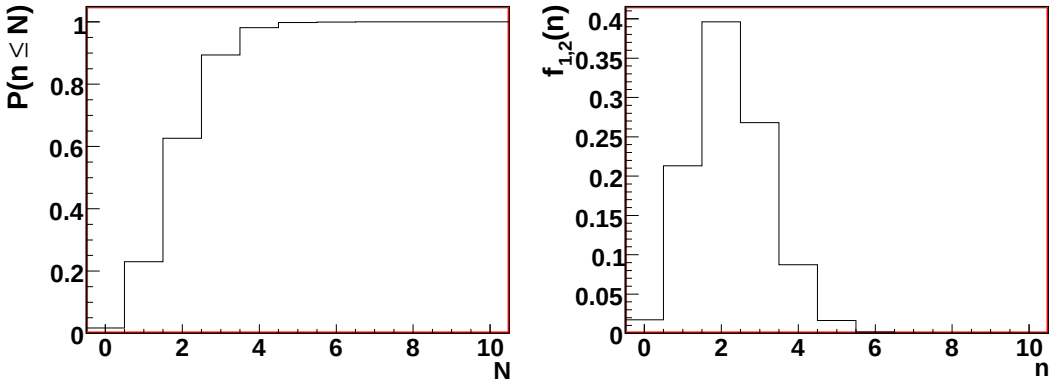

(a) Cumulated distribution (b) $f_{1,2}$

Figure 9.14: *Combining f_1 and f_2.*

to obtain the combined pdf $f_{1,2}$ itself. This is shown in figure 9.14(b). The $f_{1,2}$ distribution, however, merely represents the uncertainty on the estimate of the mean, μ. As noted earlier the RMS of the distribution goes to zero in the limit of infinite statistics. We can, however, estimate the background distribution by

$$F_{1,2}(n) = p(n) = \sum_i p(\mu = i) \times p(n|\mu = i) = \sum_i f_{1,2}(i) \times \text{Poiss}_i(n) \tag{9.3}$$

where $\text{Poiss}_i(n)$ represents a Poisson pdf with mean i.

Figure 9.15(a) shows the resulting estimated distribution, $F_{1,2}$, for the background with $f_{1,2}$ shown as a dotted line. As expected the mean does not move but the distribution flattens out.

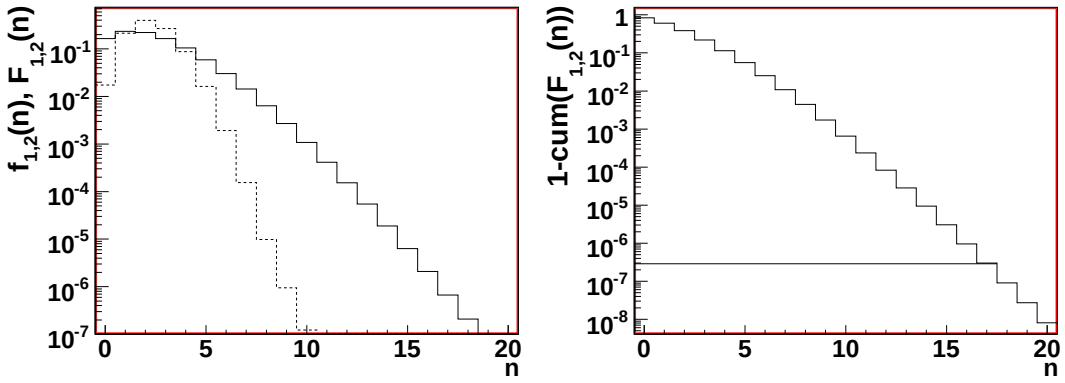

(a) Background distribution with fluctuations of the mean

(b) 1 - cum($F_{1,2}(n)$)

Figure 9.15: *Estimated background distribution.*

Figure 9.15(b) shows the probability of obtaining "n or higher" given $F_{1,2}$. This is exactly the distribution we need to estimate the significance of a given observed event count. The line drawn on 9.15(b) shows the 5σ significance level. The conclusion is that for the given example the signal plus background count needs to be 18 or more at 1 fb^{-1}.

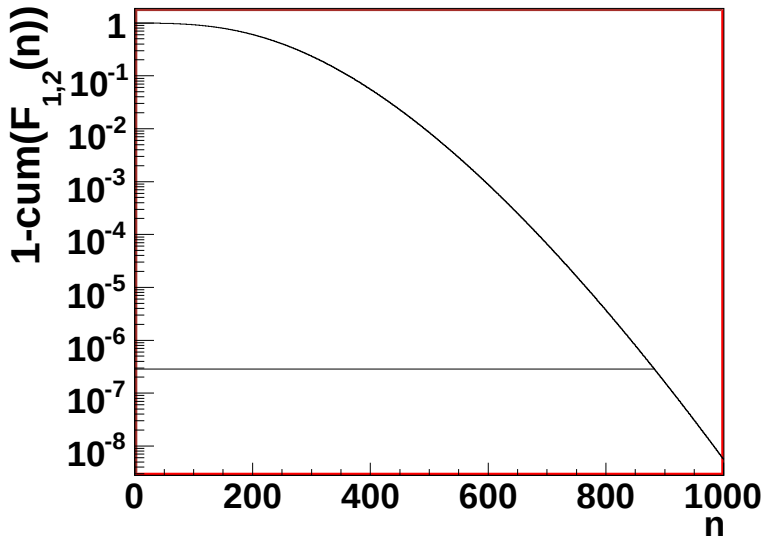

Figure 9.16: *Estimated upward fluctuation probability at $\mathcal{L}$= 100 fb^{-1}.*

Plotting the distribution in figure 9.15(b) for an integrated luminosity of 100 fb^{-1}one obtains figure 9.16. At this integrated luminosity the signal plus background count for a 5σ signal has thus been calculated to be 883 corresponding to a rate of 8.8 events/fb^{-1}.

9.4.2 Estimating the Background of the Event Selection

We now seek to apply the method outlined in section 9.4.1 to the event selection of section 9.3. There are six samples with a non-vanishing contribution to the background. However we

may not assume that the remaining part of the total cross section does not contribute to the background as it has been only been tested at a finite integrated luminosity. A conservative approach is chosen as follows. The lowest integrated luminosity among the vanishing samples is the $W \rightarrow \mu\nu$ sample at 0.94 fb^{-1}. At a 90% confidence level the part, Σ, of the total cross section covered by the samples J7, $Z \rightarrow \tau\tau$, $W \rightarrow \mu\nu$, $W \rightarrow \tau\nu$, WW, WZ and ZZ have a mean event count smaller than or equal to 2.3 [PDG06]. We therefore estimate their combined contribution with a Poisson distribution of mean 2.3 at an integrated luminosity of 0.94 fb^{-1}. We consequently end up with the background contributions summarised in table 9.7. Σ represents the part of the cross section with no events passing the selection. Applying

Sample:	Contribution:	$\mathcal{L}$
J4	3	0.98
J5	7	1.12
J6	2	1.01
J8	1	442.29
$Z \rightarrow \mu\mu$	5	1.29
$t\bar{t}$	1	0.98
Σ	2.3	0.94

Table 9.7: *Background Contributions*

the method outlined in section 9.4.1 and estimating the background distribution at 1 fb^{-1} yields figure 9.17(a). The 5σ level is reached for a signal plus background count of 58 events at

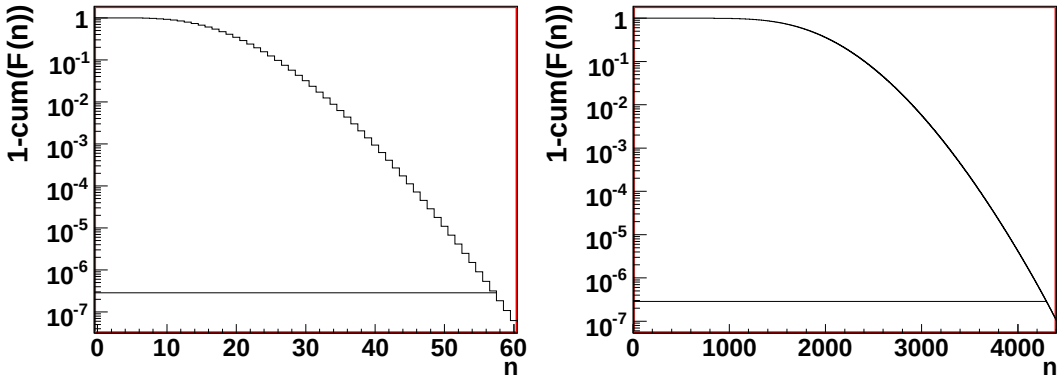

(a) $\mathcal{L}$= 1 fb^{-1} (b) $\mathcal{L}$= 100 fb^{-1}

Figure 9.17: *Estimated upward fluctuation probability for event ssec:mutrigelection.*

this integrated luminosity. We may thus immediately conclude from table 9.5 that the three lower gluino masses will be simple to discover at the LHC with en integrated luminosity of 10 fb^{-1} equivalent to one nominal year of running at low luminosity. The higher masses require a little more work. The 1 TeV/c^2 case for example has an event count of 11.72 per fb^{-1} leading to a signal plus background count of 3036 at 100 fb^{-1}equivalent to 2.6σ. As figure 9.17(b) shows, the 5σ level is crossed at 4298 events. It thus appears that having *one* set of cuts that covers the entire mass range 100 GeV/c^2 to 2 TeV/c^2 probably is not practical. It has been demonstrated that the 100 - 600 GeV/c^2 range is easily covered but the cases of higher mass will probably benefit from a set of dedicated cuts with a harder background rejection at the

expense of cutting away the low-mass signals also. It is of course also imperative to check for possible optimisations of cuts. Also systematic errors should be estimated and taken into account.

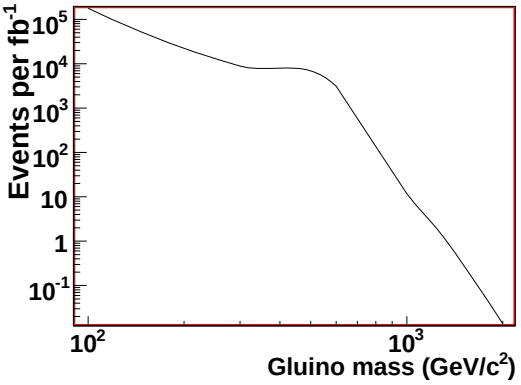

(a) Signal rate as a function of gluino mass. The bump on the curve at 600 GeV/c^2 shows the convolution between the increasing mean p_t and the falling cross section.

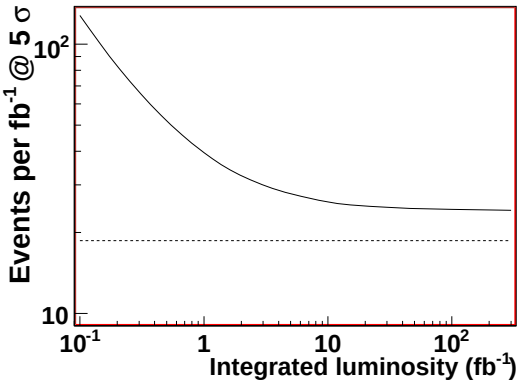

(b) Required signal rate for a 5σ signal at different integrated luminosities.

Figure 9.18: *Signal rates in the event selection.*

To summarise the example event selection figure 9.18(a) shows the acceptance rates for *signal* events to pass this event selection. This is just a visualisation of the numbers in table 9.5. Figure 9.18(b) shows in contrast the *required* number of signal events that need to pass the event selection per fb^{-1} to obtain a 5σ signal at different integrated luminosities with the given background samples. The background rate is entered as a dotted line for comparison.

9.5 Optimisation of Event Selection

The goal of this section is to investigate the possibilities for optimisation of the example event selection of section 9.3 to accommodate higher masses through a harsher background rejection. This endeavour is still undertaken with the boundary condition of the same background samples. Our knowledge of the background is thus still limited. To estimate the conditions under which the event selection has to work we consider the case where *all* background is eliminated by an event selection. By the arguments of section 9.4.2 we then estimate the combined background at 0.94 fb^{-1} by a Poisson distribution with mean 2.3. This translates into a requirement on the signal rate as described in section 9.4.2. This requirement is illustrated in figure 9.19. The 300 fb^{-1} point was the highest tested. At this integrated luminosity the requirement on the signal rate to pass an event selection is 11.6 events/fb^{-1}. Keeping in mind tables 9.1 and 9.5 (p. 114, 130) this is on the border-line of being feasible for the 1 TeV/c^2 case for an event selection that preserves all triggered signal events whilst rejecting *all* background. Discovery of higher masses is excluded with the current background description. The immediate conclusion is thus, that with the current statistical precision of the background description we can *not* guarantee discovery of a 1 TeV/c^2 quasi-stable gluino at ATLAS within 300 fb^{-1}.

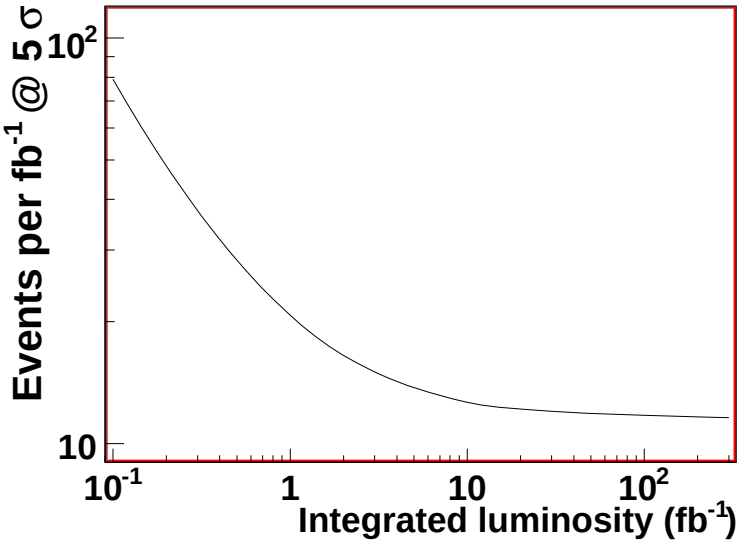

Figure 9.19: *Requirement on signal rate for a 5σ signal in the case of a selection that rejects all events* in the background samples available..

It now appears to be sensible to turn the problem around and assume a selection with *full* background rejection. No background events pass the selection. This allows us to evaluate the signal rate needed per fb^{-1} to claim discovery at a fixed integrated luminosity. As a benchmark point $\mathcal{L}$= 300 fb^{-1} is chosen. The corresponding required rates for passing the event selection are listed in table 9.8. Figure 9.20 shows the required acceptance rates as

Known+rejected background (fb^{-1})	Required rate for discovery @ 300 fb^{-1} (events/fb^{-1})
1	10.9
10	1.13
30	0.400
100	0.144
300	6.57×10^{-2}

Table 9.8: *Required rates for discovery at $\mathcal{L}$= 300 fb^{-1} for different known and rejected backgrounds. The left column shows the integrated luminosity to which the background is assumed known. Furthermore all this background is assumed to be rejected by the event selection.The right column is the rate with which the signal events will have to pass the event selection to get a discovery at 300 fb^{-1}.*

a function of the integrated luminosity to which the background is known *and completely rejected*. For comparison the trigger rates for 1.3 and 1.6 $\mathrm{TeV/c}^2$ gluino R-hadrons are superimposed on the plot. It is seen that knowing the background to $\mathcal{O}(10\mathrm{fb}^{-1})$ puts the 1.3 $\mathrm{TeV/c}^2$ gluino case within range, while 100 fb^{-1}opens the possibility for detecting 1.6 $\mathrm{TeV/c}^2$ gluino R-hadrons. The 2 $\mathrm{TeV/c}^2$ signal remains out of range.

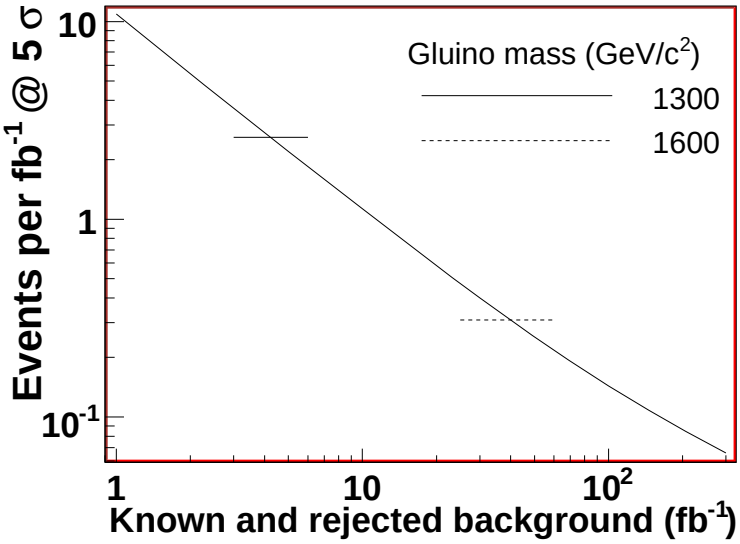

Figure 9.20: *Required acceptance rates compared to signal trigger rates. This is simply a visualisation of table 9.8.*

We now undertake the endeavour of making an optimised event selection based on the example selection. To provide a fitting framework for this, the event selection is generalised as follows.

- The R condition for a link is no longer the same as for a no-link. An interdiction cone is defined, typically with a larger radius than the link condition.

- The hard-jet condition is left free relative to the hard-track condition.

All cuts of the modified event selection are now varied. To describe this, some terminology needs to be established. This is done in table 9.9.

$p_{t,cut}$	Hardness cut on tracks
$p_{t,match}$	This is a dimensionless quantity defining how well the ID track should match the muon track in transverse momentum as $p_{t,Trk} > p_{t,match} \times p_{t,\mu}$ when matching tracks for the flip signature.
R_{cut}	The R-requirement for a track link
$R_{cut}^{no-link}$	Interdiction cone radius
$HTLT_{cut}$	The cut on #HT/#LT for back-to-back tracks
$B2B_{cut}$	The cut on $\cos\Delta\varphi$ for objects to be back-to-back
R_{veto}	How close a hard jet is allowed to a hard muon
$p_{t,veto}$	The p_t requirement for a jet to be counted as hard.

Table 9.9: *Cut terminology*

In the terminology defined here the example event selection of section 9.3 can be written as:

$$\begin{aligned} p_{t,cut} &= p_{t,veto} = 200 \ \text{GeV/c}, && (9.4)\\ p_{t,match} &= 0.5, && (9.5)\\ R_{cut} &= R_{cut}^{no-link} = 0.1, && (9.6)\\ R_{veto} &= 0.5, && (9.7)\\ HTLT_{cut} &= 0.1, && (9.8)\\ B2B_{cut} &= -0.9. && (9.9) \end{aligned}$$

9.5.1 Optimising the Example Event Selection

The starting point for this optimisation is the example event selection of section 9.3 with the generalisations made in equations (9.4) - (9.9). The significance of the selection for the 1 TeV/c^2 case with the given signal and background samples is 2.60σ at 100 fb^{-1}. The 1 TeV/c^2 gluino case will be used as a bench-mark for the event selection and the significance will be expressed at 100 fb^{-1}.

As the example event selection is not in any way optimised the first task is to find a reasonable reference selection that is not too far from supplying maximum signal significance. To do this the individual cut parameters are varied one by one with respect to the example selection to see if any simple changes might improve the significance. If any one change produces a better significance it is incorporated in the selection for the next iteration. A couple of iterations of this ad-hoc scan yields the following cuts:

$$\begin{aligned} p_{t,cut} &= 300 \ \text{GeV/c},\\ p_{t,veto} &= 100 \ \text{GeV/c},\\ p_{t,match} &= 0.5,\\ R_{cut} &= R_{cut}^{no-link} = 0.1,\\ R_{veto} &= 0.5,\\ HTLT_{cut} &= 0.05,\\ B2B_{cut} &= -0.9. \end{aligned}$$

This selection has a significance of 3.58σ and it is used as a reference selection in the following parameter scan. Figure 9.21 shows the result of a parameter scan around this reference selection. As each parameter is varied *in turn* each plot contains the reference selection around which the cuts are varied. This is in each plot marked with a dotted line at the reference value of the cut. Some cuts turn out to be insensitive to adjustment. In particular the $p_{t,match}$ shows no change in significance over the variation region but also the R and $B2B$ cuts turn out to be quite stable. The HTLT cut also has little impact on the total significance due to the low fraction of events coming from this channel as shown for instance in column IV of table 9.5.

The lesson from this preliminary optimisation is that the following cuts can be frozen: $p_{t.match}$, $B2B_{cut}$ and $HTLT_{cut}$. The R parameters are kept in the optimisation as they are expected to be correlated with the p_t cuts. The remaining parameters are now subjected to a more thorough scan where parameters are varied simultaneously. The five parameters fall naturally into two groups. The first group consists of $p_{t,veto}$ and R_{veto} as these parameters are

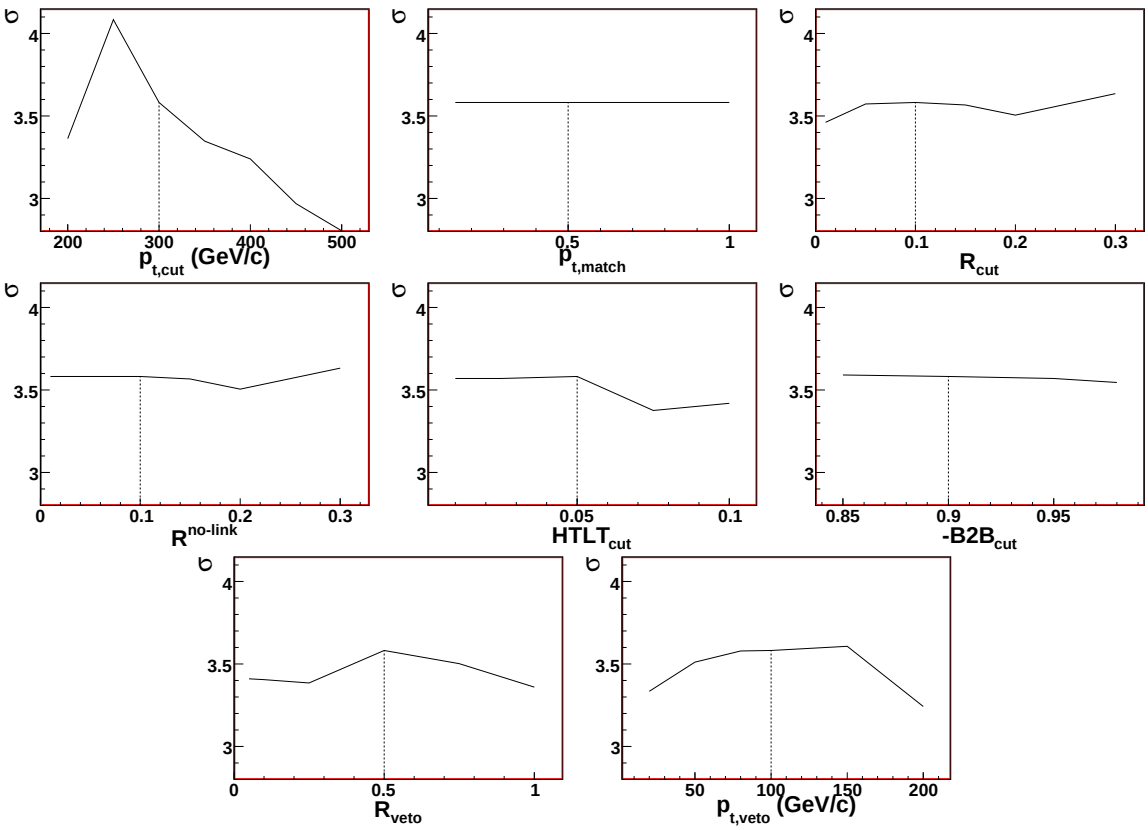

Figure 9.21: *Initial parameter scan*

directly related to the strength of the jet-veto. The other group consists of the track-related parameters. The $p_{t,cut}$ is naturally negatively correlated with the event rate as is $R_{cut}^{no-link}$ while R_{cut} is positively correlated with the same rate. We investigate these cuts by scanning the parameters in three two-dimensional grids spanned by

- $p_{t,veto} \times R_{veto}$
- $p_{t,cut} \times R_{cut}^{no-link}$
- $p_{t,cut} \times R_{cut}$

It should be noted that a possible consequence of this investigation is that the p_t-cuts used for the no-link and the charge-flip signatures are not necessarily the same.

The default cuts used in the 2D scans are based on the scan shown in figure 9.21. The cut values are

$$\begin{aligned} p_{t,cut} &= 250 \text{ GeV/c}, \\ p_{t,veto} &= 150 \text{ GeV/c}, \\ p_{t,match} &= 0.5, \\ R_{cut} &= R_{cut}^{no-link} = 0.1, \\ R_{veto} &= 0.5, \\ HTLT_{cut} &= 0.05, \\ B2B_{cut} &= -0.85. \end{aligned}$$

The scans were performed at eleven values for each parameter in the ranges as

$$\begin{aligned} p_{t,cut} &\in [200 \text{ GeV/c}, 400 \text{ GeV/c}] \\ R_{cut} &\in [0.01, 0.41] \\ R_{cut}^{no-link} &\in [0.1, 1.1] \\ p_{t,veto} &\in [25 \text{ GeV/c}, 275 \text{ GeV/c}] \end{aligned}$$

The results of the grid scans are shown in figure 9.22. It should be noted that the appearance of these figures contain more detail than the actual binning used for the scan. This is due to a smoothing and interpolation performed for ease of reading. The maximum values obtained in the scans were obtained for $p_{t,cut} = 260$ GeV/c (both scans), $R_{cut} = 0.29$, $R_{cut}^{no-link} = 0.30$, $p_{t,veto} = 100$ GeV/c and $R_{veto} = 0.4$. Both significances were lower than that obtained with 250 GeV/c (which fell between two bins in the scan) why this value was chosen instead. Note also that maximum significance is not necessarily reached by naïvely choosing these cuts in combination due to the fact that this was not a simultaneous optimisation of all parameters. In fact that set of cuts yields a significance of only 3.8σ vs. the 4.1σ reached in the $p_{t,veto}/R_{veto}$ scan. As the same value for $p_{t,cut}$ came out of the two scans the value was fixed at 250 GeV/c and a new scan of R_{cut} vs $R_{cut}^{no-link}$ was performed. The result is shown in figure 9.23. The maximum significance of 4.1σ was obtained for $R_{cut} = R_{cut}^{no-link} = 0.1$. A parameter scan was performed at a higher resolution than was done in figure 9.21. Only the five parameters of the grid scans were included in the scan. This was done as a basic cross check that the chosen cut values at least be local maxima for the significance. The result is shown in figure 9.24 with the values chosen from the grid scans shown as vertical lines.

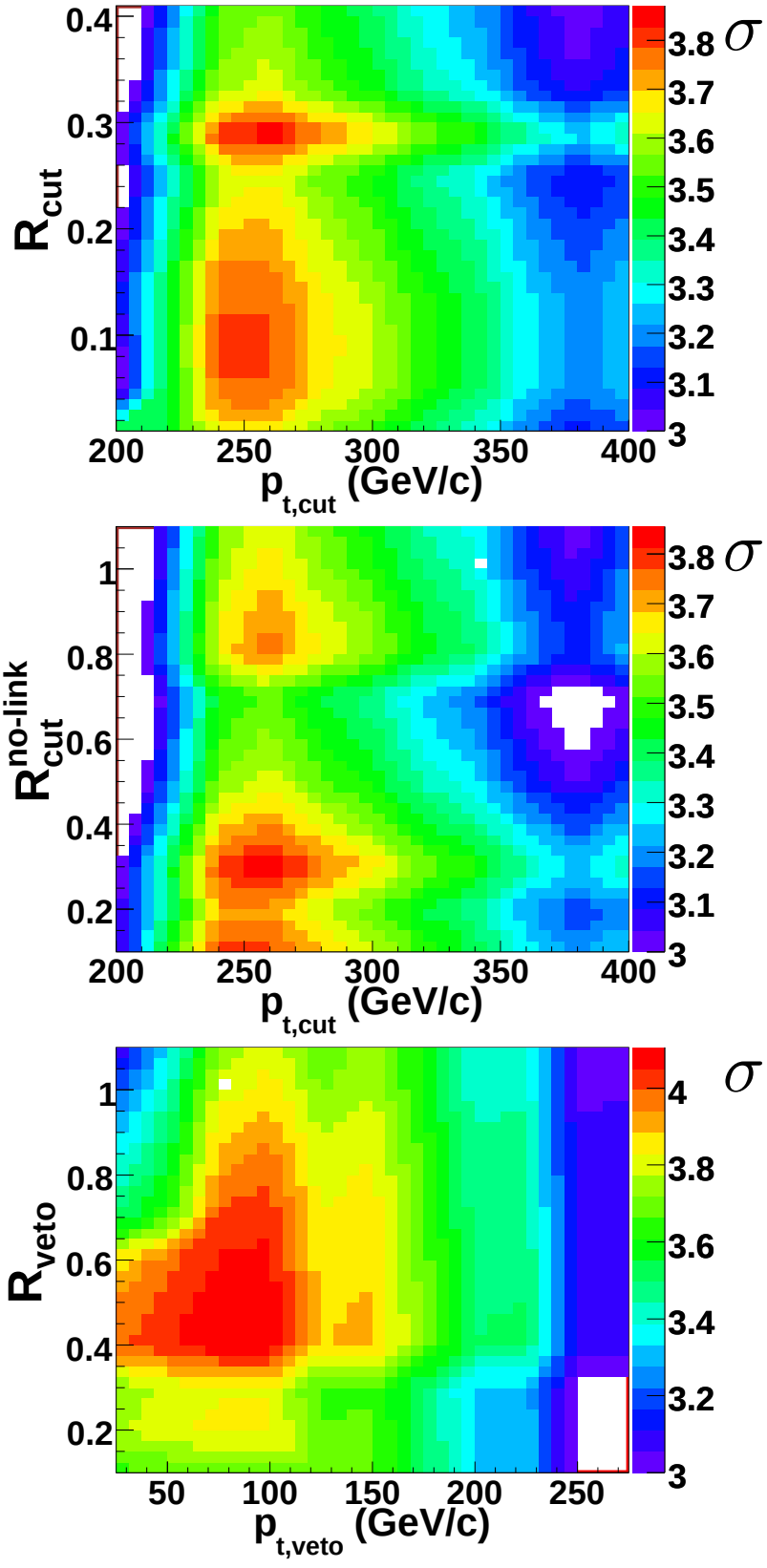

Figure 9.22: *Two-dimensional parameter scans.*

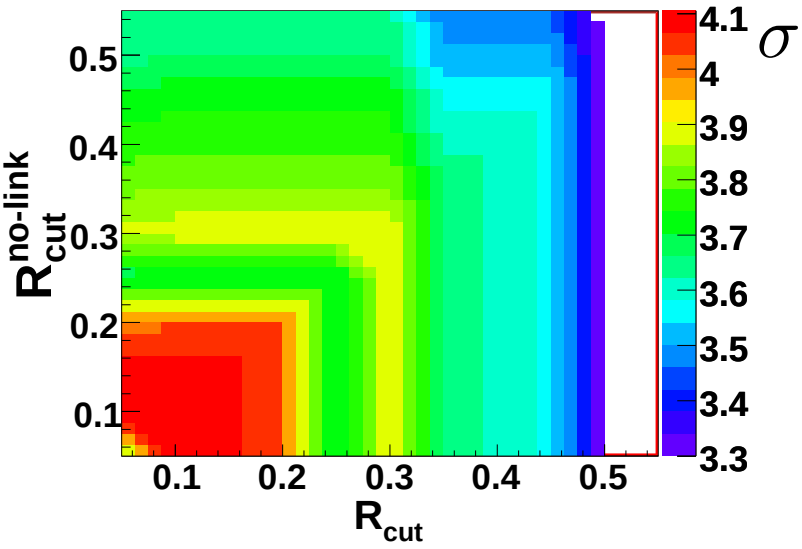

Figure 9.23: *Final scan of R_{cut} vs. $R_{cut}^{no-link}$.*

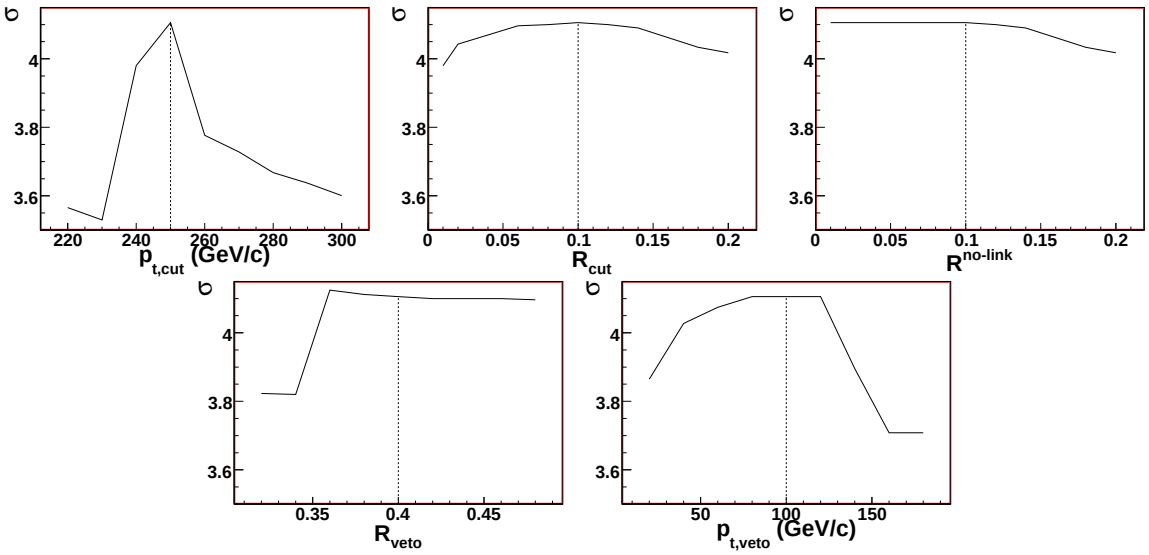

Figure 9.24: *Optimised parameter scan.*

As it turns out the higher resolution of these scans reveals a slight increase (from 4.11σ to 4.12σ) in significance by choosing $R_{veto} = 0.36$ instead of 0.4 as indicated by the grid scans. The final event selection thus becomes:

$$\begin{aligned} p_{t,cut} &= 250 \text{ GeV/c}, \\ p_{t,veto} &= 100 \text{ GeV/c}, \\ p_{t,match} &= 0.5, \\ R_{cut} &= R_{cut}^{no-link} = 0.1, \\ R_{veto} &= 0.36, \\ HTLT_{cut} &= 0.05, \\ B2B_{cut} &= -0.85. \end{aligned} \tag{9.10}$$

Table 9.10 shows the acceptance numbers and rates for the various samples. Only the background samples that are not rejected in their entirety are listed.

Sample	**Accepted events**	**Rate (Events/fb^{-1})**
100 GeV/c^2 gluino	20	1.06×10^5
300 GeV/c^2 gluino	235	6.44×10^3
600 GeV/c^2 gluino	551	2.70×10^3
1000 GeV/c^2 gluino	774	10.7
1300 GeV/c^2 gluino	732	1.20
1600 GeV/c^2 gluino	685	0.147
2000 GeV/c^2 gluino	546	1.26×10^{-2}
J5	1	0.893
J8	1	2.26×10^{-3}
$Z \rightarrow \mu\mu$	1	0.776

Table 9.10: *Number of events selected for the given samples. Background samples not mentioned here are rejected by the selection.*

Having thus settled on an event selection it may be used to estimate the evolution of the expected signal significance for different masses and integrated luminosities. This is done in figure 9.25. The acceptance rates of the lower gluino masses remain impossible to quantify. As can be readily seen from table 9.10 the background is of $\mathcal{O}(2/\text{fb}^{-1})$ while the signal rates for the three lower masses are three orders of magnitude beyond. The reason that the 1 TeV/c^2 gluino signal does not rise above 4.1 is solely the fact that we have been forced to use a quite conservative estimate on the rejected background as pointed out in section 9.4.2.

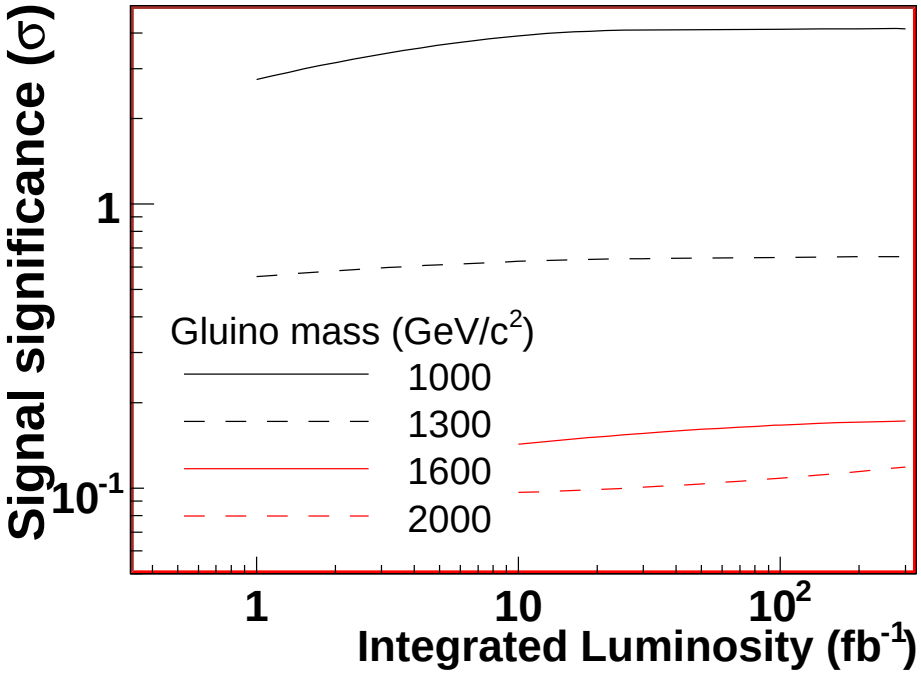

Figure 9.25: *Expected signal significance as a function of $\mathcal{L}$ for different gluino masses.*

Chapter 10

Extending the Scope of the Analysis

Having developed an analysis and a set of cuts, it is instructive to see if we can transfer some conclusions from the work done for the gluino case to other cases and perhaps draw some general conclusions. We consider a stable KK-gluon scenario implemented in PYTHIA [BA05]. The implementation calculates the cross section for KK-state pair-production based on [MMN02a, MMN02b, Riz01] with a generalisation to higher number of extra dimensions. The scenario studied here has two extra dimensions and the KK-gluon mass, $m_{g_{KK}}$ has been set to 1 TeV. The true Planck scale has been set to 5 TeV. The cross section for KK-gluon pair production through the process $gg \rightarrow g_{KK}g_{KK}$ becomes 1.23 pbarn. This is to be compared with table 8.1 in which the cross section for gluino production is given as 0.138 pbarn. In other words the cross section is roughly a factor of ten higher at this mass than is the case for the gluino.

10.1 A Note on Basic Phenomenology

It was argued in section 3.2.3 that the mass spectrum of KK-hadrons should be very close to that of gluino R-hadrons. The reason for this was that the spin played very little role in the formula (3.7) for the mass splittings of the hadrons. We therefore have a somewhat justified expectation that the *individual* KK-hadron will behave in much the same manner as an R-hadron with comparable initial kinematic properties. This means that the primary difference between the events will be due to the spin difference between the fermionic gluinos and the bosonic KK-gluons leading to a different polar angle distribution in the centre of mass system of the colliding partons. This difference will be observed in the lab-frame as a difference in the p_t and η distributions.

10.2 Generator Level Reweighting

We now study the basic kinematics of the UED events with respect to the SSUSY events. The aim is to find a suitable set of variables that can be reweighted to obtain an adequate description of UED using fully simulated and reconstructed SSUSY events. As mentioned before the primary difference is expected to be found in the η and p_t distributions. As

hadronisation code has not yet been written for the UED case the reweighting is performed using the KK-gluons and gluinos themselves.

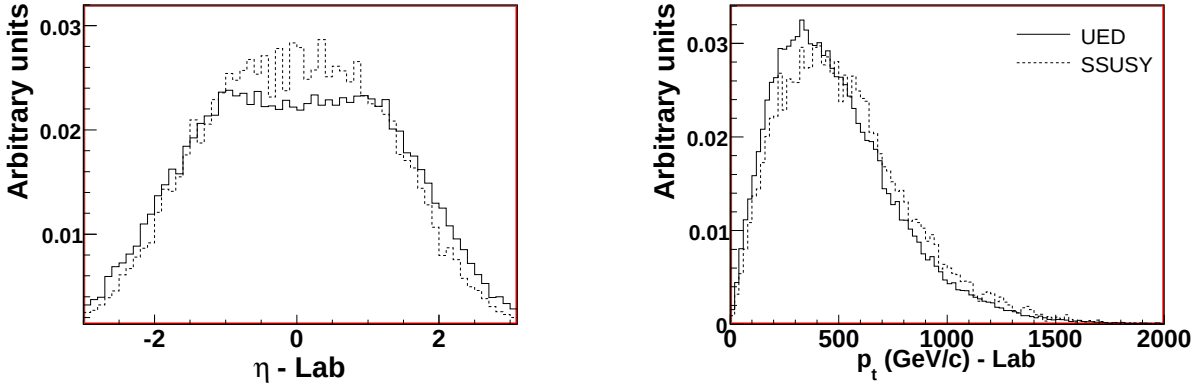

Figure 10.1: *Spectra of pseudorapidity and transverse momentum for KK-gluons and gluinos.*

Figure 10.1 shows a comparison between the spectra for UED and SSUSY. The spectra were made using 10000 SSUSY events and 30000 UED events. As is evident from the plots very little spin structure survives due to the boost of the event but there is some difference to be seen for both plots. In order perform the reweighting on a per-event basis we need a way to uniquely assign a weight to each event. As there are two KK-gluons / gluinos being produced the correct way to do it is to look at the event in the centre of mass systems of the two heavy objects. In this frame of reference the two particles are back-to-back and there is thus no ambiguity regarding which particle properties to use in the weight calculation. The transverse momenta are identical and the pseudorapidities are equal but with opposite sign. Turning therefore to the CMS of the two particles it is shown in figure 10.2 that there is a

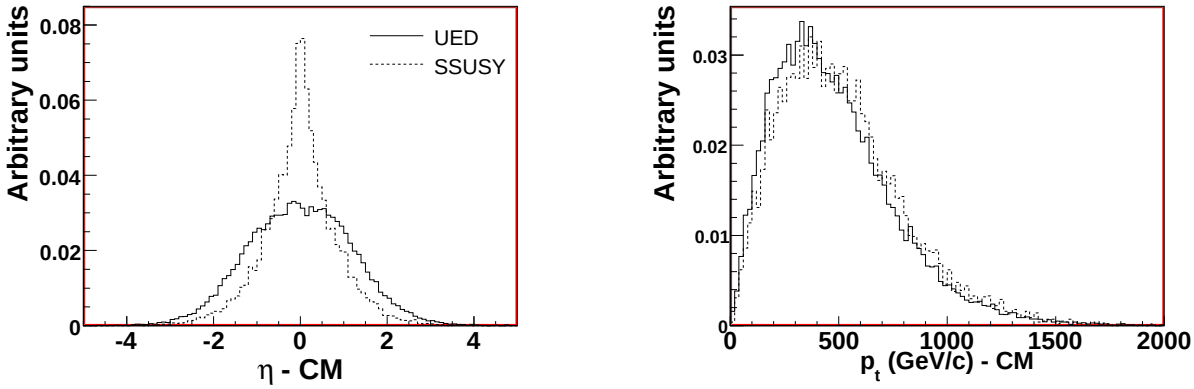

Figure 10.2: *Spectra of pseudorapidity and transverse momentum for KK-gluons and gluinos in the centre of mass system of the pair-produced particles.*

large difference in the η distribution as well a slight shift to higher values of p_t for SSUSY relative to UED. Reweighting in η, the weighting factor in the η-bin i in the CMS is defined as

$$c_i = \frac{f_{UED}(i)}{f_{SUSY}(i)}, \tag{10.1}$$

where $f_{UED}(i)$ and $f_{SUSY}(i)$ denote the value in the i'th bin of the η distributions for UED

and SUSY respectively. The weighting factors are shown in figure 10.3 as a function of pseudorapidity in the CMS. Applying these weighting factors to SSUSY events require again

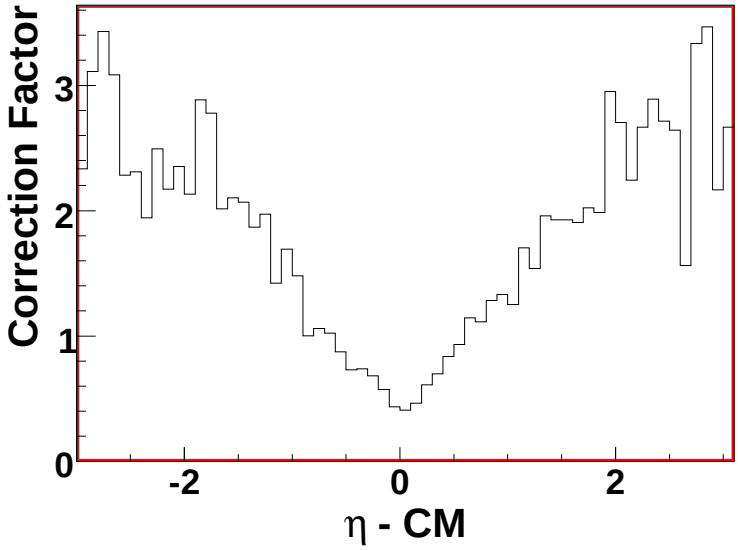

Figure 10.3: *Correction factors in terms of η in the CMS.*

a boost to the CMS of the two gluinos to calculate the pseudorapidity to reweight. The η and p_t histograms are then filled again with the modified weights to see if the reweighted SSUSY events yield an adequate description of the UED events. From figure 10.4 it is seen that the shift in the transverse momentum distribution is now slightly towards *lower* values for reweighted SUSY relative to UED. The η distributions are not shown as they are identical for UED and reweighted SSUSY by the construction of the reweighting procedure. Figure 10.5 serves as a cross check in this context. The figure shows the reweighted η and p_t distributions in the labframe. It is seen that there is good agreement between the distributions apart from afore-mentioned slight shift in the p_t distribution.

10.3 Applying the Event Selection

Once the correction factors are calculated one applies the correct weight to the individual fully reconstructed event by retrieving the event record, boosting to the centre of mass of the $\tilde{g}\tilde{g}$ system and looking up the appropriate weight in the histogram from figure 10.3. This was done for the SSUSY scenario with $m_{\tilde{g}} = 1$ TeV/c^2. The 10000 events summed up with weights corresponded to 1.17×10^4 events or 9.52 fb^{-1}. Of these 7.26×10^2 were accepted by the event selection resulting in a rate of 76.2 events/fb^{-1}with a significance of 4.78σ at an integrated luminosity of 100 pb^{-1}rising to 6.30σ @ 200 pb^{-1}and 7.34σ @ 300 pb^{-1}. These significances are based on the same background samples as were used in the previous chapter using the event selection defined in (9.10) (p. 143).

Of course a full analysis of UED would have to include a full reweighting in all kinematic variables and a rerun of the optimisations of the last chapter again due to the changes in kinematics. We do, however, get a good estimate of the expected discovery reach of ATLAS by using this selection. Redoing the reweighting for higher mass KK-gluons by using the

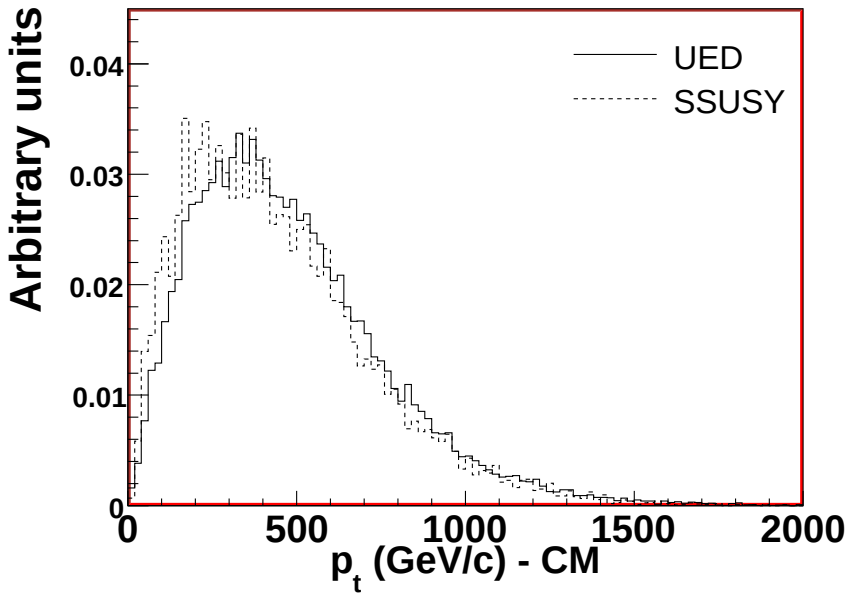

Figure 10.4: *Transverse momentum distributions in the CMS for UED compared with reweighted SSUSY. The η distributions are not shown as they are identical by construction for UED and reweighted SUSY.*

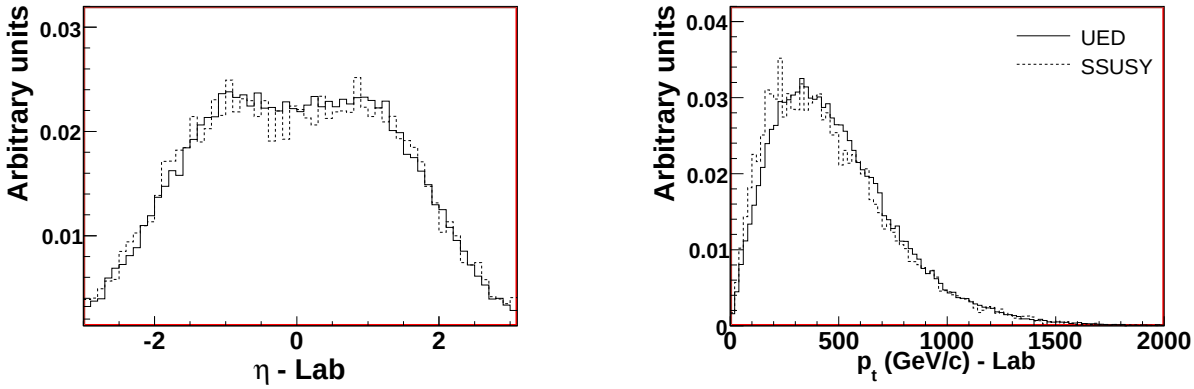

Figure 10.5: *Pseudorapidity and transverse momentum distributions in the labframe for UED compared with reweighted SSUSY.*

Sample	Number of events	$\mathcal{L}$(fb^{-1})	Selected events	Rate (Events/fb^{-1})
1 TeV/c^2	1.17×10^4	9.52	7.26×10^2	76.2
1.3 TeV/c^2	1.12×10^4	78.8	6.87×10^2	8.72
1.6 TeV/c^2	1.07×10^4	516	6.37×10^2	1.23

Table 10.1: *A summary of reweighted signal samples.*

appropriate SSUSY samples one obtains the rates in table 10.1. The corresponding signal significances are shown in figure 10.6 as a function of integrated luminosity. Masses below 1 TeV/c^2 have not been considered here as the cross section in this case makes discovery trivial as was the case for the low-mass stable gluinos in chapter 9.

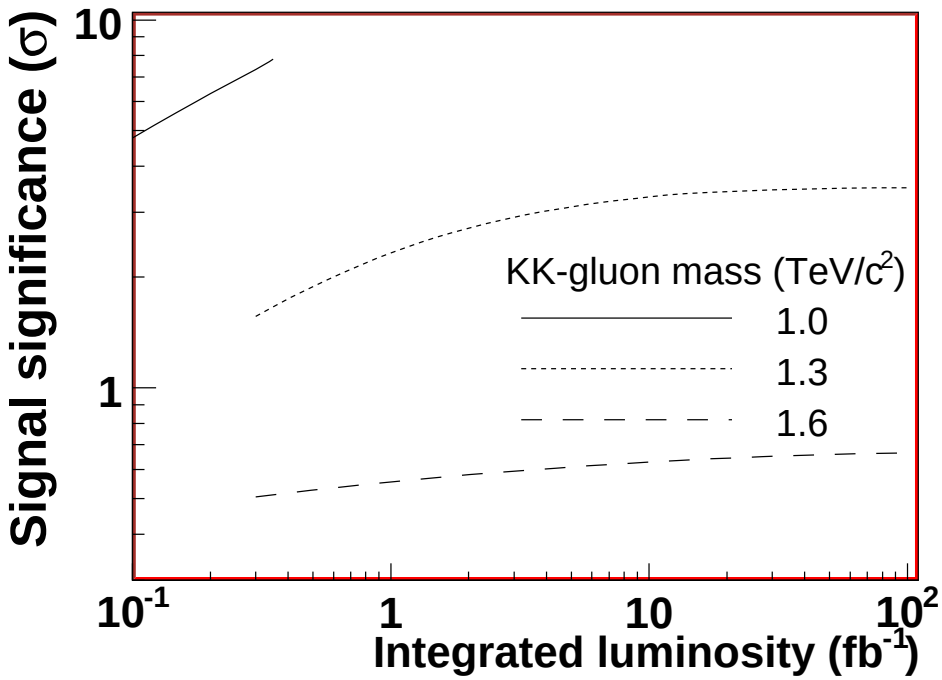

Figure 10.6: *Signal significance as a function of integrated luminosity for a couple of values of* $m_{g_{KK}}$.

Chapter 11

Systematic Errors

Systematic errors is a difficult subject to address for a detector that is only partly built. We *can*, however, evaluate systematic errors stemming from theoretical uncertainties. We are in this case left with varying the parameters of the Monte Carlo models used. The systematic contributions that will be estimated are listed below.

11.1 K-factors and PDF Uncertainties

The cross section calculated by PYTHIA is a LO cross section. Higher order corrections are commonly named K-factors. Increases in cross section of 20% have been quoted in earlier work [ATLc] where effects of 15-30% have also been observed by varying the PDFs. A 30% systematic uncertainty has been assumed here. It is important to note that these uncertainties are present for signal as well as for background (disregarding the $t\bar{t}$ sample where an NLO calculation was actually used).

11.2 Gluino Ball Formation

The default probability in PYTHIA for gluino ball formation is $P_{\tilde{g}g} = 0.1$ which is a number motivated by the colour octet properties of the gluon and the gluino. Put simply the probability for a gluon to match the gluino is

$$p \sim (3 \text{ colours} \times 3 \text{ anticolours})^{-1}, \tag{11.1}$$

which is indeed of $\mathcal{O}(10\ \%)$. Glue ball formation itself, however, is an area of semi-soft QCD which is poorly understood and in fact no unambiguous discovery has been made of glue balls [PDG06]. Varying $P_{\tilde{g}g}$ primarily influences the trigger as an enhanced glue ball formation probability implies an enhancement of both R-hadrons being produced neutral thus making the event effectively invisible to the trigger.

In order to evaluate the impact on the trigger, we now assume that every charged R-hadron has equal probability p of passing the trigger while every neutral R-hadron has exactly zero probability of triggering the event. The fractions of events that are neutral, singly charged

and doubly charged are denoted ν_{nn}, ν_{cn} and ν_{cc}. The combined trigger efficiency ϵ then follows the relation

$$\epsilon = 0\nu_{nn} + p\nu_{cn} + \left[p^2 + 2p(1-p)\right]\nu_{cc}. \tag{11.2}$$

Running PYTHIA for a 1 TeV/c^2 gluino mass with different gluino ball formation probabilities yields the fractions ν shown in table 11.1. We know ϵ for $P_{\tilde{g}g} = 0.1$ from table 9.1 (p. 114).

$P_{\tilde{g}g}$	ν_{cn}	ν_{cc}	ν_{nn}
0	47.8%	27.1%	25.1%
0.1	51.0%	18.5%	30.5%
0.2	47.8%	16.4%	35.8%

Table 11.1: *Fractions of events with zero, one or two charged R-hadrons*

The value is 17%. We can now solve equation (11.2) for p and obtain $p = 0.202$. Substituting the ν values from table 11.1 back into the equation we obtain estimated trigger efficiencies for $P_{\tilde{g}g} = 0.2$ and for $P_{\tilde{g}g} = 0$. These two values are motivated by the fact that no solid data exists on glueball formation, thus motivating $P_{\tilde{g}g} = 0$. The higher limit was chosen as simply a 100% variation on the standard value of 0.1 to estimate the effect of the glueball formation. The trigger efficiencies obtained were 15.6% and 19.5% for $P_{\tilde{g}g} = 0.2$ and $P_{\tilde{g}g} = 0$ respectively. This effect corresponds to an 8-9% effect on the trigger rate that we may for simplicity assume translates directly into a corresponding change in the acceptance rate of the full event selection.

11.3 GEANT4 Parameters

As mentioned in section 5.1 the simulation framework for R-hadrons allows for introducing resonances into the cross section as well as suppressing nuclear reactions where charge exchange occurs. Spanning the entire possible or even probable range of parameter settings is a very time consuming task in terms of CPU time. Therefore only one reference sample was run. The sample was a 1 TeV/c^2 SSUSY sample. A velocity of 0.7 c (inspired by figure 8.15) implies a kinetic energy of approximately 400 GeV. A resonance of 100 mb and a width of 100 MeV was therefore added at this kinetic energy. This amplitude and width were motivated by the resonances appearing in the πp cross section [PDG06]. The charge exchange suppression was set to 25%. Running the event selection on the resulting sample resulted in 643 accepted events instead of 774. This is an effect of 17% and it is understood as the effect of the larger cross section leading to larger energy losses. The R-hadrons that make it to the muon system will therefore be fewer, and the track fit qualities will be worse.

11.4 Combining Systematic Contributions

The three sources of systematic uncertainties listed above are fully independent and may be visualised in several ways. We begin by considering signal significance as a function of integrated luminosity for a fixed sample, namely the 1 TeV/c^2 SSUSY sample. Combining the GEANT4 contribution and the gluino ball contribution in quadrature yields an uncertainty

of 19%. It is now possible to estimate the influence on the signal significance by varying the signal rates by 19% relative to a fixed background. The K-factor/PDF contribution is treated a little differently than the background and the signal was varied *simultaneously* with 30% as motivated in section 11.1. These uncertainties result in variations in signal significance. The variations have been quantified separately for the two types of systematic errors whereupon the variation in significance is added in quadrature. The result is shown in figure 11.1.

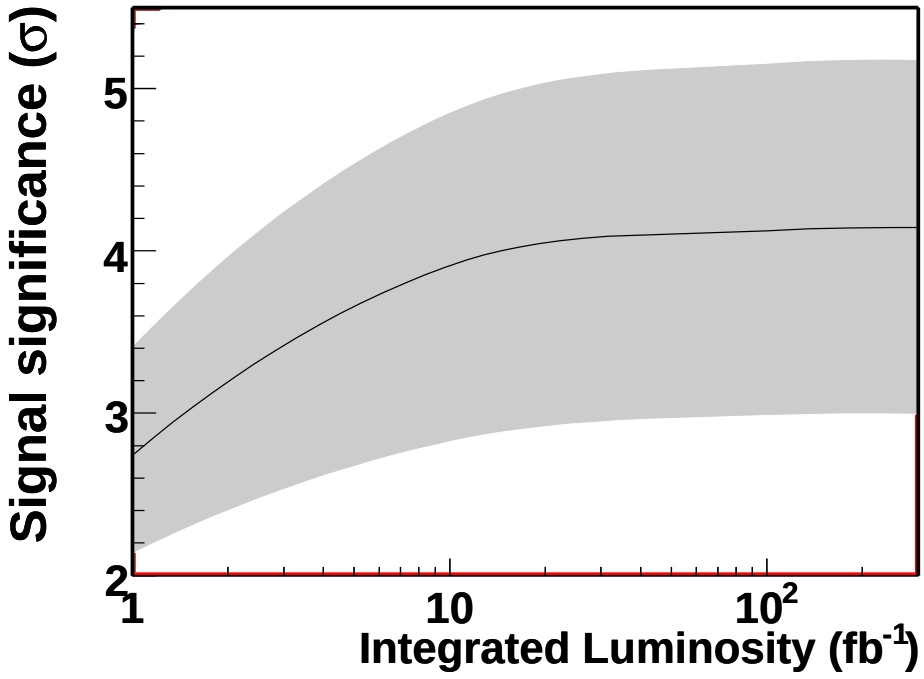

Figure 11.1: *Signal significance of the 1 TeV/c^2 gluino sample including systematic errors.*

As is seen from the figure the 5σ discovery level is only marginally within the systematic errors *with the given background description*. The analysis can now be summarised including systematic errors by considering the required signal rate that need to pass the analysis cuts in order to obtain a given signal significance at a given integrated luminosity. This is a slight generalisation of figure 9.18(b). Figure 11.2 shows three curves representing the *signal* rates required to obtain signal significances of 3, 5 and 7σ respectively as a function of integrated luminosity. The K-factors and PDF uncertainties are shown as an error band. The interesting rates are seen to be in the range of $\mathcal{O}(10-100$ events/fb$^{-1})$. There are three samples in this range. These are the cases of a 1 TeV/c^2 gluino and a KK-gluon of mass 1 TeV/c^2 and 1.3 TeV/c^2. These rates are superimposed on the plot. The small error bars on the rates represent the statistical errors associated with having a finite signal sample. The shaded error rectangles represent (from inside out) the addition in quadrature of a 17% GEANT4 uncertainty motivated in section 11.3, the 30% theoretical error from PDFs and K-factors and a 9% error from varying the gluino ball formation probability as described in section 11.2. It is seen that the 1 TeV/c^2 gluino case remains as a borderline case for discovery with the present background description while the KK-gluon scenario is easily discoverable. The 1.3 TeV/c^2 KK-gluon case exhibits rates comparable to that of the 1 TeV/c^2 gluino with roughly the same discovery potential.

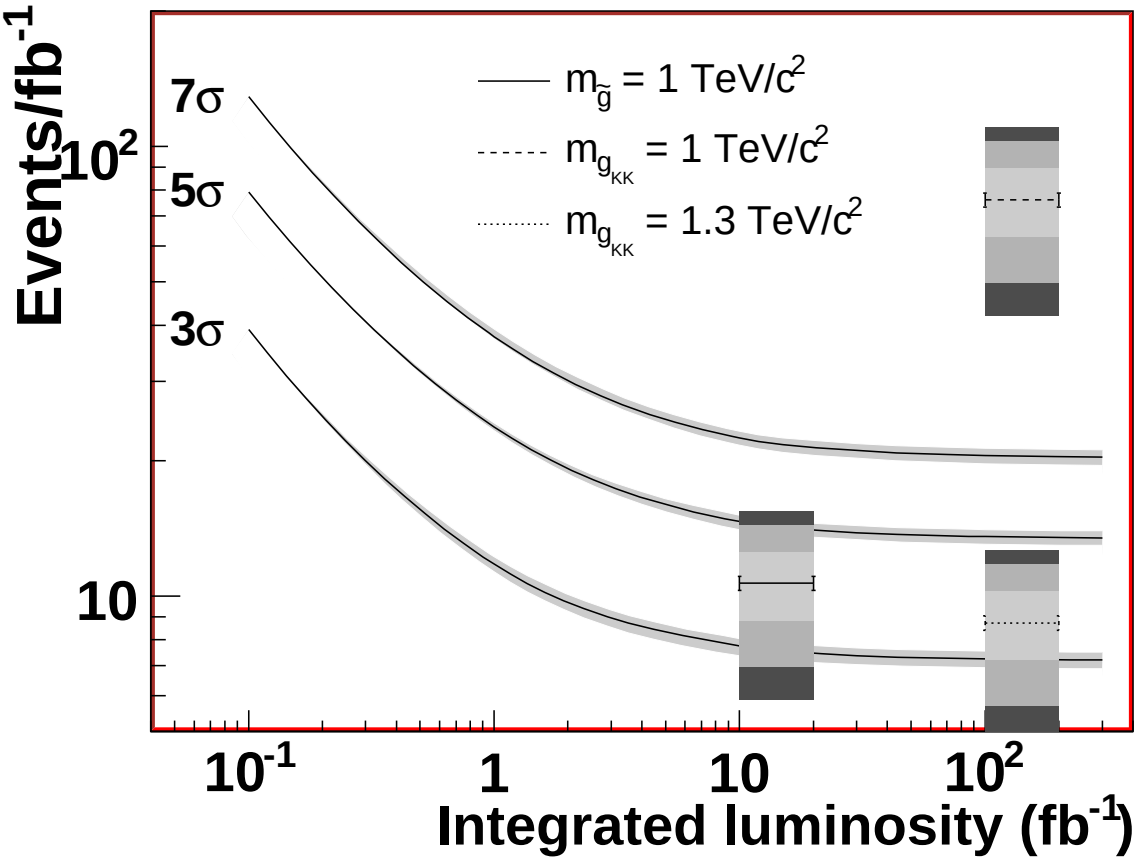

Figure 11.2: *Required signal rate at different integrated luminosities to obtain various degrees of significance. The three curves show the required rate for signal events to pass he event selection to obtain 3, 5 or 7σ respectively. The rates for three physics cases are superimposed on the plot with statistical and systematic uncertainties (see text). Their position along the x-axis was chosen exclusively for readability.*

Chapter 12

Summary and Outlook

In this thesis a GEANT4 based toolkit has been presented that describes the interactions with matter of heavy hadrons formed by heavy stable particles carrying the strong nuclear force. The toolkit can be easily interfaced to standard software packages as they are developed by high-energy physics experiments today. It has been demonstrated that the simulation package reproduces the expected phenomenology of earlier work, most prominently of course the simulation of stable gluinos presented in [Kra04b]. In addition to this a simulation has been presented which treats the simulation of stable stop squarks in matter.

The analysis presented in preceding chapters has illustrated the feasibility of discovering heavy stable hadrons at the LHC. The primary lesson to be learnt from this is that a good background description is of paramount importance to obtain a solid result. For instance a 1 TeV/c^2 gluino acceptance rate of 10.7 events/fb^{-1} might appear to be a strong signal on top of a background of $\sim$ 2 but if the rejected background is not known better than to $\mathcal{O}$(1 fb^{-1}) obtaining a strong signal significance becomes increasingly hard as has been illustrated thoroughly througout the analysis. Had the *rejected* background alone been known a factor of ten better a 5.34σ signal would have resulted for the 1 TeV/c^2 gluino case already at an integrated luminosity of 10 fb^{-1}using the present analysis cuts. This highlights the need for a data-driven background description. It is also probable that the analysis might benefit from the application of b-tagging to implement a heavy-flavour veto. A such veto might allow for a relaxation of the analysis cuts, thus conserving more signal events.

The present thesis also illustrates the first time the trigger simulation of the ATLAS experiment has been brought into use on the R-hadron case. Previous analyses [Kra04a, ATLc, KHN07] have all relied on geometric considerations to estimate a trigger efficiency. These considerations were shown to be somewhat justified for charged R-hadrons in the second-level trigger. A trigger study has been presented in section 8.2.2 in which, for the first time, it has been shown directly that the initial charge of a hadronised heavy parton is of great importance to the feasibility of triggering on it. Also it must be concluded that the present ATLAS triggering strategy for muons could be greatly enhanced for R-hadron studies if the matching requirement between the Inner Detector and the Muon Spectrometer was abandoned. This is of course not feasible for the full p_t-range but figure 9.4 shows quite clearly that the SM contamination of a 500 GeV/c muon trigger with no ID matching requirement would be minuscule and even for the SM processes contributing at those energies much could be learnt if nothing else then at least about the detector response at such transverse momenta.

It should be emphasised that the present analysis is bound to change immensely, once ATLAS starts taking data. The theoretical systematic errors will go down as reference cross sections are measured. On the other hand systematic errors from the detector itself will have to be taken into account. A fact that has also been neglected throughout the analysis is that triggers and performance of ATLAS is bound to change once the LHC shifts from low- to high-luminosity running after three years. Any conclusions reaching beyond an integrated luminosity of 30 fb^{-1} should therefore be assessed with caution once the ATLAS performance is better known.

Acknowledgements

Over the last years many people have contributed in different ways to the work presented here. I apologise in advance the ones I forget in the following.

First and foremost I wish to thank my advisor, John Renner Hansen for being supportive throughout the process and always sharing an insight or a perspective I had not considered. The other "grown-ups" in the group have also always been invaluable sources of discussions and information. Jørgen (#5) Beck Hansen was always willing to take a look at the gritty details and then tell you how *he* would have done it and Troels Petersen has never shunned a physics discussion. Also, I would like to thank Andrea Rizzi. It was nice to have someone to discuss with while figuring out how to put this stuff into GEANT4. In this connection I also received much help and valuable input with respect to earlier work from Aafke Kraan. Torbjörn Sjöstrand has time and again been very patient with me when I was having trouble with the configuration of PYTHIA, and I have enjoyed much help from Günter Folger, Denis Wright and John Apostolakis from the GEANT4 collaboration.

When I saw sunlight again after having traveled deep in the bowels of GEANT4 I received much help from Andrea dell'Acqua on the interfacing of my simulation software with the ATLAS simulation framework. It was not as easy as it looks today but we managed to understand all the snags in the end.

In the analysis work I appreciated immensely the input, cooperation and general support I received from the Stockholm group (David Milstead, Marianne Johansen and Sten Hellman). It really was most refreshing to work with you guys.

As is probably no secret for anyone making it this far in the thesis a *lot* of CPU time has been spent running simulations of varying complexity. In this context let me here take a moment to thank the friendly workaholics at the Danish Centre for Scientific Computing. Getting immediate answers to emails sent at 1 am and seeing immediate actions from Daniel Kalici means a great deal at times.

A very important factor during a ph.d. is the social environment. That has never been found lacking. Thomas, Trine & Esben have always been great company, no matter where in the world we where (or at which altitude). The movie nights at Daniel's have been nice (and at times necessary) diversions from everyday life.

Toward the end of the writing of this thesis a large amount of people have been extremely helpful with the proof reading. Any mistakes left behind are surely my own.

Finally, thanks to all of the family and friends who have made these... many years at the University of Copenhagen memorable and of course thanks to my love, Birte just for being there.

When all is said and done...

Appendix A

On Software Versions and ATLAS Releases

A technical question that often appears in the presentation of any type of analysis within the ATLAS collaboration and indeed in many places in High-Energy Physics is which versions were used of different applications. In this Appendix a summary is given on choices for releases and settings.

A.1 Releases in Play

The releases used in the production steps of the analysis were both candidates to be production releases in ATLAS. The releases that were used were 12.0.31 and 12.0.6. All analysis was performed on AOD (Analysis Object Data, [ATL04]) using release 12.0.6.

A.2 Single-Particle Samples

At the time where the first single-particle samples were being produced release 12.0.31 was the newest candidate for a production release why it was used for the private production. The higher masses were not generated until later leading to the release summary in table

$m_{sparticle}$ (GeV/c^2)	Simulation	Digitization	Reconstruction
100	12.0.31	12.0.31	12.0.6
300	12.0.31	12.0.31	12.0.6
600	12.0.31	12.0.31	12.0.6
1000	12.0.31	12.0.31	12.0.6
1300	12.0.6	12.0.6	12.0.6
1600	12.0.6	12.0.6	12.0.6
2000	12.0.6	12.0.6	12.0.6

Table A.1: *Releases used for different single-particle samples.*

A.3 Split SUSY Samples

The details of the physics setup of PYTHIA are covered in detail in section 8.1.1. One deviation from ATLAS standards deserve mentioning here, though. The standard ATLAS PYTHIA setup dictates that the treatment of Multiple Interactions (MI) be done using the switch `MSTP(82)=4`. This scheme results in colour string configurations that are not handled by the R-hadron fragmentation [Sjo]. The setup was therefore switched to `MSTP(81)=1`.

As the implementation of the custom hadronisation routines into the ATLAS PYTHIA framework required some coding all event generation was performed using release 12.0.31.

The releases used for the SSUSY samples are listed in table A.2.

$m_{\tilde{g}}$ (GeV/c^2)	Simulation	Digitization	Reconstruction
100	12.0.31	12.0.31	12.0.6
300	12.0.31	12.0.31	12.0.6
600	12.0.31	12.0.31	12.0.6
1000	12.0.6	12.0.6	12.0.6
1300	12.0.6	12.0.6	12.0.6
1600	12.0.6	12.0.6	12.0.6
2000	12.0.6	12.0.6	12.0.6

Table A.2: *Releases used for SSUSY samples*

A.4 Background Samples

As mentioned in section 8.3 standard CSC sample definitions were used as templates for the background generation with a generator level muon filter applied. All stages of the full chain were run using release 12.0.6.

A.5 Geometry Tags

The ATLAS geometry database contains many different configurations and descriptions of the individual sub-components. These are logically ordered into *geometry tags*. A geometry tag is a tag specifying a coherent set of conditions such as magnetic field inhomogeneities or detector misalignments. All single particle samples were run using `ATLAS-CSC-00-00-00` while the full events were run with the more realistic setup defined by the tag `ATLAS-CSC-01-02-00`. The details on these geometry tags may be found in [ATLb].

Bibliography

[A$^+$] D. Ayres et al., *DESIGN REPORT OF THE FERMILAB COLLIDER DETECTOR FACILITY (CDF), AUGUST, 1981*, Batavia, Usa: Fermilab (1981) 331p.

[A$^+$00] S. Ambrosanio et al., *SUSY long-lived massive particles: Detection and physics at the LHC*, (1200), hep-ph/0012192.

[ACD01] T. Appelquist, H. C. Cheng and B. A. Dobrescu, *Bounds on universal extra dimensions*, Phys. Rev. **D64** (2001).

[ADG$^+$05] A. Arvanitaki, C. Davis, P. W. Graham, A. Pierce and J. G. Wacker, *Limits on split supersymmetry from gluino cosmology*, Phys. Rev. **D72**, 075011 (2005), hep-ph/0504210.

[AEBC06] M. Aharrouche et al. (ATLAS Electromagnetic Barrel Calorimeter Collaboration), *Energy linearity and resolution of the ATLAS electromagnetic barrel calorimeter in an electron test- beam*, (2006), physics/0608012.

[AHDD98] N. Arkani-Hamed, S. Dimopoulos and G. R. Dvali, *The hierarchy problem and new dimensions at a millimeter*, Phys. Lett. **B429**, 263–272 (1998).

[AHDGR05] N. Arkani-Hamed, S. Dimopoulos, G. F. Giudice and A. Romanino, *Aspects of split supersymmetry*, Nucl. Phys. **B709**, 3–46 (2005), hep-ph/0409232.

[AL] *ALICE: Technical proposal for a large ion collider experiment at the CERN LHC*, CERN-LHCC-95-71.

[ℵ90] D. Decamp et al. (ALEPH Collaboration), *A PRECISE DETERMINATION OF THE NUMBER OF FAMILIES WITH LIGHT NEUTRINOS AND OF THE Z BOSON PARTIAL WIDTHS*, Phys. Lett. **B235**, 399 (1990).

[ATLa] A. Airapetian et al. (ATLAS Collaboration), *ATLAS calorimeter performance*, CERN-LHCC-96-40.

[ATLb] Top level tags in the ATLAS Geometry Database, `https://twiki.cern.ch/twiki/bin/view/Atlas/AtlasGeomDBTags`.

[ATLc] S. Hellman, D. Milstead and M. Ramstedt (ATLAS Collaboration), *A Strategy to Detect and Identify Gluino R-hadrons with the ATLAS Experiment at the LHC*, ATL-COM-PHYS-2005-065.

[ATL04] D. Adams et al. (ATLAS Collaboration), *The ATLAS Computing Model*, (2004), ATL-SOFT-2004-007.

[AYM75] X. Artru, G. B. Yodh and G. Mennessier, *Practical Theory of the Multilayered Transition Radiation Detector*, Phys. Rev. **D12**, 1289 (1975).

[B+a] E. . Benedikt, M. et al., *LHC Design Report. Vol III. The LHC injector chain*, CERN-2004-003-V-3.

[B+b] E. . Bruning, O. et al., *LHC design report. Vol. I: The LHC main ring*, CERN-2004-003-V-1.

[B+00] H. Baer et al., *Low-energy supersymmetry phenomenology*, (0300), hep-ph/9503479.

[B+90] C. Beard et al., *THIN, HIGH GAIN WIRE CHAMBERS FOR ELECTROMAGNETIC PRESAMPLING IN OPAL*, Nucl. Instr. Meth. **A286**, 117 (1990).

[B+97] K. H. Becks et al., *Progress in the construction of the DELPHI pixel detector*, Nucl. Instrum. Meth. **A395**, 398–403 (1997).

[BA05] P.-H. Beauchemin and G. Azuelos, *Dijet Signals from Universal Extra Dimension Scenario in ATLAS*, (2005), ATL-PHYS-PUB-2005-003.

[BCCW03] J. M. Butterworth, J. P. Couchman, B. E. Cox and B. M. Waugh, *KtJet: A C++ implementation of the K(T) clustering algorithm*, Comput. Phys. Commun. **153**, 85–96 (2003), hep-ph/0210022.

[BV] R. K. Bock and A. Vasilescu, *The particle detector briefbook*, Berlin, Germany: Springer (1998) 131 p.

[C+01] G. Corcella et al., *HERWIG 6: An event generator for hadron emission reactions with interfering gluons (including supersymmetric processes)*, JHEP **01**, 010 (2001), hep-ph/0011363.

[CDF] CDF Website, `http://www-cdfonline.fnal.gov/`.

[Clo] F. E. Close, *AN INTRODUCTION TO QUARKS AND PARTONS*, Academic Press/london 1979, 481p.

[CM67] S. R. Coleman and J. Mandula, *All Possible Symmetries of the S Matrix*, Phys. Rev. **159**, 1251–1256 (1967).

[CMS06] M. Della Negra et al. (CMS Collaboration), *CMS physics : Technical Design Report v.1 : Detector performance and software*, (2006), CERN-LHCC-2006-001, CMS-TDR-008-1.

[D+74] S. Deser et al., *Nonrenormalizability of Einstein Yang-Mills Interactions at the One Loop Level*, Phys. Lett. **B50**, 491 (1974).

[dB94] W. de Boer, *Grand unified theories and supersymmetry in particle physics and cosmology*, Prog. Part. Nucl. Phys. **33**, 201–302 (1994), hep-ph/9402266.

[DM00] M. Drees and S. P. Martin, *Implications of SUSY model building*, (0300), hep-ph/9504324.

[DP96] G. R. Dvali and A. Pomarol, *Anomalous U(1) as a mediator of supersymmetry breaking*, Phys. Rev. Lett. **77**, 3728–3731 (1996), hep-ph/9607383.

[DRGG75] A. De Rujula, H. Georgi and S. L. Glashow, *Hadron Masses in a Gauge Theory*, Phys. Rev. **D12**, 147–162 (1975).

[Ege] U. Egede, *Electron identification with the ATLAS detector at the Large Hadron Collider*, CERN-THESIS-97-003.

[F$^+$07] M. Fairbairn et al., *Stable massive particles at colliders*, Phys. Rept. **438**, 1–63 (2007), hep-ph/0611040.

[Fes85] H. Fesefeldt, *GHEISHA user manual:* The Simultion of Hadronic Showers, PITHA **02** (1985).

[FW02] S. Frixione and B. R. Webber, *Matching NLO QCD computations and parton shower simulations*, JHEP **06**, 029 (2002), hep-ph/0204244.

[G4] *Physics Reference Manual v. 7.1 Ch. 20*, [http://geant4.web.cern.ch/geant4/].

[G403] S. Agostinelli et al. (GEANT4 Collaboration), *GEANT4: A simulation toolkit*, Nucl. Instrum. Meth. **A506**, 250–303 (2003).

[GG82] L. Girardello and M. T. Grisaru, *Soft Breaking of Supersymmetry*, Nucl. Phys. **B194**, 65 (1982).

[GH] J. Gonzalez and A. L. Hueros, *The Conformal Anomaly as a Sourse for Supersymmetry Breaking*, FTUAM/87-12.

[GR99] G. F. Giudice and R. Rattazzi, *Theories with gauge-mediated supersymmetry breaking*, Phys. Rept. **322**, 419–499 (1999), hep-ph/9801271.

[GR04] G. F. Giudice and A. Romanino, *Split supersymmetry*, Nucl. Phys. **B699**, 65–89 (2004), hep-ph/0406088.

[Gro] T. Group, *Design Report Tevatron 1 project*, FERMILAB-DESIGN-1984-01.

[Hig64] P. W. Higgs, *Broken Symmetries and the Masses of Gauge Bosons*, Phys. Rev. Lett. **13**, 508–509 (1964).

[Hig66] P. W. Higgs, *Spontaneous Symmetry Breakdown Without Massless Bosons*, Phys. Rev. **145**, 1156–1163 (1966).

[HLMR04] J. L. Hewett, B. Lillie, M. Masip and T. G. Rizzo, *Signatures of long-lived gluinos in split supersymmetry*, JHEP **09**, 070 (2004), hep-ph/0408248.

[HLS75] R. Haag, J. T. Lopuszanski and M. Sohnius, *All Possible Generators of Supersymmetries of the s Matrix*, Nucl. Phys. **B88**, 257 (1975).

[HLT] *ATLAS high-level trigger, data acquisition and controls: Technical design report*, CERN-LHCC-2003-022.

[ID] *ATLAS inner detector: Technical design report. Vol. 2*, CERN-LHCC-97-17.

[Jet] Jet Reconstruction in ATLAS, `https://twiki.cern.ch/twiki/bin/view/Atlas/JetS/`.

[K+07] D. J. Kapner et al., *Tests of the gravitational inverse-square law below the dark-energy length scale*, Phys. Rev. Lett. **98**, 021101 (2007), hep-ph/0611184.

[KHN07] A. C. Kraan, J. B. Hansen and P. Nevski, *Discovery potential of R-hadrons with the ATLAS detector*, Eur. Phys. J. **C49**, 623–640 (2007), hep-ex/0511014.

[Kit07] T. H. Kittelmann, *Slepton Spin Determination and Simulation of the Transition Radiation Tracker at the ATLAS Experiment*, PhD thesis, University of Copenhagen, 2007.

[Kra] A. C. Kraan, Personal communication.

[Kra04a] A. C. Kraan, *Interactions and Detection of R-hadrons*, (2004), available at http://www.nbi.dk/~ackraan/.

[Kra04b] A. C. Kraan, *Interactions of heavy stable hadronizing particles*, Eur. Phys. J. **C37**, 91–104 (2004), hep-ex/0404001.

[LAr] *ATLAS liquid argon calorimeter: Technical design report*, CERN-LHCC-96-41.

[Lb] S. Amato et al. (LHCb Collaboration), *LHCb technical proposal*, CERN-LHCC-98-04.

[Leo93] W. R. Leo, *Techniques for Nuclear and Particle Physics Experiments, A How-to Approach*, Springer-Verlag, 2nd edition, 1993.

[LEP] *LEP Design Report: Vol. 2. The LEP Main Ring*, CERN-LEP-84-01.

[LEPH03] R. Barate et al. (LEP Working Group for Higgs boson searches Collaboration), *Search for the standard model Higgs boson at LEP*, Phys. Lett. **B565**, 61–75 (2003), hep-ex/0306033.

[Mat00] A. D. Mattia, *The Level-2 Muon Trigger for the ATLAS Muon Spectrometer*, PhD thesis, University of Roma "La Sapienza", December 2000.

[MCBM83] S. Majewski, G. Charpak, A. Breskin and G. Mikenberg, *A THIN MULTIWIRE CHAMBER OPERATING IN THE HIGH MULTIPLICATION MODE*, Nucl. Instrum. Meth. **217**, 265–271 (1983).

[MMN02a] C. Macesanu, C. D. McMullen and S. Nandi, *Collider implications of universal extra dimensions*, Phys. Rev. **D66**, 015009 (2002), hep-ph/0201300.

[MMN02b] C. Macesanu, C. D. McMullen and S. Nandi, *New signal for universal extra dimensions*, Phys. Lett. **B546**, 253–260 (2002), hep-ph/0207269.

[MP06] S. Mehlhase and T. C. Petersen, A probability based approach to PID in the TRT detector of ATLAS, ATL-COM-INDET-2006-017, October 2006.

[MSTV04] M. Maltoni, T. Schwetz, M. A. Tortola and J. W. F. Valle, *Status of global fits to neutrino oscillations*, New J. Phys. **6**, 122 (2004), hep-ph/0405172.

[mTD] *ATLAS muon spectrometer: Technical design report*, CERN-LHCC-97-22.

[Off] C. P. Office, `http://press.web.cern.ch/press/`.

[Ole07] P. Olesen, *General Relativity and Cosmology*, University of Copenhagen, The Niels Bohr Institute, 2007.

[P+02] J. Pumplin et al., *New generation of parton distributions with uncertainties from global QCD analysis*, JHEP **07**, 012 (2002), hep-ph/0201195.

[PDF] Parton Distribution Functions, `http://durpdg.dur.ac.uk/HEPDATA/PDF`.

[PDG06] W. M. Yao et al. (Particle Data Group Collaboration), *Review of particle physics*, J. Phys. **G33**, 1–1232 (2006).

[Pes97] M. E. Peskin, *Beyond the standard model*, (1997), hep-ph/9705479.

[Pet94] J. Petersen, *Elementarpartikelfysik*, NBI-tryk (1994), Lecture notes 3. rev. edition.

[PPA] Pythia 6 HepForge Page, `http://projects.hepforge.org/pythia6/`.

[PS] M. E. Peskin and D. V. Schroeder, *An Introduction to quantum field theory*, Reading, USA: Addison-Wesley (1995) 842 p.

[Px07] C. Meroni (ATLAS Pixel Collaboration), *Overview and status of the ATLAS pixel detector*, Nucl. Instrum. Meth. **A572**, 92–95 (2007).

[Riz07] A. Rizzi, *Search and Reconstruction of Heavy Stable Charged Particles with the CMS Experiment at LHC*, PhD thesis, Scuola Normale Superiore, 2006/07.

[Riz01] T. G. Rizzo, *Probes of universal extra dimensions at colliders*, Phys. Rev. **D64**, 095010 (2001), hep-ph/0106336.

[RS99] L. Randall and R. Sundrum, *Out of this world supersymmetry breaking*, Nucl. Phys. **B557**, 79–118 (1999), hep-th/9810155.

[S+04] P. Skands et al., *SUSY Les Houches accord: Interfacing SUSY spectrum calculators, decay packages, and event generators*, JHEP **07**, 036 (2004), hep-ph/0311123.

[Sjo] T. Sjostrand, Personal communication.

[Sjo94] T. Sjostrand, *High-energy physics event generation with PYTHIA 5.7 and JETSET 7.4*, Comput. Phys. Commun. **82**, 74–90 (1994).

[SMS06] T. Sjostrand, S. Mrenna and P. Skands, *PYTHIA 6.4 physics and manual*, JHEP **05**, 026 (2006), hep-ph/0603175.

[SSC] *Conceptual Design of the Superconducting Super Collider*, SSC-SR-2020.

[ST00] U. Sarid and S. D. Thomas, *Mesino-antimesino oscillations*, Phys. Rev. Lett. **85**, 1178–1181 (2000), hep-ph/9909349.

[Str00] M. J. Strassler, *Possible effects of a hidden valley on supersymmetric phenomenology*, (0700), hep-ph/0607160.

[SuperK99] Y. Hayato et al. (Super-Kamiokande Collaboration), *Search for proton decay through p –¿ anti-nu K+ in a large water Cherenkov detector*, Phys. Rev. Lett. **83**, 1529–1533 (1999), hep-ex/9904020.

[SZ00] M. J. Strassler and K. M. Zurek, *Echoes of a hidden valley at hadron colliders*, (0400), hep-ph/0604261.

[TCSG05] A. Tricoli, A. M. Cooper-Sarkar and C. Gwenlan, *Uncertainties on W and Z production at the LHC*, (2005), hep-ex/0509002.

[TDRa] *ATLAS: Detector and physics performance technical design report. Volume 1*, CERN-LHCC-99-14.

[TDRb] *ATLAS detector and physics performance. Technical design report. Vol. 2*, CERN-LHCC-99-15.

[Usa] Usage Documentation, `http://cern.ch/r-hadrons/`.

[VvV07] W. Verkerke and I. van Vulpen, *Commissioning ATLAS using top-quark pair production*, (2007), ATL-COM-PHYS-2007-023.